MATHEMATICAL ANALYSIS AND NUMERICAL SIMULATION OF BOSE-EINSTEIN CONDENSATION

ZHANG YANZHI

(B.Sc., Chongqing University)

A THESIS SUBMITTED

FOR THE DEGREE OF DOCTOR OF PHILOSOPHY

DEPARTMENT OF MATHEMATICS

NATIONAL UNIVERSITY OF SINGAPORE

2006

Acknowledgements

First and foremost, I would like to thank my supervisor, Assoc. Prof. Bao Weizhu, who gave me the opportunity to work on such an interesting research project, paid patient guidance to me, reviewed my thesis and gave me invaluable help and constructive suggestion on it.

It's my pleasure to express my appreciation to Prof. Du Qiang and Prof. Fu Libin for their invaluable suggestions and stimulating discussions, and for sharing wealth of knowledge and experience so freely.

I would also like to thank National University of Singapore for awarding me the Research Scholarship which financially supported me throughout my Ph.D candidature.

My sincere thanks go to all my fellow postgraduates and friends, especially Lim Fong Yin, Yang Li, Wang Hanquan and Cai Minghuang for their discussions and helps in my research. I thank my friends, Wu Xiaowa, Chen Shuli, Wang Xiaoyan, Lin Ying, Li Huiping and Sandy Tin Maung, for all the encouragement, emotional support, comradeship and entertainment they offered.

I am forever grateful to my parents for their encouragement, steadfast support and

endless love when it was most required. They have continued to give off themselves so that their children will prosper. I am also indebted to my entire family for providing a loving environment for me.

Zhang Yanzhi

March 2006

Contents

Summary

Since its first realization in dilute bosonic atomic gases, Bose-Einstein condensation (BEC) has been extensively studied in both theory and experiment. It has spurred great excitement in the atomic physics community and attracted the interest of scientists from different fields. Recently, with the observation of quantized vortices in rotating BEC, much attention has been focused on its dynamical phenomena associated with superfluidity.

The main purpose of this thesis is to conduct an extensive analytical and numerical investigation of Bose-Einstein condensation in dilute alkali gases. In both weakly interacting regime, i.e. $|\beta_d| \ll 1$, and strongly repulsive interacting regime, i.e. $\beta_d \gg 1$, the asymptotic approximations up to $o(1)$ in terms of β_d are derived for the ground state and its energy and chemical potential. A backward forward Euler Fourier pseudospectal (BFFP) method is proposed to compute the ground state of non-rotating or rotating BEC. Due to its spectral accuracy in space, the BFFP method is very efficient and accurate, especially for the case of fast rotating BEC with strongly repulsive interaction. The ground states in different potentials are studied numerically for two dimensional (2D) and three dimensional (3D) cases.

The dynamics of BEC are also investigated analytically and numerically. Along

the analytical front, we prove the conservation of the angular momentum expectation when the external trapping potential is radially symmetric in 2D case, and respectively cylindrically symmetric in 3D case. A second-order ordinary differential equation (ODE) is derived to describe the time evolution of the condensate width as a periodic function with/without a perturbation. Also a second-order ODE system is found to characterize the dynamics of a stationary state with its center shifted. By solving this ODE system, different motion patterns of the mass center are classified. On the numerical front, several high-order numerical methods are developed to simulate the dynamics of non-rotating and rotating BEC.

We demonstrate numerically that the central vortex states with winding number $|m| = 1$ are dynamically stable, while those with winding number $|m| > 1$ are dynamically unstable. Under two different initial patterns, the interactions between two $|m| = 1$ vortices are studied, and it is found that the interactions in non-interacting BEC, i.e. $\beta_d = 0$, and in interacting BEC, i.e. $\beta_d \neq 0$, are distinctly different. The dynamics of vortex lattices in an anisotropic potential are also reported, which demonstrates the efficiency and high accuracy of our numerical methods.

Our investigations on single-component BEC are also extended to two-component rotating condensates, where both ground states and dynamics are studied analytically and numerically.

Based on the Ginzburg-Landau-Schrödinger equation (GLSE), the vortex dynamics and interactions in superconductivity and superfluidity are studied asymptotically and numerically. The reduced dynamic laws for the vortex motion are reviewed, and under some proper initial data, they are solved analytically. On the other hand, by directly simulating the GLSE, the vortex dynamics and interaction are investigated numerically to compare with those from the reduced dynamic laws. Some conclusive experimental findings are obtained, and discussions on numerical and theoretical results are made to provide further understanding of vortex dynamics of the GLSE.

List of Notations

$\hbar$	Planck constant
a_s	s-wave scattering length
t	time
$\mathbf{x}$	Cartesian coordinate
(r, θ)	polar coordinate
(r, θ, z)	cylindrical coordinate
∇	gradient operator
div	divergence operator
$\otimes$	tensor product
$\mathbf{P} = -i\hbar\nabla$	momentum operator
$\mathbf{L} = \mathbf{x} \times \mathbf{P}$	angular momentum operator
$L_z = -i\hbar(x\partial_y - y\partial_x)$	z-component of angular momentum rotation
f^*	conjugate of a complex function f
$\mathrm{Re}\,(f)$	real part of a complex function f
$\mathrm{Im}\,(f)$	imaginary part of a complex function f
Ω	angular velocity of the laser beam
ω_x, ω_y, ω_z	trapping frequencies in x-, y- and z-direction

$\widehat{\Psi}(\mathbf{x}, t)$	Bose field operator
$\psi(\mathbf{x}, t)$	macroscopic wave function
$\phi(\mathbf{x})$	stationary state
$\deg \psi$	index (winding number) of $\psi(\mathbf{x}, t)$
$\langle L_z \rangle(t)$	angular momentum expectation
$\sigma_\alpha(t)$ $(\alpha = x, y \text{ or } z)$	condensate width in α-direction
$\rho(\mathbf{x}, t) = \lvert\psi(\mathbf{x}, t)\rvert^2$	position density
$S(\mathbf{x}, t) = \arg(\psi(\mathbf{x}, t))$	phase of the wave function
$\mathbf{J}(\mathbf{x}, t) = \rho(\mathbf{x}, t)\nabla S(\mathbf{x}, t)$	current density
$\mathbf{u}(\mathbf{x}, t) = \nabla S(\mathbf{x}, t)$	quantum hydrodynamic velocity

Chapter 1

Introduction

An important consequence of quantum mechanics is that all objects appear to be wavy for sufficiently short length scales. We cannot see this effect in our everyday life because the wavelengths of the objects larger than an electron are too short to be observed by the naked eyes. However, there is an exception in the case of extreme cold. As objects are cooled very close to absolute zero, their characteristic quantum-mechanical wavelengths become increasingly long. This tendency towards ever-expanding wavelength ends in a dramatic phenomenon known as Bose-Einstein condensation (BEC).

1.1 Bose-Einstein condensation

Bose-Einstein condensation (BEC) was predicted in 1924 by Einstein [56], as he reviewed and translated a work of Bose [26] about the statistics of photons. Therein, Bose derived Planck's famous black-body radiation formula on the basis of the thermodynamic properties of quantized massless harmonic oscillators generating a free electromagnetic field. Einstein devoted to using Bose statistics to describe the quanta of light, and he predicted that a phase transition should occur in a gas of noninteracting atoms at some critical temperature. Below this critical temperature, a finite fraction of the total number of particles would "condense" into the

lowest-energy single-particle state, the quantum mechanical ground state. As these condensed particles do not contribute to the entropy of the system, Einstein interpreted this phenomenon as a phase transition.

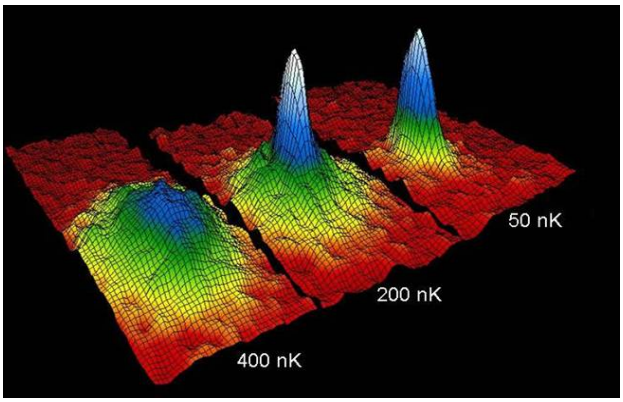

Figure 1.1: Images of the velocity distribution of Rubidium (Rb) atoms taken by means of expansion method [42]. Left: just before the appearance of the Bose-Einstein condensate; Middle: just after the appearance of the condensate; Right: after further evaporation, leaving a sample of nearly pure condensate.

In 1995, with the development of different cooling techniques, Bose-Einstein condensation was first observed in vapours of ^{87}Rb (cf. Fig. 1.1) [8] and ^{23}Na [42]. Later, it was achieved in many alkali gases, including ^{7}Li [27], ^{85}Rb [40], ^{41}K [102], ^{133}Cs [132], spin-polarized hydrogen [65] and metastable triplet ^{4}He [119, 46]. Over the last few years, these systems have been the subject of an explosion of research both experimental and theoretical. Many different fields of physics, like atomic collision, quantum optics, condensed matter physics and even astrophysics, contributed ideas and problems to these specific systems displaying the attractiveness of BEC for researchers.

To appreciate the remarkable new development in this growing field, one should understand the basic properties of BEC in a dilute atomic gas. The most striking feature of BEC is that the wave-like behavior of matter is exhibited on a macroscopic scale due to the condensation of a large number of identical atoms into the same quantum state. This is counter intuitive to our daily experience of world where

objects are distinguishable and behave like particles that follow classical trajectories described by Newton's second laws for motion. Another intriguing property of Bose-condensed system is the unrestricted flow of particles in the sample, such as persistent currents in superfluid helium that flow without observable viscosity, and electric currents in superconductors that flow without observable resistance. These properties of Bose-condensed systems occur because the macroscopic occupation of a quantized mode, such as a vortex which is a localized phase singularity with integer topological charge, can provide a stabilizing mechanism. The recent observation of vortices in fast rotating Bose-Einstein condensation has opened the door to the study of superfluidity in these systems [123, 28].

In a dilute atomic gas, the interactions between particles are very weak so that the wave-like condensate dominates the system and collisions can be treated perturbatively. In this case, one can sum the interaction of all of the particles on a single particle to give an average effect. This approach is called as mean-field theory and with suitable approximations, it gives rise to the Gross-Pitaevskii equation (GPE) that describes the time evolution of the condensate, in which the effect of interactions leads to a density dependent effective potential that makes the dynamics of the condensate nonlinearity. This simple description does not include the fluctuations due to collisions, but just treats their averaged effect.

1.2 Contemporary studies

There has been a series of recent studies which deal with the numerical solution of the time-dependent Gross-Pitaevskii equation (GPE) for time evolution of the condensate and time-independent GPE for stationary states, especially for ground states. In this section, we summarize the main numerical methods and results in the study of BEC and its relative fields.

To compute the ground state of non-rotating BEC, there have been a lot of methods.

Ruprecht *et al.* [122] presented a Crank-Nicolson finite difference (CNFD) method, and also used it to simulate the time evolution of BEC. Edwards and Burnett [54] developed a Runge-Kutta type (RKFD) method and applied it to solve one dimensional (1D) ground states and three dimensional (3D) ground states with spherical symmetry. Later, Adhikari [1] used this approach to compute two dimensional (2D) ground states with radial symmetry. Bao and Tang [22] proposed a method by directly minimizing the energy functional via finite element approximation. Recently, Bao and Du [13] introduced a continuous normalized gradient flow with diminishing energy, and proposed two methods: backward Euler finite difference (BEFD) method and time-splitting sine-pseudospectral (TSSP) method, to discretize it. Chang *et al.* [33, 34] also proposed a Gauss-Seidel-type method to compute the energy state of multi-component BEC. Other approaches include a direct inversion in the iterated subspace (DIIS) [127], an explicit imaginary-time algorithm [32, 37] and a simple analytical type method [45].

Basically, the methods for computing the ground state of non-rotating BEC can be classified into two groups: pseudospectral method, e.g. TSSP method, and finite difference method, e.g. CNFD, RKFD and BEFD method. Each method has its own advantages and disadvantages: i) The TSSP method is explicit, conditionally stable and of spectral accuracy in space. It is energy diminishing when time step satisfies a constraint. However, the time-splitting error does not vanish at steady states, and thus the time step must be chosen very small to get the ground state in high accuracy, which makes the total computational time very large. ii) Among all finite difference methods, the most popular one is the BEFD method. It is implicit, unconditionally stable and energy diminishing for any time step, and thus the time step can be chosen very large in practical computation. However, it is only of second-order accuracy in space. When high accuracy is required or the solution has multiscale structures, much more grid points must be taken so as to get a reasonable solution. Therefore, the memory requirement is a big burden in this case. iii) Other finite difference or finite element methods are usually of low-order accuracy in space

and in many cases they have a very severe constraint for time step due to stability or energy diminishing requirement. On the other hand, for rotating BEC, currently the numerical methods are very limited, and the available methods are all low-order finite difference methods [130, 4, 5, 23].

In order to study the dynamics of BEC, especially in the strongly repulsive interacting regime, an efficient and accurate numerical method is one of the key issues, which should preserve the analytical properties of the time-dependent GPE. So far, the methods for computing the dynamics of non-rotating BEC are mainly grouped into twofold. One is the finite difference method, e.g. Crank-Nicolson finite difference (CNDF) method [122], explicit finite difference method [32] and alternating direction implicit (ADI) method [129]. Generally, this type of method has second or fourth order accuracy in space. The other one is the pseudospectral method with spectral accuracy in space, such as time-splitting spectral method [16, 21] and Runge-Kutta pseudospectral method [2, 104]. It has been demonstrated that the pseudospctral methods are much better than the finite difference methods; thus they were applied to study collapse and explosion of BEC in three dimension [17] and dynamics of multi-component BEC [11], which are very challenging problems in numerical simulations of BEC. However, due to the appearance of the rotational term, these high-order accuracy pseudospectral methods [16, 21] cannot be directly used to compute the dynamics of rotating BEC. Currently, the numerical methods used in the physics literature for studying dynamics of rotating BEC still remain limited, and the available ones are usually low-order finite difference methods [84, 131]. But in fast rotating BEC with strongly repulsive interaction, a large number of vortices would appear in the condensate, and the numerical description of them needs high resolution; thus the low-order accuracy methods have difficulty in this case.

Vortices are a characteristic feature of a superfluid; it is only their presence which permits circulation of the fluid, or allows two flows with different velocities to join.

There have been numerous investigations about the properties of vortices in condensates. For non-rotating condensation, Edwards *et al.* [55] calculated vortex and ground states of a trap, and showed that the gap between the vortex and ground state energies decreases as the number of atoms in the condensate increases. Dalfovo and Stringari [41] have made extensive numerical investigations of the shape characteristics of condensates. Lundh *et al.* [98] studied the expansion of a condensate containing a vortex both analytically and numerically. Rokhsar [120] argued that central vortex states are all thermodynamically unstable, although in that work he does not make the distinction between thermodynamical and dynamical stability. Fetter [62] investigated the stability of vortices, and found that excitations could cause the vortex to move about the condensate. Similarly, many investigations have been conducted on vortices in rotating BEC. In the line of adding a far-blue-detuned Gaussian laser stirrer, Caradoc-Davies *et al.* [30, 29], Jackson *et al.* [75, 76] and Bao *et al.* [19] studied the generation of vortices from the ground state and the dynamics of vortices. In the line of BEC in a rotational frame, Aftalion and Du [6], Aftalion and Riviere [7] studied numerically and asymptotically the ground state, critical angular velocity and energy diagram in the Thomas-Fermi (TF) or semiclassical regime; Aftalion and Danaila [4] and Modugno *et al.* [103] reported bent vortices, e.g. S-shaped vortex and U-shaped vortex, in a cigar-shaped condensate and compared with experimental results [121]; García-Ripoll and Pérez-García [66, 67, 68] studied the stability of central vortex states; Tsubota *et al.* [130] reported vortex lattice formation. Moreover, Svidzinsky and Fetter [127] have studied the dynamics of a vortex line depending on its curvature. However, there is still no report about the interactions between a few vortices, which is an attracting topic in physics.

Recently, there have been many analytical and numerical studies on vortex dynamics and interactions in superconductivity and superfluidity by considering the Ginzburg-Landau-Schödinger equation (GLSE). For the Ginzburg-Landau equation (GLE), Neu [105, 106] found numerically that vortices with winding number $m = \pm 1$ are dynamically stable, and respectively those with $|m| > 1$ are dynamically unstable.

Using asymptotic analysis, he showed that a pair of vortices evolving under GLE with like (opposite) winding numbers undergoes a repulsive (attractive) interaction. Later Pismen *et. al* [115] extended Neu's studies. E [53] studied the dynamics of vortices in the asymptotic limit when the core size of a vortex is much smaller than the inter-vortex distance, and he derived ODEs to govern the evolution of these vortices. Similar investigations have also been conducted by Chapman [35], Weinstein and Xin [134]. Lin [94, 95] showed that the energies of solutions in the GLE flow are concentrated at vortices in 2D case, and respectively filaments in 3D case. Ovchinnikov and Sigal [107, 108, 110, 111] studied the energy of vortices and their asymptotic behavior; they also examined the stability properties of vortices. The pinning effect of vortices due to impurities was established in [96, 80, 81, 82]. On the numerical side, finite element methods were presented to investigate numerical solutions of the Ginzburg-Landau equation and related Ginzburg-Landau models of superconductivity [49, 47, 83, 6, 36]. The interaction between a few vortices [96, 91, 48], dynamics of vortex lattices [44] as well as the stochastic dynamics [43] have been studied numerically.

For the nonlinear Schrödinger equation (NLSE), Neu [105] found that the vortices behave like point vortices in ideal fluid, and obtained the Hamiltonian equations to govern the dynamics of the vortex centers. Lin and Xin [97] derived vortex motion laws in the incompressible fluid limit on a bounded domain with Dirichlet or Neumann boundary condition. Colliander and Jerrard [39] investigated vortex structures in a torus. Ovchinnikov and Sigal [109, 108] studied vortex structures of the corresponding solutions as well as corrections due to radiation; they also derived equations for the vortex dynamics and radiation by using the method of effective action and geometric solvability. Furthermore, they obtained analytically the dynamical laws for two vortices with like (opposite) winding numbers by solving the governing Hamiltonian equations when the initial distance between two vortex centers is large enough [108]. Due to its dispersive nature and highly oscillating nature in the transverse direction of the nonzero far-field boundary condition, it

is extremely difficult to solve the NLSE numerically. There is still no conclusive numerical result reported in the literature for the stability and interaction of vortices in NLSE. In fact, the dynamical stability of vortices as solutions of the NLSE remains largely an open problem [105].

1.3 Overview of this work

The main purpose of this thesis is to conduct an extensive analytical and numerical investigation of Bose-Einstein condensation (BEC) in dilute alkali gases. The thesis is organized as follows.

In Chapter 2, the Gross-Pitaevskii equation (GPE) describing BEC at low temperatures is derived from the second quantized Hamiltonian. Then it is scaled to become a four-parameter model and further reduced to a lower-dimensional one. A semiclassical scaling is also introduced for the GPE in the strongly repulsive interacting regime. In addition, the stationary states of BEC are discussed based on the time-independent GPE.

In Chapter 3, we derive approximate solutions for the ground state in both weakly and strongly repulsive interacting regimes. To verify these approximations, we propose a backward forward Euler Fourier pseudospectral (BFFP) method which is very efficient, especially for computing the ground state solution of fast rotating BEC. The numerical results in different potentials are also reported for both two-dimensional (2D) and three-dimensional (3D) cases.

In Chapter 4, the conservation of angular momentum expectations and dynamics of condensate widths are investigated analytically, and the dynamics of the mass-center of a stationary state with its center shifted are also discussed in details. Along the numerical front, a second/fourth-order time-splitting sine-pseudospectral (TSSP) method is proposed for computing the dynamics of non-rotating BEC. While for rotating BEC, we present a time-splitting type method and a leap-frog Fourier pseudospectral (LFFP) method.

In Chapter 5, the stability of central vortex states is investigated numerically. Then the interactions between two $m = \pm 1$ vortices are studied under two different initial patterns, and the dynamics of vortex lattices are also reported.

Chapter 6 devotes to the ground states and dynamics of rotating two-component BEC. After introducing the coupled Gross-Pitaevskii equations (CGPEs), we discuss the relationship between the single-component and two-component condensate in certain limiting regime of particle numbers. Then the ground states of rotating two-component BEC are studied for different experiment setups. Along the dynamical side, an efficient numerical method is developed and some numerical results are also reported.

In Chapter 7, the vortex dynamics and interaction in superconductivity and superfluidity are investigated asymptotically and numerically based on the Ginzburg-Landau-Schrödinger equation (GLSE). We review the reduced dynamic laws for the vortex motion and solve them analytically under some proper initial data. By introducing an efficient and accurate method for the GLSE with non-zero far-field condition, the vortex dynamics and interaction are studied numerically and compared with those from the reduced dynamic laws. Some conclusive experimental findings are obtained, and discussions on numerical and theoretical results are also made to provide further understanding of vortex dynamics in the GLSE.

Finally, some conclusive comments are made in Chapter 8, and the directions for future research works are also discussed.

Chapter 2

Gross-Pitaevskii equation

In this chapter, the mathematical model is derived for describing Bose-Einstein condensation (BEC) in the mean field limit, and some notations are also introduced, which are used throughout the remainder of this thesis.

First, the time-dependent Gross-Pitaevskii equation (GPE) is derived from the second quantized Hamiltonian under the approximation of the weakly-interacting Bose gas model. Then to minimize the number of adjustable parameters in simulations, the GPE is scaled to obtain a four-parameter model, and furthermore in certain limiting regimes, it is reduced to a lower-dimensional one. Some important properties of GPE are discussed, and the stationary states of BEC are also studied based on the time-independent GPE. Finally, in the strongly repulsive interacting regime, a semiclassical scaling is introduced to the GPE.

2.1 Gross-Pitaevskii equation

A system of N interacting bosons can be described exactly by the second quantized Hamiltonian in terms of the Bose field operator $\widehat{\Psi}(\mathbf{x}, t)$ which is a function of space $\mathbf{x} = (x, y, z)^T$ and time t. For convenience, here we denote $\widehat{\Psi}(\mathbf{x}) \equiv \widehat{\Psi}(\mathbf{x}, t)$ and only consider the limit condition under which all the particles are condensed into

the same single-particle state. Then the second quantized Hamiltonian for a gas of bosons (all in the same internal state) interacting by binary collisions and contained by an external trapping potential is given by [63, 117, 114, 116],

$$\widehat{H} = \int \widehat{\Psi}^\dagger(\mathbf{x}')H_0\widehat{\Psi}(\mathbf{x}')\,d\mathbf{x}' + \frac{1}{2}\iint \widehat{\Psi}^\dagger(\mathbf{x}')\widehat{\Psi}^\dagger(\mathbf{x})V_{\text{int}}(\mathbf{x}',\mathbf{x})\widehat{\Psi}(\mathbf{x})\widehat{\Psi}(\mathbf{x}')\,d\mathbf{x}d\mathbf{x}', \quad (2.1)$$

where $V_{\text{int}}(\mathbf{x}',\mathbf{x})$ is the interaction potential acting between particles, and $H_0 = -\mathbf{P}^2/2m + V_{\text{ext}}(\mathbf{x}')$ is the single particle Hamiltonian with m the particle mass, $\hbar$ the Planck constant, $\mathbf{P} = -i\hbar\nabla = (p_x, p_y, p_z)^T$ the momentum operator and $V_{\text{ext}}(\mathbf{x}')$ the external trapping potential acting on the system. The operators $\widehat{\Psi}^\dagger(\mathbf{x})$ and $\widehat{\Psi}(\mathbf{x})$ represent the creation and annihilation of a particle at position $\mathbf{x}$ respectively, and they satisfy the crucial Bose commutation rules [63, 116]:

$$\left[\widehat{\Psi}(\mathbf{x}'), \widehat{\Psi}^\dagger(\mathbf{x})\right] = \delta(\mathbf{x}'-\mathbf{x}), \qquad \left[\widehat{\Psi}(\mathbf{x}'), \widehat{\Psi}(\mathbf{x})\right] = \left[\widehat{\Psi}^\dagger(\mathbf{x}'), \widehat{\Psi}^\dagger(\mathbf{x})\right] = 0, \quad (2.2)$$

where $\delta(\mathbf{x})$ is the Dirac delta function.

When cold dilute alkali gases are considered, the atomic interactions are dominated by low-energy two-body s-wave collisions. These essentially elastic, hard-sphere collisions can be approximated by the pseudopotential defined as [133],

$$V_{\text{int}}(\mathbf{x}',\mathbf{x}) = U_0\,\delta(\mathbf{x}-\mathbf{x}'), \quad (2.3)$$

where $U_0 = 4\pi\hbar^2 a_s/m$ with a_s the s-wave scattering length (positive for a repulsive interaction and negative for an attractive interaction). Substituting (2.3) into (2.1) and integrating over all $\mathbf{x}$-space leads to

$$\widehat{H} \;=\; \int \widehat{\Psi}^\dagger(\mathbf{x}')H_0\widehat{\Psi}(\mathbf{x}')\,d\mathbf{x}' + \frac{U_0}{2}\int \widehat{\Psi}^\dagger(\mathbf{x}')\widehat{\Psi}^\dagger(\mathbf{x}')\widehat{\Psi}(\mathbf{x}')\widehat{\Psi}(\mathbf{x}')\,d\mathbf{x}'. \quad (2.4)$$

On the other hand, the Heisenberg equation for motion of $\widehat{\Psi}(\mathbf{x})$ is given by

$$i\hbar\frac{\partial}{\partial t}\widehat{\Psi}(\mathbf{x}) = \left[\widehat{\Psi}(\mathbf{x}),\, \widehat{H}\right]. \quad (2.5)$$

Noticing (2.4) and the commutation rules in (2.2), we can get

$$\begin{aligned} i\hbar\frac{\partial}{\partial t}\widehat{\Psi}(\mathbf{x}) &= \widehat{\Psi}(\mathbf{x})\widehat{H} - \int \left[\widehat{\Psi}(\mathbf{x})\widehat{\Psi}^{\dagger}(\mathbf{x}') - \delta(\mathbf{x}-\mathbf{x}')\right] H_0\widehat{\Psi}(\mathbf{x}')\, d\mathbf{x}' \\ &\quad -\frac{U_0}{2}\int \left[\widehat{\Psi}(\mathbf{x})\widehat{\Psi}^{\dagger}(\mathbf{x}') - 2\delta(\mathbf{x}-\mathbf{x}')\right] \widehat{\Psi}^{\dagger}(\mathbf{x}')\widehat{\Psi}(\mathbf{x}')\widehat{\Psi}(\mathbf{x}')\, d\mathbf{x}' \\ &= \left[H_0 + U_0\widehat{\Psi}^{\dagger}(\mathbf{x})\widehat{\Psi}(\mathbf{x})\right]\widehat{\Psi}(\mathbf{x}). \end{aligned} \tag{2.6}$$

Since the system is in a single-particle state with macroscopic occupation, the Bose field operator $\widehat{\Psi}(\mathbf{x})$ can be replaced by a macroscopic wave function $\psi(\mathbf{x},t)$ and a fluctuation term $\widehat{\delta}(\mathbf{x},t)$ [63], i.e.

$$\widehat{\Psi}(\mathbf{x}) = \sqrt{N}\psi(\mathbf{x},t) + \widehat{\delta}(\mathbf{x},t), \tag{2.7}$$

where N is the total particle number in the condensate and the fluctuation operator $\widehat{\delta}(\mathbf{x},t)$ satisfies $\langle\widehat{\delta}(\mathbf{x},t)\rangle \equiv 0$. It is easy to see that the macroscopic wave function $\psi(\mathbf{x},t)$ can be written as the expectation value of $\widehat{\Psi}(\mathbf{x})$, i.e. $\psi(\mathbf{x},t) = \langle\widehat{\Psi}(\mathbf{x})\rangle/\sqrt{N}$. Inserting (2.7) into (2.6), taking only the leading order terms in ψ and neglecting all terms of $\widehat{\delta}$, we can obtain the time-dependent Gross-Pitaevskii equation (GPE), also known as the nonlinear Schrödinger equation (NLSE) [114, 116],

$$i\hbar\frac{\partial\psi(\mathbf{x},t)}{\partial t} = \left(-\frac{\hbar^2}{2m}\nabla^2 + V(\mathbf{x}) + NU_0|\psi(\mathbf{x},t)|^2\right)\psi(\mathbf{x},t), \tag{2.8}$$

where the potential $V(\mathbf{x}) = V_{\text{ext}}(\mathbf{x})$. In the above approximation, neglecting lower order terms involving the fluctuation operator $\widehat{\delta}$ amounts to neglecting thermal and quantum depletion of the condensate. Therefore, the GPE (2.8) is valid only when the condensate is weakly-interacting and at low temperatures. Due to the nonlinearity of (2.8), it is essential to specify the normalization of the wave function $\psi(\mathbf{x},t)$, i.e.

$$\int_{\mathbb{R}^3} |\psi(\mathbf{x},t)|^2\, d\mathbf{x} = 1. \tag{2.9}$$

With the realization of BEC in atomic gases, much work has devoted to its relationship with superfluids. One of the characteristic features of a superfluid is its response to rotation, in particular the occurrence of quantized vortices. By choosing

a special external potential, quantized vortices can also be observed in BEC, which is viewed as the manifestation of its superfluidity. Currently, there are at least two typical ways to generate quantized vortices from the BEC ground state: i) impose a laser beam rotating with an angular velocity on the magnetic trap holding the atoms to create a harmonic anisotropic potential [127]; ii). add to the stationary magnetic trap a narrow, moving Gaussian potential, representing a far-blue-detuned laser [76]. In a rotating frame, the GPE (2.8) becomes [63, 31, 59, 60, 127, 61, 117],

$$i\hbar\frac{\partial\psi(\mathbf{x},t)}{\partial t} = \left(-\frac{\hbar^2}{2m}\nabla^2 + V(\mathbf{x}) + NU_0|\psi(\mathbf{x},t)|^2 - \Omega L_z\right)\psi(\mathbf{x},t), \tag{2.10}$$

where Ω is the angular velocity of the laser beam, and

$$L_z = xp_y - yp_x = -i\hbar(x\partial_y - y\partial_x) \tag{2.11}$$

is the z-component of the angular momentum $\mathbf{L} = \mathbf{x} \times \mathbf{P}$. Many experimental trapping configurations can be described as a harmonic trapping potential,

$$V(\mathbf{x}) = \frac{m}{2}\left(\omega_x^2x^2 + \omega_y^2y^2 + \omega_z^2z^2\right), \tag{2.12}$$

with ω_x, ω_y and ω_z being the trapping frequencies in x-, y- and z-directions, respectively.

2.2 Dimensionless formalism

To minimize the number of adjustable parameters in simulations and also to scale quantities closer to unity for improving the computational precision, under the normalization condition (2.9), we introduce the dimensionless quantities [23, 14, 138]

$$\widetilde{t} = \omega_{\min}\, t, \qquad \widetilde{\mathbf{x}} = \frac{\mathbf{x}}{a_0}, \qquad \widetilde{\psi} = a_0^{3/2}\psi, \qquad \widetilde{\Omega} = \omega_{\min}\,\Omega \tag{2.13}$$

to nondimensionalize the GPE (2.10), where $\omega_{\min} = \min\{\omega_x, \omega_y, \omega_z\}$ is the inverse of the time unit and $a_0 = \sqrt{\hbar/m\omega_{\min}}$ is the length unit. Then the dimensionless momentum operator $\widetilde{\mathbf{P}}$ can be defined as

$$\widetilde{\mathbf{P}} = \frac{\mathbf{P}}{\sqrt{\hbar m\omega_{\min}}} = -i\,\nabla. \tag{2.14}$$

Inserting (2.13) and (2.14) into (2.10), we can obtain the following dimensionless GPE (here all $\tilde{}$ are removed for simplicity),

$$i\frac{\partial\psi(\mathbf{x},t)}{\partial t} = \left(-\frac{1}{2}\nabla^2 + V(\mathbf{x}) + \beta|\psi(\mathbf{x},t)|^2 - \Omega L_z\right)\psi(\mathbf{x},t), \quad \mathbf{x}\in\mathbb{R}^3, \tag{2.15}$$

where the dimensionless angular momentum rotation term becomes

$$L_z = -i(x\partial_y - y\partial_x), \tag{2.16}$$

and the strength of particle interactions is characterized by the single parameter β given as

$$\beta = \frac{NU_0}{\omega_{\min}\hbar a_0^{3/2}} = \frac{4\pi a_s N}{a_0}. \tag{2.17}$$

The dimensionless harmonic potential is

$$V(\mathbf{x}) = \frac{1}{2}\left(\gamma_x^2x^2 + \gamma_y^2y^2 + \gamma_z^2z^2\right), \qquad \mathbf{x}\in\mathbb{R}^3 \tag{2.18}$$

with $\gamma_x = \omega_x/\omega_{\min}$, $\gamma_y = \omega_y/\omega_{\min}$ and $\gamma_z = \omega_z/\omega_{\min}$.

2.3 Dimension reduction

Experimental investigations have shown that a tight constraint in one or two dimensions can reduce the effective dimensionality of the GPE (2.15). In these treatments, a proper approximation can be used to separate out the dynamics of the tightly confined dimensions [74, 92, 52, 22]. In the following subsections, we first reduce the three-dimensional (3D) GPE to a two-dimensional (2D) one, and if $\Omega = 0$, i.e. for non-rotating BEC, we further reduce the 2D GPE to a one-dimensional (1D) GPE. Without loss of generality, here we assume $\omega_x \le \omega_y \le \omega_z$ in (2.12), i.e. $\gamma_x = 1$ and $1 \le \gamma_y \le \gamma_z$ in (2.18) by choosing $\omega_{\min} = \omega_x$.

2.3.1 Reduction to 2D GPE

In a disk-shaped condensate which is tightly confined in the z-direction, i.e.

$$\omega_y \approx \omega_x, \quad \omega_z \gg \omega_x, \qquad \Longleftrightarrow \qquad \gamma_y \approx 1, \quad \gamma_z \gg 1, \tag{2.19}$$

the 3D GPE (2.15) can be reduced to a 2D GPE with $\mathbf{x} = (x, y)^T$ by assuming that the time evolution does not cause excitations along the z-axis since their energies are much larger than those of the excitations along the x- and y-axis. We may also assume that along the z-axis the condensate wave function can be well described by the ground state wave function and set [74, 22]

$$\psi(\mathbf{x}, t) = \psi_2(x, y, t)\phi_3(z), \tag{2.20}$$

where

$$\phi_3(z) = \left(\int_{\mathbb{R}^2} |\phi_g(x, y, z)|^2 \, dxdy \right)^{1/2} \approx \phi^{\mathrm{w}}(z) = \frac{\gamma_z^{1/4}}{\pi^{1/4}} \exp\left(-\frac{\gamma_z z^2}{2} \right) \tag{2.21}$$

with $\phi_g(x, y, z)$ being the ground state solution of the 3D GPE (2.15). Substituting (2.20) into (2.15), multiplying it by $\phi_3^*(z)$ and integrating with respect to z over $(-\infty, \infty)$, we can get

$$i\frac{\partial \psi_2(\mathbf{x}, t)}{\partial t} = \left[-\frac{1}{2}\nabla^2 + \frac{1}{2}\left(\gamma_x^2 x^2 + \gamma_y^2 y^2 + C\right) + \left(\beta \int_{-\infty}^{\infty} \phi_3^4(z) \, dz \right) |\psi_2|^2 - \Omega L_z \right] \psi_2,$$

where

$$C = \gamma_z^2 \int_{-\infty}^{\infty} z^2 |\phi_3|^2 \, dz + \int_{-\infty}^{\infty} \left| \frac{d\phi_3}{dz} \right|^2 \, dz.$$

Since the GPE is time transverse invariant, ψ_2 can be replaced by $\psi_2 \to \psi e^{-iCt/2}$ which drops the constant C in the trapping potential and gives the 2D GPE [23, 24],

$$i\frac{\partial \psi(\mathbf{x}, t)}{\partial t} = \left(-\frac{1}{2}\nabla^2 + V_2(\mathbf{x}) + \beta_2 |\psi|^2 - \Omega L_z \right) \psi(\mathbf{x}, t), \quad \mathbf{x} \in \mathbb{R}^2, \tag{2.22}$$

where

$$\beta_2 = \beta \int_{-\infty}^{\infty} \phi_3^4(z) \, dz \approx \beta \int_{-\infty}^{\infty} \left(\frac{\gamma_z^{1/4}}{\pi^{1/4}} e^{-\gamma_z z^2/2} \right)^4 \, dz = \beta \sqrt{\frac{\gamma_z}{2\pi}},$$

and the potential $V_2(\mathbf{x}) = \frac{1}{2}\left(\gamma_x^2 x^2 + \gamma_y^2 y^2\right)$.

2.3.2 Reduction to 1D GPE when $\Omega = 0$

For a non-rotating and cigar-shaped condensate, i.e. $\Omega = 0$ and

$$\omega_y \gg \omega_x, \quad \omega_z \gg \omega_x, \qquad \Longleftrightarrow \qquad \gamma_y \gg 1, \quad \gamma_z \gg 1, \tag{2.23}$$

the 2D GPE (2.22) can be further reduced to 1D GPE with $\mathbf{x} = x$. Setting [74, 22]

$$\psi(\mathbf{x}, t) = \psi_1(x, t)\phi_{23}(y, z) \tag{2.24}$$

with

$$\begin{aligned} \phi_{23}(y, z) &= \left(\int_{-\infty}^{\infty} |\phi_g(x, y, z)|^2 \, dx \right)^{1/2} \\ &\approx \phi^{\mathrm{w}}(y, z) = \frac{(\gamma_y \gamma_z)^{1/4}}{\sqrt{\pi}} \exp\left(-\frac{\gamma_y y^2 + \gamma_z z^2}{2} \right), \end{aligned} \tag{2.25}$$

and following the analogous lines used to get the 2D GPE, we can obtain the 1D GPE for non-rotating BEC [24],

$$i\frac{\partial \psi(x, t)}{\partial t} = \left(-\frac{1}{2}\partial_{xx} + V_1(x) + \beta_1 |\psi(x, t)|^2 \right) \psi(x, t), \quad x \in (-\infty, \infty), \tag{2.26}$$

where

$$\beta_1 = \beta \int_{\mathbb{R}^2} \phi_{23}^4(y, z) \, dydz \approx \beta \int_{\mathbb{R}^2} \left[\frac{(\gamma_y \gamma_z)^{1/4}}{\sqrt{\pi}} \exp\left(-\frac{\gamma_y y^2 + \gamma_z z^2}{2} \right) \right]^4 dydz = \beta \frac{\sqrt{\gamma_y \gamma_z}}{2\pi},$$

and the potential $V_1(x) = \frac{1}{2}\gamma_x^2 x^2$.

2.4 Generalized GPE and its properties

For simplicity, we can write the 3D GPE (2.15), 2D GPE (2.22) and especially 1D GPE (2.26) for non-rotating BEC into a unified form, i.e. the d-dimensional GPE [24, 23, 14],

$$i\frac{\partial \psi(\mathbf{x}, t)}{\partial t} = -\frac{1}{2}\nabla^2 \psi + V_d(\mathbf{x})\psi + \beta_d |\psi|^2 \psi - \Omega L_z \psi, \quad \mathbf{x} \in \mathbb{R}^d, \quad t > 0, \tag{2.27}$$

$$\psi(\mathbf{x}, 0) = \psi_0(\mathbf{x}), \quad \mathbf{x} \in \mathbb{R}^d, \qquad \text{with} \quad \|\psi_0\|^2 := \int_{\mathbb{R}^d} |\psi_0(\mathbf{x})|^2 \, d\mathbf{x} = 1, \tag{2.28}$$

where $d = 2, 3$ if $\Omega \neq 0$, and respectively $d = 1, 2, 3$ if $\Omega = 0$, and

$$\beta_d = \beta \begin{cases} \sqrt{\gamma_y \gamma_z}/2\pi, \\ \sqrt{\gamma_z/2\pi}, \\ 1, \end{cases} \qquad V_d(\mathbf{x}) = \begin{cases} \gamma_x^2 x^2/2, & d = 1, \\ (\gamma_x^2 x^2 + \gamma_y^2 y^2)/2, & d = 2, \\ (\gamma_x^2 x^2 + \gamma_y^2 y^2 + \gamma_z^2 z^2)/2, & d = 3. \end{cases} \tag{2.29}$$

The GPE (2.27) is time reversible and time transverse invariant. It also has two important conservation quantities: the normalization of the wave function

$$\|\psi(\cdot,t)\|^2 := \int_{\mathbb{R}^d} |\psi(\mathbf{x},t)|^2 \, d\mathbf{x} \equiv \|\psi(\cdot,0)\|^2 = \int_{\mathbb{R}^d} |\psi_0(\mathbf{x})|^2 \, d\mathbf{x} = 1, \qquad t \geq 0, \quad (2.30)$$

and the energy

$$\begin{aligned} E_{\beta,\Omega}(\psi) &= \int_{\mathbb{R}^d} \left[\frac{1}{2}|\nabla\psi|^2 + V_d(\mathbf{x})|\psi|^2 + \frac{\beta_d}{2}|\psi|^4 - \Omega \mathrm{Re}(\psi^* L_z \psi) \right] d\mathbf{x} \\ &= E_{\beta,\Omega}(\psi_0), \qquad t \geq 0. \end{aligned} \quad (2.31)$$

These properties can be used, in particular, in the benchmark and validation of the numerical algorithms for the GPE (2.27)−(2.28).

2.5 Stationary states

To find a stationary state solution of (2.27), we write

$$\psi(\mathbf{x},t) = e^{-i\mu t}\phi(\mathbf{x}), \quad (2.32)$$

where μ is the chemical potential of the condensate and ϕ is a function independent of time t. Inserting (2.32) into (2.27) gives the following time-independent GPE for $\phi(\mathbf{x})$,

$$\mu\phi(\mathbf{x}) = -\frac{1}{2}\nabla^2\phi + V_d(\mathbf{x})\phi + \beta_d|\phi|^2\phi - \Omega L_z\phi, \qquad \mathbf{x} \in \mathbb{R}^d \quad (2.33)$$

with the normalization condition

$$\|\phi\|^2 := \int_{\mathbb{R}^d} |\phi(\mathbf{x})|^2 \, d\mathbf{x} = 1. \quad (2.34)$$

This is a nonlinear eigenvalue problem under a normalization constraint, and any eigenvalue μ can be computed from its corresponding eigenfunction $\phi(\mathbf{x})$ by

$$\begin{aligned} \mu &= \mu_{\beta,\Omega}(\phi) = \int_{\mathbb{R}^d} \left[\frac{1}{2}|\nabla\phi|^2 + V_d(\mathbf{x})|\phi|^2 + \beta_d|\phi|^4 - \Omega \mathrm{Re}\left(\phi^* L_z \phi\right) \right] d\mathbf{x} \\ &= E_{\beta,\Omega}(\phi) + \int_{\mathbb{R}^d} \frac{\beta_d}{2}|\phi|^4 \, d\mathbf{x}. \end{aligned} \quad (2.35)$$

In fact, under the constraint (2.34), the eigenfunctions of (2.33) are equivalent to the critical points of the energy functional $E_{\beta,\Omega}(\phi)$ over the unit sphere

$$S = \{\phi \mid \|\phi\| = 1,\ E_{\beta,\Omega}(\phi) < \infty\}. \tag{2.36}$$

Furthermore, as we noted in [13, 23], they are also equivalent to the steady state solutions of the following continuous normalized gradient flow (CNGF):

$$\partial_t \varphi = \frac{1}{2}\nabla^2\varphi - V_d(\mathbf{x})\varphi - \beta_d|\varphi|^2\varphi + \Omega L_z\varphi + \frac{\mu_{\beta,\Omega}(\varphi)}{\|\varphi(\cdot,t)\|^2}\varphi, \quad \mathbf{x}\in\mathbb{R}^d,\ t>0, \tag{2.37}$$

$$\varphi(\mathbf{x},0) = \varphi_0(\mathbf{x}), \quad \mathbf{x}\in\mathbb{R}^d, \qquad \text{with} \quad \|\varphi_0\|^2 = 1. \tag{2.38}$$

In the physics literature, the stationary state with the lowest energy is called as ground state, and all the other stationary states with larger energies are usually called as excited states [114, 116]. Among all excited states, the most studied one is the central vortex state defined as [13],

$$\phi_m(\mathbf{x}) = \begin{cases} f_m(r)\ e^{im\theta}, & d=2, \\ f_m(r,z)\ e^{im\theta}, & d=3, \end{cases} \tag{2.39}$$

where (r,θ) and (r,θ,z) are polar coordinate and cylindrical coordinate respectively, $m\in\mathbb{Z}$ is winding number (or index) and f_m is a real-valued function satisfying $f_m(0)=0$ or $f_m(0,z)=0$ when $m\neq 0$.

2.6 Semiclassical scaling and leading asymptotics

If $\beta_d \gg 1$, we can introduce another scaling, i.e. semiclassical scaling, for the GPE (2.27). By replacing ψ with ψ^ε and choosing [20, 23]

$$\mathbf{x}\to\mathbf{x}\varepsilon^{-\frac{1}{2}}, \qquad \psi\to\psi^\varepsilon\varepsilon^{\frac{d}{4}}, \qquad \text{with} \quad \varepsilon = \beta_d^{-\frac{2}{d+2}}, \tag{2.40}$$

we obtain

$$i\varepsilon\frac{\partial\psi^\varepsilon(\mathbf{x},t)}{\partial t} = \left[-\frac{\varepsilon^2}{2}\nabla^2 + V_d(\mathbf{x}) + |\psi^\varepsilon|^2 - \varepsilon\Omega L_z\right]\psi^\varepsilon(\mathbf{x},t), \quad \mathbf{x}\in\mathbb{R}^d,\ t>0, \tag{2.41}$$

$$\psi^\varepsilon(\mathbf{x},0) = \psi_0^\varepsilon(\mathbf{x}), \quad \mathbf{x}\in\mathbb{R}^d, \qquad \text{with} \quad \|\psi_0^\varepsilon\|^2 = 1. \tag{2.42}$$

The semiclassical scaling (2.41)−(2.42) is very useful in practice, especially in the asymptotic analysis. Under this scaling, we can define the energy functional as

$$\begin{aligned} E_{\varepsilon,\Omega}\left(\psi^{\varepsilon}\right) &= \int_{\mathbb{R}^d}\left[\frac{\varepsilon^2}{2}|\nabla\psi^{\varepsilon}|^2+V_d(\mathbf{x})|\psi^{\varepsilon}|^2+\frac{1}{2}|\psi^{\varepsilon}|^4-\varepsilon\Omega\mathrm{Re}\left(\left(\psi^{\varepsilon}\right)^* L_z\psi^{\varepsilon}\right)\right]d\mathbf{x} \\ &= O(1), \end{aligned} \tag{2.43}$$

by assuming that ψ^{ε} is ε-oscillatory and sufficiently integrable such that all terms have $O(1)$-integral. Similarly, the nonlinear eigenvalue problem (2.33) (under the normalization (2.34) with $\phi=\phi^{\varepsilon}$) reads

$$\mu^{\varepsilon}\phi^{\varepsilon}(\mathbf{x})=-\frac{\varepsilon^2}{2}\nabla^2\phi^{\varepsilon}+V_d(\mathbf{x})\phi^{\varepsilon}+|\phi^{\varepsilon}|^2\phi^{\varepsilon}-\varepsilon\Omega L_z\phi^{\varepsilon}, \qquad \mathbf{x}\in\mathbb{R}^d, \tag{2.44}$$

where μ^{ε} can be computed by

$$\begin{aligned} \mu^{\varepsilon} &= \mu_{\varepsilon,\Omega}\left(\phi^{\varepsilon}\right)=\int_{\mathbb{R}^d}\left[\frac{\varepsilon^2}{2}|\nabla\phi^{\varepsilon}|^2+V_d(\mathbf{x})|\phi^{\varepsilon}|^2+|\phi^{\varepsilon}|^4-\varepsilon\Omega\mathrm{Re}\left(\left(\phi^{\varepsilon}\right)^* L_z\phi^{\varepsilon}\right)\right]d\mathbf{x} \\ &= O(1). \end{aligned}$$

Furthermore from this scaling, it is easy to get the leading asymptotics of the energy functional $E_{\beta,\Omega}(\phi)$ and the chemical potential $\mu_{\beta,\Omega}(\phi)$ when $\beta_d\gg 1$:

$$E_{\beta,\Omega}(\phi)=\varepsilon^{-1}E_{\varepsilon,\Omega}\left(\phi^{\varepsilon}\right)=O\left(\varepsilon^{-1}\right)=O\left(\beta_d^{2/(d+2)}\right), \tag{2.45}$$

$$\mu_{\beta,\Omega}(\phi)=\varepsilon^{-1}\mu_{\varepsilon,\Omega}\left(\phi^{\varepsilon}\right)=O\left(\varepsilon^{-1}\right)=O\left(\beta_d^{2/(d+2)}\right). \tag{2.46}$$

Suppose that the wave function $\psi^{\varepsilon}(\mathbf{x},t)$ is rapidly oscillating on the scale of ε, and then it can be written into the WKB form:

$$\psi^{\varepsilon}(\mathbf{x},t)=\sqrt{\rho^{\varepsilon}(\mathbf{x},t)}\,\exp\left(\frac{i}{\varepsilon}S^{\varepsilon}(\mathbf{x},t)\right), \qquad \mathbf{x}\in\mathbb{R}^d, \quad t\geq 0, \tag{2.47}$$

where $\rho^{\varepsilon}=|\psi^{\varepsilon}|^2$ is the position density and $S^{\varepsilon}=\varepsilon\arg\left(\psi^{\varepsilon}\right)$ is the phase of the wave function ψ^{ε}. Inserting (2.47) into (2.41) and collecting the real and imaginary parts, we can obtain the transport equation for ρ^{ε} and the Hamilton-Jacobi equation for S^{ε} [23, 15],

$$\partial_t\rho^{\varepsilon}+\mathrm{div}\left(\rho^{\varepsilon}\nabla S^{\varepsilon}\right)+\Omega\widehat{L}_z\rho^{\varepsilon}=0, \tag{2.48}$$

$$\partial_t S^{\varepsilon}+\frac{1}{2}\left|\nabla S^{\varepsilon}\right|^2+V_d(\mathbf{x})+\rho^{\varepsilon}+\Omega\widehat{L}_z S^{\varepsilon}=\frac{\varepsilon^2}{2}\frac{1}{\sqrt{\rho^{\varepsilon}}}\nabla^2\sqrt{\rho^{\varepsilon}}, \tag{2.49}$$

where the operator $\widehat{L}_z = (x\partial_y - y\partial_x)$. Furthermore, by defining the current density [15, 19]

$$\mathbf{J}^\varepsilon(\mathbf{x},t) = \rho^\varepsilon \nabla S^\varepsilon = \varepsilon \mathrm{Im}\left((\psi^\varepsilon(\mathbf{x},t))^* \nabla \psi^\varepsilon(\mathbf{x},t)\right), \tag{2.50}$$

we can rewrite (2.48)−(2.49) as

$$\partial_t \rho^\varepsilon + \mathrm{div}\mathbf{J}^\varepsilon + \Omega \widehat{L}_z \rho^\varepsilon = 0, \tag{2.51}$$

$$\partial_t \mathbf{J}^\varepsilon + \mathrm{div}\left(\frac{\mathbf{J}^\varepsilon \otimes \mathbf{J}^\varepsilon}{\rho^\varepsilon}\right) + \nabla P(\rho^\varepsilon) + \rho^\varepsilon \nabla V_d(\mathbf{x}) + \Omega\left(\widehat{L}_z \mathbf{I} + \mathbf{G}\right)\mathbf{J}^\varepsilon = \frac{\varepsilon^2}{4}\nabla\left(\rho^\varepsilon \nabla^2 \ln \rho^\varepsilon\right), \tag{2.52}$$

where the hydrodynamic pressure $P(\rho)$ is defined as

$$P(\rho) = \frac{1}{2}\rho^2, \tag{2.53}$$

and the symplectic matrix $\mathbf{G}$ is

$$\mathbf{G} = \begin{pmatrix} 0 & 1 \\ -1 & 0 \end{pmatrix}, \quad \text{for} \quad d = 2, \qquad \mathbf{G} = \begin{pmatrix} 0 & 1 & 0 \\ -1 & 0 & 0 \\ 0 & 0 & 0 \end{pmatrix}, \quad \text{for} \quad d = 3. \tag{2.54}$$

Letting $\varepsilon \to 0^+$ in (2.48)−(2.49) and setting $\rho^0 = \lim_{\varepsilon\to 0^+} \rho^\varepsilon$ and $S^0 = \lim_{\varepsilon\to 0^+} S^\varepsilon$, we can get

$$\partial_t \rho^0 + \mathrm{div}\left(\rho^0 \nabla S^0\right) + \Omega \widehat{L}_z \rho^0 = 0, \tag{2.55}$$

$$\partial_t S^0 + \frac{1}{2}\left|\nabla S^0\right|^2 + V_d(\mathbf{x}) + \rho^0 + \Omega \widehat{L}_z S^0 = 0. \tag{2.56}$$

Similarly, letting $\varepsilon \to 0^+$ in (2.51)−(2.52), we can formally obtain the following Euler system:

$$\partial_t \rho^0 + \mathrm{div}\mathbf{J}^0 + \Omega \widehat{L}_z \rho^0 = 0, \tag{2.57}$$

$$\partial_t \mathbf{J}^0 + \mathrm{div}\left(\frac{\mathbf{J}^0 \otimes \mathbf{J}^0}{\rho^0}\right) + \nabla P(\rho^0) + \rho^0 \nabla V_d(\mathbf{x}) + \Omega\left(\widehat{L}_z \mathbf{I} + \mathbf{G}\right)\mathbf{J}^0 = 0, \tag{2.58}$$

where $\mathbf{J}^0 = \lim_{\varepsilon\to 0^+} \mathbf{J}^\varepsilon$.

Chapter 3

Ground state of Bose-Einstein condensation

In this chapter, the ground state of BEC is studied both asymptotically and numerically. Under certain limiting regimes, we derive approximate solutions for the ground state in non-rotating BEC with a box potential or a harmonic potential. To verify these approximations, we propose a backward forward Euler Fourier pseudospectral (BFFP) method to compute the ground state of rotating or non-rotating BEC. Compared to the finite difference methods in [4, 5, 23], the BFFP method is very efficient and accurate, especially for the case of fast rotating BEC with strongly respective interaction.

3.1 Ground state

As mentioned in Section 2.5, the ground state is one of the stationary states, which has the lowest energy. On the other hand, the stationary state solutions of (2.33)−(2.34) are the critical points of the energy functional $E_{\beta,\Omega}(\phi)$ over the unit sphere S (2.36). Thus to find the ground state solution $\phi_g(\mathbf{x})$, we can minimize the energy functional $E_{\beta,\Omega}(\phi)$ over S, i.e.

Find $(\mu_g, \phi_g \in S)$ such that

$$E_g := E_{\beta,\Omega}(\phi_g) = \min_{\phi \in S} E_{\beta,\Omega}(\phi), \qquad \mu_g := \mu_{\beta,\Omega}(\phi_g). \tag{3.1}$$

In the following two subsections, we discuss the existence and uniqueness of the ground state in non-rotating and rotating BEC respectively.

3.1.1 In non-rotating BEC

For non-rotating BEC, if $\beta_d = 0$, we have the following lemma [24]:

Lemma 3.1. In non-rotating BEC, i.e. $\Omega = 0$, if $\beta_d = 0$ and $V_d(\mathbf{x}) \geq 0$ for $\mathbf{x} \in \mathbb{R}^d$, we have

i). The ground state $\phi_g(\mathbf{x})$ is a global minimizer of $E_{0,0}(\phi)$ over S.

ii). Any excited state $\phi_j(\mathbf{x})$ is a saddle point of $E_{0,0}(\phi)$ over S.

Proof. Let ϕ_e be an eigenfunction of the eigenvalue problem (2.33)−(2.34) with $\beta_d = 0$ and $\Omega = 0$, and its corresponding eigenvalue is μ_e. Then for any eigenfunction ϕ satisfying $E_{0,0}(\phi) < \infty$ and $\|\phi_e + \phi\| = 1$, noticing (2.34), we have

$$\|\phi\|^2 = \|\phi_e + \phi\|^2 - \|\phi_e\|^2 - \int_{\mathbb{R}^d} (\phi^* \phi_e + \phi \phi_e^*)\ d\mathbf{x} = -\int_{\mathbb{R}^d} (\phi^* \phi_e + \phi \phi_e^*)\ d\mathbf{x}. \tag{3.2}$$

Considering the energy functional (2.31) with $\psi = \phi_e + \phi$, noticing (2.34) and (3.2), and integrating by parts, we obtain

$$\begin{aligned}
E_{0,0}(\phi_e + \phi) &= \int_{\mathbb{R}^d} \left[\frac{1}{2} |\nabla \phi_e + \nabla \phi|^2 + V_d(\mathbf{x}) |\phi_e + \phi|^2 \right] d\mathbf{x} \\
&= \int_{\mathbb{R}^d} \left[\frac{1}{2} |\nabla \phi_e|^2 + V_d(\mathbf{x}) |\phi_e|^2 \right] d\mathbf{x} + \int_{\mathbb{R}^d} \left[\frac{1}{2} |\nabla \phi|^2 + V_d(\mathbf{x}) |\phi|^2 \right] d\mathbf{x} \\
&\quad + \int_{\mathbb{R}^d} \left[\left(-\frac{1}{2} \nabla^2 \phi_e + V_d(\mathbf{x}) \phi_e \right)^* \phi + \left(-\frac{1}{2} \nabla^2 \phi_e + V_d(\mathbf{x}) \phi_e \right) \phi^* \right] d\mathbf{x} \\
&= E_{0,0}(\phi_e) + E_{0,0}(\phi) + \int_{\mathbb{R}^d} (\mu_e \phi_e^* \phi + \mu_e \phi_e \phi^*)\ d\mathbf{x} \\
&= E_{0,0}(\phi_e) + E_{0,0}(\phi) - \mu_e \|\phi\|^2 \\
&= E_{0,0}(\phi_e) + \left(E_{0,0}(\phi / \|\phi\|) - \mu_e \right) \|\phi\|^2.
\end{aligned} \tag{3.3}$$

i). Taking $\phi_e = \phi_g$ and $\mu_e = \mu_g$ in (3.3) and noticing $E_{0,0}(\phi/\|\phi\|) \geq E_{0,0}(\phi_g) = \mu_g$ for any $\phi \neq 0$, we immediately get that ϕ_g is a global minimizer of the energy functional $E_{0,0}(\phi)$ over the unit sphere S.

ii). Taking $\phi_e = \phi_j$ and $\mu_e = \mu_j$ in (3.3), it is easy to find an eigenfunction ϕ of (2.33)−(2.34) such that $E_{0,0}(\phi) > E_{0,0}(\phi_j)$. On the other hand, we have $E_{0,0}(\phi_g) < E_{0,0}(\phi_j)$. These imply that ϕ_j is a saddle point of the functional $E_{0,0}(\phi)$ over the unit sphere S. □

When $\beta_d > 0$, the energy functional $E_{\beta,0}(\phi)$ is positive, coercive and weakly lower semi-continuous on the unit sphere S, therefore the existence of its minimum follows the standard theory [93]. Note that $E_{\beta,0}(\alpha\phi_g) = E_{\beta,0}(\phi_g)$ for all $\alpha \in \mathbb{C}$ with $|\alpha| = 1$. Thus to show the uniqueness of the minimum, we have to introduce an additional constraint. According to [93, 24, 20], for non-rotating BEC, the minimization problem (3.1) has a unique real-valued nonnegative ground state solution, i.e. $\phi_g(\mathbf{x}) \geq 0$ for $\mathbf{x} \in \mathbb{R}^d$.

3.1.2 In rotating BEC

For rotating BEC confined in the harmonic potential (2.29), the existence of its ground state depends on the magnitude of the angular velocity, i.e. $|\Omega|$, relative to the trapping frequencies, and there is [124, 23],

Lemma 3.2. In defocusing rotating BEC with a harmonic potential, i.e. $\beta_d \geq 0$ and $\Omega \neq 0$, we have

i). When $|\Omega| < \gamma_{\min}$ with $\gamma_{\min} := \min\{\gamma_x, \gamma_y\}$, there exists a minimizer for the minimization problem (3.1), i.e. there exists a ground state $\phi_g(\mathbf{x})$. Note that $E_{\beta,\Omega}(\alpha\phi_g) = E_{\beta,\Omega}(\phi_g)$ for all $\alpha \in \mathbb{C}$ with $|\alpha| = 1$. Thus an additional constraint has to be introduced to show the uniqueness of the ground state.

ii). When $|\Omega| > \gamma_{\max}$ with $\gamma_{\max} := \max\{\gamma_x, \gamma_y\}$, there is no ground state.

iii). When $\gamma_{\min} < |\Omega| \leq \gamma_{\max}$, the existence of the ground state is still an open problem.

Especially, when $\beta_d = 0$, we have the following lemma:

Lemma 3.3. If $\beta_d = 0$ and $|\Omega| < \gamma_{\min}$, then we have

i). The ground state $\phi_g(\mathbf{x})$ is a global minimizer of $E_{0,\Omega}(\phi)$ over S.

ii). Any excited state $\phi_j(\mathbf{x})$ is a saddle point of $E_{0,\Omega}(\phi)$ over S.

In the following two sections, we derive approximate solutions for the ground state of non-rotating BEC with a box potential and a harmonic potential, respectively. For convenience of derivation, here we introduce some notations. In non-rotating BEC, the eigenvalue problem (2.33)−(2.34) becomes

$$\mu\phi(\mathbf{x}) = -\frac{1}{2}\nabla^2\phi + V_d(\mathbf{x})\phi + \beta_d|\phi|^2\phi, \qquad \mathbf{x} \in \Omega_{\mathbf{x}}, \tag{3.4}$$

$$\|\phi\|^2 = \int_{\Omega_{\mathbf{x}}} |\phi(\mathbf{x})|^2 \, d\mathbf{x} = 1, \tag{3.5}$$

where $\Omega_{\mathbf{x}}$ is the domain of this problem. For example, if a box potential is considered, $\Omega_{\mathbf{x}} = [0, 1]^d$, and respectively $\Omega_{\mathbf{x}} = \mathbb{R}^d$ for a harmonic potential. We denote

$$E_{\text{kin},g} = E_{\text{kin}}(\phi_g) = \frac{1}{2}\int_{\Omega_{\mathbf{x}}} |\nabla\phi_g(\mathbf{x})|^2 \, d\mathbf{x}, \tag{3.6}$$

$$E_{\text{pot},g} = E_{\text{pot}}(\phi_g) = \int_{\Omega_{\mathbf{x}}} V_d(\mathbf{x})|\phi_g(\mathbf{x})|^2 \, d\mathbf{x}, \tag{3.7}$$

$$E_{\text{int},g} = E_{\text{int}}(\phi_g) = \frac{\beta_d}{2}\int_{\Omega_{\mathbf{x}}} |\phi_g(\mathbf{x})|^4 \, d\mathbf{x}, \tag{3.8}$$

as the kinetic energy, potential energy and interaction energy of the ground state $\phi_g(\mathbf{x})$ respectively. Thus the energy and chemical potential can be computed by

$$E_g = E_{\text{kin},g} + E_{\text{pot},g} + E_{\text{int},g}, \qquad \mu_g = E_g + E_{\text{int},g}. \tag{3.9}$$

3.2 Approximation in box potential

For non-rotating BEC with a box potential, i.e.

$$V_d(\mathbf{x}) = \begin{cases} 0, & \mathbf{x} \in \Omega_{\mathbf{x}} = (0,\, 1)^d, \\ \infty, & \text{otherwise}, \end{cases} \tag{3.10}$$

the eigenvalue problem (3.4)−(3.5) collapses to

$$\mu\phi(\mathbf{x}) = -\frac{1}{2}\nabla^2\phi(\mathbf{x}) + \beta_d|\phi(\mathbf{x})|^2\phi(\mathbf{x}), \qquad \mathbf{x} \in [0,\ 1]^d, \tag{3.11}$$

$$\|\phi\|^2 = \int_{[0,1]^d} |\phi(\mathbf{x})|^2\, d\mathbf{x} = 1. \tag{3.12}$$

Since at the boundary the potential reaches infinity, we can assume that there is no particle and set the boundary condition as

$$\phi(\mathbf{x}) = 0, \qquad \mathbf{x} \in \Gamma = \partial\Omega_{\mathbf{x}}. \tag{3.13}$$

In the following subsections, we derive the approximate ground state solutions in two special regimes, i.e. the weakly interacting regime and the strongly repulsive interacting regime.

3.2.1 In weakly interacting regime

In the weakly interacting regime, i.e. $\beta_d = o(1)$, the problem (3.11)−(3.13) reduces to a linear eigenvalue problem,

$$\mu\phi(\mathbf{x}) = -\frac{1}{2}\nabla^2\phi(\mathbf{x}), \qquad \mathbf{x} \in [0,\ 1]^d, \qquad \text{with} \quad \|\phi\|^2 = 1, \tag{3.14}$$

$$\phi(\mathbf{x}) = 0, \qquad \mathbf{x} \in \Gamma. \tag{3.15}$$

By separating variables, we can obtain a complete set of orthonormal eigenfunctions of (3.14)−(3.15):

$$\phi_J(\mathbf{x}) = \prod_{m=1}^{d} \phi_{j_m}(x_m), \quad \mathbf{x} = (x_1, \ldots, x_d)^T \in [0,\ 1]^d, \quad J = (j_1, \ldots, j_d) \in \mathbb{N}^d, \tag{3.16}$$

where

$$\phi_l(\tau) = \sqrt{2}\sin(l\pi\tau), \qquad l \in \mathbb{N}, \quad \tau \in [0,\ 1]. \tag{3.17}$$

Then the eigenvalue corresponding to $\phi_J(\mathbf{x})$ is

$$\mu_J = \sum_{m=1}^{d} \mu_{j_m}, \qquad \text{with} \quad \mu_l = \frac{1}{2}\, l^2\pi^2, \quad l \in \mathbb{N}. \tag{3.18}$$

From (3.16)−(3.18), we can get the approximate ground state solution as

$$\phi_g^{\mathrm{w}}(\mathbf{x}) = \phi_{\underbrace{(1,\ldots,1)}_{d}}(\mathbf{x}) = \sqrt{2^d}\prod_{m=1}^{d}\sin(\pi x_m), \qquad \mathbf{x}\in[0,\,1]^d, \tag{3.19}$$

and the corresponding energy and chemical potential are

$$E_g^{\mathrm{w}} = \mu_g^{\mathrm{w}} = \frac{d}{2}\pi^2. \tag{3.20}$$

3.2.2 Thomas-Fermi (semiclassical) approximation

On the other hand, in the strongly repulsive interacting regime, i.e. $\beta_d \gg 1$, the diffusion term (the first term on the right side of (3.11)) is insignificant. Thus we can drop it and get

$$\mu\phi(\mathbf{x}) = \beta_d|\phi(\mathbf{x})|^2\phi(\mathbf{x}), \qquad \mathbf{x}\in[0,\,1]^d, \tag{3.21}$$

which immediately gives the Thomas-Fermi approximation of the ground state, i.e.

$$\phi_g^{\mathrm{TF}}(\mathbf{x}) = \sqrt{\frac{\mu_g^{\mathrm{TF}}}{\beta_d}}, \qquad \mathbf{x}\in[0,\,1]^d \tag{3.22}$$

with μ_g^{TF} the corresponding chemical potential. Noticing the normalization condition (3.12), we have

$$\left\|\phi_g^{\mathrm{TF}}\right\|^2 = \int_{[0,\,1]^d}\left|\phi_g^{\mathrm{TF}}(\mathbf{x})\right|^2\,d\mathbf{x} = \int_{[0,\,1]^d}\frac{\mu_g^{\mathrm{TF}}}{\beta_d}\,d\mathbf{x} = \frac{\mu_g^{\mathrm{TF}}}{\beta_d} = 1. \tag{3.23}$$

This implies that the chemical potential $\mu_g^{\mathrm{TF}} = \beta_d$, and furthermore we can compute the corresponding energy as

$$E_g^{\mathrm{TF}} = \mu_g^{\mathrm{TF}} - \frac{\beta_d}{2}\int_{[0,\,1]^d}\left|\phi_g^{\mathrm{TF}}\right|^4\,d\mathbf{x} = \frac{\mu_g^{\mathrm{TF}}}{2} = \frac{\beta_d}{2}. \tag{3.24}$$

Combining (3.22) and (3.23), we obtain

$$\phi_g^{\mathrm{TF}}(\mathbf{x}) \equiv 1, \qquad \mathbf{x}\in[0,\,1]^d. \tag{3.25}$$

It is easy to see that the Thomas-Fermi approximate solution ϕ_g^{TF} does not satisfy the boundary condition (3.13), which suggests that a boundary layer would exist in the ground state when $\beta_d \gg 1$ and the kinetic energy does not go to zero when $\beta_d \to \infty$, so near the boundary the diffusion term can not be removed from (3.11).

3.2.3 Matched asymptotic approximation

As we discussed, near the boundary, the diffusion term is important and cannot be neglected. Thus in this subsection, we include it into our analysis to present a more accurate approximation, i.e. matched asymptotic approximation. For simplicity, we first consider the one-dimensional (1D) case, and then generalize it to high dimensions.

Approximation in one dimension

In 1D case, i.e. $d = 1$, since the layers exist at two boundaries, we have to solve equation (3.11) near $x = 0$ and $x = 1$, separately. First we consider $0 \le x \le 1/2$ and rescale (3.11) by introducing

$$x = \frac{1}{\sqrt{\mu_g^{\mathrm{MA}}}}\, X, \qquad \phi_g^{\mathrm{MA}}(x) = \sqrt{\frac{\mu_g^{\mathrm{MA}}}{\beta_1}}\, \Phi(X), \tag{3.26}$$

where μ_g^{MA} is the matched asymptotic approximation of the chemical potential. Inserting (3.26) into (3.11) gives

$$\Phi(X) = -\frac{1}{2}\partial_{XX}\Phi(X) + \Phi^3(X), \qquad 0 < X < \infty, \tag{3.27}$$

$$\Phi(0) = 0, \qquad \lim_{X\to\infty} \Phi(X) = 1. \tag{3.28}$$

Solving (3.27)−(3.28), we obtain

$$\Phi(X) = \tanh(X), \qquad 0 \le X < \infty. \tag{3.29}$$

Substituting (3.29) into (3.26), we immediately get the approximation for $\phi_g(x)$ near $x = 0$ when $\beta_1 \gg 1$:

$$\phi_g^{\mathrm{MA}}(x) = \sqrt{\frac{\mu_g^{\mathrm{MA}}}{\beta_1}}\, \tanh\left(\sqrt{\mu_g^{\mathrm{MA}}}\, x\right), \qquad 0 \le x \le 1/2. \tag{3.30}$$

Similarly, near $x = 1$, we have

$$\phi_g^{\mathrm{MA}}(x) = \sqrt{\frac{\mu_g^{\mathrm{MA}}}{\beta_1}}\, \tanh\left(\sqrt{\mu_g^{\mathrm{MA}}}\, (1-x)\right), \qquad 1/2 \le x \le 1. \tag{3.31}$$

Combining (3.30) and (3.31), noticing the boundary condition (3.13) and applying the matched asymptotic method, we can get the matched asymptotic approximation for the ground state $\phi_g(x)$ when $x \in [0, 1]$:

$$\phi_g^{\mathrm{MA}}(x) = \sqrt{\frac{\mu_g^{\mathrm{MA}}}{\beta_1}} \left[\tanh\left(\sqrt{\mu_g^{\mathrm{MA}}} x\right) + \tanh\left(\sqrt{\mu_g^{\mathrm{MA}}}(1-x)\right) - \tanh\left(\sqrt{\mu_g^{\mathrm{MA}}}\right) \right]. \quad (3.32)$$

From the normalization condition (3.12), we can compute [20]

$$\left\|\phi_g^{\mathrm{MA}}\right\|^2 = \int_0^1 \left|\phi_g^{\mathrm{MA}}(x)\right|^2 \, dx \approx \frac{\mu_g^{\mathrm{MA}}}{\beta_1} - 2\frac{\sqrt{\mu_g^{\mathrm{MA}}}}{\beta_1} = 1, \quad (3.33)$$

which gives the approximation for the chemical potential as

$$\mu_g^{\mathrm{MA}} = \beta_1 + 2\sqrt{\beta_1 + 1} + 2. \quad (3.34)$$

Plugging (3.32) and (3.34) into (3.6), (3.8) and (3.9), we can compute [20]

$$E_{\mathrm{kin},g}^{\mathrm{MA}} = \frac{2}{3}\sqrt{\beta_1 + 1} + 2, \qquad E_{\mathrm{int},g}^{\mathrm{MA}} = \frac{\beta_1}{2} + \frac{2}{3}\sqrt{\beta_1 + 1}, \quad (3.35)$$

$$E_g^{\mathrm{MA}} = E_{\mathrm{kin},g}^{\mathrm{MA}} + E_{\mathrm{int},g}^{\mathrm{MA}} = \frac{\beta_1}{2} + \frac{4}{3}\sqrt{\beta_1 + 1} + 2, \qquad \beta_1 \gg 1. \quad (3.36)$$

From (3.32), (3.34)−(3.36), we can draw the following conclusions:

i). The width of the boundary layer in the matched asymptotic approximation is about $O\left(1/\sqrt{\beta_1}\right)$.

ii). The ratios between the chemical potential and the energies satisfy:

$$\lim_{\beta_1 \to \infty} \frac{E_g}{\mu_g} = \frac{1}{2}, \qquad \lim_{\beta_1 \to \infty} \frac{E_{\mathrm{int},g}}{E_g} = 1, \qquad \lim_{\beta_1 \to \infty} \frac{E_{\mathrm{kin},g}}{E_g} = 0. \quad (3.37)$$

To verify the above approximations, Table 3.1 lists the errors between the numerical results and the matched asymptotic approximation, where the convergence rate of a function $f(\alpha)$ as $\alpha \to 0$ is computed by: $\ln[f(2\alpha)/f(\alpha)]/\ln 2$. Figure 3.1 shows the numerical solutions of the ground state for different β_1. These numerical results are computed by the backward forward Euler Fourier pseudospectral (BFFP) method proposed in Section 3.4.

$1/\beta_1$	4/25	2/25	1/25	1/50	1/100	1/400
$\max\left\|\phi_g-\phi_g^{\mathrm{MA}}\right\|$	8.17E-3	9.24E-4	4.67E-5	8.0E-7	– –	– –
$\left\|\phi_g-\phi_g^{\mathrm{MA}}\right\|_{L^2}$	6.84E-3	8.05E-4	4.11E-5	6.0E-7	– –	– –
$\left\|E_{\mathrm{kin},g}-E_{\mathrm{kin},g}^{\mathrm{MA}}\right\|$	1.3018	0.9479	0.6464	0.4340	0.2946	0.1399
Rate	– –	0.4577	0.5523	0.5747	0.5589	0.5372
$\left\|E_{\mathrm{int},g}-E_{\mathrm{int,g}}^{\mathrm{MA}}\right\|$	0.5948	0.4608	0.3218	0.2171	0.1473	0.0701
Rate	– –	0.3683	0.5180	0.5678	0.5596	0.5356
$\left\|E_g-E_g^{\mathrm{MA}}\right\|$	0.7071	0.4871	0.3245	0.2171	0.1472	0.0698
Rate	– –	0.5377	0.5860	0.5799	0.5606	0.5382
$\left\|\mu_g-\mu_g^{\mathrm{MA}}\right\|$	0.1124	0.0263	0.0027	0.0001	– –	– –
E_g/μ_g	0.6854	0.6234	0.5813	0.5543	0.5368	0.5175
$E_{\mathrm{int},g}/E_g$	0.4591	0.6042	0.7204	0.8042	0.8628	0.9323
$E_{\mathrm{kin},g}/E_g$	0.5409	0.3958	0.2796	0.1958	0.1372	0.0677

Table 3.1: Convergence study of the matched asymptotic approximation in 1D box potential when $\beta_1 \gg 1$. Here ϕ_g, $E_{\mathrm{kin},g}$, $E_{\mathrm{int},g}$, E_g and μ_g are numerical results.

From Table 3.1 and Figure 3.1, we can find that:

i). When $\beta_1 \to \infty$, the matched asymptotic approximation $\phi_g^{\mathrm{MA}}(x)$ converges to the ground state solution $\phi_g(x)$ with the convergence rates

$$\max\left|\phi_g-\phi_g^{\mathrm{MA}}\right| = O\left(e^{-3\sqrt{\beta_1}/2}\right), \qquad \left\|\phi_g-\phi_g^{\mathrm{MA}}\right\|_{L^2} = O\left(e^{-3\sqrt{\beta_1}/2}\right). \tag{3.38}$$

ii). The asymptotic approximations (3.34)−(3.37) are confirmed by the numerical results. Furthermore the numerical results suggest the following convergence rates:

$$E_{\mathrm{kin},g} = E_{\mathrm{kin},g}^{\mathrm{MA}} + O\left(1/\sqrt{\beta_1}\right), \quad E_{\mathrm{int},g} = E_{\mathrm{int},g}^{\mathrm{MA}} + O\left(1/\sqrt{\beta_1}\right), \tag{3.39}$$

$$E_g = E_g^{\mathrm{MA}} + O\left(1/\sqrt{\beta_1}\right), \quad \mu_g = \mu_g^{\mathrm{MA}} + O\left(e^{-3\sqrt{\beta_1}/2}\right), \qquad \beta_1 \gg 1. \tag{3.40}$$

iii). Boundary layers are observed near $x = 0$ and $x = 1$ in the ground state when $\beta_1 \gg 1$ (cf. Fig. 3.1), and the width of the layer is about $2/\sqrt{\beta_1}$ which is numerically measured by the wave function changing from 0 to 0.7.

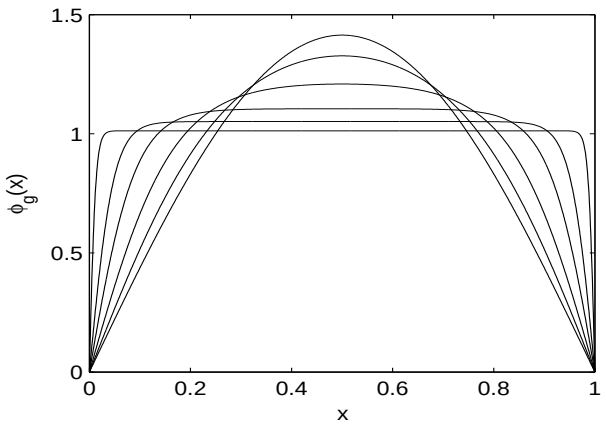

Figure 3.1: Ground state solutions in 1D box potential for $\beta_1 = 0, 6.25, 25, 100, 400, 6400$ (in the order of decreasing peak).

Extension to high dimensions

Similar to 1D case, in d-dimensions ($d > 1$), when $\beta_d \gg 1$ the matched asymptotic approximate solution for the ground state can be given by

$$\phi_g^{\mathrm{MA}}(\mathbf{x}) = \sqrt{\frac{\mu_g^{\mathrm{MA}}}{\beta_d}} \prod_{j=1}^{d} \left[\tanh\left(\sqrt{\mu_g^{\mathrm{MA}}} x_j\right) + \tanh\left(\sqrt{\mu_g^{\mathrm{MA}}}(1-x_j)\right) - \tanh\left(\sqrt{\mu_g^{\mathrm{MA}}}\right) \right], \quad \mathbf{x} = (x_1, \ldots, x_d)^T \in [0,\, 1]^d. \tag{3.41}$$

Inserting (3.41) into (3.12) and after a simple computation, we can get [20],

$$\left\|\phi_g^{\mathrm{MA}}\right\|^2 = \int_{[0,\,1]^d} \left|\phi_g^{\mathrm{MA}}(\mathbf{x})\right|^2 \, d\mathbf{x} \approx \frac{\mu_g^{\mathrm{MA}}}{\beta_d} \left(1 - \frac{2}{\sqrt{\mu_g^{\mathrm{MA}}}}\right)^d = 1. \tag{3.42}$$

Solving (3.42) gives the approximate chemical potential μ_g^{MA} as

$$\mu_g^{\mathrm{MA}} = \beta_d + 2d\sqrt{\beta_d + d(2-d)} + 2d, \qquad \beta_d \gg 1. \tag{3.43}$$

Similarly, the energies can be computed from (3.6), (3.8) and (3.9), that is,

$$E_{\mathrm{kin},g}^{\mathrm{MA}} = \frac{2d}{3}\sqrt{\beta_d + d(2-d)} + \frac{2d}{3}(d+2), \tag{3.44}$$

$$E_{\mathrm{int},g}^{\mathrm{MA}} = \frac{\beta_d}{2} + \frac{2d}{3}\sqrt{\beta_d + d(2-d)} + \frac{d}{3}(1-d), \qquad \beta_d \gg 1, \tag{3.45}$$

$$E_g^{\mathrm{MA}} = \frac{\beta_d}{2} + \frac{4d}{3}\sqrt{\beta_d + d(2-d)} + \frac{d}{3}(d+5). \tag{3.46}$$

3.3 Approximation in harmonic potential

For non-rotating BEC with the harmonic potential (2.29), the eigenvalue problem (3.4)−(3.5) becomes

$$\mu\phi(\mathbf{x}) = -\frac{1}{2}\nabla^2\phi(\mathbf{x}) + V_d(\mathbf{x})\phi(\mathbf{x}) + \beta_d|\phi(\mathbf{x})|^2\phi(\mathbf{x}), \qquad \mathbf{x} \in \mathbb{R}^d, \tag{3.47}$$

$$\|\phi\|^2 = \int_{\mathbb{R}^d} |\phi(\mathbf{x})|^2 \, d\mathbf{x} = 1. \tag{3.48}$$

Similarly, we also present the approximate solutions for the ground state in the weakly interacting regime and the strongly repulsive interacting regime.

3.3.1 In weakly interacting regime

In the weakly interacting regime, i.e. $\beta_d = o(1)$, we can drop the nonlinear term in (3.47) and get,

$$\mu\phi(\mathbf{x}) = -\frac{1}{2}\nabla^2\phi(\mathbf{x}) + V_d(\mathbf{x})\phi(\mathbf{x}), \quad \mathbf{x} \in \mathbb{R}^d, \qquad \text{with} \quad \|\phi\|^2 = 1, \tag{3.49}$$

which can be exactly solved to give the approximate ground state solution as

$$\phi_g^{\mathrm{w}}(\mathbf{x}) = \frac{1}{\pi^{d/4}} \begin{cases} \gamma_x^{1/4} \exp\left(-\frac{\gamma_x x^2}{2}\right), & d = 1, \\ (\gamma_x\gamma_y)^{1/4} \exp\left(-\frac{\gamma_x x^2 + \gamma_y y^2}{2}\right), & d = 2, \\ (\gamma_x\gamma_y\gamma_z)^{1/4} \exp\left(-\frac{\gamma_x x^2 + \gamma_y y^2 + \gamma_z z^2}{2}\right), & d = 3, \end{cases} \tag{3.50}$$

and the corresponding energy and chemical potential are

$$E_g^{\mathrm{w}} = \mu_g^{\mathrm{w}} = \frac{1}{2} \begin{cases} \gamma_x, & d = 1, \\ \gamma_x + \gamma_y, & d = 2, \\ \gamma_x + \gamma_y + \gamma_z, & d = 3. \end{cases} \tag{3.51}$$

3.3.2 Thomas-Fermi (semiclassical) approximation

For a condensate with strongly repulsive interactions, i.e. $\beta_d \gg 1$ and $\gamma_{x_j} = O(1)$ $(1 \le j \le d)$, we can drop the diffusion term in (3.47) and get,

$$\mu\phi(\mathbf{x}) = V_d(\mathbf{x})\phi(\mathbf{x}) + \beta_d|\phi(\mathbf{x})|^2\phi(\mathbf{x}), \qquad \mathbf{x} \in \mathbb{R}^d. \tag{3.52}$$

Solving (3.52) gives the Thomas-Fermi approximation for the ground state in a harmonic potential:

$$\phi_g^{\mathrm{TF}}(\mathbf{x}) = \begin{cases} \sqrt{\left(\mu_g^{\mathrm{TF}} - V_d(\mathbf{x})\right)/\beta_d}, & V_d(\mathbf{x}) \le \mu_g^{\mathrm{TF}}, \\ 0, & \text{otherwise}, \end{cases} \qquad \mathbf{x} \in \mathbb{R}^d. \tag{3.53}$$

Substituting (3.53) into the normalization condition (3.48), we can compute the corresponding chemical potential as

$$\mu_g^{\mathrm{TF}} = \frac{1}{2} \begin{cases} (3\beta_1\gamma_x/2)^{2/3}, & d = 1, \\ (4\beta_2\gamma_x\gamma_y/\pi)^{1/2}, & d = 2, \\ (15\beta_3\gamma_x\gamma_y\gamma_z/4\pi)^{2/5}, & d = 3. \end{cases} \tag{3.54}$$

Due to the fact that $\phi_g^{\mathrm{TF}}(\mathbf{x})$ is not differentiable at $V_d(\mathbf{x}) = \mu_g^{\mathrm{TF}}$, we cannot use (3.6) and (2.31) to define the kinetic energy and energy of the Thomas-Fermi approximation. However, noticing (3.9), we can use the following way to calculate them:

$$E_g^{\mathrm{TF}} = \mu_g^{\mathrm{TF}} - E_{\mathrm{int},g}^{\mathrm{TF}}, \qquad E_{\mathrm{kin},g}^{\mathrm{TF}} = E_g^{\mathrm{TF}} - E_{\mathrm{int},g}^{\mathrm{TF}} - E_{\mathrm{pot},g}^{\mathrm{TF}}. \tag{3.55}$$

After some computations, we get [20],

$$\begin{aligned} &E_{\mathrm{int},g}^{\mathrm{TF}} = \frac{2}{d+4}\,\mu_g^{\mathrm{TF}}, \qquad E_{\mathrm{pot},g}^{\mathrm{TF}} = \frac{d}{d+4}\,\mu_g^{\mathrm{TF}}, \qquad E_{\mathrm{kin},g}^{\mathrm{TF}} = 0, \\ &E_g^{\mathrm{TF}} = \frac{d+2}{d+4}\,\mu_g^{\mathrm{TF}}, \qquad \beta_d \gg 1, \quad d = 1, 2, 3. \end{aligned} \tag{3.56}$$

From (3.54) and (3.56), we can see when $\beta_d \gg 1$ ($d = 1, 2, 3$),

$$\lim_{\beta_d\to\infty} \frac{E_g}{\mu_g} = \frac{d+2}{d+4}, \quad \lim_{\beta_d\to\infty} \frac{E_{\mathrm{int},g}}{E_g} = \frac{2}{d+2}, \quad \lim_{\beta_d\to\infty} \frac{E_{\mathrm{pot},g}}{E_g} = \frac{d}{d+2}. \tag{3.57}$$

To verify the Thomas-Fermi approximation (3.53), (3.54), (3.56) and (3.57), here we study the 1D case. The errors between the numerical results and the Thomas-Fermi approximation are listed in Table 3.2, and the numerical solution of the ground state solutions are plotted in Figure 3.2. From them, we can draw the following conclusions for 1D case:

$1/\beta_1$	1/100	1/200	1/400	1/800	1/1600	1/6400
$\max\left\|\phi_g - \phi_g^{\mathrm{TF}}\right\|$	0.0788	0.0605	0.0464	0.0355	0.0272	0.0159
Rate	– –	0.3807	0.3836	0.3840	0.3852	0.3872
$\left\|\phi_g - \phi_g^{\mathrm{TF}}\right\|_{L^2}$	0.0571	0.0423	0.0312	0.0230	0.0170	0.0092
Rate	– –	0.4350	0.4371	0.4389	0.4404	0.4427
$\left\|E_{\mathrm{pot},g} - E_{\mathrm{pot},g}^{\mathrm{TF}}\right\|$	0.0246	0.0171	0.0118	0.0080	0.0054	0.0023
Rate	– –	0.5238	0.5383	0.5528	0.5687	0.6196
$\left\|E_{\mathrm{int},g} - E_{\mathrm{int},g}^{\mathrm{TF}}\right\|$	0.0204	0.0144	0.0101	0.0070	0.0047	0.0021
Rate	– –	0.4980	0.5167	0.5348	0.5531	0.6051
$E_{\mathrm{kin},g}$	0.0350	0.0245	0.0170	0.0117	0.0080	0.0037
Rate	– –	0.5134	0.5267	0.5381	0.5478	0.5599
$\left\|E_g - E_g^{\mathrm{TF}}\right\|$	0.0392	0.0272	0.0187	0.0128	0.0087	0.0039
Rate	– –	0.5280	0.5394	0.5492	0.5582	0.5725
$\left\|\mu_g - \mu_g^{\mathrm{TF}}\right\|$	0.0188	0.0128	0.0086	0.0058	0.0039	0.0019
Rate	– –	0.5613	0.5651	0.5659	0.5638	0.5329
E_g/μ_g	0.6020	0.6009	0.6004	0.6002	0.6001	0.6000
$E_{\mathrm{int},g}/E_g$	0.6612	0.6643	0.6656	0.6662	0.6665	0.6666
$E_{\mathrm{pot},g}/E_g$	0.3347	0.3339	0.3336	0.3334	0.3334	0.3333

Table 3.2: Convergence study of the Thomas-Fermi approximation in 1D harmonic potential with $\gamma_x = 1$. Here ϕ_g, $E_{\mathrm{kin},g}$, $E_{\mathrm{pot},g}$, $E_{\mathrm{int},g}$, E_g and μ_g are numerical results.

i). When $\beta_1 \to \infty$, the Thomas-Fermi approximation $\phi_g^{\mathrm{TF}}(x)$ converges to the ground state solution $\phi_g(x)$ with the convergence rates:

$$\max\left|\phi_g - \phi_g^{\mathrm{TF}}\right| = O\left(\frac{\ln\beta_1}{\beta_1^{2/5}}\right), \qquad \left\|\phi_g - \phi_g^{\mathrm{TF}}\right\|_{L^2} = O\left(\frac{\ln\beta_1}{\beta_1^{2/5}}\right).$$

ii). The Thomas-Fermi approximation (3.54), (3.56) and (3.57) are confirmed by the numerical results. Furthermore, the numerical results suggest the following

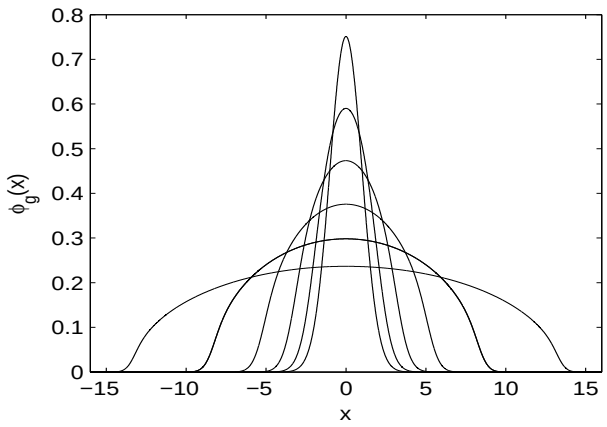

Figure 3.2: Ground state solutions in 1D harmonic potential with $\gamma_x = 1$ for $\beta_1 = 0, 6.25, 25, 100, 400, 1600$ (in the order of decreasing peak).

convergence rates when $\beta_1 \gg 1$:

$$E_{\mathrm{int},g} = E_{\mathrm{int},g}^{\mathrm{TF}} + O\left(\frac{\ln \beta_1}{\beta_1^{2/3}}\right), \quad E_{\mathrm{pot},g} = E_{\mathrm{pot},g}^{\mathrm{TF}} + O\left(\frac{\ln \beta_1}{\beta_1^{2/3}}\right),$$
$$E_{\mathrm{kin},g} = O\left(\frac{\ln \beta_1}{\beta_1^{2/3}}\right), \quad E_g = E_g^{\mathrm{TF}} + O\left(\frac{\ln \beta_1}{\beta_1^{2/3}}\right), \quad \mu_g = \mu_g^{\mathrm{TF}} + O\left(\frac{\ln \beta_1}{\beta_1^{2/3}}\right).$$

3.4 Numerical method

In this section, we propose a Fourier pseudospectral method to compute the ground state of non-rotating or rotating BEC. Compared to the finite difference methods introduced in [4, 5, 23], this method is very efficient and accurate, especially for the case of rotating BEC with strongly repulsive interaction and large rotation speed.

3.4.1 Normalized gradient flow

In the physics literature [6, 32, 37], the minimization problem (3.1) is solved by evolving the discrete normalized gradient flow (DNGF) which is obtained by applying an imaginary time, i.e. $t \to -it$, in the GPE (2.27). The DNGF preserves the normalization at each time step and makes the energy diminish during the time

evolution, and thus its steady state solutions can be viewed as the ground state solutions of the problem (2.33)−(2.34). The details of DNGF are: choosing a time step $\Delta t > 0$ and a time sequence $t_n = n\Delta t$ for $n = 0, 1, 2, \ldots$, then for $t \in [t_n, t_{n+1})$, the DNGF is given by

$$\partial_t \phi(\mathbf{x}, t) = \frac{1}{2}\nabla^2 \phi - V_d(\mathbf{x})\phi - \beta_d |\phi|^2 \phi + \Omega L_z \phi, \qquad \mathbf{x} \in \mathbb{R}^d, \tag{3.58}$$

$$\phi(\mathbf{x}, t_{n+1}) = \phi(\mathbf{x}, t_{n+1}^+) = \frac{\phi(\mathbf{x}, t_{n+1}^-)}{\|\phi(\cdot, t_{n+1}^-)\|}, \qquad \mathbf{x} \in \mathbb{R}^d, \tag{3.59}$$

$$\phi(\mathbf{x}, 0) = \phi_0(\mathbf{x}), \quad \mathbf{x} \in \mathbb{R}^d, \qquad \text{with} \quad \|\phi_0\|^2 = 1, \tag{3.60}$$

where $\phi(\mathbf{x}, t_{n+1}^{\pm}) = \lim_{t \to t_{n+1}^{\pm}} \phi(\mathbf{x}, t)$. The DNGF (3.58)−(3.60) can also be viewed as: i). applying the steepest decent method to minimize the energy functional $E_{\beta,\Omega}(\phi)$ without any constraint, and ii). projecting the solution back to the unit sphere S in order to satisfy the normalization condition.

In fact, when $\Delta t \to 0$, the DNGF converges to the continuous normalized gradient flow (CNGF) (2.37)−(2.38), where we can view $\mu_{\beta,\Omega}(\phi)/\|\phi(\cdot, t)\|^2$ as a Lagrange multiplier of the constraint (2.34) [13].

3.4.2 Backward Forward Euler Fourier pseudospectral method

In this subsection, we propose the backward forward Euler Fourier pseudospectral (BFFP) method to discretize the DNGF (3.58)−(3.60). Without loss of generality, here we consider rotating BEC with the harmonic potential given in (2.29). Due to the property of the trapping potential, the solution of (3.58)−(3.60) decays to zero exponentially fast when $|\mathbf{x}| \to \infty$. Thus in practical computation, we can truncate this problem into a bounded domain with homogeneous Dirichlet boundary conditions [24, 23, 14]. For simplicity, we introduce the BFFP method for 2D case, i.e. $d = 2$, and generalizations to other dimensions are straightforward.

In 2D case, the truncated problem for (3.58)−(3.60) is

$$\partial_t \phi(\mathbf{x},t) = \left(\frac{1}{2}\nabla^2 - V_2(\mathbf{x}) - \beta_2|\phi|^2 + \Omega L_z\right)\phi, \quad \mathbf{x}\in\Omega_{\mathbf{x}}, \ \ t\in[t_n,t_{n+1}), \tag{3.61}$$

$$\phi(\mathbf{x},t_{n+1}) = \phi(\mathbf{x},t_{n+1}^+) = \frac{\phi(\mathbf{x},t_{n+1}^-)}{\|\phi(\cdot,t_{n+1}^-)\|}, \qquad \mathbf{x}\in\Omega_{\mathbf{x}}, \tag{3.62}$$

$$\phi(\mathbf{x},t) = 0, \qquad \mathbf{x}\in\Gamma=\partial\Omega_{\mathbf{x}}, \quad t\in[t_n,t_{n+1}), \tag{3.63}$$

$$\phi(\mathbf{x},0) = \phi_0(\mathbf{x}), \quad \mathbf{x}\in\overline{\Omega}_{\mathbf{x}}, \qquad \text{with} \quad \|\phi_0\|^2 = \int_{\Omega_{\mathbf{x}}} |\phi_0(\mathbf{x})|^2\, d\mathbf{x} = 1, \tag{3.64}$$

where the computational domain $\Omega_{\mathbf{x}} = [a,b]\times[c,d]$ with $|a|$, b, $|c|$ and d sufficiently large.

Choose the spatial mesh size $\Delta x = (b-a)/J$ and $\Delta y = (d-c)/K$ with J and K even positive integers, define grid points $x_j := a + j\Delta x$ and $y_k := c + k\Delta y$ for $0\le j\le J$ and $0\le k\le K$ respectively, and let $\phi_{j,k}^n$ be the numerical approximation of $\phi(x_j,y_k,t_n)$. Then the BFFP method for discretizing the problem (3.61)−(3.64) can be given by

$$\begin{aligned}\frac{\phi_{j,k}^{(1)} - \phi_{j,k}^n}{\Delta t} = {} & \frac{1}{2}\left(\nabla_h^2\phi^{(1)}\right)\Big|_{j,k} - V_2(x_j,y_k)\phi_{j,k}^n - \beta_2|\phi_{j,k}^n|^2\phi_{j,k}^n + \Omega\left(L_h\phi^n\right)\Big|_{j,k} \\ & -\alpha^n\left(\phi_{j,k}^{(1)} - \phi_{j,k}^n\right), \qquad n=0,1,2,\ldots,\end{aligned} \tag{3.65}$$

$$\phi_{j,k}^{n+1} = \frac{\phi_{j,k}^{(1)}}{\|\phi^{(1)}\|}, \quad \text{with } \phi_{j,k}^0 = \phi_0(x_j,y_k), \quad 1\le j\le J-1,\ 1\le k\le K-1, \tag{3.66}$$

where ∇_h^2 and L_h are the pseudospectral differential operators approximating ∇^2 and L_z respectively, and the norm $\left\|\phi^{(1)}\right\|$ is defined as

$$\left\|\phi^{(1)}\right\| := \sqrt{\Delta x\Delta y\sum_{j=1}^{J-1}\sum_{k=1}^{K-1}\left|\phi_{j,k}^{(1)}\right|^2}.$$

The parameter $\alpha^n = \alpha(t_n) \ge 0$ is called as stabilization parameter, and in practical simulations, we need choose the "optimal" stabilization parameter α_{opt}^n to get the steady state solution as fast as possible [12], i.e. letting

$$\alpha_{\text{opt}}^n = \frac{1}{2}\left(b_{\max}^n + b_{\min}^n\right) \tag{3.67}$$

with

$$b^n_{\max} = \max_{1\le j\le J-1,\ 1\le k\le K-1} \left[V_2\left(x_j, y_k\right) + \beta_2|\phi^n_{j,k}|^2\right],$$
$$b^n_{\min} = \min_{1\le j\le J-1,\ 1\le k\le K-1} \left[V_2\left(x_j, y_k\right) + \beta_2|\phi^n_{j,k}|^2\right].$$

By assuming that

$$\phi_{j,k} = \sum_{p=-J/2}^{J/2-1}\sum_{q=-K/2}^{K/2-1} \widehat{\phi}_{p,q}\, e^{i\mu_p(x_j-a)} e^{i\lambda_q(y_k-c)}, \quad 0\le j\le J,\ \ 0\le k\le K \tag{3.68}$$

with

$$\mu_p = \frac{2p\pi}{b-a}, \quad \lambda_q = \frac{2q\pi}{d-c}, \quad \widehat{\phi}_{p,q} = \frac{1}{JK}\sum_{j=0}^{J-1}\sum_{k=0}^{K-1} \phi_{j,k} e^{-i\mu_p(x_j-a)} e^{-i\lambda_q(y_k-c)},$$

we can define $\nabla^2_h\phi$ and $L_h\phi$ as

$$\left(\nabla^2_h\phi\right)\big|_{j,k} = -\sum_{p=-J/2}^{J/2-1}\sum_{q=-K/2}^{K/2-1} \left(\mu_p^2+\lambda_q^2\right)\, \widehat{\phi}_{p,q}\, e^{i\mu_p(x_j-a)} e^{i\lambda_q(y_k-c)}, \tag{3.69}$$

$$\left(L_h\phi\right)\big|_{j,k} = x_j\, \left(D^h_y\phi\right)\big|_{j,k} - y_k\, \left(D^h_x\phi\right)\big|_{j,k}, \quad 0\le j\le J,\ \ 0\le k\le K, \tag{3.70}$$

$$\left(D^h_x\phi\right)\big|_{j,k} = \sum_{p=-J/2}^{J/2-1}\sum_{q=-K/2}^{K/2-1} \mu_p\, \widehat{\phi}_{p,q}\, e^{i\mu_p(x_j-a)}\, e^{i\lambda_q(y_k-c)}, \tag{3.71}$$

$$\left(D^h_y\phi\right)\big|_{j,k} = \sum_{p=-J/2}^{J/2-1}\sum_{q=-K/2}^{K/2-1} \lambda_q\, \widehat{\phi}_{p,q}\, e^{i\mu_p(x_j-a)}\, e^{i\lambda_q(y_k-c)}. \tag{3.72}$$

Taking the discrete Fourier transform at both sides of (3.65), we get, for $-J/2 \le p \le J/2-1$ and $-K/2 \le q \le K/2-1$,

$$\left(\frac{1}{\Delta t} + \frac{1}{2}\left(\mu_p^2+\lambda_q^2\right) + \alpha^n\right)\left(\widehat{\phi^{(1)}}\right)_{p,q} = \left(\frac{1}{\Delta t} + \alpha^n\right)\left(\widehat{\phi^n}\right)_{p,q} + \left(\widehat{F^n}\right)_{p,q}, \tag{3.73}$$

where $\left(\widehat{F^n}\right)_{p,q}$ is the Fourier coefficient of $F^n_{j,k}$ which is defined as

$$F^n_{j,k} := F(\phi^n_{j,k}) = -V_2(x_j,y_k)\phi^n_{j,k} - \beta_2|\phi^n_{j,k}|^2\phi^n_{j,k} + \Omega\left(L_h\phi^n\right)\big|_{j,k}. \tag{3.74}$$

Solving (3.73) for $\left(\widehat{\phi^{(1)}}\right)_{p,q}$ and then substituting it into (3.68) and (3.66), we can get the solution $\phi^{n+1}_{j,k}$ immediately.

3.5 Numerical results

In this section, we apply the BFFP method to study the ground state of rotating BEC. In order to do so, we first test different choices of initial data which is very important for correctly obtaining the ground state solutions, and then present numerical results in different potentials for 2D and 3D cases.

In our practical computation, the steady state solutions are obtained by setting

$$\varepsilon = \max_{1\le j\le J-1,\, 1\le k\le K-1} \frac{\left|\phi_{j,k}^{n+1} - \phi_{j,k}^{n}\right|}{\Delta t} < 10^{-6}. \tag{3.75}$$

3.5.1 Choices of initial data

For non-rotating BEC with a harmonic potential, there are two kinds of approximation for the ground state $\phi_g(\mathbf{x})$, i.e. (3.50) when $|\beta_d| \ll 1$ and respectively (3.53) when $\beta_d \gg 1$. These two approximations can be used as the initial data when we compute the ground state of non-rotating BEC in weakly interacting regime and strongly repulsive interacting regime, respectively. With some modification on (3.50) and (3.53), here we present four kinds of initial data for rotating BEC:

$$\text{Type 1.}\quad \phi_0(\mathbf{x}) = \phi_g^{\mathrm{w}}(\mathbf{x}), \qquad \mathbf{x}\in\Omega_{\mathbf{x}};$$

$$\text{Type 2.}\quad \phi_0(\mathbf{x}) = \phi_g^{\mathrm{TF}}(\mathbf{x}), \qquad \mathbf{x}\in\Omega_{\mathbf{x}};$$

$$\text{Type 3.}\quad \phi_0(\mathbf{x}) = \frac{(1-\Omega)\phi_g^{\mathrm{w}}(\mathbf{x}) + \Omega\phi_v^{\mathrm{w}}(\mathbf{x})}{\left\|(1-\Omega)\phi_g^{\mathrm{w}}(\mathbf{x}) + \Omega\phi_v^{\mathrm{w}}(\mathbf{x})\right\|}, \qquad \mathbf{x}\in\Omega_{\mathbf{x}};$$

$$\text{Type 4.}\quad \phi_0(\mathbf{x}) = \frac{(1-\Omega)\phi_g^{\mathrm{TF}}(\mathbf{x}) + \Omega\phi_v^{\mathrm{TF}}(\mathbf{x})}{\left\|(1-\Omega)\phi_g^{\mathrm{TF}}(\mathbf{x}) + \Omega\phi_v^{\mathrm{TF}}(\mathbf{x})\right\|}, \qquad \mathbf{x}\in\Omega_{\mathbf{x}}.$$

where $\phi_v^{\mathrm{w}}(\mathbf{x}) = (x+iy)\phi_g^{\mathrm{w}}(\mathbf{x})$ and $\phi_v^{\mathrm{TF}}(\mathbf{x}) = (x+iy)\phi_g^{\mathrm{TF}}(\mathbf{x})$ with $\phi_g^{\mathrm{w}}(\mathbf{x})$ and $\phi_g^{\mathrm{TF}}(\mathbf{x})$ given in (3.50) and (3.53) respectively.

To test the effectiveness of the initial data, one important quantity is the energy (2.31), and the lower is the energy, the better is the initial data. Another important

quantity is angular momentum expectation defined as

$$\langle L_z\rangle(\phi) = i\int_{\Omega_{\mathbf{x}}} \phi^*(y\partial_x - x\partial_y)\phi \, d\mathbf{x} = -i\int_{\Omega_{\mathbf{x}}} \phi^*(x\partial_y - y\partial_x)\phi \, d\mathbf{x}, \tag{3.76}$$

which can be used to distinguish the pattern of the ground states when they have the same energy.

In the following, we take $V_2(x,y) = \frac{1}{2}(x^2+y^2)$ and $\beta_2 = 10$ or 1000, and compute the steady states of (3.61)−(3.64) with these four different initial data. For different $0 \le \Omega < \min\{\gamma_x, \gamma_y\}$, Figure 3.3 shows the energy and angular momentum expectation of the steady state solutions corresponding to different initial data. Here we denote $E^{(j)}$ and $\langle L_z\rangle^{(j)}$ as the energy and angular momentum expectation of the steady state solution $\phi^{(j)}$ which is computed by using Type j $(1 \le j \le 4)$ initial data.

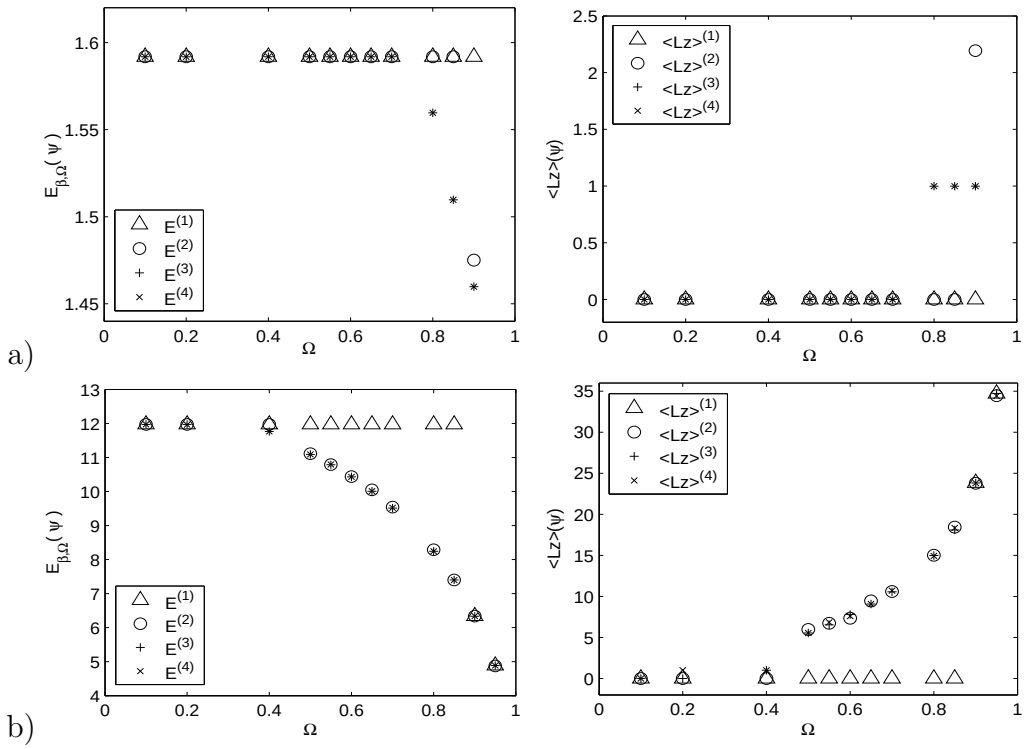

Figure 3.3: Energy (left) and angular momentum expectation (right) of the steady state solutions computed from different initial data. a). $\beta_2 = 10$; b). $\beta_2 = 1000$.

From Fig. 3.3, we can draw the following conclusions:

i). When β_2 is small, for small Ω, e.g. $0 < \Omega < 0.75$, these four initial data can

yield steady state solutions with the same energy; while for large Ω, only the Type 3 and 4 initial data can lead to the steady state solutions with smaller energy (cf. Fig. 3.3a).

ii). When both β_2 and Ω are large, Types 2, 3 and 4 initial data can generate steady state solutions with the same energy which is lower than that from Type 1 initial data (cf. Fig. 3.3b). However, the angular momentum expectations $\langle L_z \rangle$ of these steady state solutions are a bit different. This again suggests that the ground state solution is not unique, and different initial data give different solutions in some regimes of β_2 and Ω.

iii). Generally, the steady state solutions computed by using Types 3 and 4 initial data always have lower energies. Thus it is better to use them as the initial data when computing the ground state solutions of rotating BEC.

iv). Furthermore, from our additional computation, we can find when β_2 is small, Type 3 initial data can converge to the steady state solutions faster that Type 4, but when β_2 is large, Type 4 initial data converges faster. Thus in practical computation, we can choose them according to the magnitude of β_2 so as to get steady state solutions efficiently.

3.5.2 Ground state in harmonic potential

In this subsection, we study the ground state of rotating BEC with a harmonic potential. As discussed in Section 3.1, in this case the ground state exists only when $|\Omega| < \gamma_{\min} = \min\{\gamma_x, \gamma_y\}$, so we just consider $0 \leq \Omega < \gamma_{\min}$. Similar studies were also carried out in [23], by using the backward Euler finite difference (BEFD) method which is of the second-order accuracy in space and thus has difficulty to compute the ground state when both β_d and $|\Omega|$ are large. To compare these two methods, we apply our BFFP method to compute the ground state in 2D case, and the contour plots of these solutions are displayed in Figures 3.4−3.6.

From Figs. 3.4−3.6, we can see that in 2D case, the ground state in a harmonic

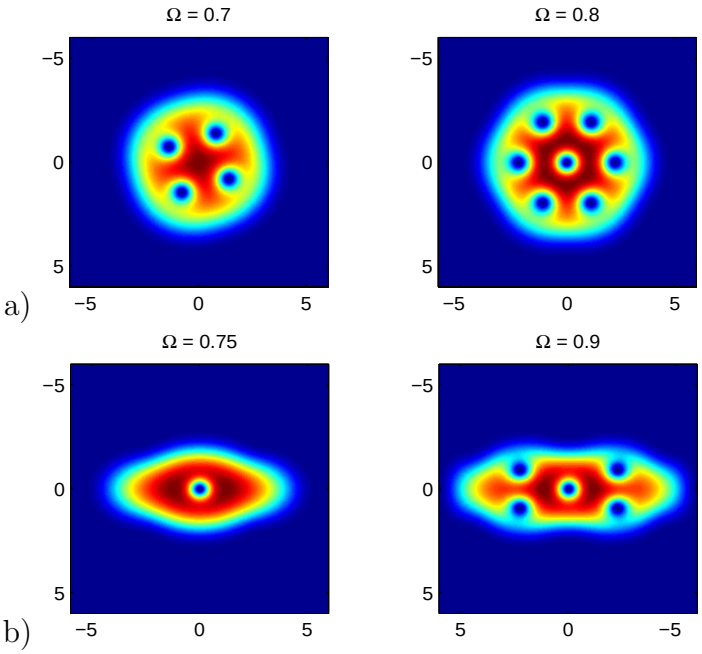

Figure 3.4: Contour plots of the ground state solution in 2D case with a harmonic potential and $\beta_2 = 100$. a). $\gamma_x = \gamma_y = 1$; b). $\gamma_x = 1$, $\gamma_y = 1.5$.

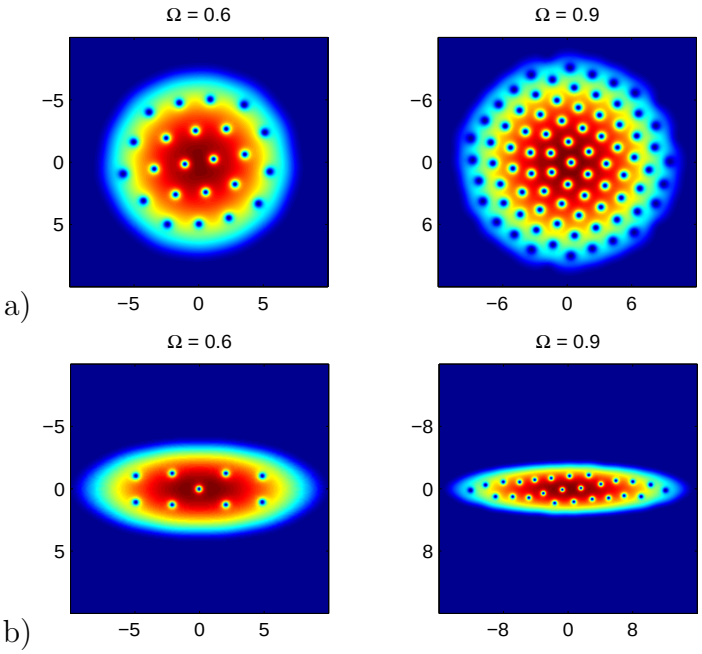

Figure 3.5: Contour plots of the ground state solution in 2D case with a harmonic potential and $\beta_2 = 2000$. a). $\gamma_x = \gamma_y = 1$; b). $\gamma_x = 1$, $\gamma_y = 2$.

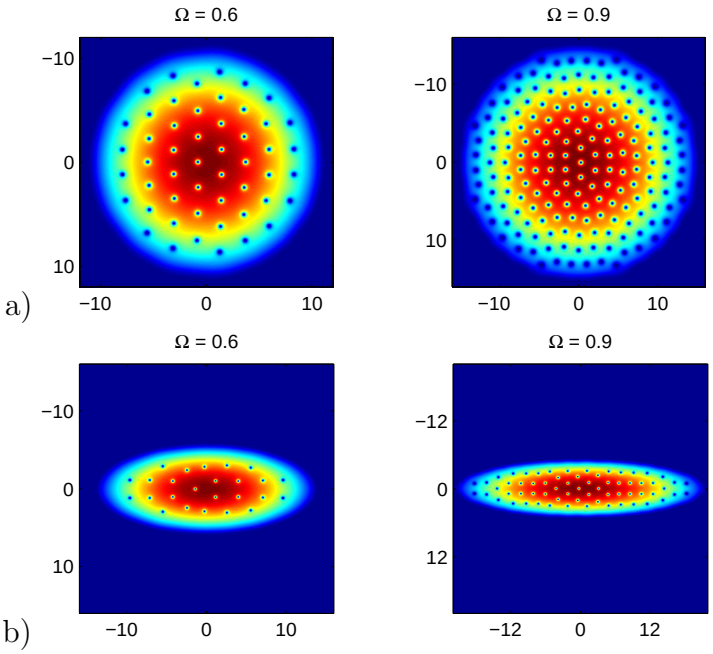

Figure 3.6: Contour plots of the ground state solution in 2D case with a harmonic potential and $\beta_2 = 8000$. a). $\gamma_x = \gamma_y = 1$; b). $\gamma_x = 1$, $\gamma_y = 2$.

potential is a vortex lattice with a number of single vortices. The results in Fig. 3.4 are computed by using the same parameters as those used in [23]. Comparing them with the results in [23], we can find that they agree very well with each other. This suggests that when β_2 is small, e.g. $\beta_2 = 100$, both BEFD and BFFP can accurately compute the ground state solution which has a few vortices.

However, for fixed $0 < |\Omega| < \gamma_{\min}$, when β_2 increases, the number of vortices also increases to form a dense lattice, and thus its numerical description needs high spatial resolution. This implies that when β_2 is large, the BEFD method has difficulty to compute the ground state solutions of rotating BEC, due to its lower-order accuracy in space. To show the effectiveness of our BFFP method, we also compute the ground state for larger β_2, e.g. $\beta_2 = 2000, 8000$, in symmetric (cf. Fig. 3.5a, 3.6a) and asymmetric (cf. Fig. 3.5b, 3.6b) harmonic potentials. From them, we can find for fixed Ω, when β_2 increases, the number of vortices increases dramatically and the lattice becomes much denser. For example, in the case of $\Omega = 0.9$ and $\gamma_x = \gamma_y = 1$,

when $\beta_2 = 2000$, there are 81 vortices in the lattice (cf. Fig. 3.5a), while when β_2 increases to 8000, the number of vortices increases to 176 (cf. Fig. 3.6a), and it is very hard to obtain them by using the low-order accuracy methods [122, 4, 5, 23]. Therefore, we may conclude that the BFFP method is an efficient and accurate method for computing the ground state, especially in rotating BEC with strongly repulsive interaction and large rotation speed.

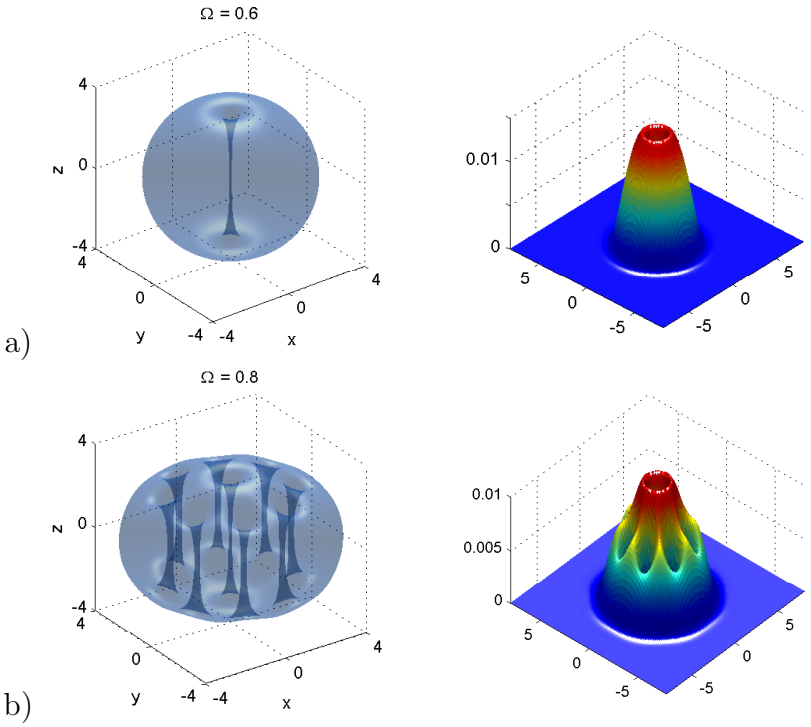

Figure 3.7: Ground states in 3D case with a harmonic potential. Left: isosurface plots for $|\phi_g(x, y, z)|^2 = 0.0005$; Right: surface plots of $|\phi_g(x, y, 0)|^2$.

In addition, we also show the ground state solution for 3D case in Figure 3.7, where the parameters are chosen as $\beta_3 = 400$ and $\gamma_x = \gamma_y = \gamma_z = 1$ in (2.29). From Fig. 3.7 and our additional computation, we can find that the ground state in 3D case is composed of single vortex lines. For fixed β_3, when Ω increases, the number of vortex lines increases, while for fixed Ω, the larger β_3, the more vortex lines, which is consistent with the 2D results in Figs. 3.4−3.6.

3.5.3 Giant vortex in harmonic plus quartic potential

As mentioned in Section 3.1, when $|\Omega| > \gamma_{\max} = \max\{\gamma_x, \gamma_y\}$, there is no ground state for rotating BEC with a harmonic potential. This is because under this condition, the centrifugal force caused by the angular rotation is large enough to compensate the trapping force, and thus the trap confinement vanishes. To study the ground state when $|\Omega| > \gamma_{\max}$, we often introduce a stiffer trapping potential, called as harmonic-plus-quartic potential, which takes the form [75, 5, 70],

$$\widetilde{V}_d(\mathbf{x}) = \begin{cases} (1-\alpha)r^2 + \frac{1}{4}kr^4, & d = 2, \\ (1-\alpha)r^2 + \frac{1}{4}kr^4 + \gamma_z^2 z^2, & d = 3, \end{cases} \tag{3.77}$$

where $r = \sqrt{x^2+y^2}$, and α, k and γ_z are positive constants. Under this potential, the ground state exists for any $|\Omega|$, but its structure is completely different from that in a harmonic potential.

Figure 3.8 shows the 2D ground state solution in a harmonic-plus-quartic potential for different Ω. The parameters used here are $\alpha = 1.2$, $k = 0.3$ and $\beta_2 = 1000$, and the initial data is chosen as the Thomas-Fermi approximation, i.e.

$$\phi_0(\mathbf{x}) = \phi_g^{\mathrm{TF}}(\mathbf{x}) = \begin{cases} \sqrt{\left(\mu - \widetilde{V}_2(\mathbf{x})\right)/\beta_2}, & \mu > \widetilde{V}_2(\mathbf{x}), \\ 0, & \text{otherwise}, \end{cases} \quad \mathbf{x} \in \mathbb{R}^2, \tag{3.78}$$

where $\mu = \frac{1}{k}\left[(3k^2\beta_2/8\pi)^{2/3} - (1-\alpha)^2\right]$.

From Fig. 3.8, we can draw the following conclusions for a fixed β_2:

i). There exist two critical angular velocities Ω_1 and Ω_2, e.g. when $\beta_2 = 1000$, $\Omega_1 \approx 0.9$ and $\Omega_2 \approx 2.2$, which determine the structure of the ground state. When $|\Omega| < \Omega_1$, no vortex appears in the ground state; when $\Omega_1 \le |\Omega| < \Omega_2$, the ground state is a vortex lattice but its structure is different from that in a harmonic potential (cf. Figs. 3.4−3.6); when $|\Omega| \ge \Omega_2$, a giant vortex appears in the ground state.

ii). In the case of $\Omega_1 \le |\Omega| < \Omega_2$, when $|\Omega|$ increases, the number of vortices increases, which makes the lattice become denser and denser, but the density at the center of the condensate decreases.

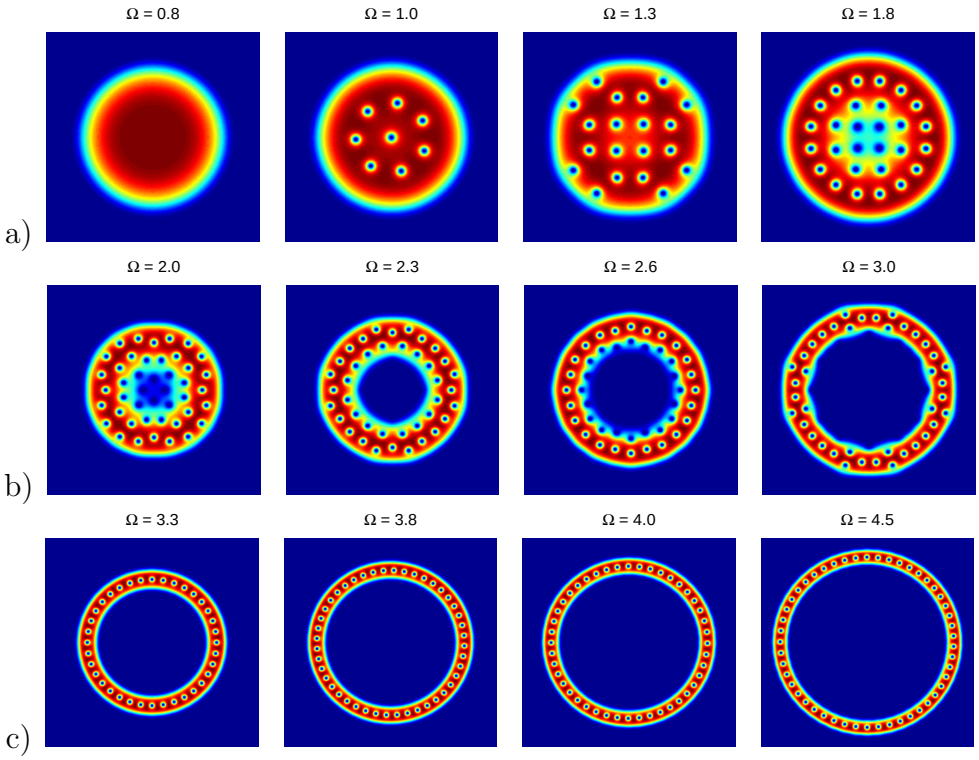

Figure 3.8: Ground states in 2D case with a harmonic-plus-quartic potential. Plot domain: a). $[-6, 6]^2$; b). $[-8, 8]^2$; c). $[-10, 10]^2$.

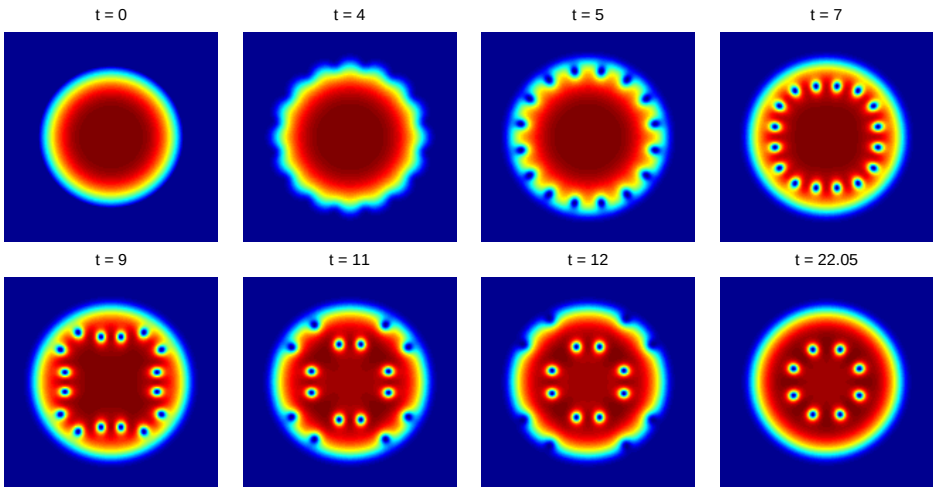

Figure 3.9: Formation of the vortex lattice in a harmonic-plus-quartic potential with $\Omega = 1.2$. Plot domain: $[-6, 6]^2$.

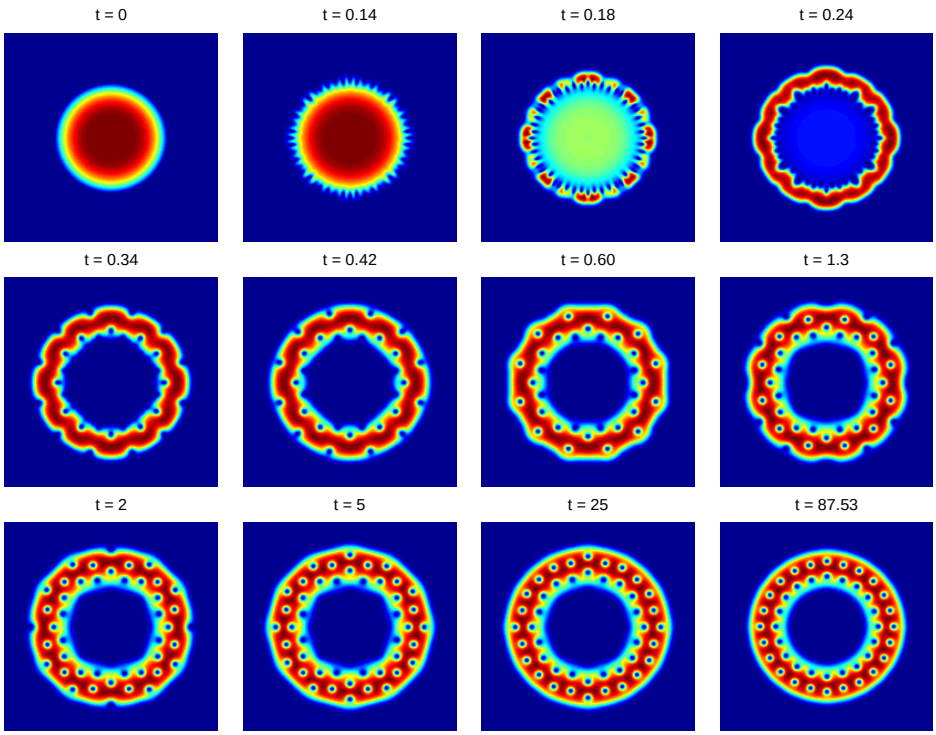

Figure 3.10: Formation of the giant vortex in a harmonic-plus-quartic potential with $\Omega = 2.5$. Plot domain: $[-8, 8]^2$.

iii). When $|\Omega| > \Omega_2$, a giant "hole" surrounded by a few cycles of single vortices appears at the center of the condensate. When $|\Omega|$ increases, the size of the giant hole increases, while the width of the vortex cycle decreases.

To show the formation of a vortex lattice or a giant vortex in the harmonic-plus-quartic potential, Figures 3.9 and 3.10 present the contour plots of $|\phi(x, y, t)|^2$ at different times during the time evolution of the gradient flow (3.61)−(3.64). We first consider the formation of a vortex lattice by choosing small Ω, e.g. $\Omega = 1.2$. As shown in Fig. 3.9, initially it is the Thomas-Fermi approximate ground state without vortices. When $t \approx 4$, the boundary becomes unstable and there are 16 vortices generated along the boundary. Then the rotating force pulls these vortices towards the rotation axis, but the repulsive interaction between vortices tends to push them apart. At time $t \approx 12$, eight out of them are almost pushed out of the

condensate, and the rest arranges and forms a stable lattice until $t = 22.05$.

The formation of a giant vortex is a bit different from that of the vortex lattice. In this case, the vortices are generated not only from the boundary but also from the interior (cf. Fig. 3.10) because of the large angular velocity Ω. Similarly, the competition between the rotating force and the repulsive interaction of vortices makes a steady giant vortex eventually.

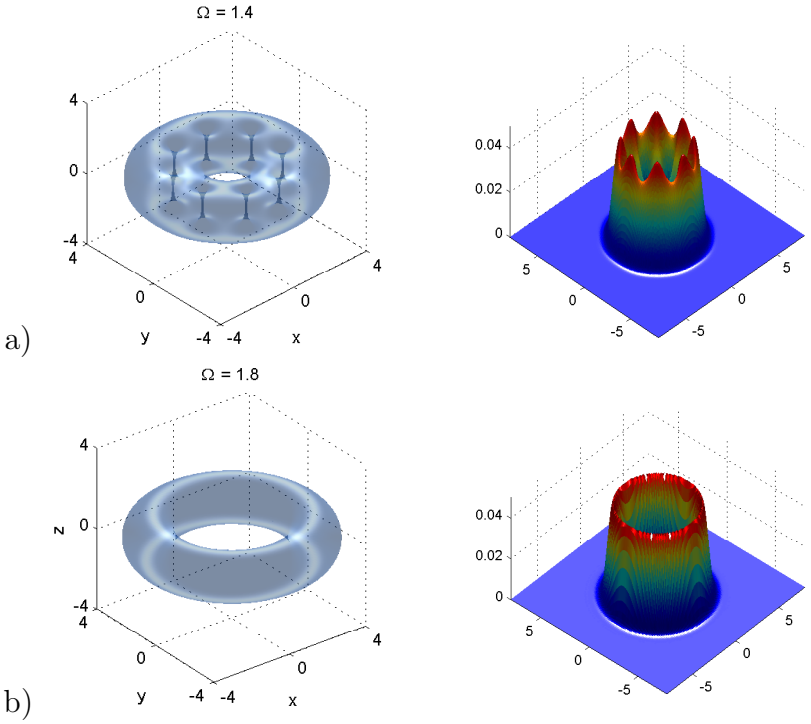

Figure 3.11: Ground states in 3D case with a harmonic-plus-quartic potential. Left: isosurface plots of $|\phi_g(x, y, z)|^2 = 0.0005$; Right: surface plots of $|\phi_g(x, y, 0)|^2$.

We also study the ground states in 3D case with a harmonic-plus-quartic potential by choosing $\beta_3 = 100$, $\alpha = 1.2$, $k = 0.3$ and $\gamma_z = 3$. The numerical results are shown in Figure 3.11. From it, we can see when Ω is small, e.g. $\Omega = 1.4$, the ground state is a giant vortex formed by a giant hole and a few single vortex lines; when Ω is large, e.g. $\Omega = 1.8$, there is only a giant hole and no vortex line appears.

Chapter 4

Dynamics of Bose-Einstein condensation

In this chapter, we investigate the dynamics of BEC both analytically and numerically. Some important quantities are introduced and the dynamical laws are derived for them. The dynamics of the mass center of a stationary state with its center shifted are also discussed in details. On the numerical front, several high-order numerical methods are proposed for computing the dynamics of non-rotating and rotating BEC.

4.1 Angular momentum expectation

To characterize the dynamics of BEC, an important quantity is the angular momentum expectation which is defined as

$$\langle L_z\rangle(t) := \int_{\mathbb{R}^d} \psi^*(\mathbf{x},t) L_z \psi(\mathbf{x},t)\, d\mathbf{x} = i\int_{\mathbb{R}^d} \psi^*(\mathbf{x},t)(y\partial_x - x\partial_y)\psi(\mathbf{x},t)\, d\mathbf{x}. \quad (4.1)$$

The angular momentum expectation can be used to measure the vortex flux, and we have the following lemma for its dynamics:

Lemma 4.1. Suppose $\psi(\mathbf{x},t)$ be the solution of the problem (2.27)−(2.28). Then we have,

$$\frac{d\langle L_z\rangle(t)}{dt} = \left(\gamma_x^2 - \gamma_y^2\right)\delta_{xy}(t), \quad \text{where } \delta_{xy}(t) = \int_{\mathbb{R}^d} xy|\psi(\mathbf{x},t)|^2\, d\mathbf{x}, \quad t \geq 0\,. \quad (4.2)$$

Consequently, the angular momentum expectation is conserved at least for 2D case with a radially symmetric trap or 3D case with a cylindrically symmetric trap. That is, for any given initial data $\psi_0(\mathbf{x})$ in (2.28), if $\gamma_x = \gamma_y$ in (2.29), we have

$$\langle L_z\rangle(t) \equiv \langle L_z\rangle(0), \qquad t \geq 0. \tag{4.3}$$

Proof. Differentiating (4.1) with respect to t, noticing (2.27), integrating by parts, and taking into account that $\psi(\mathbf{x}, t)$ decays to 0 exponentially when $|\mathbf{x}| \to \infty$, we get, for $t \geq 0$,

$$\begin{aligned}
\frac{d\langle L_z\rangle(t)}{dt} &= i\int_{\mathbb{R}^d} \left[(\partial_t\psi^*)\,(y\partial_x - x\partial_y)\psi + \psi^*(y\partial_x - x\partial_y)(\partial_t\psi)\right]\, d\mathbf{x} \\
&= \int_{\mathbb{R}^d} \left[(-i\partial_t\psi^*)\,(x\partial_y - y\partial_x)\psi + (i\partial_t\psi)\,(x\partial_y - y\partial_x)\psi^*\right]\, d\mathbf{x} \\
&= \int_{\mathbb{R}^d} \Big[-\frac{1}{2}\left[\nabla^2\psi^*(x\partial_y - y\partial_x)\psi + \nabla^2\psi(x\partial_y - y\partial_x)\psi^*\right] \\
&\qquad + \left(V_d(\mathbf{x}) + \beta_d|\psi|^2\right)\left[\psi^*(x\partial_y - y\partial_x)\psi + \psi(x\partial_y - y\partial_x)\psi^*\right] \Big]\, d\mathbf{x} \\
&= -\int_{\mathbb{R}^d} |\psi|^2\left[(x\partial_y - y\partial_x)V_d(\mathbf{x})\right]\, d\mathbf{x} = (\gamma_x^2 - \gamma_y^2)\int_{\mathbb{R}^d} xy|\psi|^2\, d\mathbf{x}.
\end{aligned} \tag{4.4}$$

This gives the ODE (4.2) immediately. Furthermore, if $\gamma_x = \gamma_y$, then (4.2) can be reduced to

$$\frac{d\langle L_z\rangle(t)}{dt} = 0, \qquad t \geq 0, \tag{4.5}$$

which implies that $\langle L_z\rangle$ is conserved for any $t \geq 0$. □

4.2 Condensate width

Another important quantity characterizing the dynamics of BEC is the condensate width defined as

$$\sigma_\alpha(t) = \sqrt{\delta_\alpha(t)}, \quad \text{where } \delta_\alpha(t) = \langle\alpha^2\rangle(t) = \int_{\mathbb{R}^d} \alpha^2|\psi(\mathbf{x}, t)|^2 d\mathbf{x}, \quad t \geq 0 \tag{4.6}$$

with α being the spatial variable x, y or z.

For the dynamics of condensate widths, we have the following lemma:

Lemma 4.2. Suppose $\psi(\mathbf{x},t)$ be the solution of the problem (2.27)−(2.28). We have,

$$\frac{d^2\delta_\alpha(t)}{dt^2} = \int_{\mathbb{R}^d}\Big[(\partial_y\alpha-\partial_x\alpha)\left(4i\Omega\psi^*(x\partial_y+y\partial_x)\psi+2\Omega^2(x^2-y^2)|\psi|^2\right) +2|\partial_\alpha\psi|^2+\beta_d|\psi|^4-2\alpha|\psi|^2\partial_\alpha(V_d(\mathbf{x}))\Big]\,d\mathbf{x},\quad t\geq 0, \tag{4.7}$$

$$\delta_\alpha(0)=\delta_\alpha^{(0)}=\int_{\mathbb{R}^d}\alpha^2|\psi_0|^2\,d\mathbf{x},\qquad \alpha=x,y,z, \tag{4.8}$$

$$\dot\delta_\alpha(0)=\delta_\alpha^{(1)}=2\int_{\mathbb{R}^d}\alpha\left[-\Omega|\psi_0|^2\left(x\partial_y-y\partial_x\right)\alpha+\mathrm{Im}\left(\psi_0^*\partial_\alpha\psi_0\right)\right]\,d\mathbf{x}. \tag{4.9}$$

Proof. Differentiating (4.6) with respect to t, and applying (2.27) and integration by parts, we get

$$\begin{aligned}\frac{d\delta_\alpha(t)}{dt} &= \frac{d}{dt}\int_{\mathbb{R}^d}\alpha^2|\psi(\mathbf{x},t)|^2d\mathbf{x}=\int_{\mathbb{R}^d}\alpha^2\left(\psi\partial_t\psi^*+\psi^*\partial_t\psi\right)\,d\mathbf{x}\\ &= \int_{\mathbb{R}^d}\left[\frac{i}{2}\alpha^2\left(\psi^*\nabla^2\psi-\psi\nabla^2\psi^*\right)+\Omega\alpha^2\left(x\partial_y-y\partial_x\right)|\psi|^2\right]\,d\mathbf{x}\\ &= \int_{\mathbb{R}^d}\left[i\alpha\left(\psi\partial_\alpha\psi^*-\psi^*\partial_\alpha\psi\right)-2\Omega\alpha|\psi|^2\left(x\partial_y-y\partial_x\right)\alpha\right]\,d\mathbf{x}.\end{aligned} \tag{4.10}$$

Differentiating (4.10), noticing (2.27) and integrating by parts, we have,

$$\begin{aligned}&\frac{d^2\delta_\alpha(t)}{dt^2}\\ =\;&\int_{\mathbb{R}^d}\Big[i\alpha\left(\partial_t\psi\partial_\alpha\psi^*+\psi\partial_{\alpha t}\psi^*-\partial_t\psi^*\partial_\alpha\psi-\psi^*\partial_{\alpha t}\psi\right)\\ &\quad-2\Omega\alpha\left(\psi\partial_t\psi^*+\psi^*\partial_t\psi\right)\left(x\partial_y-y\partial_x\right)\alpha\Big]\,d\mathbf{x}\\ =\;&\int_{\mathbb{R}^d}\Big[2i\alpha\left(\partial_t\psi\partial_\alpha\psi^*-\partial_t\psi^*\partial_\alpha\psi\right)+i\left(\psi^*\partial_t\psi-\psi\partial_t\psi^*\right)\\ &\quad-2\Omega\alpha(x\partial_y-y\partial_x)\alpha\left(\frac{i}{2}\left(\psi^*\nabla^2\psi-\psi\nabla^2\psi^*\right)+\Omega(x\partial_y-y\partial_x)|\psi|^2\right)\Big]\,d\mathbf{x}\\ =\;&\int_{\mathbb{R}^d}\Big[-\alpha\left(\partial_\alpha\psi^*\nabla^2\psi+\partial_\alpha\psi\nabla^2\psi^*\right)+2\alpha\left(V_d(\mathbf{x})+\beta_d|\psi|^2\right)\left(\psi\partial_\alpha\psi^*+\psi^*\partial_\alpha\psi\right)\\ &\quad-2i\Omega\alpha\left[\partial_\alpha\psi\left(x\partial_y-y\partial_x\right)\psi^*-\partial_\alpha\psi^*\left(x\partial_y-y\partial_x\right)\psi\right]-\frac{1}{2}\left(\psi^*\nabla^2\psi+\psi\nabla^2\psi^*\right)\\ &\quad+2\left(V_d(\mathbf{x})|\psi|^2+\beta_d|\psi|^4\right)-i\Omega\left[\psi\left(x\partial_y-y\partial_x\right)\psi^*-\psi^*\left(x\partial_y-y\partial_x\right)\psi\right]\\ &\quad-2i\Omega\psi^*\left[\partial_x\alpha\left(\alpha\partial_y+y\partial_\alpha\right)\psi-\partial_y\alpha\left(\alpha\partial_x+x\partial_\alpha\right)\psi\right]\end{aligned}$$

$$
\begin{aligned}
&+2\Omega^2|\psi|^2\left[\left(y^2-\alpha x\right)\partial_x\alpha+\left(x^2-\alpha y\right)\partial_y\alpha\right]\Big]\,d\mathbf{x}\\
=&\int_{\mathbb{R}^d}\Big[-4i\Omega\psi^*\left[\partial_x\alpha\left(\alpha\partial_y+y\partial_\alpha\right)\psi-\partial_y\alpha\left(\alpha\partial_x+x\partial_\alpha\right)\psi\right]+2|\partial_\alpha\psi|^2+\beta_d|\psi|^4\\
&+2\Omega^2|\psi|^2\left[\left(y^2-\alpha x\right)\partial_x\alpha+\left(x^2-\alpha y\right)\partial_y\alpha\right]-2\alpha|\psi|^2\partial_\alpha\left(V_d(\mathbf{x})\right)\Big]\,d\mathbf{x}\\
=&\int_{\mathbb{R}^d}\Big[\left(\partial_y\alpha-\partial_x\alpha\right)\left[4i\Omega\psi^*(x\partial_y+y\partial_x)\psi+2\Omega^2\left(x^2-y^2\right)|\psi|^2\right]\\
&+2|\partial_\alpha\psi|^2+\beta_d|\psi|^4-2\alpha|\psi|^2\partial_\alpha\left(V_d(\mathbf{x})\right)\Big]\,d\mathbf{x},\qquad t\geq 0. \qquad (4.11)
\end{aligned}
$$

Furthermore, noticing (2.28), and taking $t=0$ in (4.6) and (4.10), we can obtain (4.8) and (4.9) immediately. □

Lemma 4.3. i). In 1D without rotation and interaction, i.e. $d=1$, $\Omega=0$ and $\beta_1=0$, for any initial data $\psi_0(x)$ in (2.28), we have

$$
\delta_x(t)=\frac{E_{0,0}(\psi_0)}{\gamma_x^2}+\left(\delta_x^{(0)}-\frac{E_{0,0}(\psi_0)}{\gamma_x^2}\right)\cos\left(2\gamma_x t\right)+\frac{\delta_x^{(1)}}{2\gamma_x}\sin\left(2\gamma_x t\right),\quad t\geq 0. \qquad (4.12)
$$

ii). In 2D with a radially symmetric trap, i.e. $d=2$ and $\gamma_x=\gamma_y:=\gamma_r$, for any initial data $\psi_0(x,y)$ in (2.28), we have, for any $t\geq 0$,

$$
\delta_r(t)=\frac{E_{\beta,\Omega}(\psi_0)+\Omega\langle L_z\rangle(0)}{\gamma_r^2}\left[1-\cos(2\gamma_r t)\right]+\delta_r^{(0)}\cos(2\gamma_r t)+\frac{\delta_r^{(1)}}{2\gamma_r}\sin(2\gamma_r t), \qquad (4.13)
$$

where $\delta_r(t)=\delta_x(t)+\delta_y(t)$, $\delta_r^{(0)}:=\delta_x(0)+\delta_y(0)$ and $\delta_r^{(1)}:=\dot\delta_x(0)+\dot\delta_y(0)$. Furthermore, if the initial data $\psi_0(x,y)$ is the central vortex state solution (2.39), then we have, for $t\geq 0$,

$$
\begin{aligned}
\delta_x(t)&=\delta_y(t)=\frac{1}{2}\delta_r(t)\\
&=\frac{E_{\beta,\Omega}(\psi_0)+m\Omega}{2\gamma_x^2}\left[1-\cos(2\gamma_x t)\right]+\delta_x^{(0)}\cos(2\gamma_x t)+\frac{\delta_x^{(1)}}{2\gamma_x}\sin(2\gamma_x t). \qquad (4.14)
\end{aligned}
$$

Noticing (4.6) and (4.14), we immediately get

$$
\sigma_x(t)=\sigma_y(t)=\sqrt{\frac{E_{\beta,\Omega}(\psi_0)+m\Omega}{2\gamma_x^2}\left[1-\cos(2\gamma_x t)\right]+\delta_x^{(0)}\cos(2\gamma_x t)+\frac{\delta_x^{(1)}}{2\gamma_x}\sin(2\gamma_x t)}.
$$

Therefore, in this case, the condensate widths $\sigma_x(t)$ and $\sigma_y(t)$ are periodic functions with frequency doubling the trapping frequency.

iii). In all other cases, we have, for $t \geq 0$,

$$\delta_\alpha(t) = \frac{E_{\beta,\Omega}(\psi_0)}{\gamma_\alpha^2} + \left(\delta_\alpha^{(0)} - \frac{E_{\beta,\Omega}(\psi_0)}{\gamma_\alpha^2}\right)\cos(2\gamma_\alpha t) + \frac{\delta_\alpha^{(1)}}{2\gamma_\alpha}\sin(2\gamma_\alpha t) + f_\alpha(t), \qquad (4.15)$$

where $f_\alpha(t)$ is the solution of the following second-order ODE:

$$\frac{d^2 f_\alpha(t)}{dt^2} + 4\gamma_\alpha^2\, f_\alpha(t) = F_\alpha(t), \qquad f_\alpha(0) = \dot{f}_\alpha(0) = 0, \qquad (4.16)$$

with

$$\begin{aligned} F_\alpha(t) &= \int_{\mathbb{R}^d} \Big[2|\partial_\alpha\psi|^2 - 2|\nabla\psi|^2 - \beta_d|\psi|^4 + \left(2\gamma_\alpha^2\alpha^2 - 4V_d(\mathbf{x})\right)|\psi|^2 + 4\Omega\psi^* L_z\psi \\ &\quad + (\partial_y\alpha - \partial_x\alpha)\left(4i\Omega\psi^*\left(x\partial_y + y\partial_x\right)\psi + 2\Omega^2(x^2-y^2)|\psi|^2\right)\Big]d\mathbf{x}. \end{aligned}$$

Proof. i). From (4.7) with $d = 1$, $\Omega = 0$ and $\beta_1 = 0$, noticing (2.31), we get

$$\frac{d^2\delta_x(t)}{dt^2} = 4E_{0,0}(\psi_0) - 4\gamma_x^2\delta_x(t), \qquad t \geq 0, \qquad (4.17)$$

$$\delta_x(0) = \delta_x^{(0)}, \qquad \dot{\delta}_x(0) = \delta_x^{(1)}. \qquad (4.18)$$

Thus (4.12) is the unique solution of the second-order ODE (4.17)−(4.18).

ii). From (4.7) with $d = 2$, we get

$$\begin{aligned} \frac{d^2\delta_x(t)}{dt^2} &+ 2\gamma_x^2\delta_x(t) \\ &= \int_{\mathbb{R}^2}\left[2|\partial_x\psi|^2 + \beta_2|\psi|^4 - 4i\Omega\psi^*\left(x\partial_y + y\partial_x\right)\psi - 2\Omega^2\left(x^2-y^2\right)|\psi|^2\right]d\mathbf{x}, \\ \frac{d^2\delta_y(t)}{dt^2} &+ 2\gamma_y^2\delta_y(t) \\ &= \int_{\mathbb{R}^2}\left[2|\partial_y\psi|^2 + \beta_2|\psi|^4 + 4i\Omega\psi^*\left(x\partial_y + y\partial_x\right)\psi + 2\Omega^2\left(x^2-y^2\right)|\psi|^2\right]d\mathbf{x}. \end{aligned}$$

When $\gamma_x = \gamma_y := \gamma_r$ in (2.29), summing up the above two equations, and noticing (2.31) and (4.3), we obtain the following ODE for $\delta_r(t)$:

$$\begin{aligned} \frac{d^2\delta_r(t)}{dt^2} &= -2\gamma_r^2\delta_r(t) + \int_{\mathbb{R}^2}\left[2|\nabla\psi|^2 + 2\beta_2|\psi|^4\right]d\mathbf{x} \\ &= -2\gamma_r^2\delta_r(t) - 4\int_{\mathbb{R}^2}\left[V_2(\mathbf{x})|\psi|^2 - \Omega\psi^* L_z\psi\right]d\mathbf{x} \end{aligned}$$

$$
\begin{aligned}
&+4\int_{\mathbb{R}^2}\left[\frac{1}{2}|\nabla\psi|^2+V_2(\mathbf{x})|\psi|^2+\frac{\beta_2}{2}|\psi|^4-\Omega\psi^*L_z\psi\right]d\mathbf{x}\\
=\;& -2\gamma_r^2\delta_r(t)-2\gamma_r^2\delta_r(t)+4\Omega\langle L_z\rangle(t)+4E_{\beta,\Omega}(\psi(\cdot,t))\\
=\;& -4\gamma_r^2\delta_r(t)+4E_{\beta,\Omega}(\psi_0)+4\Omega\langle L_z\rangle(0), \qquad t\geq 0, \qquad (4.19)\\
\delta_r(0) =\;& \delta_r^{(0)}, \qquad \dot{\delta}_r(0)=\delta_r^{(1)}. \qquad (4.20)
\end{aligned}
$$

Thus (4.13) is the unique solution of the second-order ODE (4.19)−(4.20). Furthermore, if the initial data $\psi_0(x,y)$ satisfies (2.39), then the solution $\psi(x,y,t)$ of (2.27)−(2.28) can be given by

$$
\psi(x,y,t)=g(r,t)e^{im\theta}, \qquad \text{with} \quad g(r,0)=f(r). \qquad (4.21)
$$

This implies

$$
\begin{aligned}
\delta_x(t) =\;& \int_{\mathbb{R}^2}x^2|\psi(x,y,t)|^2\,d\mathbf{x}=\int_0^\infty\int_0^{2\pi}r^2\cos^2\theta|g(r,t)|^2r\,d\theta dr\\
=\;& \pi\int_0^\infty r^2|g(r,t)|^2r\,dr=\int_0^\infty\int_0^{2\pi}r^2\sin^2\theta|g(r,t)|^2r\,d\theta dr\\
=\;& \int_{\mathbb{R}^2}y^2|\psi(x,y,t)|^2\,d\mathbf{x}=\delta_y(t), \qquad t\geq 0. \qquad (4.22)
\end{aligned}
$$

Since $\gamma_x=\gamma_y$, by Lemma 4.1, we can get

$$
\begin{aligned}
\langle L_z\rangle(t)=\langle L_z\rangle(0) =\;& -i\int_{\mathbb{R}^2}\psi_0^*(x,y)\partial_\theta\psi_0(x,y)\,d\mathbf{x}\\
=\;& 2\pi m\int_0^\infty|f(r)|^2r\,dr=m\|\psi_0\|^2=m. \qquad (4.23)
\end{aligned}
$$

Thus (4.14) is a combination of (4.13), (4.22) and (4.23).

iii). From (4.7), noticing the energy conservation (2.31), we can get

$$
\begin{aligned}
\frac{d^2\delta_\alpha(t)}{dt^2} =\;& \int_{\mathbb{R}^d}\Big[(\partial_y\alpha-\partial_x\alpha)\left[4i\Omega\psi^*(x\partial_y+y\partial_x)\psi+2\Omega^2\left(x^2-y^2\right)|\psi|^2\right]\\
&+2|\partial_\alpha\psi|^2+\beta_d|\psi|^4-2\gamma_\alpha^2\alpha^2|\psi|^2\Big]\,d\mathbf{x}\\
=\;& -4\gamma_\alpha^2\delta_\alpha(t)+4\int_{\mathbb{R}^2}\left[\frac{1}{2}|\nabla\psi|^2+V_d(\mathbf{x})|\psi|^2+\frac{\beta_d}{2}|\psi|^4-\Omega\psi^*L_z\psi\right]d\mathbf{x}\\
&+\int_{\mathbb{R}^d}\Big[2|\partial_\alpha\psi|^2-2|\nabla\psi|^2-\beta_d|\psi|^4+\left(2\gamma_\alpha^2\alpha^2-4V_d(\mathbf{x})\right)|\psi|^2+4\Omega\psi^*L_z\psi\\
&+(\partial_y\alpha-\partial_x\alpha)\left(4i\Omega\psi^*\left(x\partial_y+y\partial_x\right)\psi+2\Omega^2(x^2-y^2)|\psi|^2\right)\Big]d\mathbf{x}\\
=\;& -4\gamma_\alpha^2\delta_\alpha(t)+4E_{\beta,\Omega}(\psi(\cdot,t))+F_\alpha(t)
\end{aligned}
$$

$$= -4\gamma_\alpha^2\delta_\alpha(t) + 4E_{\beta,\Omega}(\psi_0) + F_\alpha(t), \qquad t \geq 0. \tag{4.24}$$

Thus (4.15) is the unique solution of the second-order ODE (4.24) with the initial data (4.8)−(4.9). □

4.3 Mass center of a stationary state

Let $\phi_e(\mathbf{x})$ be a stationary state solution of the GPE (2.27) with a chemical potential μ_e, i.e. (μ_e, ϕ_e) satisfying the eigenvalue problem (2.33)−(2.34). If the initial data $\psi_0(\mathbf{x})$ in (2.28) is chosen as $\phi_e(\mathbf{x})$ with a shift in its center, then we can construct an exact solution of the GPE (2.27) with a harmonic potential (2.29). This kind of analytical construction can be used, in particular, in the benchmark and validation of numerical algorithms for the time-dependent GPE. In [69], a similar kind of solution was constructed and a second-order ODE system was derived for the dynamics of the center, but their results were valid only for non-rotating BEC, i.e. $\Omega = 0$. Modifications must be made for rotating BEC, i.e. $\Omega \neq 0$. Later, in [25], similar results were extended to the case of a general Hamiltonian but without specifying the initial data for the ODE system, and there is no analysis about the ODE system. In this section, we present a simple and complete derivation of the dynamic laws in rotating BEC [14]. By solving the ODE system in different cases, we classify the motion patterns of the center [138].

Lemma 4.4. If the initial data $\psi_0(\mathbf{x})$ in (2.28) is chosen as

$$\psi_0(\mathbf{x}) = \phi_e(\mathbf{x} - \mathbf{x}_0), \qquad \mathbf{x} \in \mathbb{R}^d \tag{4.25}$$

with $\mathbf{x}_0 \in \mathbb{R}^d$ a given point, then the exact solution of (2.27) satisfies:

$$\psi(\mathbf{x}, t) = \phi_e(\mathbf{x} - \mathbf{x}(t))\, e^{-i\mu_e t}\, e^{iw(\mathbf{x},t)}, \qquad \mathbf{x} \in \mathbb{R}^d, \quad t \geq 0, \tag{4.26}$$

where for any time $t \geq 0$, $w(\mathbf{x}, t)$ is a linear function with respect to $\mathbf{x}$, i.e.

$$w(\mathbf{x}, t) = \mathbf{c}(t) \cdot \mathbf{x} + g(t), \qquad \mathbf{c}(t) = (c_1(t), \cdots, c_d(t))^T, \qquad \mathbf{x} \in \mathbb{R}^d, \quad t \geq 0, \tag{4.27}$$

and $\mathbf{x}(t)$ satisfies the following second-order ODE system:

$$\ddot{x}(t) - 2\Omega\dot{y}(t) + \left(\gamma_x^2 - \Omega^2\right) x(t) = 0, \tag{4.28}$$

$$\ddot{y}(t) + 2\Omega\dot{x}(t) + \left(\gamma_y^2 - \Omega^2\right) y(t) = 0, \qquad t \geq 0, \tag{4.29}$$

$$x(0) = x_0, \quad y(0) = y_0, \quad \dot{x}(0) = \Omega y_0, \quad \dot{y}(0) = -\Omega x_0. \tag{4.30}$$

Moreover, if in 3D case, another ODE needs to be added:

$$\ddot{z}(t) + \gamma_z^2 z(t) = 0, \qquad z(0) = z_0, \qquad \dot{z}(0) = 0. \tag{4.31}$$

Proof. For $d = 2$, we introduce

$$\mathbf{A} = \begin{pmatrix} \gamma_x^2 & 0 \\ 0 & \gamma_y^2 \end{pmatrix}.$$

Differentiating (4.26) with respect to t and $\mathbf{x}$ respectively, plugging it into (2.27), changing variable $\mathbf{x} - \mathbf{x}(t) \to \mathbf{x}$ and noticing (2.33), we obtain for $\phi_e = \phi_e(\mathbf{x})$ and $w = w(\mathbf{x} + \mathbf{x}(t), t)$:

$$\begin{aligned} \phi_e \partial_t w + i\dot{\mathbf{x}}(t) \cdot \nabla\phi_e = \frac{1}{2}\left[i\phi_e \nabla^2 w - \phi_e |\nabla w|^2 - \mathbf{x}(t)^T \mathbf{A}(2\mathbf{x} + \mathbf{x}(t))\phi_e\right] \\ + i\nabla\phi_e \cdot \nabla w - \phi_e \Omega(\mathbf{x} + \mathbf{x}(t)) \cdot (\mathbf{G}\nabla w) + i\Omega\mathbf{x}(t) \cdot (\mathbf{G}\nabla\phi_e), \end{aligned} \tag{4.32}$$

where $\mathbf{G}$ is the symplectic matrix given in (2.54). Taking the real and imaginary parts of (4.32) and noticing (4.27), we have

$$[\dot{\mathbf{x}}(t) - \nabla w(\mathbf{x} + \mathbf{x}(t), t) - \Omega\mathbf{G}\mathbf{x}(t)] \cdot \nabla\phi_e = 0, \tag{4.33}$$

$$\left[\partial_t w + \frac{1}{2}|\nabla w|^2 + \frac{1}{2}\mathbf{x}(t)^T \mathbf{A}(2\mathbf{x} + \mathbf{x}(t)) - \Omega(\mathbf{x} + \mathbf{x}(t)) \cdot (\mathbf{G}\nabla w)\right] \phi_e = 0, \tag{4.34}$$

that is,

$$\dot{\mathbf{x}}(t) = \nabla w(\mathbf{x} + \mathbf{x}(t), t) + \Omega\mathbf{G}\mathbf{x}(t), \tag{4.35}$$

$$\begin{aligned} \partial_t w(\mathbf{x} + \mathbf{x}(t), t) = -\frac{1}{2}\left[|\nabla w|^2 + \mathbf{x}(t)^T \mathbf{A}(2\mathbf{x} + \mathbf{x}(t))\right] \\ + \Omega(\mathbf{x} + \mathbf{x}(t)) \cdot (\mathbf{G}\nabla w). \end{aligned} \tag{4.36}$$

Differentiating (4.35) and (4.36) with respect to t and $\mathbf{x}$ respectively, noticing (4.27) which implies that $|\nabla w|^2$ is independent of $\mathbf{x}$, we get

$$\begin{aligned}
0 &= \ddot{\mathbf{x}}(t) - \partial_t(\nabla w(\mathbf{x}+\mathbf{x}(t),t)) - \Omega\mathbf{G}\dot{\mathbf{x}}(t) \\
&= \ddot{\mathbf{x}}(t) - \nabla(\partial_t w(\mathbf{x}+\mathbf{x}(t),t)) - \dot{\mathbf{x}}(t)\,\nabla^2 w(\mathbf{x}+\mathbf{x}(t),t) - \Omega\mathbf{G}\dot{\mathbf{x}}(t) \\
&= \ddot{\mathbf{x}}(t) - \nabla(\partial_t w(\mathbf{x}+\mathbf{x}(t),t)) - \Omega\mathbf{G}\dot{\mathbf{x}}(t) \\
&= \ddot{\mathbf{x}}(t) + \mathbf{A}\mathbf{x}(t) - \Omega\mathbf{G}\left[\dot{\mathbf{x}}(t) - \Omega\mathbf{G}\mathbf{x}(t)\right] - \Omega\mathbf{G}\dot{\mathbf{x}}(t) \\
&= \ddot{\mathbf{x}}(t) - 2\Omega\mathbf{G}\dot{\mathbf{x}}(t) + \left(\mathbf{A} + \Omega^2\mathbf{G}^2\right)\mathbf{x}(t) \\
&= \ddot{\mathbf{x}}(t) - 2\Omega\mathbf{G}\dot{\mathbf{x}}(t) + \left(\mathbf{A} - \Omega^2\mathbf{I}\right)\mathbf{x}(t), \qquad t \geq 0, \qquad (4.37)
\end{aligned}$$

where $\mathbf{I}$ is an identity matrix. From (4.26) with $t = 0$, we have

$$\mathbf{x}(0) = \mathbf{x}_0, \qquad w(\mathbf{x},0) \equiv 0, \quad \mathbf{x} \in \mathbb{R}^d. \qquad (4.38)$$

Thus (4.30) is a combination of (4.38) and (4.35) with $t = 0$. For $d = 3$, the proof is similar and the details are omitted here. □

From (2.27), (2.34) and (4.26), by changing variables, we obtain

$$\begin{aligned}
\langle\mathbf{x}\rangle(t) : &= \int_{\mathbb{R}^d} \mathbf{x}|\psi(\mathbf{x},t)|^2\,d\mathbf{x} = \int_{\mathbb{R}^d} \mathbf{x}|\phi_e(\mathbf{x}-\mathbf{x}(t))|^2\,d\mathbf{x} \qquad (4.39) \\
&= \int_{\mathbb{R}^d} (\mathbf{x}+\mathbf{x}(t))|\phi_e(\mathbf{x})|^2\,d\mathbf{x} = \mathbf{x}(t), \qquad t \geq 0. \qquad (4.40)
\end{aligned}$$

This immediately implies that the dynamics of the mass center $\langle\mathbf{x}\rangle(t)$ is the same as that of $\mathbf{x}(t)$, i.e. satisfying the ODE system (4.28)−(4.31).

Notice that with $\mathbf{y}(t) = \dot{\mathbf{x}}(t) - \Omega\mathbf{G}\mathbf{x}(t)$, (4.37) gives a coupled first-order ODE system,

$$\begin{cases}
\dot{\mathbf{x}}(t) = \Omega\mathbf{G}\mathbf{x}(t) + \mathbf{y}(t)\,, \\
\dot{\mathbf{y}}(t) = -\mathbf{A}\mathbf{x}(t) + \Omega\mathbf{G}\mathbf{y}(t)\,, \qquad t \geq 0, \\
\mathbf{x}(0) = \mathbf{x}_0, \quad \mathbf{y}(0) = 0\,,
\end{cases} \qquad (4.41)$$

which is a Hamiltonian system with the Hamiltonian $H(\mathbf{x},\mathbf{y}) = \Omega\mathbf{y}^T\mathbf{G}\mathbf{x} + (\mathbf{y}^T\mathbf{y} + \mathbf{x}^T\mathbf{A}\mathbf{x})/2$. The characteristic roots λ of the system are given by

$$\lambda^4 + \left(\gamma_x^2 + \gamma_y^2 + 2\Omega^2\right)\lambda^2 + \left(\gamma_x^2 - \Omega^2\right)\left(\gamma_y^2 - \Omega^2\right) = 0\,. \qquad (4.42)$$

The exact solutions of (4.41) may thus be completely determined. We note that not only results on the dynamics of a stationary state with its center shifted are physically interesting, but also this type of exact solution can serve as a good benchmark for numerical algorithms and is useful in the mathematical studies of the dynamic stabilities of central vortex states in BEC.

It is easy to see that the solution of (4.31) is

$$z(t) = z_0 \cos(\gamma_z t), \qquad t \geq 0, \tag{4.43}$$

that is, $z(t)$ is a periodic function with period $T_z = 2\pi/\gamma_z$.

In the following subsections, we discuss the solution of the ODE system (4.28)−(4.30) in different parameter regimes of the trapping frequencies and angular speed. Without loss of generality, next we assume $\gamma_x = 1$ and $\gamma_x \leq \gamma_y$.

4.3.1 For non-rotating BEC

For non-rotating BEC, i.e. $\Omega = 0$ in (2.27), the second-order ODE system (4.28)−(4.30) collapses to

$$\ddot{x}(t) + \gamma_x^2 x(t) = 0, \qquad \ddot{y}(t) + \gamma_y^2 y(t) = 0, \qquad t \geq 0, \tag{4.44}$$

$$x(0) = x_0, \qquad y(0) = y_0, \qquad \dot{x}(0) = \dot{y}(0) = 0. \tag{4.45}$$

It is straightforward to see that the solution of (4.44)−(4.45) is

$$x(t) = x_0 \cos(\gamma_x t), \qquad y(t) = y_0 \cos(\gamma_y t), \qquad t \geq 0. \tag{4.46}$$

This implies that both $x(t)$ and $y(t)$ are periodic functions with periods $T_x = 2\pi/\gamma_x$ and $T_y = 2\pi/\gamma_y$, respectively.

Figure 4.1 displays time evolutions of the center $\mathbf{x}(t)$ with $\mathbf{x}_0 = (1, 1)^T$ for different trapping frequencies γ_x and γ_y. From it, we can draw the following conclusions for the motion of the mass-center in non-rotating BEC:

i). Each component of $\mathbf{x}(t)$ is a periodic function with the same frequency as the

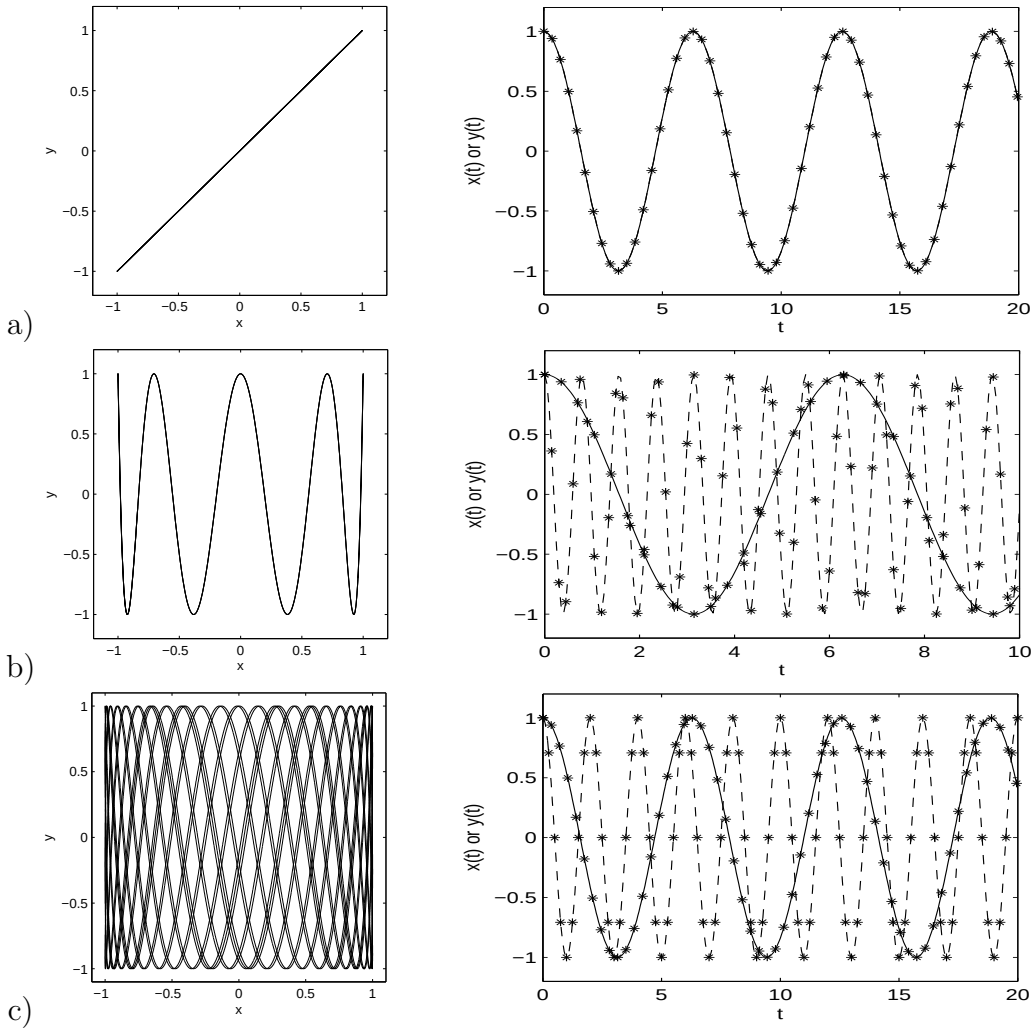

Figure 4.1: Motion of the center $\mathbf{x}(t)$ in non-rotating BEC. Left: trajectory for $t \in [0, 50]$; Right: time evolution of $x(t)$ (solid line) and $y(t)$ (dash line), where '*' is obtained by directly simulating the GPE (2.27)−(2.28). a). $\gamma_x = \gamma_y = 1$; b). $\gamma_x = 1$, $\gamma_y = 8$; c). $\gamma_x = 1$, $\gamma_y = 2\pi$.

trapping frequency in that direction.

ii). When $\gamma_x = \gamma_y := \gamma_r$, i.e. in a radially symmetric trap, the center moves like a pendulum with period $T = 2\pi/\gamma_r$, and its trajectory is a straight segment (cf. Fig. 4.1a).

iii). If γ_y/γ_x is a rational number, i.e. $\gamma_y/\gamma_x = q/p$ with q and p positive integers and no common factor, then the center moves periodically with period $T = 2p\pi$ (cf.

Fig. 4.1b). On the other hand, if γ_y/γ_x is an irrational number, the center moves chaotically in the rectangle $\Omega_{\mathbf{x}} = [-|x_0|, |x_0|] \times [-|y_0|, |y_0|]$, and the envelope of its trajectory is the boundary of the rectangle $\Omega_{\mathbf{x}}$ (cf. Fig. 4.1c).
iv). All the above observations can be confirmed by the numerical results from directly simulating the GPE (2.27)−(2.28).

4.3.2 For rotating BEC in symmetric trap

For rotating BEC in a radially symmetric trap, i.e. $\Omega \neq 0$ and $\gamma_x = \gamma_y$, we have the following solutions for the second-order ODE system (4.28)−(4.30):

Lemma 4.5. If $\Omega \neq 0$ and $\gamma_x = \gamma_y$, then the solutions of the ODE system (4.28)−(4.30) can be given by

$$x(t) = \frac{x_0}{2}\left[\cos(at) + \cos(bt)\right] + \frac{|\Omega| y_0}{2\Omega}\left[\sin(at) - \sin(bt)\right], \tag{4.47}$$

$$y(t) = \frac{y_0}{2}\left[\cos(at) + \cos(bt)\right] + \frac{|\Omega| x_0}{2\Omega}\left[-\sin(at) + \sin(bt)\right], \qquad t \geq 0, \tag{4.48}$$

where $a = \gamma_x + |\Omega|$ and $b = \gamma_x - |\Omega|$. Furthermore, we can get that the distance between the mass center and the trap center is a periodic function with period $T = \pi/\gamma_x$, i.e.

$$|\mathbf{x}(t)| := \sqrt{x^2(t) + y^2(t)} = \sqrt{x_0^2 + y_0^2}\,|\cos(\gamma_x t)|, \qquad t \geq 0. \tag{4.49}$$

Proof. If $\gamma_x = \gamma_y$, the characteristic equation (4.42) collapses to

$$\lambda^4 + 2\left(\gamma_x^2 + \Omega^2\right)\lambda^2 + \left(\gamma_x^2 - \Omega^2\right)^2 = 0. \tag{4.50}$$

Solving (4.50), we get its roots as

$$\lambda_{1,2} = \pm i(\gamma_x + |\Omega|) = \pm a\, i, \qquad \lambda_{3,4} = \pm i(\gamma_x - |\Omega|) = \pm b\, i, \tag{4.51}$$

which gives the general solution of $x(t)$ as

$$x(t) = c_1 \cos(at) + c_2 \sin(at) + c_3 \cos(bt) + c_4 \sin(bt), \qquad t \geq 0 \tag{4.52}$$

with c_1, c_2, c_3 and c_4 constants. On the other hand, from (4.28), we have

$$\dot{y}(t) = \frac{1}{2\Omega}\left(\ddot{x}(t) + \left(\gamma_x^2 - \Omega^2\right) x(t)\right), \qquad t \geq 0. \tag{4.53}$$

Plugging (4.52) into (4.53) and integrating with respect to t, we can obtain the general solution of $y(t)$ as

$$y(t) = -\frac{|\Omega|}{\Omega}\left[c_1 \sin(at) - c_2 \cos(at)\right] + \frac{|\Omega|}{\Omega}\left[c_3 \sin(bt) - c_4 \cos(bt)\right] + c_5, \quad t \geq 0. \tag{4.54}$$

Taking $t = 0$ in (4.52) and (4.54), and noticing (4.28) and (4.30), we get

$$c_1 = c_3 = \frac{x_0}{2}, \qquad c_2 = -c_4 = \frac{\Omega y_0}{2|\Omega|}, \qquad c_5 = 0. \tag{4.55}$$

Thus the solution (4.47)−(4.48) is a combination of (4.52), (4.54) and (4.55). Furthermore, from (4.47)−(4.48), it is easy to compute

$$\begin{aligned} |\mathbf{x}(t)|^2 &= x(t)^2 + y(t)^2 = \left[\frac{x_0}{2}\left(\cos(at) + \cos(bt)\right) + \frac{|\Omega| y_0}{2\Omega}\left(\sin(at) - \sin(bt)\right)\right]^2 \\ &\qquad + \left[\frac{y_0}{2}\left(\cos(at) + \cos(bt)\right) + \frac{|\Omega| x_0}{2\Omega}\left(-\sin(at) + \sin(bt)\right)\right]^2 \\ &= \frac{x_0^2}{4}\left[2 + 2\cos((a+b)t)\right] + \frac{y_0^2}{4}\left[2 + 2\cos((a+b)t)\right] \\ &= \left(x_0^2 + y_0^2\right)\cos^2(\gamma_x t), \qquad t \geq 0, \end{aligned} \tag{4.56}$$

which gives (4.49) immediately. □

Figure 4.2 shows time evolutions of the center $\mathbf{x}(t)$ with $\gamma_x = \gamma_y = 1$ and $\mathbf{x}_0 = (1, 1)^T$ for different Ω. Figure 4.3 depicts the distance between the mass-center and the trap center, i.e. $|\mathbf{x}(t)|$, for different Ω. From them, we can draw the following conclusions:

i). For any angular velocity Ω, the distance between the mass center and the trap center is a periodic function with period $T = \pi/\gamma_x$ (cf. Fig. 4.3).

ii). When Ω is a rational number, i.e. $|\Omega| = q/p$ with q and p positive integers and no common factor, the center moves periodically with period $T = p\pi$ if both q and p are odd integers (cf. Fig. 4.2a, c), and otherwise $T = 2p\pi$ (cf. Fig. 4.2b, d, e). Furthermore, the graph of the trajectory is unchanged under a rotation of the angle $\theta = 2m\pi\omega$, where m is an integer and $\omega = 2\pi/T$ is the angular frequency of the

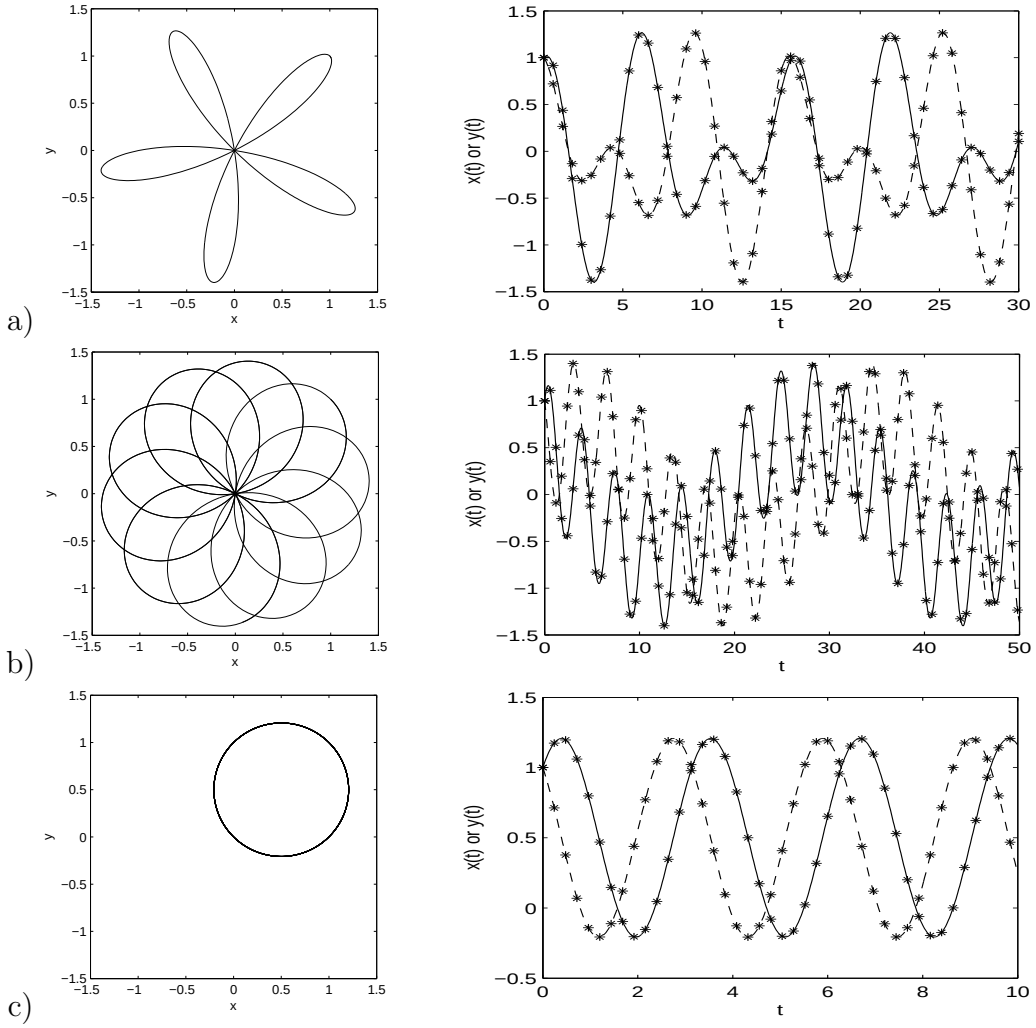

Figure 4.2: Motion of the center $\mathbf{x}(t)$ in rotating BEC with a radially symmetric trap. Left: trajectory for $t \in [0, 100]$; Right: time evolution of $x(t)$ (solid line) and $y(t)$ (dash line), where '*' is obtained by directly simulating the GPE (2.27)−(2.28). a). $\Omega = 1/5$; b). $\Omega = 4/5$; c). $\Omega = 1$.

motion (cf. Fig. 4.2a−e).

iii). If Ω is an irrational number, the center moves chaotically, but the envelope of its trajectory is a circle centered at the origin $(0, 0)$ and with the radius $r = |\mathbf{x}_0|$ (cf. Fig. 4.2f).

iv). All the above observations can be confirmed by the numerical results from directly simulating the GPE (2.27)−(2.28).

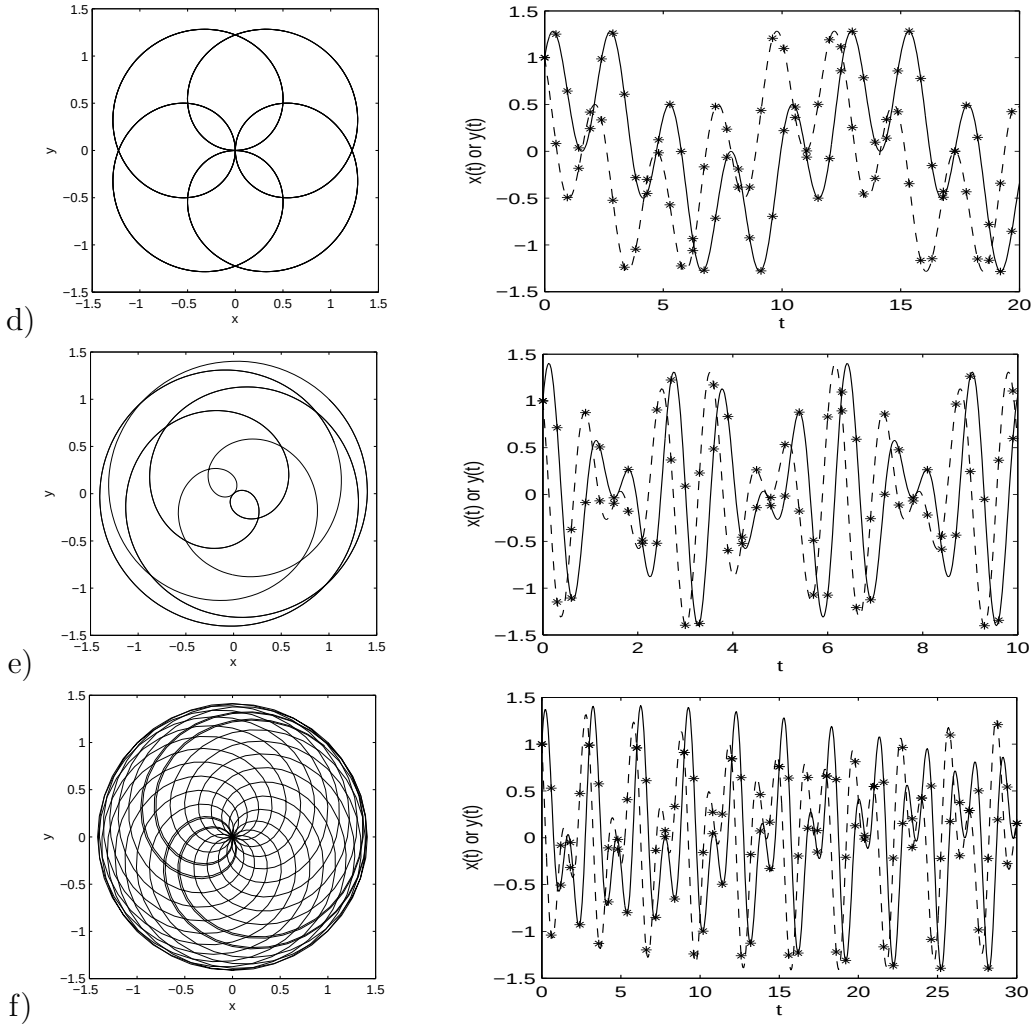

Figure 4.2 (cont'd): d). $\Omega = 3/2$; e). $\Omega = 6$; f). $\Omega = \pi$.

4.3.3 For rotating BEC in asymmetric trap

For rotating BEC in an asymmetric trap, i.e. $\Omega \neq 0$ and $\gamma_x \neq \gamma_y$, the solutions of (4.28)−(4.30) can be analytically given for four different cases: (a). $|\Omega| = \gamma_x$; (b). $|\Omega| = \gamma_y$; (c). $0 < |\Omega| < \gamma_x$ or $|\Omega| > \gamma_y$, and (d). $\gamma_x < |\Omega| < \gamma_y$.

For case (a): $|\Omega| = \gamma_x$, we have

Lemma 4.6. If $|\Omega| = \gamma_x < \gamma_y$, then the solutions of the ODE system (4.28)−(4.30)

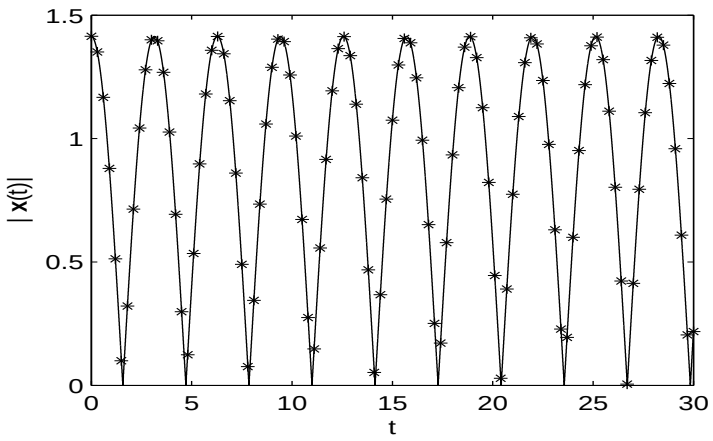

Figure 4.3: Distance between the mass center and the trap center for $\gamma_x = \gamma_y = 1$ and different Ω, where '*' is obtained by directly simulating the GPE (2.27)−(2.28).

can be given by

$$x(t) = \frac{x_0}{a^2}\left[(\gamma_y^2+\Omega^2)+2\Omega^2\cos(at)\right] + \frac{\Omega y_0}{a^2}\left[-(\gamma_y^2-\Omega^2)t + \frac{2(\gamma_y^2+\Omega^2)}{a}\sin(at)\right], \tag{4.57}$$

$$y(t) = \frac{y_0}{a^2}\left[2\Omega^2+(\gamma_y^2+\Omega^2)\cos(at)\right] - \frac{\Omega x_0}{a}\sin(at), \qquad t \geq 0, \tag{4.58}$$

where $a = \sqrt{\gamma_y^2+3\Omega^2}$. This implies that the center moves on an ellipse when $y_0 = 0$, and moves to infinity when $y_0 \neq 0$.

Proof. When $|\Omega| = \gamma_x < \gamma_y$, the ODE system (4.28)−(4.29) reduced to

$$\ddot{x}(t) - 2\Omega\dot{y}(t) = 0, \tag{4.59}$$

$$\ddot{y}(t) + 2\Omega\dot{x}(t) + \left(\gamma_y^2-\Omega^2\right)y(t) = 0, \qquad t \geq 0. \tag{4.60}$$

Differentiating (4.60) with respect to t and noticing (4.59), we obtain

$$y^{(3)}(t) + \left(\gamma_y^2+3\Omega^2\right)\dot{y}(t) = 0, \qquad t \geq 0. \tag{4.61}$$

The characteristic equation of (4.61) is

$$\lambda^3 + \left(\gamma_y^2+3\Omega^2\right)\lambda = 0. \tag{4.62}$$

Solving the above equation, we obtain

$$\lambda_1 = 0, \qquad \lambda_{2,3} = \pm i\sqrt{\gamma_y^2 + 3\Omega^2} = \pm a\, i. \tag{4.63}$$

Thus the general solution of $y(t)$ takes the form

$$y(t) = c_1 + c_2\cos(at) + c_3\sin(at) \tag{4.64}$$

with c_1, c_2 and c_3 constants. Plugging (4.64) into (4.59) and integrating with respect to t, we obtain the general solution of $x(t)$ as

$$x(t) = -\frac{\left(\gamma_y^2 - \Omega^2\right) c_1}{2\Omega} t + \frac{2\Omega}{a}\left[c_2\sin(at) - c_3\cos(at)\right] + c_4 \tag{4.65}$$

with c_4 a constant. Taking $t = 0$ in (4.64) and (4.65), and noticing (4.30), we get

$$c_1 = \frac{2\Omega^2 y_0}{a^2}, \quad c_2 = \frac{\left(\gamma_y^2 + \Omega^2\right) y_0}{a^2}, \quad c_3 = -\frac{\Omega x_0}{a}, \quad c_4 = \frac{\left(\gamma_y^2 + \Omega^2\right) x_0}{a^2}. \tag{4.66}$$

Thus the solution (4.57)−(4.58) is a combination of (4.64)−(4.66). □

Similarly, for case (b): $\gamma_x < \gamma_y = |\Omega|$, we have

Lemma 4.7. If $\gamma_x < \gamma_y = |\Omega|$, the solutions of the ODE system (4.28)−(4.30) are

$$x(t) = \frac{x_0}{a^2}\left[2\Omega^2 + (\gamma_x^2 + \Omega^2)\cos(at)\right] + \frac{\Omega y_0}{a}\sin(at), \qquad t \geq 0, \tag{4.67}$$

$$y(t) = \frac{y_0}{a^2}\left[(\gamma_x^2 + \Omega^2) + 2\Omega^2\cos(at)\right] + \frac{\Omega x_0}{a^2}\left[(\gamma_x^2 - \Omega^2)t - \frac{2(\gamma_x^2 + \Omega^2)}{a}\sin(at)\right], \tag{4.68}$$

where $a = \sqrt{\gamma_x^2 + 3\Omega^2}$. Again this implies that the center moves on an ellipse when $x_0 = 0$, and moves to infinity when $x_0 \neq 0$.

Proof. The proof follows the line of the analogous results in Lemma 4.6. □

Figure 4.4 displays time evolutions of the center $\mathbf{x}(t)$ with $\Omega = \gamma_x = 1$ and $\gamma_y = 2$ for different $\mathbf{x}_0$. From it and our additional results, we can draw the following conclusions for cases (a)−(b):

i). When $|\Omega| = \gamma_x < \gamma_y$ and $y_0 \neq 0$, the trajectory of the center is a spiral coil going

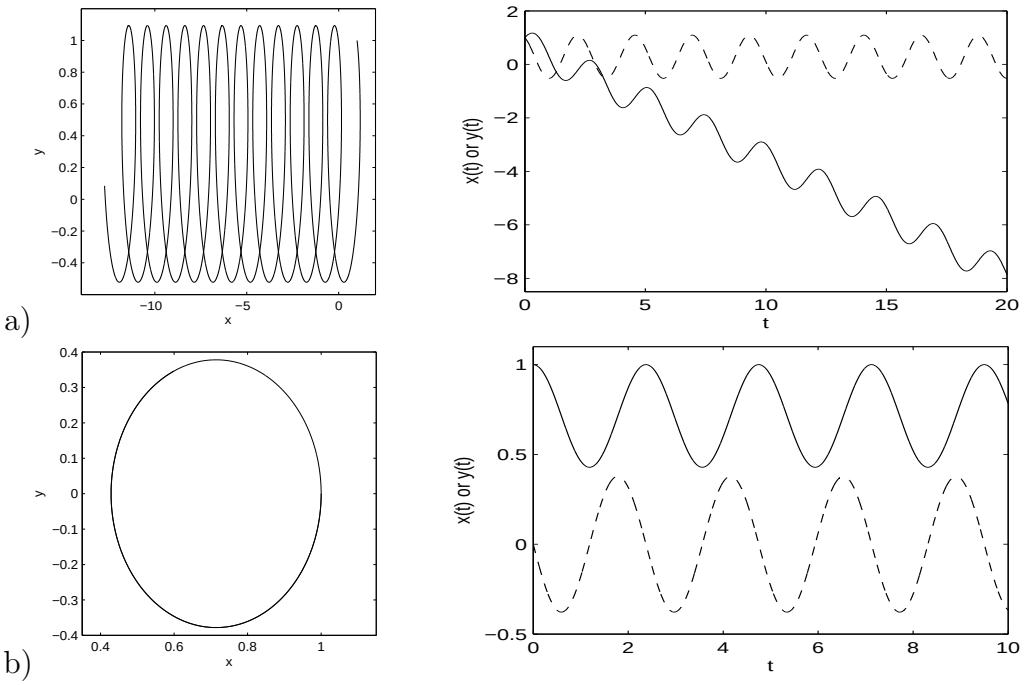

Figure 4.4: Motion of the center $\mathbf{x}(t)$ in rotating BEC with $\Omega = \gamma_x = 1$ and $\gamma_y = 2$. Left: trajectory for $t \in [0, 30]$; Right: time evolution of $x(t)$ (solid line) and $y(t)$ (dash line). a). $\mathbf{x}_0 = (1, 1)^T$; b). $\mathbf{x}_0 = (1, 0)^T$.

to infinity in x-direction (cf. Fig. 4.4a).

ii). When $|\Omega| = \gamma_x < \gamma_y$ and $y_0 = 0$, the trajectory is an ellipse (cf. Fig. 4.4b).

iii). Similarly, when $\gamma_x < \gamma_y = |\Omega|$, if $x_0 \neq 0$, the trajectory is a spiral coil going to infinity in y-direction, while if $x_0 = 0$, it is an ellipse.

If $|\Omega| \neq 0$, γ_x or γ_y, we denote

$$\zeta_1 = \left(\gamma_x^2 + \gamma_y^2 + 2\Omega^2\right)/2, \qquad \zeta_2 = \sqrt{\zeta_1^2 - \left(\gamma_x^2 - \Omega^2\right)\left(\gamma_y^2 - \Omega^2\right)},$$

and let $a = \sqrt{|\zeta_1 - \zeta_2|}$ and $b = \sqrt{\zeta_1 + \zeta_2}$. When $0 < |\Omega| < \gamma_x$ or $|\Omega| > \gamma_y$, we have $0 < \zeta_2 < \zeta_1$, and get the four roots of the characteristic equation (4.42) as

$$\lambda_{1,2} = \pm i\sqrt{\zeta_1 - \zeta_2} = \pm a\, i, \qquad \lambda_{3,4} = \pm i\sqrt{\zeta_1 + \zeta_2} = \pm b\, i. \tag{4.69}$$

Following the procedure in the proof of Lemma 4.5, after a detailed computation,

we can get the solutions of the ODE system (4.28)−(4.30) in this case,

Lemma 4.8. If $0 < |\Omega| < \gamma_x$ or $|\Omega| > \gamma_y$, the solutions of the ODE system (4.28)−(4.30) are

$$x(t) = c_1\cos(at) + c_2\sin(at) + c_3\cos(bt) + c_4\sin(bt), \tag{4.70}$$

$$y(t) = c_5\cos(at) + c_6\sin(at) + c_7\cos(bt) + c_8\sin(bt), \qquad t \geq 0, \tag{4.71}$$

where

$$c_1 = \frac{(\gamma_x^2+\Omega^2-b^2)\,x_0}{a^2-b^2}, \qquad c_2 = \frac{a\Omega\,(\gamma_x^2-\Omega^2+b^2)\,y_0}{(\gamma_x^2-\Omega^2)\,(a^2-b^2)},$$
$$c_3 = -\frac{(\gamma_x^2+\Omega^2-a^2)\,x_0}{a^2-b^2}, \qquad c_4 = -\frac{b\Omega\,(\gamma_x^2-\Omega^2+a^2)\,y_0}{(\gamma_x^2-\Omega^2)\,(a^2-b^2)},$$
$$c_5 = -\frac{(\gamma_x^2-\Omega^2-a^2)\,(\gamma_x^2-\Omega^2+b^2)\,y_0}{2\,(\gamma_x^2-\Omega^2)\,(a^2-b^2)}, \quad c_6 = \frac{(\gamma_x^2-\Omega^2-a^2)\,(\gamma_x^2+\Omega^2-b^2)\,x_0}{2a\Omega\,(a^2-b^2)},$$
$$c_7 = \frac{(\gamma_x^2-\Omega^2+a^2)\,(\gamma_x^2-\Omega^2-b^2)\,y_0}{2\,(\gamma_x^2-\Omega^2)\,(a^2-b^2)}, \quad c_8 = -\frac{(\gamma_x^2-\Omega^2-b^2)\,(\gamma_x^2+\Omega^2-a^2)\,x_0}{2b\Omega\,(a^2-b^2)}.$$

This implies that the graph of the trajectory is a bounded set.

Similarly, when $\gamma_x < |\Omega| < \gamma_y$, we have $\zeta_2 > \zeta_1$. Thus the four roots of the characteristic equation (4.42) are

$$\lambda_{1,2} = \pm\sqrt{\zeta_2-\zeta_1} = \pm a, \qquad \lambda_{3,4} = \pm i\sqrt{\zeta_1+\zeta_2} = \pm b\,i. \tag{4.72}$$

Following the procedure in the proof of Lemma 4.5, after a detailed computation, we obtain the solutions of the ODE system (4.28)−(4.30) as

Lemma 4.9. If $\gamma_x < |\Omega| < \gamma_y$, the solutions of the ODE system (4.28)−(4.30) are

$$x(t) = d_1e^{at} + d_2e^{-at} + d_3\cos(bt) + d_4\sin(bt), \tag{4.73}$$

$$y(t) = d_5e^{at} + d_6e^{-at} + d_7\cos(bt) + d_8\sin(bt), \qquad t \geq 0, \tag{4.74}$$

where

$$d_1 = \frac{1}{2}(c_1-c_2), \quad d_2 = -\frac{1}{2}(c_1+c_2), \quad d_3 = c_3, \quad d_4 = c_4, \quad d_7 = c_7, \quad d_8 = c_8,$$
$$d_5 = \frac{(\gamma_x^2-\Omega^2+a^2)}{4a\Omega}(c_1-c_2), \quad d_6 = \frac{(\gamma_x^2-\Omega^2+a^2)}{4a\Omega}(c_1+c_2)$$

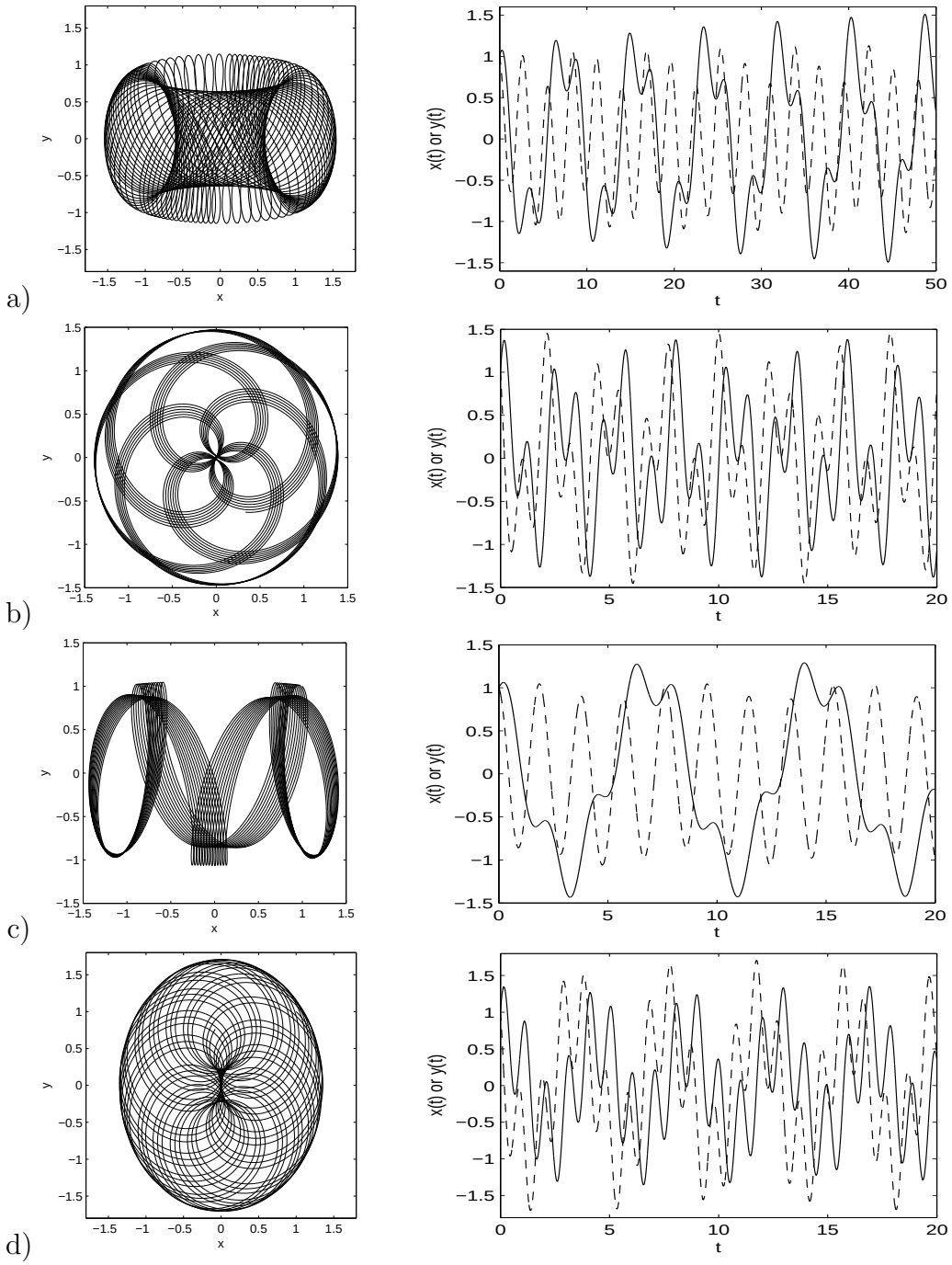

Figure 4.5: Motion of the center $\mathbf{x}(t)$ in rotating BEC with an asymmetric potential. Left: trajectory for $t \in [0, 100]$; Right: time evolution of $x(t)$ (solid line) and $y(t)$ (dash line). a). $\Omega = 1/2$, $\gamma_x = 1$, $\gamma_y = 2$; b). $\Omega = 4$, $\gamma_x = 1$, $\gamma_y = 2$; c). $\Omega = 1/2$, $\gamma_x = 1$, $\gamma_y = \pi$; d). $\Omega = 4$, $\gamma_x = 1$, $\gamma_y = \pi$.

with $c_1, \ldots, c_8$ constants defined in Lemma 4.8. From the above solutions, we can see if $c_1 = c_2$, i.e.

$$\frac{y_0}{x_0} = \frac{(\gamma_x^2 - \Omega^2)(\gamma_x^2 + \Omega^2 - b^2)}{a\Omega(\gamma_x^2 - \Omega^2 + b^2)}, \tag{4.75}$$

the center moves in a bounded domain; otherwise, it moves to the infinity exponentially fast and satisfies

$$\lim_{t\to\infty} \frac{y(t)}{x(t)} = \frac{d_5}{d_1} = \frac{(\gamma_x^2 - \Omega^2 + a^2)}{2a\Omega}. \tag{4.76}$$

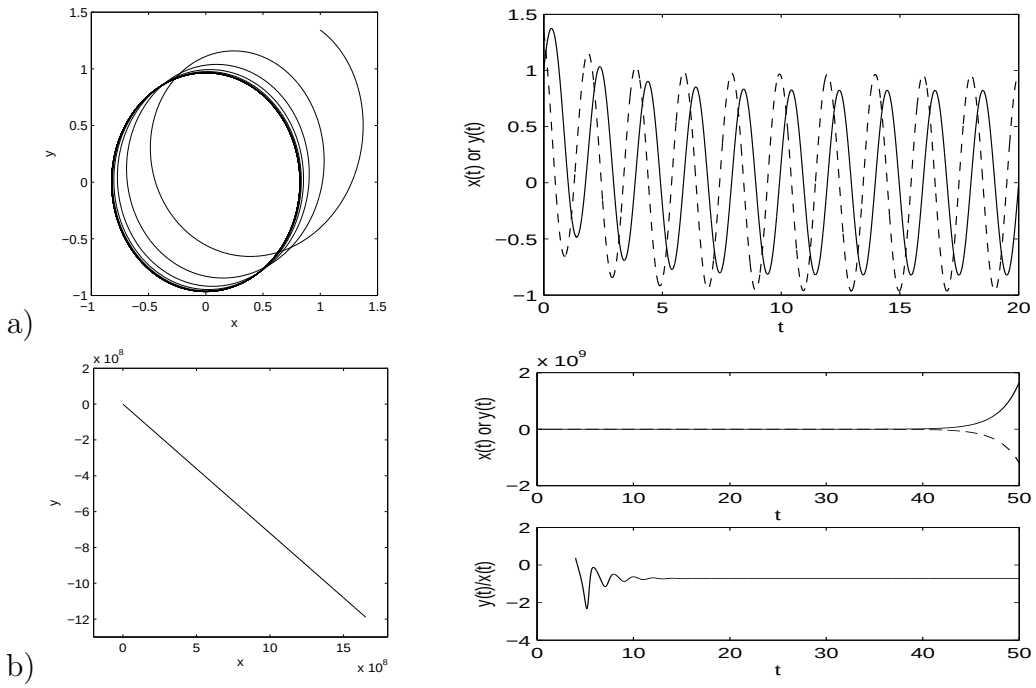

Figure 4.6: Motion of the center $\mathbf{x}(t)$ in rotating BEC with $\Omega = 1.5$, $1 = \gamma_x$ and $\gamma_y = 2$. Left: trajectory for $t \in [0, 50]$; Right: time evolution of $x(t)$ (solid line) and $y(t)$ (dash line). a). $\mathbf{x}_0 = (1, 1.3424)^T$; b). $\mathbf{x}_0 = (1, 1)^T$.

Figure 4.5 shows time evolutions of the center $\mathbf{x}(t)$ with $\mathbf{x}_0 = (1, 1)^T$ for different $\gamma_x < \gamma_y$ and Ω satisfying $0 < |\Omega| < \gamma_x$ or $|\Omega| > \gamma_y$, and Figure 4.6 shows similar results for $1 = \gamma_x < \Omega = 1.5 < \gamma_y = 2$ for different $\mathbf{x}_0$. From them, we can draw the following conclusions for cases (c)−(d):

i). In case (c), i.e. $0 < |\Omega| < \gamma_x$ or $|\Omega| > \gamma_y$, the graph of the trajectory is a bounded set, and generally, the center moves chaotically (cf. Fig. 4.5).
ii). In case (d), i.e. $\gamma_x < |\Omega| < \gamma_y$, if (x_0, y_0) satisfy (4.75), the graph of the trajectory is a bounded set (cf. Fig. 4.6a); otherwise it moves to the infinity exponentially fast, and after a short time, it almost moves along a straight line with a slope $\left(\gamma_x^2 - \Omega^2 + a^2\right)/2a\Omega$ (cf. Fig. 4.6b).

4.4 Numerical methods

In this section, we propose several numerical methods for computing the dynamics of non-rotating and rotating BEC. Due to the potential $V_d(\mathbf{x})$ given in (2.29), the solution $\psi(\mathbf{x}, t)$ of the GPE (2.27) decays to zero exponentially fast when $|\mathbf{x}| \to \infty$. Thus in practical computation, we can truncate the problem (2.27)−(2.28) into a bounded computational domain $\Omega_{\mathbf{x}}$ with homogeneous Dirichlet boundary conditions. The more sophisticated boundary condition is an interesting topic that remains to be examined in the future. Without loss of generality, here we consider the following problem:

$$i\partial_t \psi(\mathbf{x}, t) = -\frac{1}{2}\nabla^2 \psi + V_d(\mathbf{x}, t)\psi + \beta_d |\psi|^2 \psi - \Omega L_z \psi, \quad \mathbf{x} \in \Omega_{\mathbf{x}}, \quad t \geq 0, \tag{4.77}$$

$$\psi(\mathbf{x}, t) = 0, \quad \mathbf{x} \in \Gamma = \partial\Omega_{\mathbf{x}}, \quad t \geq 0, \tag{4.78}$$

$$\psi(\mathbf{x}, 0) = \psi_0(\mathbf{x}), \quad \mathbf{x} \in \overline{\Omega}_{\mathbf{x}}, \tag{4.79}$$

where $V_d(\mathbf{x}, t) = V_d(\mathbf{x}) + W_d(\mathbf{x}, t)$ is a time-dependent trapping potential with $V_d(\mathbf{x})$ given in (2.29) and $W_d(\mathbf{x}, t)$ an external driven field. There are two typical external driven fields used in the physics literature: one is the far-blued detuned Gaussian laser beam stirrer [30, 24],

$$W_d(\mathbf{x}, t) = W_s(t) \exp\left[-\left(\frac{|\mathbf{x} - \mathbf{x}_s(t)|^2}{w_s/2}\right)\right], \qquad \mathbf{x} \in \mathbb{R}^d \tag{4.80}$$

with W_s the height, w_s the width, and $\mathbf{x}_s(t)$ the position of the stirrer; the other one is the Delta-kicked potential [78],

$$W_1(x,t) = K\cos(kx)\sum_{n=-\infty}^{\infty}\delta(t-n\tau), \qquad x\in\mathbb{R} \tag{4.81}$$

with K the kick strength, k the wavenumber, τ the time interval between kicks and $\delta(\tau)$ the Dirac delta function.

4.4.1 For non-rotating BEC

Here, we present a time-splitting sine pseudospectral (TSSP) method for computing the dynamics of non-rotating BEC with/without the external driven field. For simplicity of notation, the method is introduced for the case of one space dimension ($d = 1$). Generalizations to high dimensions ($d > 1$) are straightforward for tensor product grids and the results remain valid without modifications. In 1D case with $\Omega = 0$, the problem (4.77)−(4.79) collapses to

$$i\partial_t\psi = -\frac{1}{2}\partial_{xx}\psi + V_1(x)\psi + W_1(x,t)\psi + \beta_1|\psi|^2\psi, \quad a < x < b, \quad t > 0, \tag{4.82}$$

$$\psi(a,t) = \psi(b,t) = 0, \quad t \geq 0, \qquad \psi(x,0) = \psi_0(x), \quad a \leq x \leq b \tag{4.83}$$

with $|a|$ and b sufficiently large.

In order to present the TSSP method, we can rewrite the GPE (4.77) into the form

$$i\partial_t\psi = A\,\psi + B\,\psi, \tag{4.84}$$

where A and B are two operators and they do not need to commute. Choose the time step $\Delta t > 0$ and spatial mesh size $\Delta x = (b-a)/J$ with J an even positive integer, and define the time sequence $t_n = n\Delta t$ for $n = 0, 1, 2, \ldots$, and grid points $x_j := a + j\Delta x$ for $0 \leq j \leq J$. Let ψ_j^n be the approximation of $\psi(x_j, t_n)$ and Ψ^n be the solution vector with components ψ_j^n.

Fourth-order TSSP for GPE without external driven field

When $W_1(x,t) \equiv 0$, i.e. without the external driven field, the GPE (4.82) can be written in the form of (4.84) with

$$A\psi = V_1(x)\psi(x,t) + \beta_1|\psi(x,t)|^2\psi(x,t), \qquad B\psi = -\frac{1}{2}\partial_{xx}\psi(x,t). \tag{4.85}$$

Thus the key for an efficient implementation of time-splitting is to efficiently solve the following two subproblems:

$$i\partial_t\psi(x,t) = B\psi = -\frac{1}{2}\partial_{xx}\psi, \tag{4.86}$$

and

$$i\partial_t\psi(x,t) = A\,\psi = V_1(x)\psi(x,t) + \beta_1|\psi(x,t)|^2\psi(x,t). \tag{4.87}$$

Equation (4.86) can be discretized in space by the sine pseudospectral method and integrated in time *exactly*. For $t \in [t_n, t_{n+1}]$, the ODE (4.87) leaves $|\psi|$ invariant in time t [18, 19] and thus becomes

$$i\psi_t(x,t) = V_1(x)\psi(x,t) + \beta_1|\psi(x,t_n)|^2\psi(x,t), \qquad t_n \le t \le t_{n+1}, \tag{4.88}$$

which can be integrated *exactly*.

From time $t = t_n$ to $t = t_{n+1}$, we combine the splitting steps via the fourth-order split-step method [136, 64, 21] and obtain the fourth-order time-splitting sine pseudospectral (TSSP4) method for the problem (4.82)−(4.83). The detailed method is given by

$$\begin{aligned}
&\psi_j^{(1)} = e^{-i2w_1\Delta t(V_1(x_j)+\beta_1|\psi_j^n|^2)}\,\psi_j^n, \quad \psi_j^{(2)} = \sum_{l=1}^{J-1} e^{-iw_2\mu_l^2\Delta t}\left(\widehat{\psi^{(1)}}\right)_l \sin(\mu_l(x_j-a)),\\
&\psi_j^{(3)} = e^{-i2w_3\Delta t(V_1(x_j)+\beta_1|\psi_j^{(2)}|^2)}\,\psi_j^{(2)}, \quad \psi_j^{(4)} = \sum_{l=1}^{J-1} e^{-iw_4\mu_l^2\Delta t}\left(\widehat{\psi^{(3)}}\right)_l \sin(\mu_l(x_j-a)),\\
&\psi_j^{(5)} = e^{-i2w_3\Delta t(V_1(x_j)+\beta_1|\psi_j^{(4)}|^2)}\,\psi_j^{(4)}, \quad \psi_j^{(6)} = \sum_{l=1}^{J-1} e^{-iw_2\mu_l^2\Delta t}\left(\widehat{\psi^{(5)}}\right)_l \sin(\mu_l(x_j-a)),\\
&\psi_j^{n+1} = e^{-i2w_1\Delta t(V_1(x_j)+\beta_1|\psi_j^{(6)}|^2)}\,\psi_j^{(6)}, \qquad 1 \le j \le J-1,
\end{aligned} \tag{4.89}$$

where $\widehat{U}_l$, the sine-transform coefficients of a complex vector $\mathbf{U} = (U_0, U_1, \cdots, U_J)$ with $U_0 = U_J = 0$, are defined as

$$\mu_l = \frac{\pi l}{b-a}, \qquad \widehat{U}_l = \frac{2}{J}\sum_{j=1}^{J-1} U_j \ \sin(\mu_l(x_j - a)), \quad 1 \le l \le J-1, \tag{4.90}$$

and the constants w_1, w_2, w_3 and w_4 are [64, 21]

$$w_1 = 0.33780\ 17979\ 89914\ 40851, \qquad w_2 = 0.67560\ 35959\ 79828\ 81702,$$
$$w_3 = -0.08780\ 17979\ 89914\ 40851, \quad w_4 = -0.85120\ 71979\ 59657\ 63405.$$

The initial data is discretized as

$$\psi_j^0 = \psi(x_j, 0) = \psi_0(x_j), \qquad 0 \le j \le J. \tag{4.91}$$

Note that the only time discretization error of TSSP4 is the splitting error, which is fourth order in Δt for any fixed mesh size $\Delta x > 0$. This scheme is explicit, time reversible just as the initial value problem (IVP) for the GPE. Also, a main advantage of the time-splitting method is its time-transverse invariance, just as it holds for the GPE itself. If a constant α is added to the potential $V_1(x)$, then the discrete wave functions ψ_j^{n+1} obtained from TSSP4 is multiplied by the phase factor $e^{-i\alpha(n+1)\Delta t}$, which leaves the discrete quadratic observables unchanged. This property does not hold for finite difference schemes [122, 32, 129].

Second-order TSSP for GPE with external driven field

When $W_1(x,t) \neq 0$, i.e. with an external driven field, the GPE (4.82) can be similarly rewritten into the form (4.84) with

$$\begin{aligned} A\psi &= -\frac{1}{2}\partial_{xx}\psi(x,t), \\ B\psi &= V_1(x)\psi(x,t) + W_1(x,t)\psi(x,t) + \beta_1|\psi(x,t)|^2\psi(x,t). \end{aligned} \tag{4.92}$$

As the external driven field could be very complicated, e.g. the Delta-function [78], here we only use a second-order split-step scheme in time discretization [126, 24].

More precisely, from time $t = t_n$ to $t = t_{n+1}$, we proceed as follows:

$$\begin{aligned}
\psi_j^{(1)} &= \sum_{l=1}^{J-1} e^{-i\mu_l^2 \Delta t/4} \left(\widehat{\psi^n}\right)_l \sin(\mu_l(x_j - a)),\\
\psi_j^{(2)} &= \psi_j^{(1)} \exp\left[-i\Delta t \left(V_1(x_j) + \beta_1 \left|\psi_j^n\right|^2\right) - i\int_{t_n}^{t_{n+1}} W_1(x_j, t)\, dt\right],\\
\psi_j^{n+1} &= \sum_{l=1}^{J-1} e^{-i\mu_l^2 \Delta t/4} \left(\widehat{\psi^{(2)}}\right)_l \sin(\mu_l(x_j - a)), \qquad 1 \le j \le J-1.
\end{aligned} \tag{4.93}$$

Remark 4.1. If the integral in (4.93) could not be integrated analytically, we can use numerical quadrature to evaluate it, e.g.

$$\int_{t_n}^{t_{n+1}} W_1(x_j, t)\, dt \approx \frac{\Delta t}{6}\left[W_1(x_j, t_n) + 4W_1(x_j, t_n + \Delta t/2) + W_1(x_j, t_{n+1})\right].$$

Let $\mathbf{U} = (U_0, U_1, \cdots, U_J)^T$ be a complex vector with $U_0 = U_J = 0$, and $\|\cdot\|_{L^2}$ be the usual discrete L^2-norm on the interval (a, b), i.e.

$$\|\mathbf{U}\|_{L^2} = \sqrt{\frac{b-a}{J}\sum_{j=1}^{J-1} |U_j|^2}. \tag{4.94}$$

For the stability of the time-splitting pseudospectral approximations TSSP4 (4.89) and the second-order scheme (4.93), we have the following lemma:

Lemma 4.10. The fourth-order time-splitting sine pseudospectral scheme (TSSP4) (4.89) and the second-order scheme (4.93) are unconditionally stable. In fact, for every mesh size $\Delta x > 0$ and time step $\Delta t > 0$,

$$\|\Psi^n\|_{L^2} = \|\Psi^0\|_{L^2} = \|\psi(x, 0)\|_{L^2}, \qquad n = 1, 2, \cdots \tag{4.95}$$

Proof. The proof follows the line of the analogous results for the linear Schrödinger equation by time-splitting Fourier pseudospectral approximation [18, 19, 15]. □

Another important issue is how to choose mesh size Δx and time step Δt in the strongly repulsive interacting regime or semiclassical regime, i.e. $\beta_d \gg 1$, in order to get"correct" physical observables. As introduced in Section 2.6, in the semiclassical regime we can rescale the GPE (2.27) into the form (2.41). Then similar as

demonstrated in [18, 19], the admissible meshing strategy of TSSP4 for the GPE the strongly repulsive interacting regime is

$$\Delta x = O(\varepsilon) = O\left(1/\beta_d^{2/(d+2)}\right), \quad \Delta t = O(\varepsilon) = O\left(1/\beta_d^{2/(d+2)}\right), \quad d = 1, 2, 3. \tag{4.96}$$

4.4.2 For rotating BEC

As discussed above, the TSSP method is very efficient for computing the dynamics of non-rotating BEC. However, due to the appearance of the angular momentum rotation term in the GPE, it can no longer be directly used for rotating BEC. In order to simulate the dynamics of rotating BEC, here we proposed another two efficient numerical methods. For simplicity, the methods are introduced for 2D case, and generalization to 3D is straightforard.

If we consider the damping effect in rotating BEC, the GPE (4.77)−(4.79) in 2D case can be written as

$$(i-\lambda)\partial_t\psi = -\frac{1}{2}\nabla^2\psi + V_2(\mathbf{x},t)\psi + \beta_2|\psi|^2\psi - \Omega L_z\psi, \quad \mathbf{x}\in\Omega_{\mathbf{x}}, \ \ t\geq 0, \tag{4.97}$$

$$\psi(\mathbf{x},t) = 0, \quad \mathbf{x}\in\Gamma = \partial\Omega_{\mathbf{x}}, \quad t\geq 0, \tag{4.98}$$

$$\psi(\mathbf{x},0) = \psi_0(\mathbf{x}), \quad \mathbf{x}\in\overline{\Omega}_{\mathbf{x}}, \tag{4.99}$$

where λ is the damping parameter and $\Omega_{\mathbf{x}}$ is the 2D bounded computational domain.

Time-splitting type method

To develop this method, we use the polar coordinate in 2D, i.e. $\Omega_{\mathbf{x}} = \{(x,y) \mid r = \sqrt{x^2+y^2} < R\}$, and respectively the cylindrical coordinate in 3D, i.e. $\Omega_{\mathbf{x}} = \{(x,y,z) \mid r = \sqrt{x^2+y^2} < R,\ e < z < f\}$, with R, $|e|$ and f sufficiently large.

Choose a time step size $\Delta t > 0$. For $n = 0, 1, 2, \cdots$, from time $t = t_n = n\Delta t$ to $t = t_{n+1} = t_n + \Delta t$, the GPE (4.97) is solved in two splitting steps. One first solves

$$(i-\lambda)\ \partial_t\psi(\mathbf{x},t) = V_2(\mathbf{x},t)\psi + \beta_2|\psi|^2\psi \tag{4.100}$$

for the time step of length Δt, followed by solving

$$(i-\lambda)\,\partial_t\psi(\mathbf{x},t) = -\frac{1}{2}\nabla^2\psi - \Omega L_z\psi \tag{4.101}$$

for the same time step. For $t \in [t_n, t_{n+1}]$, dividing (4.100) by $(i-\lambda)$, multiplying it by $\psi^*(\mathbf{x},t)$ and adding to its complex conjugate, we obtain the following ODE for $\rho(\mathbf{x},t) = |\psi(\mathbf{x},t)|^2$:

$$\partial_t\rho(\mathbf{x},t) = -\eta_0\left[V_2(\mathbf{x},t)\rho(\mathbf{x},t) + \beta_2\rho^2(\mathbf{x},t)\right], \quad \mathbf{x}\in\Omega_{\mathbf{x}}, \quad t_n \le t \le t_{n+1}, \tag{4.102}$$

where $\eta_0 = 2\lambda/(1+\lambda^2)$. The ODE for the phase $S(\mathbf{x},t)$ (determined as $\psi = \sqrt{\rho}e^{iS}$) is given by

$$\partial_t S(\mathbf{x},t) = -\frac{1}{1+\lambda^2}\left[V_2(\mathbf{x},t) + \beta_2\rho(\mathbf{x},t)\right], \quad \mathbf{x}\in\Omega_{\mathbf{x}}, \quad t_n \le t \le t_{n+1}. \tag{4.103}$$

Typically if $\lambda \neq 0$, the above ODE is equivalent to

$$\partial_t S = \frac{1}{2\lambda}\partial_t \ln\rho, \qquad \mathbf{x}\in\Omega_{\mathbf{x}}, \quad t_n \le t \le t_{n+1}. \tag{4.104}$$

Denoting $V_2^n(\mathbf{x},t) = \int_{t_n}^t V_2(\mathbf{x},\tau)d\tau$, we can solve (4.102) and get

$$\rho(\mathbf{x},t) = \frac{\rho(\mathbf{x},t_n)\ \exp[-\eta_0 V_2^n(\mathbf{x},t)]}{1+\eta_0\beta_2\rho(\mathbf{x},t_n)\int_{t_n}^t \exp[-\eta_0 V_2^n(\mathbf{x},\tau)]\,d\tau}\ . \tag{4.105}$$

Consequently, in the special case $V_2(\mathbf{x},t) = V_2(\mathbf{x})$, the exact analytical solutions of (4.102) can be given by

$$\rho(\mathbf{x},t) = \begin{cases} \rho(\mathbf{x},t_n), & \lambda = 0, \\ \dfrac{\rho(\mathbf{x},t_n)}{1+\eta_0\beta_2(t-t_n)\rho(\mathbf{x},t_n)}, & \lambda \neq 0,\ \ V_2(\mathbf{x}) = 0, \\ \dfrac{V_2(\mathbf{x})\rho(\mathbf{x},t_n)\ \exp[-\eta_0 V_2(\mathbf{x})(t-t_n)]}{V_2(\mathbf{x}) + \beta_2\left[1-\exp[-\eta_0 V_2(\mathbf{x})(t-t_n)]\right]\rho(\mathbf{x},t_n)}, & \lambda \neq 0,\ \ V_2(\mathbf{x}) \neq 0. \end{cases}$$

Plugging (4.105) into (4.100), we obtain, for $t \in [t_n, t_{n+1}]$,

$$\psi(\mathbf{x},t) = \psi(\mathbf{x},t_n)\sqrt{U_n(\mathbf{x},t)}\exp\left[-\frac{\eta_0 i}{2\lambda}\left(V_2^n(\mathbf{x},t) + \beta_2\int_{t_n}^t \rho(\mathbf{x},\tau)d\tau\right)\right], \tag{4.106}$$

where

$$U_n(\mathbf{x},t) = \frac{\exp[-\eta_0 V_2^n(\mathbf{x},t)]}{1+\eta_0\beta_2|\psi(\mathbf{x},t_n)|^2\int_{t_n}^{t}\exp[-\eta_0 V_2^n(\mathbf{x},\tau)]\,d\tau}\,. \tag{4.107}$$

Again, with $V_2(\mathbf{x},t) = V_2(\mathbf{x})$, we can integrate (4.106) exactly to get

$$\psi(\mathbf{x},t) = \psi(\mathbf{x},t_n)\begin{cases} \exp\left[-i(\beta_2|\psi(\mathbf{x},t_n)|^2 + V_2(\mathbf{x}))(t-t_n)\right], & \lambda = 0, \\ \sqrt{\widehat{U}_n(\mathbf{x},t)}\exp\left[\frac{i}{2\lambda}\ln\widehat{U}_n(\mathbf{x},t)\right], & \lambda \neq 0; \end{cases} \tag{4.108}$$

where

$$\widehat{U}_n(\mathbf{x},t) = \begin{cases} \dfrac{1}{1+\eta_0\beta_2(t-t_n)|\psi(\mathbf{x},t_n)|^2}, & V_2(\mathbf{x}) = 0, \\ \dfrac{V_2(\mathbf{x})\exp[-\eta_0 V_2(\mathbf{x})(t-t_n)]}{V_2(\mathbf{x}) + \beta_2\left[1-\exp[-\eta_0 V_2(\mathbf{x})(t-t_n)]\right]|\psi(\mathbf{x},t_n)|^2}, & V_2(\mathbf{x}) \neq 0. \end{cases}$$

Remark 4.2. If the function $V_2^n(\mathbf{x},t)$ as well as other integrals in (4.105), (4.106), and (4.107) can not be evaluated analytically, we can use numerical quadrature to approximate them. See details in Remark 4.1.

To solve (4.101), we try to formulate it in a variable separable form by using the polar coordinate, and then discretize it in θ-direction by Fourier pseudospectral method, in r-direction by finite difference method (FDM) and in time by the Crank-Nicolson (C-N) scheme. Assume that

$$\psi(r,\theta,t) = \sum_{l=-L/2}^{L/2-1}\widehat{\psi}_l(r,t)\,e^{il\theta}, \tag{4.109}$$

where L is an even positive integer and $\widehat{\psi}_l(r,t)$ is the Fourier coefficient for the lth mode. Plugging (4.109) into (4.101) and noticing the orthogonality of the Fourier functions, we obtain, for $0 < r < R$ and $-\frac{L}{2} \le l \le \frac{L}{2}-1$,

$$(i-\lambda)\,\partial_t\widehat{\psi}_l(r,t) = -\frac{1}{2r}\frac{\partial}{\partial r}\left(r\frac{\partial\widehat{\psi}_l(r,t)}{\partial r}\right) + \left(\frac{l^2}{2r^2} - l\Omega\right)\widehat{\psi}_l(r,t), \tag{4.110}$$

$$\widehat{\psi}_l(R,t) = 0 \quad (\text{for all } l), \qquad \widehat{\psi}_l(0,t) = 0 \quad (\text{for } l \neq 0). \tag{4.111}$$

Choose a mesh size $\Delta r = 2R/(2J+1)$ with $J > 0$ an integer, define shifted grid points $r_j = (j-1/2)\Delta r$ for $0 \le j \le J+1$, and let $\widehat{\psi}_{l,j}(t)$ be the approximation of $\widehat{\psi}_l(r_j,t)$. A second-order finite difference discretization for (4.110)−(4.111) in space can be given by [89, 88, 14]

$$\begin{aligned}(i-\lambda)\frac{d\widehat{\psi}_{l,j}(t)}{dt} &= -\frac{r_{j+1/2}\,\widehat{\psi}_{l,j+1}(t) - 2r_j\,\widehat{\psi}_{l,j}(t) + r_{j-1/2}\,\widehat{\psi}_{l,j-1}(t)}{2\,(\Delta r)^2\; r_j} \\ &\quad + \left(\frac{l^2}{2r_j^2} - l\Omega\right)\widehat{\psi}_{l,j}(t), \quad t_n \le t \le t_{n+1},\;\; 1 \le j \le J \end{aligned} \tag{4.112}$$

with essential boundary conditions:

$$\widehat{\psi}_{l,0}(t) = (-1)^l\widehat{\psi}_{l,1}(t), \qquad \widehat{\psi}_{l,J+1}(t) = 0, \qquad t_n \le t \le t_{n+1}. \tag{4.113}$$

The ODE system (4.112)−(4.113) may then be discretized by the C-N scheme. Although an implicit time discretization is applied for (4.112), the 1D nature of the problem makes the coefficient matrix a tridiagonal linear system, and thus it can be solved by fast algorithms with $O(J)$ arithmetic operations.

In practice, we always uses the second-order Strang splitting method [126], i.e. from time $t = t_n$ to $t = t_{n+1}$: i) evolve (4.100) for half time step $\Delta t/2$ with initial data given at $t = t_n$; ii) evolve (4.101) for one time step Δt starting with the new data; iii) evolve (4.100) for half time step $\Delta t/2$ with the newer data.

For the discretization considered here, the total memory requirement is $O(JL)$ and the total computational cost per time step is $O(JL\ln L)$. Furthermore, following the similar proofs in [15, 19, 24], the total density can be shown to be conserved in the discrete level when $\lambda = 0$ and to be decreased when $\lambda > 0$.

Remark 4.3. As noticed in [89, 88, 14], another way for discretizing (4.110)−(4.111) in space is to use the fourth-order finite difference method, i.e. for $t \in [t_n, t_{n+1}]$,

$$\begin{aligned}(i-\lambda)\frac{d\widehat{\psi}_{l,j}(t)}{dt} &= \left(\frac{l^2}{2r_j^2} - l\Omega\right)\widehat{\psi}_{l,j}(t) \\ &\quad - \frac{-\widehat{\psi}_{l,j+2}(t) + 16\widehat{\psi}_{l,j+1}(t) - 30\widehat{\psi}_{l,j}(t) + 16\widehat{\psi}_{l,j-1}(t) - \widehat{\psi}_{l,j-2}(t)}{24(\Delta r)^2} \\ &\quad - \frac{-\widehat{\psi}_{l,j+2}(t) + 8\widehat{\psi}_{l,j+1}(t) - 8\widehat{\psi}_{l,j-1}(t) + \widehat{\psi}_{l,j-2}(t)}{24\Delta r\; r_j}, \qquad 1 \le j \le J, \end{aligned} \tag{4.114}$$

$$
\begin{aligned}
(i-\lambda)\,\frac{d\widehat{\psi}_{l,J+1}(t)}{dt} &= \left(\frac{l^2}{2r_{J+1}^2} - l\Omega\right)\widehat{\psi}_{l,J+1}(t) \\
&\quad - \frac{11\widehat{\psi}_{l,J+2}(t) - 20\widehat{\psi}_{l,J+1}(t) + 6\widehat{\psi}_{l,J}(t) + 4\widehat{\psi}_{l,J-1}(t) - \widehat{\psi}_{l,J-2}(t)}{24(\Delta r)^2} \\
&\quad - \frac{3\widehat{\psi}_{l,J+2}(t) + 10\widehat{\psi}_{l,J+1}(t) - 18\widehat{\psi}_{l,J}(t) + 6\widehat{\psi}_{l,J-1}(t) - \widehat{\psi}_{l,J-2}(t)}{24\Delta r\; r_{J+1}}\,, \qquad (4.115)
\end{aligned}
$$

$$
\widehat{\psi}_{l,-1}(t) = (-1)^l\widehat{\psi}_{l,2}(t), \quad \widehat{\psi}_{l,0}(t) = (-1)^l\widehat{\psi}_{l,1}(t), \quad \widehat{\psi}_{l,J+1}(t) = 0. \qquad (4.116)
$$

Again the ODE system (4.114)−(4.116) may be discretized by the C-N scheme and only a pentadiagonal linear system is to be solved, which can be done very efficiently too, i.e. via $O(J)$ arithmetic operations.

Leap-frog Fourier pseudospectral (LFFP) method

Another efficient method for rotating BEC is the leap-frog Fourier pseudospectral (LFFP) method which adopts the Cartesian coordinate, and thus the 2D computational domain $\Omega_{\mathbf{x}} = [a,b]\times[c,d]$ with $|a|$, b, $|c|$ and d sufficiently large. Choose a time step $\Delta t > 0$ and spatial mesh sizes $\Delta x = (b-a)/J$ and $\Delta y = (d-c)/K$ with J and K even positive integers. Denote the grid points as

$$
x_j := a + j\Delta x, \quad 0 \le j \le J, \qquad y_k := c + k\Delta y, \quad 0 \le k \le K,
$$

and let $\psi_{j,k}^n$ be the approximation of $\psi(x_j, y_k, t_n)$.

For $n = 1, 2, \cdots$, from time $t = t_{n-1} = (n-1)\Delta t$ to $t = t_{n+1} = (n+1)\Delta t$, we can discretize the GPE (4.97) in space by the Fourier pseudospectral method and in time by the leap-frog scheme, i.e. for $1 \le j \le J-1$ and $1 \le k \le K-1$,

$$
(i-\lambda)\frac{\psi_{j,k}^{n+1} - \psi_{j,k}^{n-1}}{2\Delta t} = -\frac{1}{2}\left(\nabla_h^2\psi^n\right)\big|_{j,k} + V_2(x_j,y_k)\psi_{j,k}^n + \beta_2|\psi_{j,k}^n|^2\psi_{j,k}^n - \Omega\left(L_h\psi^n\right)\big|_{j,k}\,, \qquad (4.117)
$$

where ∇_h^2 and L_h, the pseudospectral differential operators approximating the operators ∇^2 and L_z respectively, are defined in (3.69) and (3.70).

For $n = 1$, to compute $\psi_{j,k}^1$, we apply the modified trapezoidal rule on the interval $[0, t_1]$, i.e.

$$\begin{aligned}
(i-\lambda)\frac{\psi_{j,k}^{(1)} - \psi_{j,k}^0}{\Delta t} &= -\frac{1}{2}\left(\nabla_h^2 \psi^0\right)\big|_{j,k} + V_2(x_j, y_k)\psi_{j,k}^0 + \beta_2 \left|\psi_{j,k}^0\right|^2 \psi_{j,k}^0 \\
&\quad -\Omega\left(L_h \psi^0\right)\big|_{j,k}, \\
(i-\lambda)\frac{\psi_{j,k}^{(2)} - \psi_{j,k}^{(1)}}{\Delta t} &= -\frac{1}{2}\left(\nabla_h^2 \psi^{(1)}\right)\big|_{j,k} + V_2(x_j, y_k)\psi_{j,k}^{(1)} + \beta_2 \left|\psi_{j,k}^{(1)}\right|^2 \psi_{j,k}^{(1)} \\
&\quad -\Omega\left(L_h \psi^{(1)}\right)\big|_{j,k}, \\
\psi_{j,k}^1 &= \frac{1}{2}\left(\psi_{j,k}^{(1)} + \psi_{j,k}^{(2)}\right), \qquad 1 \le j \le J-1, \quad 1 \le k \le K-1.
\end{aligned} \tag{4.118}$$

The initial data (4.99) is discretized as

$$\psi_{j,k}^0 = \psi_0(x_j, y_k), \qquad 0 \le j \le J, \quad 0 \le k \le K. \tag{4.119}$$

The leap-frog Fourier pseudospectral discretization (4.117)−(4.119) is explicit and time reversible. The total memory requirement is $O(JK)$ and the total computational cost per time step is $O(JK \ln(JK))$. Following the standard Von Neumann analysis, the stability condition is

$$\Delta t < \frac{2(\Delta x)^2}{\pi^2\left[1 + \left(\frac{\Delta x}{\Delta y}\right)^2\right] + 2\left(\Delta x\right)^2 \max_{\mathbf{x}\in\Omega_\mathbf{x}}\left[\pi|\Omega|\left(\frac{|x|}{\Delta x} + \frac{|y|}{\Delta y}\right) + V_2(\mathbf{x}) + \beta_2|\psi(\mathbf{x},t)|^2\right]}.$$

Comparing these two methods for rotating BEC, the time-splitting type method uses the polar coordinate in 2D or cylindrical coordinate in 3D, which makes the coefficient of the angular momentum rotation term become a constant; the leap-frog Fourier pseudospectral (LFFP) method adopts the Cartesian coordinate. Both two methods are time reversible just as the GPE (2.27) does. On the other hand, each one has its own advantages and disadvantages. The former is unconditionally stable and of second or fourth-order accuracy in radial direction and spectral accuracy in other directions of space. It also conserves the total density. The latter is explicit, of spectral accuracy in all directions of space and easy to program. It is stable

under a stability condition. Due to its fully spectral resolution in space, the LFFP method may resolve better dynamics of vortex lattices in rotating BEC, especially in the regimes with strongly repulsive interaction, i.e. $\beta_d \gg 1$, and fast rotation, i.e. $|\Omega| \approx \min\{\gamma_x, \gamma_y\}$, where a large number of vortices appear in the condensate and thus spatial resolution is one of the key issues.

4.5 Numerical results

In this section, we apply our numerical methods to verify the conservation of the angular momentum expectation and to study the dynamics of condensate widths.

In order to do so, we consider the 2D GPE (2.27)−(2.28) with $\beta_2 = 100$ and $\Omega = 0.8$. The initial data (2.28) is the central vortex state (2.39) with index $m = 1$, which is computed by setting $\gamma_x = \gamma_y = 1$ in (2.29). At time $t = 0$, we change the external potential by setting the trapping frequencies $\gamma_x = \gamma_y = 1.5$ or $\gamma_x = 1.2$, $\gamma_y = 1.5$.

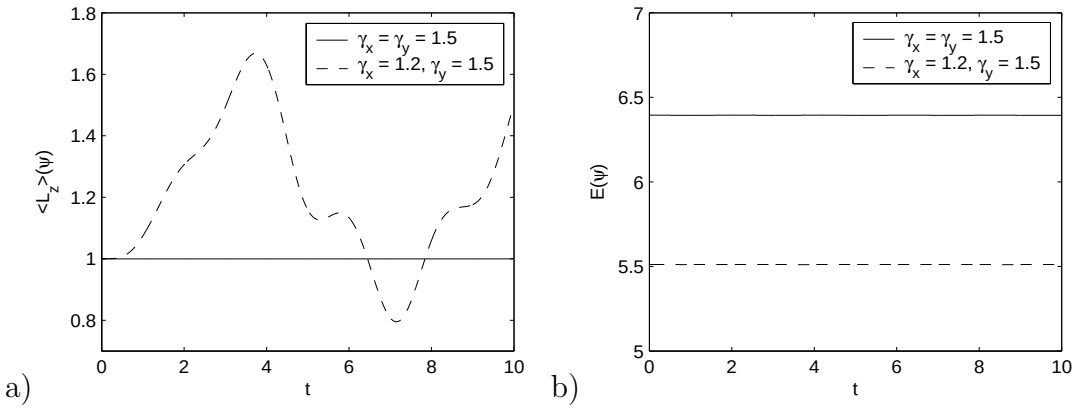

Figure 4.7: Time evolution of angular momentum expectation and energy. a). Angular momentum expectation $\langle L_z \rangle(t)$; b). energy $E_{\beta,\Omega}(\psi)$.

Figure 4.7 shows time evolutions of the angular momentum expectation $\langle L_z \rangle(t)$ and energy $E_{\beta,\Omega}(\psi)$. From it, we can see when $\gamma_x = \gamma_y$, the angular momentum expectation $\langle L_z \rangle(t)$ is conserved very well, which confirms the analytical result in (4.3). However, if $\gamma_x \neq \gamma_y$, $\langle L_z \rangle(t)$ is no longer conserved. On the other hand,

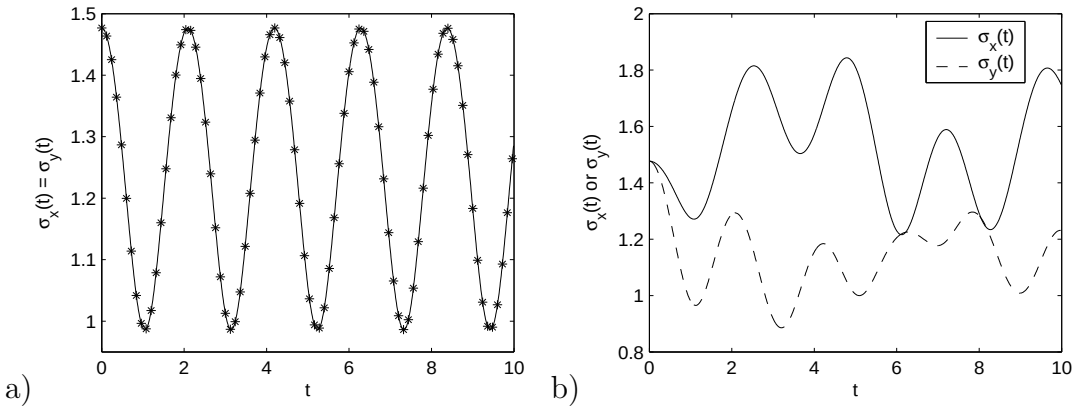

Figure 4.8: Time evolution of condensate widths. a). $\gamma_x = \gamma_y = 1.5$; solid line: obtained by solving the 2D GPE (2.27); $*$: obtained from the analytical solution (4.14); b). $\gamma_x = 1.2$ and $\gamma_y = 1.5$.

the total energy $E_{\beta,\Omega}$ is always conserved (cf. Fig. 4.7b), which agrees with the conservation law in (2.31).

Figure 4.8 presents time evolutions of condensate widths $\sigma_x(t)$ and $\sigma_y(t)$. Form it, we can find when $\gamma_x = \gamma_y = 1.5$, the condensate widths $\sigma_x(t) = \sigma_y(t)$ are periodic functions with period $T = 2\pi/3$, i.e. $T = \pi/\gamma_x$ (cf. Fig. 4.8a), which confirms the results in (4.14). If $\gamma_x \neq \gamma_y$, then $\sigma_x(t) \neq \sigma_y(t)$ and both of them are periodic functions with a perturbation (cf. Fig. 4.8b). These numerical observations agree very well with the analytical results in Lemma 4.3.

Chapter 5

Vortex dynamics in Bose-Einstein condensation

In this chapter, we investigate the vortex dynamics in Bose-Einstein condensation by applying the numerical methods introduced in Chapter 4. First, the stability of central vortex states is studied and we find that the central vortex with winding number $|m| = 1$ is dynamically stable, and respectively that with $|m| > 1$ is unstable. Then under two different initial patterns, the interactions between two $|m| = 1$ vortices with like or opposite winding numbers are investigated. Finally, the dynamics of vortex lattices in an asymmetric potential are also reported, which again demonstrates the efficiency and high accuracy of our numerical methods.

5.1 Central vortex state

In this section, the central vortex state is introduced for 2D and 3D cases. Central vortex state is one of the stationary states, and its wave function $\phi(\mathbf{x})$ can be written into a variable separable form. As we mentioned in Section 2.5, in 2D with a radially symmetric trap, i.e. $d = 2$ and $\gamma_x = \gamma_y := \gamma_r$ in (2.29), to find the central vortex

state, we can write

$$\phi(\mathbf{x}) = \phi_m(x,y) = f_m(r)e^{im\theta}, \qquad \mathbf{x} \in \mathbb{R}^2, \tag{5.1}$$

where $m \neq 0$ is an integer called as index or winding number and $f_m(r)$ is a real-valued function. Defining μ_m as the chemical potential corresponding to $\phi_m(\mathbf{x})$ and inserting (5.1) into the eigenvalue problem (2.33)−(2.34), we can get the following stationary problem for $f_m(r)$:

$$\mu_m f_m(r) = \left[-\frac{1}{2r}\frac{d}{dr}\left(r\frac{d}{dr}\right) + \frac{1}{2}\left(\gamma_r^2 r^2 + \frac{m^2}{r^2}\right) + \beta_2 \left|f_m\right|^2 + m\Omega \right] f_m(r), \tag{5.2}$$

$$f_m(0) = 0, \qquad \lim_{r\to\infty} f_m(r) = 0 \tag{5.3}$$

with the normalization condition

$$2\pi \int_0^\infty |f_m(r)|^2 \, r \, dr = 1. \tag{5.4}$$

In order to find the central vortex state (5.1), we can find a real nonnegative function $f_m(r)$ which minimizes the energy functional

$$\begin{aligned} E^m_{\beta,\Omega}(f(r)) &= E_{\beta,\Omega}\left(f(r)\, e^{im\theta}\right) \\ &= \pi \int_0^\infty \left[|f'(r)|^2 + \left(\gamma_r^2 r^2 + \frac{m^2}{r^2}\right) f^2(r) + \beta_2 |f(r)|^4 \right] r \, dr + m\Omega \end{aligned}$$

over the set

$$S_0 = \left\{ f \mid 2\pi \int_0^\infty |f(r)|^2 r \, dr = 1, \ f(0) = 0, \ E^m_{\beta,\Omega}(f) < \infty \right\}.$$

Note that the set $S_m = \{f(r)e^{im\theta} \mid f \in S_0\}$ is a subset of the unit sphere S given in (2.36), so $f_m(r)\ e^{im\theta}$ is a minimizer of the energy functional $E^m_{\beta,\Omega}(f)$ over the set $S_m \subset S$. The existence and uniqueness of the nonnegative minimizer for this minimization problem can be obtained similarly as for the ground state [93]. When $\beta_2 = 0$ and $\Omega = 0$, we can construct exactly the central vortex solution $\phi_m(\mathbf{x})$ as [13]

$$\phi_m(\mathbf{x}) = \frac{\gamma_r^{1/2}}{\sqrt{\pi |m|!}} r^{|m|} e^{-\gamma_r r^2/2}\ e^{im\theta}, \qquad \mathbf{x} \in \mathbb{R}^2, \quad m \in \mathbb{Z}, \tag{5.5}$$

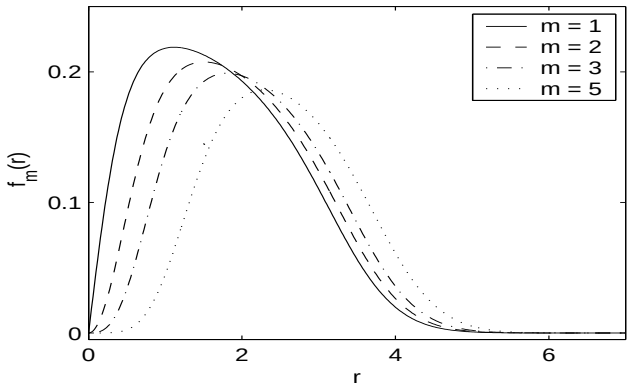

Figure 5.1: Numerical solutions of the function $f_m(r)$ for different winding numbers.

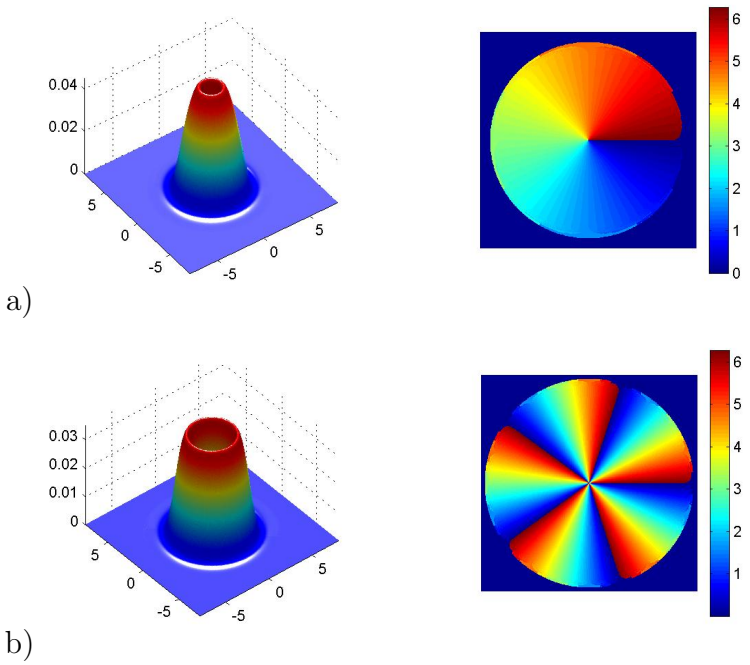

Figure 5.2: Surface (left) and phase (right) plots of the central vortex states with different winding numbers m. a). $m = 1$; b). $m = 5$.

by solving $f_m(r)$ from the eigenvalue problem (5.2)−(5.4).

Figure 5.1 shows the numerical solutions of $f_m(r)$ for different winding numbers m with $\beta_2 = 100$, $\Omega = 0$ and $\gamma_r = 1$ in (5.2), and Figure 5.2 displays the corresponding surface and phase plots of the central vortex states with winding number $m = 1$ and $m = 5$. From them, we can see that along a close path around the vortex center,

there is a $2m\pi$ jump in the phase of $\phi_m(x,y)$ (cf. Fig. 5.2), and for fixed parameters β_2 and γ_r, when the winding number m increases, the peak of the function $f_m(r)$ decreases (cf. Fig. 5.1), due to the normalization constraint. Let

$$f_m\left(r_m^0\right) = \alpha f_m\left(r_m^1\right), \qquad \text{where} \quad f_m\left(r_m^1\right) = \max_{r\geq 0} f_m(r) \quad \text{and} \quad 0<\alpha<1.$$

Then r_m^0 satisfying $0 < r_m^0 < r_m^1$ is called as core size of the central vortex state $\phi_m(x,y)$. In practice, the constant α is often chosen as $\alpha = \sqrt{2}/2$.

Similarly, in order to find central vortex line states in 3D case with a cylindrically symmetric trap, i.e. $d=3$ and $\gamma_x = \gamma_y := \gamma_r$ in (2.29), we can write

$$\phi(\mathbf{x}) = \phi_m(x,y,z) = f_m(r,z)e^{im\theta}, \qquad \mathbf{x}\in\mathbb{R}^3, \quad m\in\mathbb{Z}, \tag{5.6}$$

where $f_m(r,z)$ is a real-valued function. Inserting (5.6) into (2.33)−(2.34), we can obtain the following eigenvalue problem

$$\begin{aligned}\mu_m f_m(r,z) = \Bigg[&-\frac{1}{2r}\frac{\partial}{\partial r}\left(r\frac{\partial}{\partial r}\right) - \frac{\partial^2}{2\partial z^2} + \frac{1}{2}\left(\gamma_r^2 r^2 + \frac{m^2}{r^2} + \gamma_z^2 z^2\right) \\ &+\beta_3|f_m|^2 + m\Omega\Bigg] f_m(r,z), \qquad 0\leq r<\infty, \quad -\infty<z<\infty, \end{aligned} \tag{5.7}$$

$$f_m(0,z) = 0, \qquad \lim_{r\to\infty} f_m(r,z) = 0, \qquad -\infty<z<\infty, \tag{5.8}$$

$$\lim_{|z|\to\infty} f_m(r,z) = 0, \qquad 0\leq r<\infty \tag{5.9}$$

with the normalization condition

$$2\pi\int_{-\infty}^{\infty}\int_0^{\infty} |f_m(r,z)|^2 r\, drdz = 1. \tag{5.10}$$

Similar to the 2D case, to find the central vortex line state (5.6), we can find a real nonnegative function $f_m(r,z)$ minimizing the energy functional

$$\begin{aligned} E_{\beta,\Omega}^m(f(r,z)) &= E_{\beta,\Omega}(f(r,z)e^{im\theta}) \\ &= \pi\int_{-\infty}^{\infty}\int_0^{\infty}\left[|f_r|^2 + |f_z|^2 + \left(\gamma_r^2 r^2 + \gamma_z^2 z^2 + \frac{m^2}{r^2}\right)|f|^2 + \beta_3|f|^4\right] r\, drdz + m\Omega \end{aligned}$$

over the set

$$S_0 = \left\{ f \mid 2\pi\int_{-\infty}^{\infty}\int_0^{\infty} |f|^2 r\, drdz = 1,\ f(0,z)=0,\ -\infty<z<\infty,\ E_{\beta,\Omega}^m(f)<\infty \right\}.$$

The existence and uniqueness of the nonnegative minimizer for this minimization problem can be obtained similarly as for the ground state [93]. When $\beta_3 = 0$ and $\Omega = 0$ in (5.7), we can obtain the exact solution of the central vortex line states with winding number m [13],

$$\phi_m(\mathbf{x}) = \frac{\gamma_r^{1/2}\gamma_z^{1/4}}{\pi^{3/4}\sqrt{|m|!}} r^{|m|} e^{-(\gamma_r r^2+\gamma_z z^2)/2} e^{im\theta}, \qquad \mathbf{x} \in \mathbb{R}^3, \quad m \in \mathbb{Z}. \tag{5.11}$$

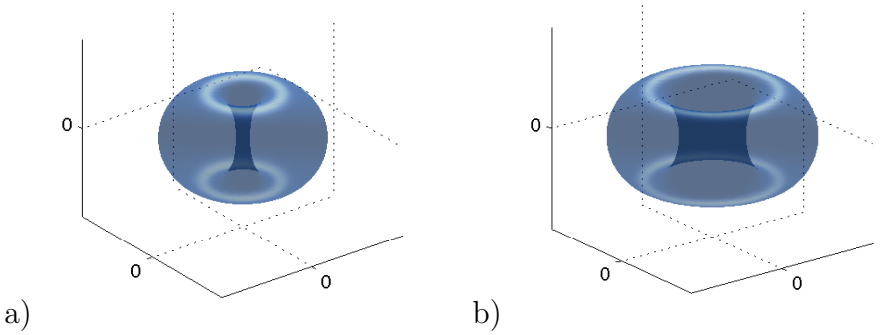

a) b)

Figure 5.3: Isosurface plots of the central vortex line states in 3D with different winding numbers. a). $m = 1$; b). $m = 3$.

Figure 5.3 presents the isosurface plots of the central vortex line states in 3D cases with winding number $m = 1$ and $m = 3$.

5.2 Stability of central vortex states

In this section, we study the stability of central vortex states by directly simulating the 2D GPE (2.27)−(2.28). In order to do so, we choose $\beta_2 = 100$, $\Omega = 0.8$ and $\gamma_x = \gamma_y = 1$ in (2.29). The initial data is taken as the central vortex state in (5.1) with winding number $|m| = 1$ or $|m| > 1$. Notice that similar study was also carried out for non-rotating BEC by using different numerical methods [75, 30, 77], and those methods have difficulty in strongly repulsive interacting regime.

From our numerical simulations, we find that if there is no perturbation, the central vortex states with winding number $|m| \geq 1$ are always stable in both rotating and

non-rotating BEC. In the following part, we introduce a small perturbation on the external potential to study the vortex stability, that is, when $t \in [0, \pi/2]$, a far-blue detuned Gaussian laser beam stirrer defined in (4.80) is introduced to perturb the condensate, and when $t > \pi/2$, it is removed. The parameters in (4.80) are chosen as

$$(x_s(t), y_s(t)) \equiv (3, 0), \qquad \omega_s = 1, \qquad W_s(t) = \begin{cases} 10\sin^2(2t), & t \in [0, 2\pi], \\ 0, & t \geq \pi/2. \end{cases}$$

To quantify the numerical results, we define the quantum hydrodynamic velocity as

$$\mathbf{u}(\mathbf{x}, t) = \nabla S(\mathbf{x}, t) = \mathrm{Im}(\psi^* \nabla \psi)/|\psi|^2.$$

Figures 5.4 and 5.5 show the velocity fields during time evolution of the central vortex states with winding number $m = 1$ and $m = 2$, respectively, and Figure 5.6 displays the time evolution of the energy and angular momentum expectation.

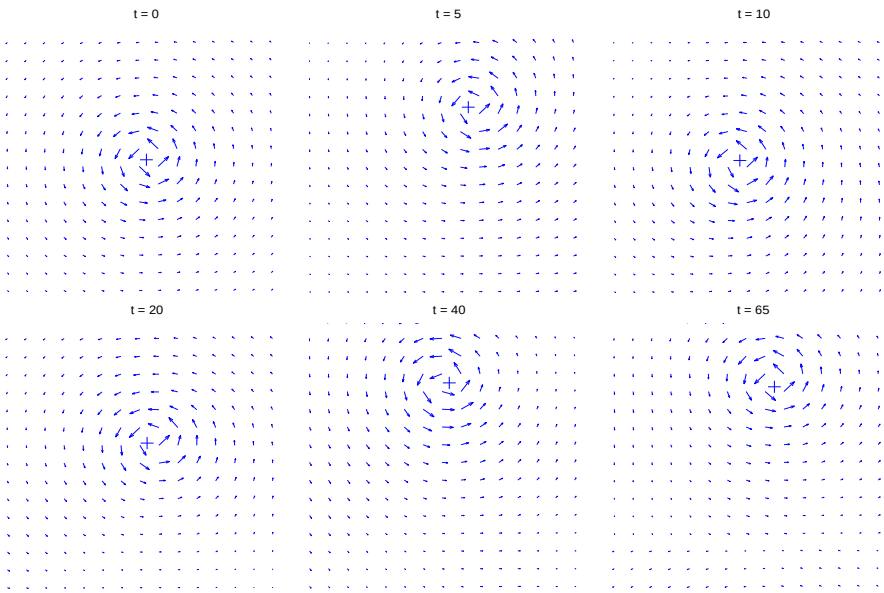

Figure 5.4: Velocity field at different times for the stability study of a central vortex state with winding number $m = 1$. Plot domain: $[-1, 1]^2$.

From Figs. 5.4−5.5 and our additional numerical experiments conducted, we can find that in both rotating and non-rotating BEC, the central vortex states with

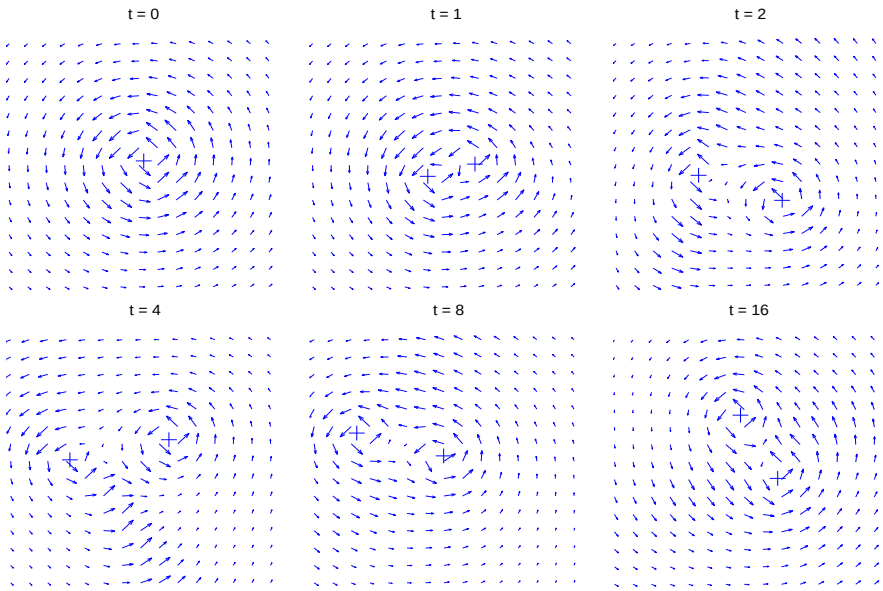

Figure 5.5: Velocity field at different times for the stability study of a central vortex state with winding number $m = 2$. Plot domain: $[-1, 1]^2$.

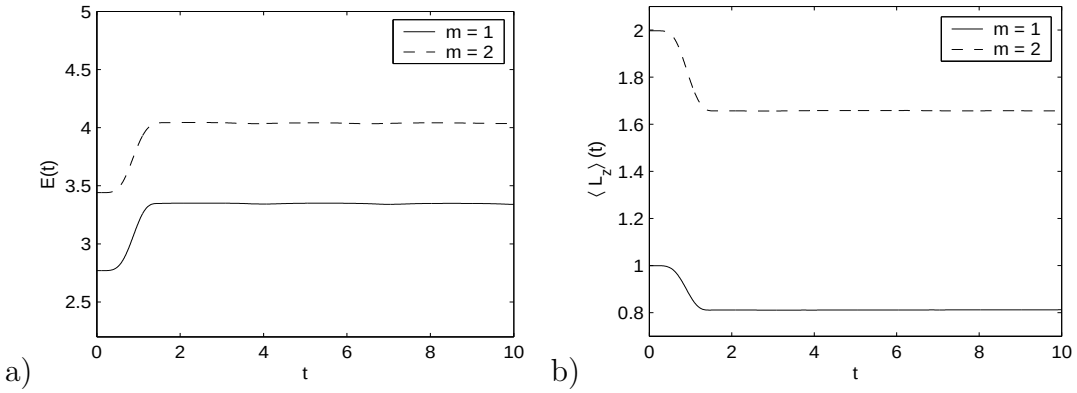

Figure 5.6: Time evolution of energy $E(t) := E_{\beta,\Omega}(\psi(t))$ and angular momentum expectation $\langle L_z \rangle$ in the stability study of central vortex states.

winding number $m = \pm 1$ are dynamically stable, and respectively those with $|m| > 1$ are unstable. After a short time, the central vortex initially with winding number $|m| > 1$ splits into $|m|$ vortices with winding number $+1$ if $m > 0$ and respectively -1 if $m < 0$ (cf. Fig. 5.5). These $|m|$ vortices are well overlapped and they would rotate with respect to each other. Fig. 5.6 suggests that the energy increases and the angular momentum expectation decreases when $t \in [0, \pi/2]$ due to the appearance

of the perturber. After removing the stirrer at $t = \pi/2$, they are conserved with time, which again confirms the conservation laws in (2.31) and (4.3).

5.3 Interaction of vortices with $m = \pm 1$

Since the central vortex states with winding number $|m| = 1$ are dynamically stable, it is of great interest to investigate the interaction between several vortices which have winding number $m = \pm 1$. This is an attractive topic both mathematically and physically, and so far there are still many open problems about it.

In this section, we study the interaction between two vortices with like or opposite winding numbers. Due to the property of the central vortex state (5.1), we can classify the interactions into two patterns:

$$\text{Pattern I.} \quad \psi(\mathbf{x},0) = \frac{\prod_{j=1}^{N}\phi_{m_j}\left(\mathbf{x}-\mathbf{x}_j^0\right)}{\left\|\prod_{j=1}^{N}\phi_{m_j}\left(\mathbf{x}-\mathbf{x}_j^0\right)\right\|} = \frac{\prod_{j=1}^{N}\phi_{m_j}\left(x-x_j^0, y-y_j^0\right)}{\left\|\prod_{j=1}^{N}\phi_{m_j}\left(x-x_j^0, y-y_j^0\right)\right\|},$$

$$\text{Pattern II.} \quad \psi(\mathbf{x},0) = \frac{\sum_{j=1}^{N}\phi_{m_j}\left(\mathbf{x}-\mathbf{x}_j^0\right)}{\left\|\sum_{j=1}^{N}\phi_{m_j}\left(\mathbf{x}-\mathbf{x}_j^0\right)\right\|} = \frac{\sum_{j=1}^{N}\phi_{m_j}\left(x-x_j^0, y-y_j^0\right)}{\left\|\sum_{j=1}^{N}\phi_{m_j}\left(x-x_j^0, y-y_j^0\right)\right\|},$$

where N is the total number of vortices (in this section we consider $N = 2$), ϕ_{m_j} is the central vortex state with winding number m_j ($m_j = +1$ or -1) and $\mathbf{x}_j^0$ is the initial location of the jth vortex. Both of these two interaction patterns are of interest, and in view of the small core size of a single vortex, in Pattern I the initial distance between two vortex centers should be small, while in Pattern II it must be large such that the support of the vortices is not overlapped.

5.3.1 Pattern I

As it is known that the properties of non-interacting and interacting BEC are distinctly different, thus here we consider the vortex interaction for $\beta_2 = 0$ and $\beta_2 \neq 0$ separately.

Case	$(x_1^0,\ y_1^0)$	m_1	$(x_2^0,\ y_2^0)$	m_2
I	$(a,\ 0)$	m_0	$(-a,\ 0)$	m_0
II	$(a,\ 0)$	m_0	$(-a,\ 0)$	$-m_0$

Table 5.1: Initial setups in Pattern I, where $m_0 = +1$ or -1.

Table 5.1 lists the initial setups to be considered, where two vortices are symmetrically located with respect to the trap center $(0, 0)^T$. A radially symmetric potential is chosen by setting $\gamma_x = \gamma_y := \gamma_r = 1$ in (2.29). In the following, the numerical results are reported only for $m_0 = +1$, and those for $m_0 = -1$ are similar and thus omitted here for brevity.

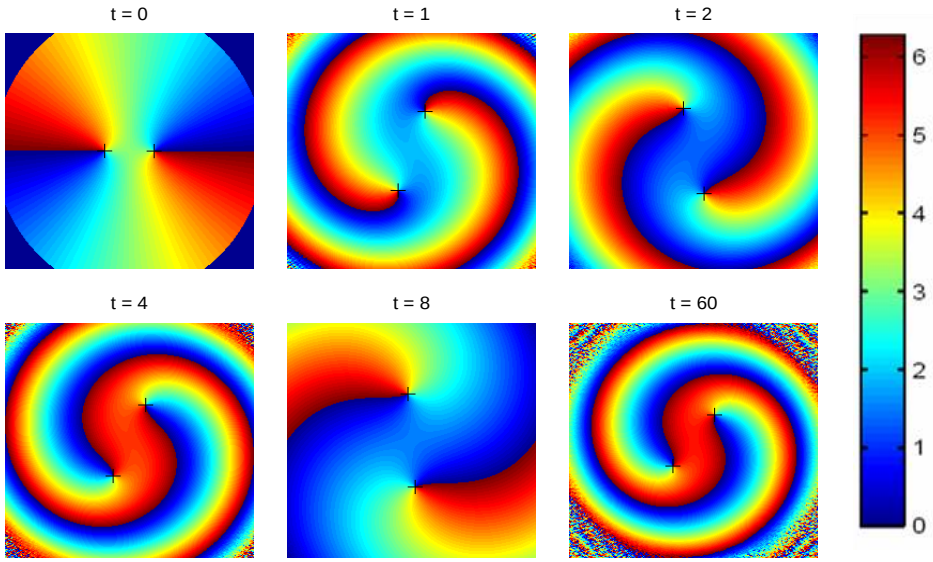

Figure 5.7: Phase plots of $\psi(\mathbf{x}, t)$ at different times in Case I of Pattern I with $\Omega = 0$, $\beta_2 = 0$ and $a = 1$ ('+': location of vortex center). Plot domain: $[-5, 5]^2$.

For Case I, i.e. two vortices with the same winding numbers, Figures 5.7 and 5.9 show the phase plots of $\psi(\mathbf{x}, t)$ at different times with $\beta_2 = 0$ and $\beta_2 = 100$ respectively. Figure 5.8 displays the time evolutions of two vortex centers for different Ω when $\beta_2 = 0$, while Figure 5.10 plots the time evolutions of the 1st vortex center, i.e. $\mathbf{x}_1(t) = -\mathbf{x}_2(t)$, when $\beta_2 = 100$.

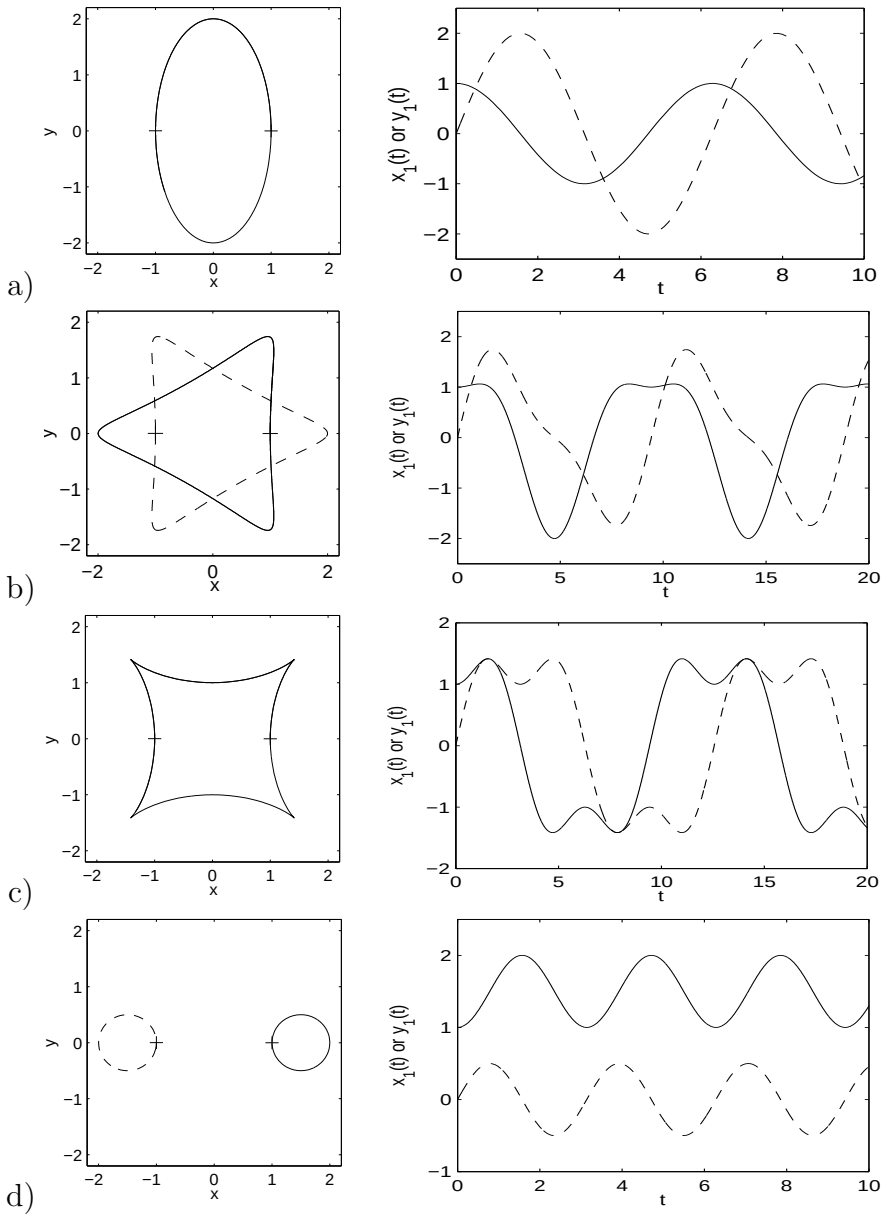

Figure 5.8: Time evolution of two vortex centers in Case I of Pattern I with $\beta_2 = 0$ and $a = 1$. Left: trajectory for $t \in [0, 30]$ ('+': initial location); Right: time evolution of $x_1(t)$ (solid line) and $y_1(t)$ (dash line). a). $\Omega = 0$; b). $\Omega = 1/3$; c). $\Omega = 1/2$; d). $\Omega = 1$.

From Figs. 5.7−5.10, we can draw the following conclusions for the interaction of two like vortices in Pattern I:

i). During the interaction, two vortices with the same winding numbers do not

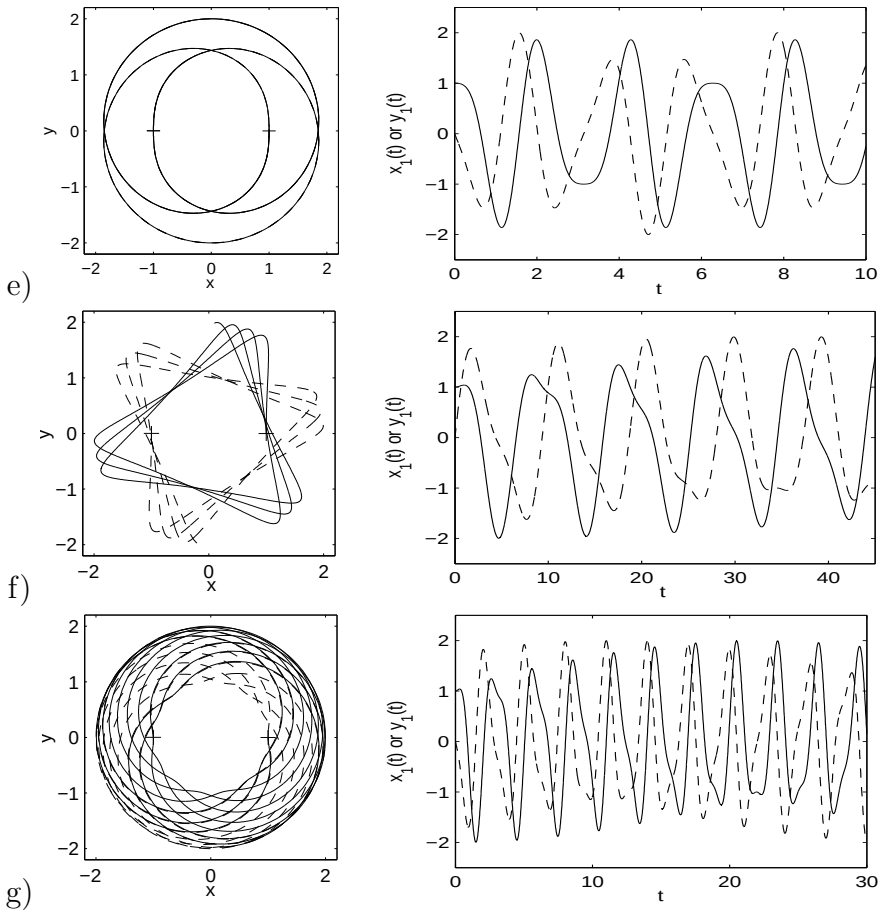

Figure 5.8 (cont'd): e). $\Omega = 4$; f). $\Omega = 1/\pi$; g). $\Omega = \pi$.

collide, and they are always symmetrically located with respect to the trap center, i.e. $\mathbf{x}_1(t) = -\mathbf{x}_2(t)$, for any time $t \geq 0$.

ii). In non-interacting BEC, i.e. $\beta_2 = 0$, if Ω is a rational number, i.e. $|\Omega| = q/p$ with q and p positive integers and no common factor, the two vortices rotate periodically with the same period. If both p and q are odd integers, the period $T = p\pi$, but the trajectories of two vortex centers are different (cf. Fig. 5.8b&d); otherwise $T = 2p\pi$ and their trajectories are exactly the same (cf. Fig. 5.8c&e). Especially, if $\Omega = 0$, the two vortices rotate (counter clockwise if $m_0 = +1$, and respectively clockwise if $m_0 = -1$) with period $T = 2\pi$ (cf. Fig. 5.7, 5.8a), and their trajectory is an ellipse which satisfies:

$$x_j(t) = x_j^0 \cos(t), \qquad y_j(t) = 2x_j^0 \sin(t), \qquad t \geq 0, \quad j = 1, 2. \tag{5.12}$$

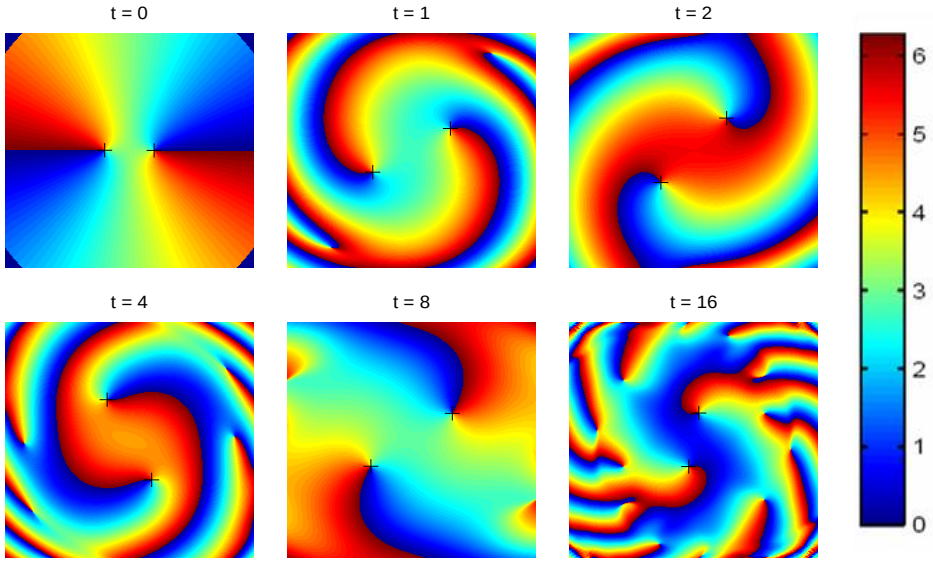

Figure 5.9: Phase plots of $\psi(\mathbf{x}, t)$ at different times in Case I of Pattern I with $\Omega = 0$, $\beta_2 = 100$ and $a = 1$ ('+': location of vortex center). Plot domain: $[-5, 5]^2$.

On the other hand, if Ω is an irrational number, the two vortex centers rotate chaotically in a bounded domain (cf. Fig. 5.8f&g).

iii). In interacting BEC, i.e. $\beta_2 \neq 0$, the two vortex centers move chaotically, but the envelope of their trajectories is a circle centered at the origin $(0, 0)$. If the initial distance between two vortex centers is fixed, i.e. fixed $d_0 = |\mathbf{x}_1^0 - \mathbf{x}_2^0|$, the time evolution of the distance $d(t) = |\mathbf{x}_1(t) - \mathbf{x}_2(t)|$ is the same for different Ω. Furthermore, it is a quasi-periodic function with period $T = \pi$ (cf. Fig. 5.11).

The interactions of two opposite vortices are more complicated than those of two like vortices, because in this case not only the parameters β_2 and Ω but also the initial distance between two vortex centers, i.e. $d_0 = |\mathbf{x}_1^0 - \mathbf{x}_2^0| = 2a$, play important roles in the interaction. For simplicity, here we consider the case of $\Omega = 0$ and define

$$\langle L_z \rangle_l(t) = \int_{-\infty}^{\infty} \left(\int_{-\infty}^{0} \psi^* L_z \psi \, dx \right) dy, \qquad t \geq 0, \tag{5.13}$$

$$\langle L_z \rangle_r(t) = \int_{-\infty}^{\infty} \left(\int_{0}^{\infty} \psi^* L_z \psi \, dx \right) dy, \qquad t \geq 0, \tag{5.14}$$

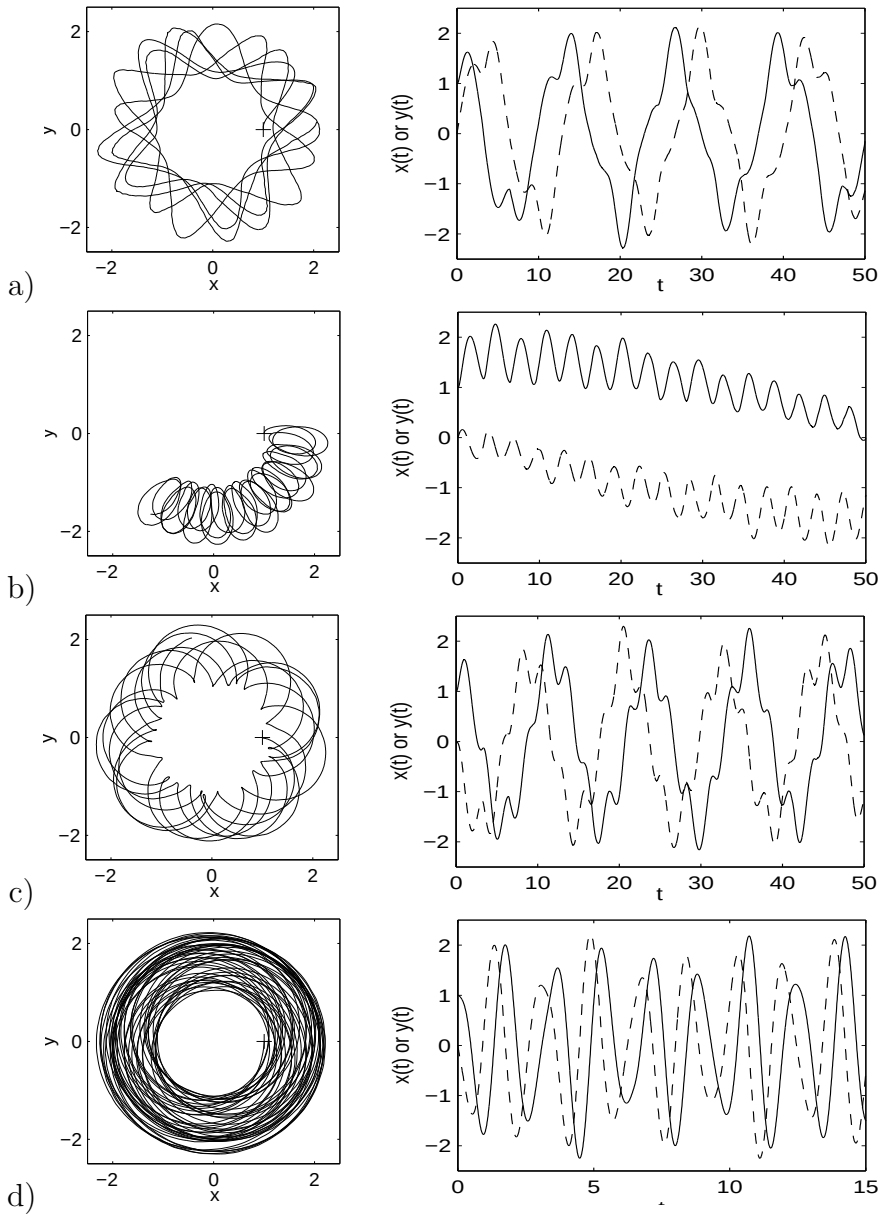

Figure 5.10: Time evolution of the 1st vortex center $\mathbf{x}_1(t)$ in Case I of Pattern I with $\beta_2 = 100$ and $a = 1$. Left: trajectory for $t \in [0, 80]$ ('+': initial location); Right: time evolution of $x(t)$ (solid line) and $y(t)$ (dash line). a). $\Omega = 0$; b). $\Omega = 1/2$; c). $\Omega = 1$; d). $\Omega = 4$.

as the angular momentum expectation of the left and right half-plane respectively.

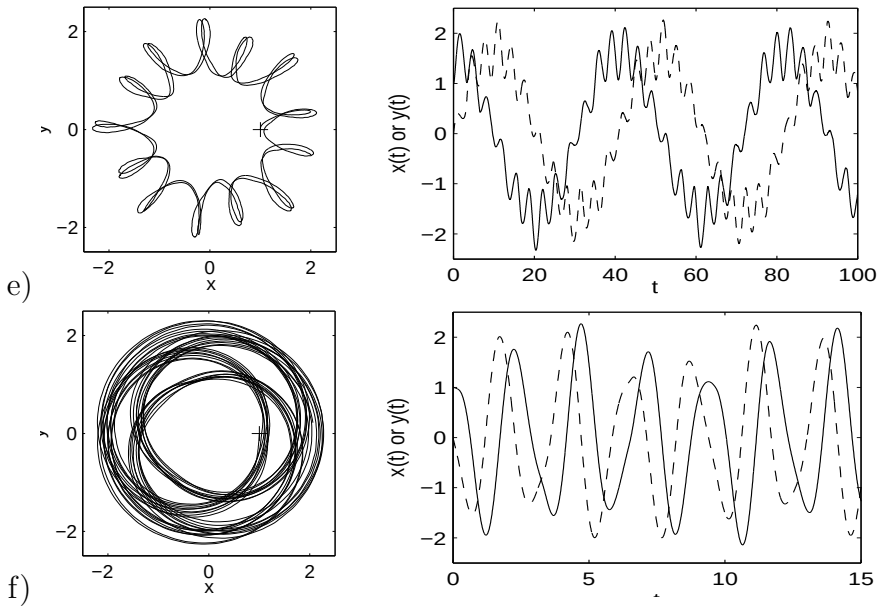

Figure 5.10 (cont'd): e). $\Omega = 1/\pi$; f). $\Omega = \pi$.

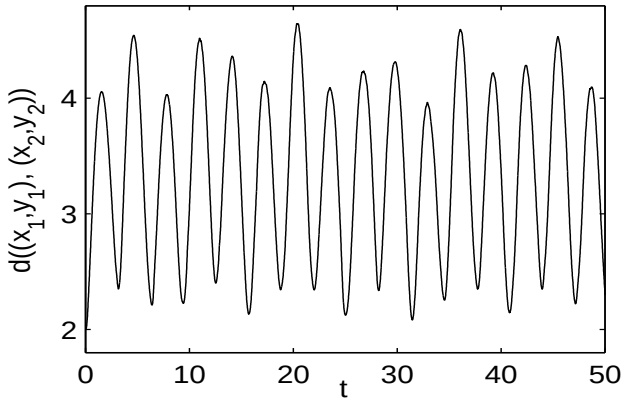

Figure 5.11: Time evolution of the distance between two vortex centers in Case I of Pattern I for different Ω with $\beta_2 = 100$ and $a = 1$.

Consequently, the total angular momentum expectation of this system can be computed by

$$\langle L_z \rangle(t) = \langle L_z \rangle_l(t) + \langle L_z \rangle_r(t), \qquad t \geq 0. \tag{5.15}$$

Figure 5.12 shows the phase plot of $\psi(\mathbf{x}, t)$ at different times with $\beta_2 = 0$ and $a = 1$, and Figure 5.13 displays the corresponding time evolution of the angular momentum expectations. Figures 5.14 and 5.15 plot the time evolutions of two vortex centers

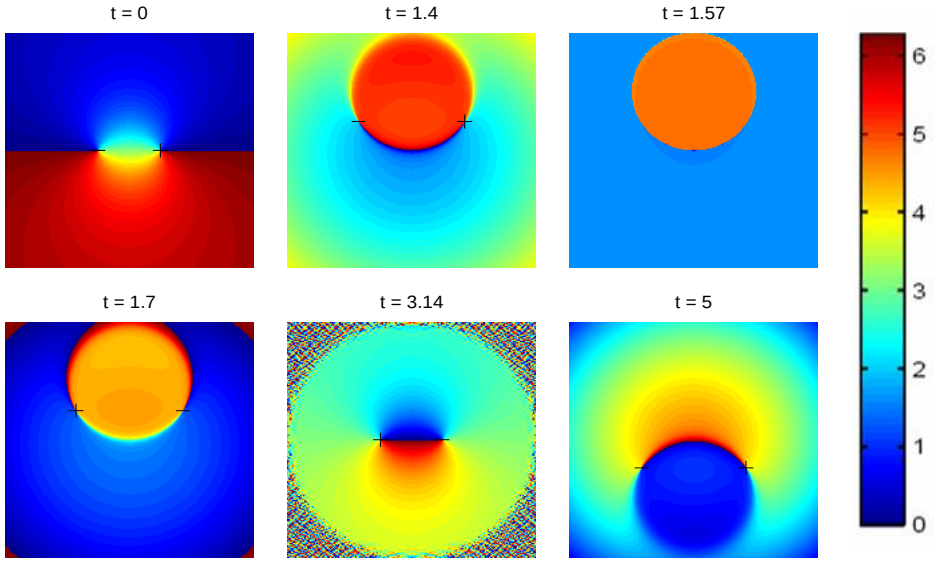

Figure 5.12: Phase plots of $\psi(\mathbf{x}, t)$ at different times in Case II of Pattern I with $\Omega = 0$, $\beta_2 = 0$ and $a = 1$ ('+/-': location of positive/negative vortex center). Plot domain: $[-4, 4]^2$.

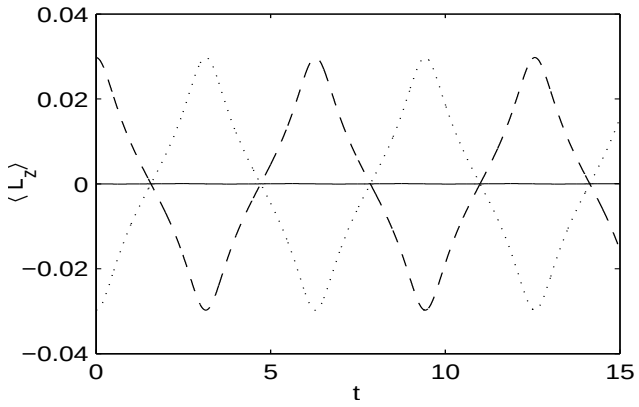

Figure 5.13: Time evolution of the angular momentum expectation $\langle L_z \rangle_r(t)$ (dash line), $\langle L_z \rangle_l(t)$ (dot line) and $\langle L_z \rangle(t) = \langle L_z \rangle_l(t) + \langle L_z \rangle_r(t)$ (solid line) in Case II of Pattern I with $\Omega = 0$, $\beta_2 = 0$ and $a = 1$.

for $\beta_2 = 0$ and $\beta_2 \neq 0$, respectively.

From Figs. 5.12−5.14, we can draw the following conclusions for the interaction of two opposite vortices in Pattern I with $\Omega = 0$ and $\beta_2 = 0$:

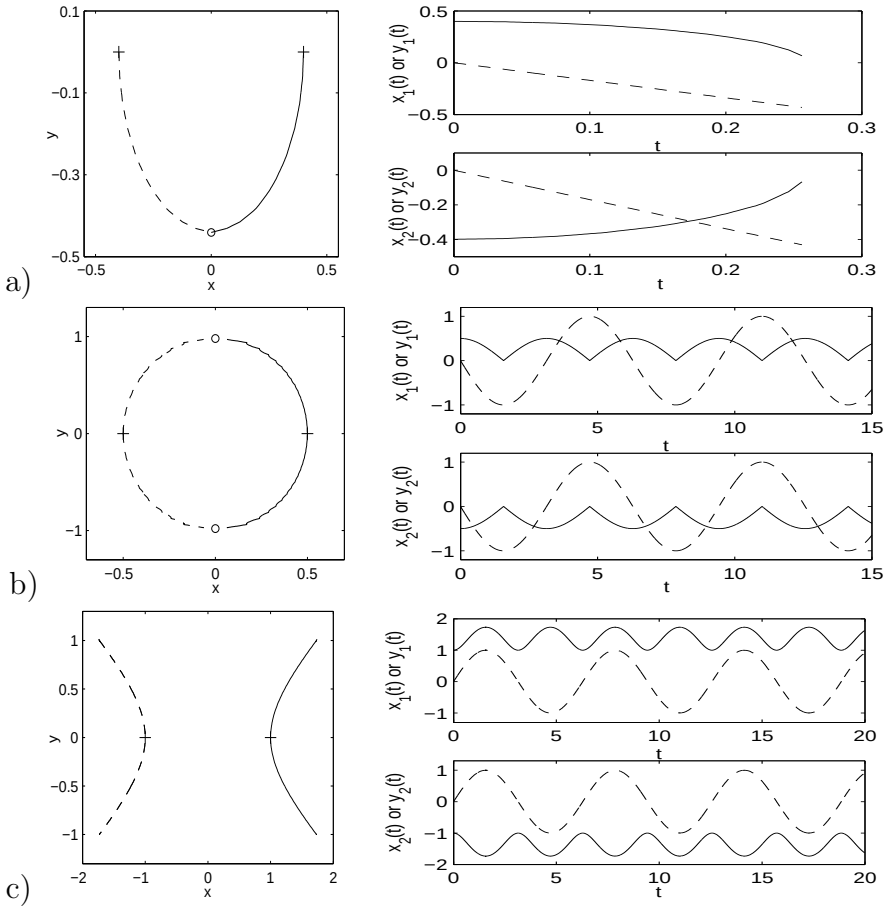

Figure 5.14: Time evolution of two vortex centers in Case II of Pattern I with $\Omega = 0$ and $\beta_2 = 0$. Left: trajectory ('+': initial location, 'o': collision location); Right: time evolution of $x(t)$ (solid line) and $y(t)$ (dash line). a). $a = 0.4$; b). $a = 0.5$; c). $a = 1$.

i). There exist two critical initial distances $d_1 \approx 0.8$ and $d_2 \approx 1.1$, which determine the interaction of two vortices.

ii). If the initial distance $d_0 \leq d_1$, the two vortices approach each other and then collide and annihilate at $t = t_c < \pi/2$ (cf. Fig. 5.14a).

iii). If $d_1 < d_0 < d_2$, the two vortices move to each other, and when $t = \pi/2$, they collide and annihilate at the point $(0, b)^T$ with $b < 0$. At the same time, there are two new vortices generated at this point. Comparing to the old vortex on each (left or right) half-plane, the new one has an opposite winding number. These two new

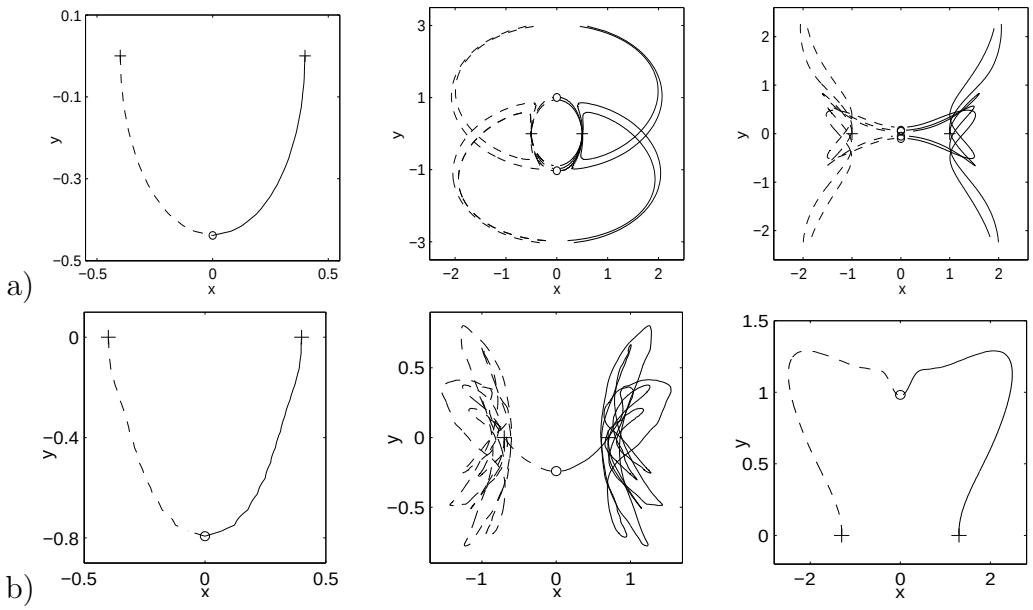

Figure 5.15: Time evolution of two vortex centers in Case II of Pattern I with $\Omega = 0$ and $\beta_2 \neq 0$ ('+': initial location, 'o': collision location). a). $\beta_2 = 1$ (left-right: $d_0 = 0.8$, 1 and 2); b). $\beta_2 = 50$ (left-right: $d_0 = 0.8$, 1.4 and 2.6)

vortices would move on their own half-planes along the trajectories of the old ones, and at $t = \pi$, they reach the initial locations of the two old vortices, i.e. point $(a, 0)^T$ and $(-a, 0)^T$. Similar to the old ones, they would move to each other and collide and annihilate at the point $(0, -b)^T$ when $t = 3\pi/2$ (cf. Fig. 5.14b). Then two newer vortices are generated and they repeat the similar process of the older ones.

iv). If $d_0 \geq d_2$, the two vortices move far away from each other while drifting sideways, and do not collide. When $t = \pi/2$, each of them collides with the external potential and annihilates there, and meanwhile a new vortex with opposite winding number appears at the same location (cf. Fig. 5.12). Similar to the vortices in iii), the new vortices would move back to the initial locations of the old ones along their trajectories, and then the similar process is repeated. In this case, both the angular momentum expectation $\langle L_z \rangle_l(t)$ and $\langle L_z \rangle_r(t)$ evolve periodically with period $T = 2\pi$, but the total angular momentum expectation $\langle L_z \rangle(t)$ is conserved for any

time $t \geq 0$ (cf. Fig. 5.13).

v). Furthermore, when $d_0 > d_1$, there are always two opposite vortices in the condensate. The life time of any pair of opposite vortices is $T = \pi$, except for that of the initial two vortices, which is $T = \pi/2$.

Similarly, from Fig. 5.15 and our additional results (omitted here for brevity), we can draw the following conclusions for the interaction of two opposite vortices in Pattern I with $\Omega = 0$ and $\beta_2 \neq 0$:

i). The total angular momentum expectation of this system is always conserved, i.e. $\langle L_z \rangle(t) \equiv \langle L_z \rangle(0)$ for any time $t \geq 0$.

ii). When the initial distance d_0 is small, the two vortices move to each other, and then collide and annihilate at a critical time t_c (cf. Fig. 5.15), but after a short time, one or more pairs of opposite vortices would be generated in the condensate.

iii). When the initial distance d_0 is large, the interaction is more complicated, which depends on the magnitude of β_2 (cf. Fig. 5.15). During the interaction, many pairs of opposite vortices would be generated and annihilate frequently.

5.3.2 Pattern II

Here, we also consider the interactions of two vortices for $\beta_2 = 0$ and $\beta_2 \neq 0$ separately. As we mentioned, in this pattern, the initial distance between two vortex centers should be large, i.e. no overlap between two vortex cores. The initial setup is shown in Table 5.2, and the external potential is given in (2.29) with $\gamma_x = \gamma_y := \gamma_r = 1$. Similarly, here we only consider $m_0 = +1$, and the results for $m_0 = -1$ are similar.

Case	$(x_1^0,\ y_1^0)$	m_1	$(x_2^0,\ y_2^0)$	m_2
I	$(a,\ a)$	m_0	$(-a,\ -a)$	m_0
II	$(a,\ a)$	m_0	$(-a,\ -a)$	$-m_0$

Table 5.2: Initial setups in Pattern II, where $m_0 = +1$ or -1.

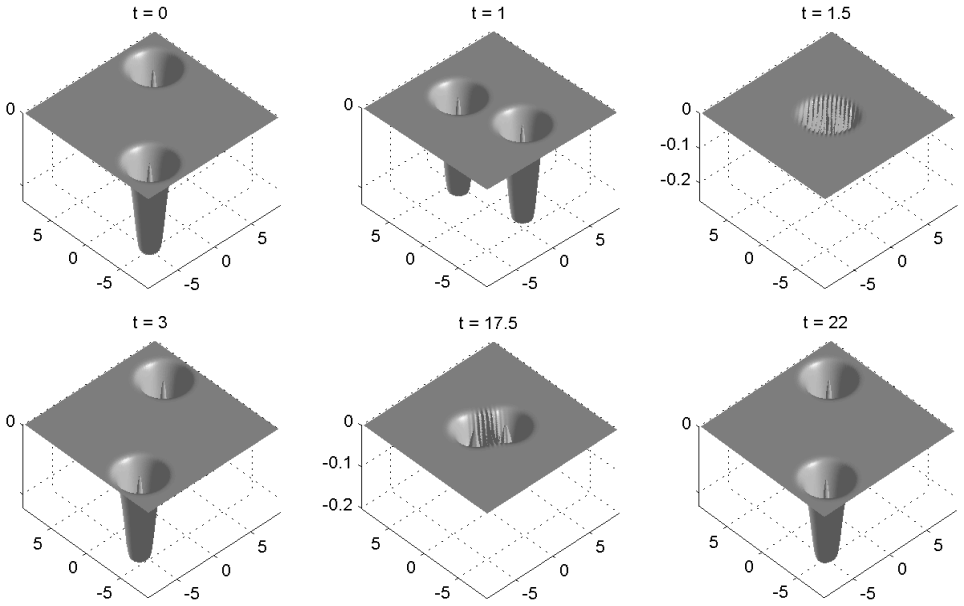

Figure 5.16: Surface plots of $|\psi(\mathbf{x}, t)|^2$ at different times in Case I of Pattern II, where $\beta_2 = 0$, $\Omega = 1$ and $a = 5$.

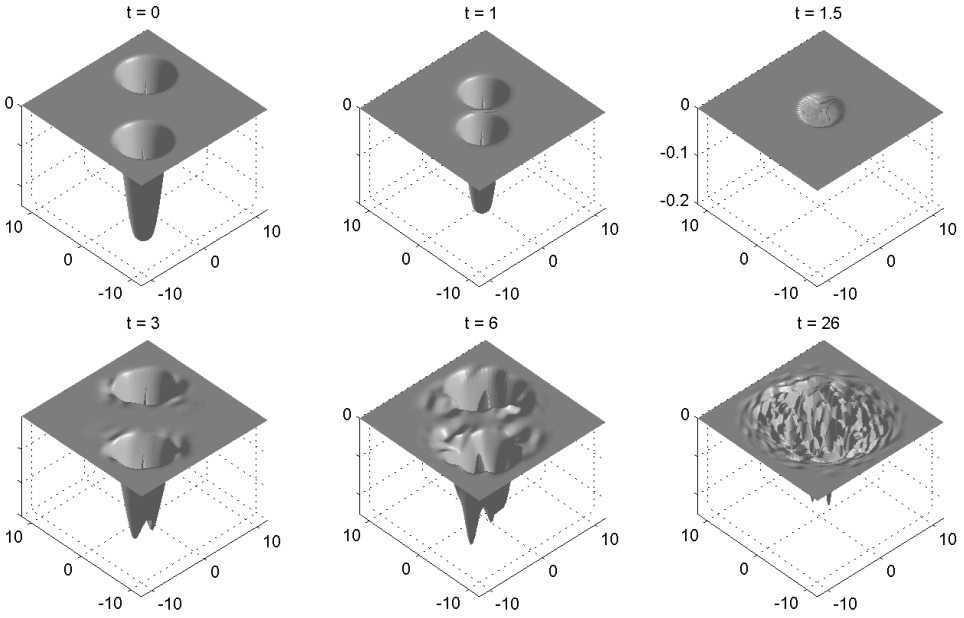

Figure 5.17: Surface plots of $|\psi(\mathbf{x}, t)|^2$ at different times in Case I of Pattern II, where $\beta_2 = 100$, $\Omega = 0$ and $a = 5$.

For Case I, Figure 5.16 shows the surface plots of $|\psi(\mathbf{x},t)|^2$ at different times with $\beta_2 = 0$ and $\Omega = 1$, while Figure 5.17 displays the similar results with $\beta_2 = 100$ and $\Omega = 0$.

From them and additional numerical experiments conducted, we can draw the following conclusions for the interaction of two vortices in Pattern II:

i). For fixed parameters β_2, Ω and a, the interactions in Case I and Case II are exactly the same, and the two like or opposite vortices would collide during the interaction.

ii). In non-interacting BEC, i.e. $\beta_2 = 0$, after collision, two vortices would separate and recover their initial shapes completely (cf. Fig. 5.16), and the motion of each vortex center is governed by the ODE system (4.28)−(4.30).

iii). In interacting BEC, i.e. $\beta_2 \neq 0$, there is a critical time t_c, and when $t \leq t_c$, the two vortices can separate after collision, but when $t > t_c$, they do not separate and turn into a chaos (cf. Fig. 5.17).

5.4 Dynamics of vortex lattice

In this section, we study the dynamics of vortex lattices by imposing a small perturbation on the external potential (2.29). The initial data is the stationary state solution of rotating BEC with $\beta_2 = 1000$, $\Omega = 0.9$ and $\gamma_x = \gamma_y = 1$. For $t \geq 0$, we introduce a perturber on the external potential (2.29), which is defined as

$$W(\mathbf{x},t) = \frac{\varepsilon}{2}\gamma_r^2\left[(x^2-y^2)\cos(2\omega t) + 2xy\sin(2\omega t)\right], \quad \mathbf{x}\in\mathbb{R}^2, \ \ t\geq 0,$$

where $\gamma_r := \gamma_x = \gamma_y = 1$, and ε and ω are positive constants. This implies that the total potential $V(\mathbf{x},t)$ is

$$V(\mathbf{x},t) = \frac{1}{2}\gamma_r^2\left[(1+\varepsilon)X^2(t) + (1-\varepsilon)Y^2(t)\right]$$

with $X(t) = x\cos(\omega t) + y\sin(\omega t)$ and $Y(t) = y\cos(\omega t) - x\sin(\omega t)$.

Figure 5.18 shows the contour plots of $|\psi(\mathbf{x},t)|^2$ at different times, where the parameters are chosen as $\varepsilon = 0.35$ and $\omega = 0.75$. From it, we can see that initially

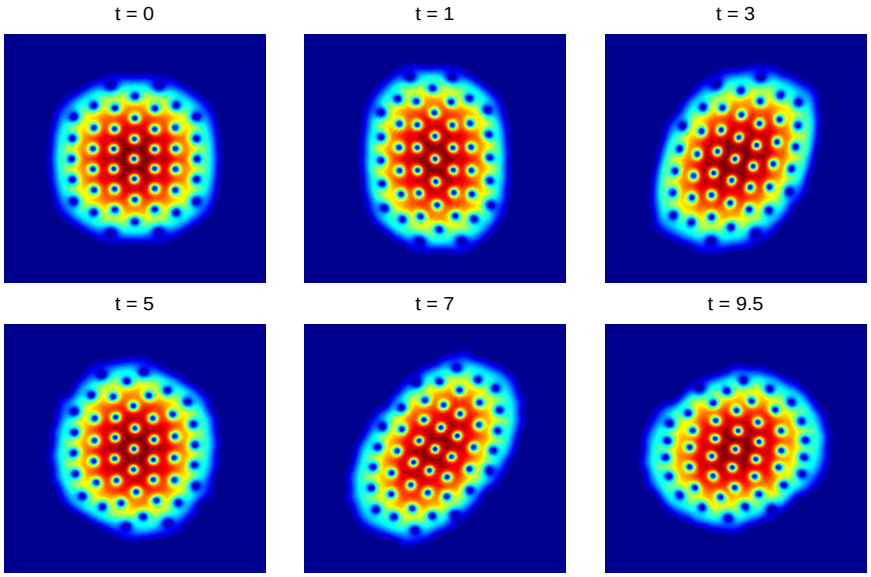

Figure 5.18: Contour plots of $|\psi(\mathbf{x},t)|^2$ at different times for the dynamics of a vortex lattice. Plot domain: $[-12,12]^2$.

there are 45 vortices in the lattice and during the time evolution, the number of vortices is preserved. Due to the angular momentum term and anisotropic external stirrer $W(\mathbf{x},t)$, the lattice rotates to form different patterns. Our numerical results can be compared with the experimental observations in [57], where the anisotropic compression of the vortex lattices was observed due to the dynamic distortion of the trap potentials.

Chapter 6

Two-component Bose-Einstein condensation

In this chapter, we extend our investigation on single-component BEC to two-component one. Starting from the three-dimensional (3D) coupled Gross-Pitaevskii equations (CGPEs) with an angular momentum rotation term and an external driven field, we rescale them to obtain a dimensionless model, and further reduce them to the single GPE in certain limiting regime of particle numbers. By applying the BFFP method introduced in Chapter 3, the ground states of two-component rotating BEC are numerically studied for different experiment setups. Some dynamical laws are also derived for the density, condensate widths, angular momentum expectation and other important quantities in the dynamics of two-component BEC. Finally, an efficient numerical method is proposed for computing its dynamics.

6.1 Coupled Gross-Pitaevskii equations

At temperatures T much smaller than the critical temperature T_c [90], in the rotating frame, a two-component BEC with an external driven field can be well described by two self-consistent nonlinear Schrödinger equations (NLSEs), also known as coupled

Gross-Pitaevskii equations (CGPEs) [113, 85, 11, 86],

$$i\hbar\frac{\partial\psi_j(\mathbf{x},t)}{\partial t}=\left[-\frac{\hbar^2}{2m}\nabla^2+V_j(\mathbf{x})-\Omega L_z+\sum_{l=1}^{2}U_{jl}|\psi_l|^2\right]\psi_j-\lambda\hbar\psi_{k_j}, \tag{6.1}$$

where $\psi_j(\mathbf{x},t)$ denotes the macroscopic wave function of the jth ($j=1,2$) component, m is the atomic mass (here we assume that the atomic mass of the two components is the same), Ω is the angular velocity of the rotating laser beam, L_z defined in (2.11) is the z-component of the angular momentum and $\lambda>0$ is the Rabi frequency describing the strength of the external driven field. $V_j(\mathbf{x})$ is the external trapping potential acting on the jth component, and if the harmonic potential is considered, it takes the form

$$V_j(\mathbf{x})=\frac{m}{2}\left(\omega_{x,j}^2\,x^2+\omega_{y,j}^2\,y^2+\omega_{z,j}^2\,z^2\right), \qquad j=1,2, \tag{6.2}$$

where $\omega_{x,j}$, $\omega_{y,j}$ and $\omega_{z,j}$ are the trapping frequencies of the jth component in x-, y- and z-direction, respectively. Without loss of generality, in the following we assume that $\omega_{x,1}=\min_{1\le j\le 2}\{\omega_{x,j},\omega_{y,j},\omega_{z,j}\}$. The interaction of particles is described by $U_{jl}=4\pi\hbar^2a_{jl}/m$, where $a_{jl}=a_{lj}$ is the s-wave scattering length between the jth and lth component (positive for a repulsive interaction and negative for an attractive interaction). The integer k_j is chosen as

$$k_j=\begin{cases}2, & j=1,\\ 1, & j=2.\end{cases} \tag{6.3}$$

It is necessary to ensure that the wave functions are properly normalized. Especially, we require

$$\int_{\mathbb{R}^3}\left(|\psi_1(\mathbf{x},t)|^2+|\psi_2(\mathbf{x},t)|^2\right)d\mathbf{x}=N=N_1^0+N_2^0, \qquad t\ge 0, \tag{6.4}$$

where

$$N_j^0=\int_{\mathbb{R}^3}|\psi_j(\mathbf{x},0)|^2d\mathbf{x}, \qquad j=1,2, \tag{6.5}$$

is the particle number of the jth component at time $t=0$, and N is the total particle number in the condensate.

6.1.1 Dimensionless CGPEs

In order to scale the CGPEs (6.1), we introduce

$$t \to \omega_{x,1}\, t, \quad \mathbf{x} \to a_0 \mathbf{x}, \quad \psi_j \to \frac{\sqrt{N}}{a_0^{3/2}} \psi_j, \quad \Omega \to \omega_{x,1}\, \Omega, \quad \lambda \to \omega_{x,1}\, \lambda \tag{6.6}$$

with $1/\omega_{x,1}$ and $a_0 = \sqrt{\hbar/m\omega_{x,1}}$ being the dimensionless time unit and length unit, respectively. Inserting (6.6) into (6.1), we obtain the following dimensionless CGPEs:

$$i\frac{\partial \psi_j(\mathbf{x},t)}{\partial t} = \left[-\frac{1}{2}\nabla^2 + V_j(\mathbf{x}) - \Omega L_z + \sum_{l=1}^{2} \beta_{jl}|\psi_l|^2\right]\psi_j - \lambda\psi_{k_j}, \quad j = 1,2, \tag{6.7}$$

where the dimensionless potential is

$$V_j(\mathbf{x}) = \frac{1}{2}\left(\gamma_{x,j}^2\, x^2 + \gamma_{y,j}^2\, y^2 + \gamma_{z,j}^2\, z^2\right), \qquad j = 1,2 \tag{6.8}$$

with $\gamma_{x,j} = \omega_{x,j}/\omega_{x,1}$, $\gamma_{y,j} = \omega_{y,j}/\omega_{x,1}$ and $\gamma_{z,j} = \omega_{z,j}/\omega_{x,1}$, and the dimensionless angular momentum rotation term becomes $L_z = -i(x\partial_y - y\partial_x)$. The strength of particle interactions is characterized by

$$\beta_{jl} = \beta_{lj} = \frac{mU_{jl}N}{\hbar^2 a_0} = \frac{4\pi N a_{jl}}{a_0}, \qquad j,l = 1,2. \tag{6.9}$$

Similar to the single-component BEC, in the limiting regime,

$$\omega_{x,j} \approx \omega_{y,j} \approx \omega_{x,1}, \quad \omega_{z,j} \gg \omega_{x,1} \quad \Longleftrightarrow \quad \gamma_{x,j} \approx \gamma_{y,j} \approx 1, \quad \gamma_{z,j} \gg 1, \quad j = 1,2,$$

the 3D CGPEs (6.7) can be reduced to 2D CGPEs with $\mathbf{x} = (x,y)^T$ [11, 141]. Here we write the d-dimensional ($d = 2,3$) CGPEs into a unified form,

$$i\frac{\partial \psi_j(\mathbf{x},t)}{\partial t} = \left[-\frac{1}{2}\nabla^2 + V_j(\mathbf{x}) - \Omega L_z + \sum_{l=1}^{2} \beta_{j\,l}|\psi_l|^2\right]\psi_j - \lambda\psi_{k_j}, \quad t \geq 0, \tag{6.10}$$

$$\psi_j(\mathbf{x},0) = \psi_j^0(\mathbf{x}), \quad \mathbf{x} \in \mathbb{R}^d, \tag{6.11}$$

where the initial data are normalized as

$$\|\psi_1^0\|^2 + \|\psi_2^0\|^2 := \int_{\mathbb{R}^d} \left(|\psi_1^0(\mathbf{x})|^2 + |\psi_2^0(\mathbf{x})|^2\right) d\mathbf{x} = \frac{N_1^0}{N} + \frac{N_2^0}{N} = 1, \tag{6.12}$$

and the external potentials are given as

$$V_j(\mathbf{x}) = \begin{cases} \frac{1}{2}\left(\gamma_{x,j}^2\, x^2 + \gamma_{y,j}^2\, y^2\right), & d = 2, \\ \frac{1}{2}\left(\gamma_{x,j}^2\, x^2 + \gamma_{y,j}^2\, y^2 + \gamma_{z,j}^2\, z^2\right), & d = 3, \end{cases} \qquad j = 1, 2. \tag{6.13}$$

The dimensionless CGPEs (6.10) conserve the total density

$$N(t) = N_1(t) + N_2(t) \equiv \|\psi_1^0\|^2 + \|\psi_2^0\|^2 = 1, \qquad t \geq 0 \tag{6.14}$$

with

$$N_j(t) = \|\psi(\cdot, t)\|^2 := \int_{\mathbb{R}^d} |\psi_j(\mathbf{x}, t)|^2 d\mathbf{x}, \qquad t \geq 0, \quad j = 1, 2, \tag{6.15}$$

and the energy

$$E(\psi_1, \psi_2) = \int_{\mathbb{R}^d} \left[\sum_{j=1}^{2} \left(\frac{1}{2}|\nabla \psi_j|^2 + V_j(\mathbf{x})|\psi_j|^2 - \Omega \mathrm{Re}\left(\psi_j^* L_z \psi_j\right) \right.\right.$$
$$\left.\left. + \sum_{l=1}^{2} \frac{\beta_{jl}}{2}|\psi_j|^2|\psi_l|^2 \right) - 2\lambda \mathrm{Re}(\psi_1^* \psi_2) \right] d\mathbf{x} = E\left(\psi_1^0, \psi_2^0\right), \quad t \geq 0. \tag{6.16}$$

6.1.2 Reduction to single GPE when $\lambda = 0$

If there is no external driven field, i.e. $\lambda = 0$, the CGPEs (6.10) become

$$i\frac{\partial \psi_j(\mathbf{x}, t)}{\partial t} = \left[-\frac{1}{2}\nabla^2 + V_j(\mathbf{x}) - \Omega L_z + \sum_{l=1}^{2} \beta_{jl}|\psi_l|^2 \right] \psi_j, \quad j = 1, 2. \tag{6.17}$$

The CGPEs (6.17) are time reversible, time transverse invariant. The density of each component is conserved, i.e.

$$N_j(t) = \|\psi_j(\cdot, t)\|^2 \equiv \|\psi_j(\cdot, 0)\|^2 = \frac{N_j^0}{N}, \qquad t \geq 0, \quad j = 1, 2. \tag{6.18}$$

Furthermore, if the initial particle numbers N_1^0 and N_2^0 (w.l.o.g., assuming that $N_2^0 \geq N_1^0$), satisfy $N_2^0 \gg N_1^0$, i.e. $N_1^0 = o(N)$ and $N_2^0 = O(N)$ when $N \gg 1$, then we have

$$N_1(t) = \frac{N_1^0}{N} := \varepsilon \ll 1, \qquad N_2(t) = \frac{N_2^0}{N} := 1 - \varepsilon \approx 1, \qquad t \geq 0. \tag{6.19}$$

These imply that the effect of the first component is insignificant and the original two-component BEC is dominated by the second component. Formally, we can drop the first component from this system and get a single-component condensate, and in this case the CGPEs (6.17) are reduced to

$$i\frac{\partial\psi(\mathbf{x},t)}{\partial t} = \left[-\frac{1}{2}\nabla^2 + V(\mathbf{x}) + \beta|\psi|^2 - \Omega L_z\right]\psi, \qquad t \geq 0, \tag{6.20}$$

by setting $\psi(\mathbf{x},t) = \sqrt{N/N_2^0}\psi_2(\mathbf{x},t)$, $V(\mathbf{x}) = V_2(\mathbf{x})$ and $\beta = N_2^0\beta_{22}/N \approx \beta_{22}$. The GPE (6.20) conserves the normalization of the wave function

$$\|\psi(\cdot,t)\|^2 \equiv \|\psi(\cdot,0)\|^2 = \int_{\mathbb{R}^d} \frac{N}{N_2^0}|\psi_2(\mathbf{x},0)|^2 d\mathbf{x} = \frac{N}{N_2^0}\frac{N_2^0}{N} = 1, \quad t \geq 0, \tag{6.21}$$

and the energy (2.31).

6.1.3 Semiclassical scaling

Let $\beta_{\max} = \max\{\beta_{11}, \beta_{12}, \beta_{22}\}$. If $\beta_{\max} \gg 1$, i.e. in the strongly repulsive interacting regime, under the normalization (6.14), we can introduce a semiclassical scaling for the CGPEs (6.10) by choosing

$$\mathbf{x} = \varepsilon^{-1/2}\mathbf{x}, \qquad \psi_j^\varepsilon = \varepsilon^{d/4}\psi_j, \qquad \varepsilon = \beta_{\max}^{-2/(d+2)}. \tag{6.22}$$

Substituting (6.22) into (6.10) gives the following CGPEs:

$$i\varepsilon\frac{\partial\psi_j^\varepsilon(\mathbf{x},t)}{\partial t} = \left[-\frac{\varepsilon^2}{2}\nabla^2 + V_j(\mathbf{x}) - \varepsilon\Omega L_z + \sum_{l=1}^{2}\alpha_{jl}|\psi_l^\varepsilon|^2\right]\psi_j^\varepsilon - \varepsilon\lambda\psi_{k_j}^\varepsilon, \tag{6.23}$$

where $\alpha_{jl} = \beta_{jl}/\beta_{\max} = O(1)$ (or $o(1)$). In this case, the energy functional $E^\varepsilon(\psi_1^\varepsilon, \psi_2^\varepsilon)$ is defined as

$$\begin{aligned} E^\varepsilon(\psi_1^\varepsilon, \psi_2^\varepsilon) = \int_{\mathbb{R}^d} \Bigg[\sum_{j=1}^{2} \Bigg(& \frac{\varepsilon^2}{2}|\nabla\psi_j^\varepsilon|^2 + V_j(\mathbf{x})|\psi_j^\varepsilon|^2 - \varepsilon\Omega\mathrm{Re}\left((\psi_j^\varepsilon)^* L_z\psi_j^\varepsilon\right) \\ & + \sum_{l=1}^{2}\frac{\alpha_{jl}}{2}|\psi_j^\varepsilon|^2|\psi_l^\varepsilon|^2\Bigg) - 2\varepsilon\lambda\mathrm{Re}\left((\psi_1^\varepsilon)^*\psi_2^\varepsilon\right)\Bigg] d\mathbf{x} = O(1), \quad t \geq 0, \end{aligned} \tag{6.24}$$

by assuming that ψ_j^ε $(j=1,2)$ is ε-oscillatory and "sufficiently" integrable such that all terms have $O(1)$-integral. Then the leading asymptotics of the energy functional $E(\psi_1,\psi_2)$ in (6.16) can be given by

$$E(\psi_1,\psi_2)=\varepsilon^{-1}E^\varepsilon(\psi_1^\varepsilon,\psi_2^\varepsilon)=O(\varepsilon^{-1})=O\left(\beta_{\max}^{2/(d+2)}\right). \tag{6.25}$$

If $\lambda=0$ and $0<\varepsilon\ll 1$ in (6.23), we can set

$$\psi_j^\varepsilon(\mathbf{x},t)=\sqrt{\rho_j^\varepsilon(\mathbf{x},t)}\exp\left(\frac{i}{\varepsilon}S_j^\varepsilon(\mathbf{x},t)\right),\qquad j=1,2, \tag{6.26}$$

where $\rho_j^\varepsilon=|\psi_j^\varepsilon|^2$ and $S_j^\varepsilon=\varepsilon\arg\left(\psi_j^\varepsilon\right)$. Inserting (6.26) into (6.23) and collecting the real and imaginary parts, we can get the transport equations for the density ρ_j^ε and the Hamilton-Jacobi equations for the phase S_j^ε:

$$\partial_t\rho_j^\varepsilon+\operatorname{div}\left(\rho_j^\varepsilon\nabla S_j^\varepsilon\right)+\Omega\widehat{L}_z\rho_j^\varepsilon=0, \tag{6.27}$$

$$\partial_t S_j^\varepsilon+\frac{1}{2}|\nabla S_j^\varepsilon|^2+V_j(\mathbf{x})+\sum_{l=1}^{2}\alpha_{jl}\rho_l^\varepsilon=\frac{\varepsilon^2}{2\sqrt{\rho_j^\varepsilon}}\nabla^2\sqrt{\rho_j^\varepsilon},\qquad j=1,2, \tag{6.28}$$

where the operator $\widehat{L}_z=(x\partial_y-y\partial_x)$. Furthermore, by defining the current density

$$\mathbf{J}_j^\varepsilon(\mathbf{x},t)=\rho_j^\varepsilon\nabla S_j^\varepsilon=\varepsilon\operatorname{Im}\left[\left(\psi_j^\varepsilon(\mathbf{x},t)\right)^*\nabla\psi_j^\varepsilon(\mathbf{x},t)\right],\qquad j=1,2, \tag{6.29}$$

we can rewrite (6.27)$-$(6.28) as

$$\partial_t\rho_j^\varepsilon+\operatorname{div}\mathbf{J}_j^\varepsilon+\Omega\widehat{L}_z\rho_j^\varepsilon=0,\qquad j=1,2, \tag{6.30}$$

$$\partial_t\mathbf{J}_j^\varepsilon+\operatorname{div}\left(\frac{\mathbf{J}_j^\varepsilon\otimes\mathbf{J}_j^\varepsilon}{\rho_j^\varepsilon}\right)+\rho_j^\varepsilon\nabla V_j(\mathbf{x})+\nabla P_j\left(\rho_1^\varepsilon,\rho_2^\varepsilon\right)$$
$$+\Omega\left(\widehat{L}_z\mathbf{I}+\mathbf{G}\right)\mathbf{J}_j^\varepsilon=\frac{\varepsilon^2}{4}\nabla\left(\rho_j^\varepsilon\nabla^2\ln\rho_j^\varepsilon\right), \tag{6.31}$$

where $\mathbf{G}$ is the symplectic matrix given in (2.54) and the pressure

$$P_j\left(\rho_1^\varepsilon,\rho_2^\varepsilon\right)=\frac{1}{2}\sum_{l=1}^{2}\alpha_{jl}\,\rho_j^\varepsilon\,\rho_l^\varepsilon,\qquad j=1,2.$$

Let $\varepsilon\to 0^+$ in (6.27)$-$(6.28) and set $\rho_j^0=\lim_{\varepsilon\to0^+}\rho_j^\varepsilon$ and $S_j^0=\lim_{\varepsilon\to0^+}S_j^\varepsilon$. Then we can formally get

$$\partial_t\rho_j^0+\operatorname{div}\left(\rho_j^0\nabla S_j^0\right)+\Omega\widehat{L}_z\rho_j^0=0, \tag{6.32}$$

$$\partial_t S_j^0+\frac{1}{2}\left|\nabla S_j^0\right|^2+V_j(\mathbf{x})+\sum_{l=1}^{2}\alpha_{j\,l}\rho_l^0=0,\qquad j=1,2. \tag{6.33}$$

Similarly, letting $\varepsilon \to 0^+$ in (6.30)−(6.31), formally we can get the following Euler system coupling through the pressures:

$$\partial_t \rho_j^0 + \mathrm{div}\mathbf{J}_j^0 + \Omega \widehat{L}_z \rho_j^0 = 0, \qquad j = 1, 2, \tag{6.34}$$

$$\partial_t \mathbf{J}_j^0 + \mathrm{div}\left(\frac{\mathbf{J}_j^0 \otimes \mathbf{J}_j^0}{\rho_j^0}\right) + \rho_j^0 \nabla V_j(\mathbf{x}) + \nabla P_j\left(\rho_1^0, \rho_2^0\right) + \Omega\left(\widehat{L}_z \mathbf{I} + \mathbf{G}\right)\mathbf{J}_j^0 = 0, \tag{6.35}$$

where $\mathbf{J}_j^0 = \lim_{\varepsilon \to 0^+} \mathbf{J}_j^\varepsilon = \rho_j^0 \nabla S_j^0$. The system (6.34)−(6.35) is a coupled isotropic Euler system with quadratic pressure-density constitutive relations in the rotational frame.

6.2 Ground state

In this section, we investigate the ground state of rotating two-component BEC by considering the CGPEs (6.17), i.e. without the external driven field. To find the stationary solution, we write

$$\psi_j(\mathbf{x}, t) = e^{-i\mu_j t}\phi_j(\mathbf{x}), \qquad j = 1, 2, \tag{6.36}$$

where ϕ_j is a function independent of time. Substituting (6.36) into (6.17) gives the following equations for $(\mu_j,\, \phi_j)$:

$$\mu_j \phi_j(\mathbf{x}) = -\frac{1}{2}\nabla^2 \phi_j + V_j(\mathbf{x})\phi_j - \Omega L_z \phi_j + \sum_{l=1}^{2} \beta_{jl}|\phi_l|^2 \phi_j, \qquad \mathbf{x} \in \mathbb{R}^d \tag{6.37}$$

with the normalization condition

$$\int_{\mathbb{R}^d} |\phi_j(\mathbf{x})|^2 \, d\mathbf{x} = \frac{N_j^0}{N}, \qquad j = 1, 2. \tag{6.38}$$

This is a nonlinear eigenvalue problem under the constraint (6.38), and the eigenvalues $\mu_j = \mu_j(\phi_1, \phi_2)$ can be computed by

$$\begin{aligned} \mu_j(\phi_1, \phi_2) &= \frac{N}{N_j^0}\int_{\mathbb{R}^d}\left[\frac{1}{2}|\nabla\phi_j|^2 + V_j(\mathbf{x})|\phi_j|^2 - \Omega \mathrm{Re}\left(\phi_j^* L_z \phi_j\right) + \sum_{l=1}^{2}\beta_{jl}|\phi_j|^2|\phi_l|^2\right] d\mathbf{x} \\ &= \frac{N}{N_j^0} E_j(\phi_1, \phi_2) + \frac{N}{2N_j^0}\int_{\mathbb{R}^d}\sum_{l=1}^{2}\beta_{jl}|\phi_j|^2|\phi_l|^2 \, d\mathbf{x}, \qquad j = 1, 2. \end{aligned}$$

It is easy to see that critical points of the energy functional $E(\phi_1, \phi_2)$ under the constraint (6.38) are eigenfunctions of the nonlinear eigenvalue problem (6.37) under the constraint (6.38) and vice versa. In fact, (6.37) can be viewed as the Euler-Lagrange equations of the energy functional $E(\phi_1, \phi_2)$ under the constraint (6.38). The ground state solution of two-component BEC can be found by minimizing the energy functional under the constraint (6.38), i.e.

Find $(\mathcal{U}_g = (\mu_{g,1}, \mu_{g,2}), \Phi_g = (\phi_{g,1}, \phi_{g,2}) \in U)$, such that

$$E_g = E(\Phi_g) = \min_{\Phi \in U} E(\Phi), \quad \mu_{g,j} = \mu_j(\Phi_g), \qquad j = 1, 2, \tag{6.39}$$

where the set U is defined as

$$U = \left\{ \Phi = (\phi_1, \phi_2) \mid E(\Phi) < \infty, \int_{\mathbb{R}^d} |\phi_j(\mathbf{x})|^2 \, d\mathbf{x} = \frac{N_j^0}{N}, \ j = 1, 2 \right\}.$$

When $\beta_{jl} \geq 0$ $(j, l = 1, 2)$, for non-rotating two-component BEC, the minimization problem (6.39) has a unique real-valued nonnegative ground state solution $\Phi_g(\mathbf{x}) \geq 0$ for $\mathbf{x} \in \mathbb{R}^d$ [93, 11], while for rotating two-component BEC, if $|\Omega| < \min_{1 \leq j \leq 2}\{\gamma_{x,j}, \gamma_{y,j}\}$, there exists minimizer for the minimization problem (6.39).

As we seen in Chapter 3, the BFFP method is a very efficient method for computing the ground state of rotating BEC. In the section, we extend it to compute the ground state of rotating two-component BEC. The detailed discrietization is omitted here.

In the following subsections, we report 2D numerical results for different experiment setups, and for simplicity of notation, we denote $\beta_{11} : \beta_{12} : \beta_{22} = (a_{11} : a_{12} : a_{22})\, \beta_0$ with $\beta_0 \geq 0$.

6.2.1 Different angular velocity Ω

In this part, we study the ground state for different angular velocity $0 \leq \Omega \leq \min_{1 \leq j \leq 2}\{\gamma_{x,j}, \gamma_{y,j}\}$. In order to do so, we take $a_{11} : a_{12} : a_{22} = 1.03 : 1.0 : 0.97$ [72, 101, 73], $\beta_0 = 200$, $N_1^0 = N_2^0$ and $\gamma_{x,j} = \gamma_{y,j} = 1$ $(j = 1, 2)$.

Figure 6.1 displays the contour plots of the ground state $|\phi_{g,j}|^2$ $(j = 1, 2)$. From it, we can see when $\Omega = 0.3$, there is only one vortex in one component and no vortex

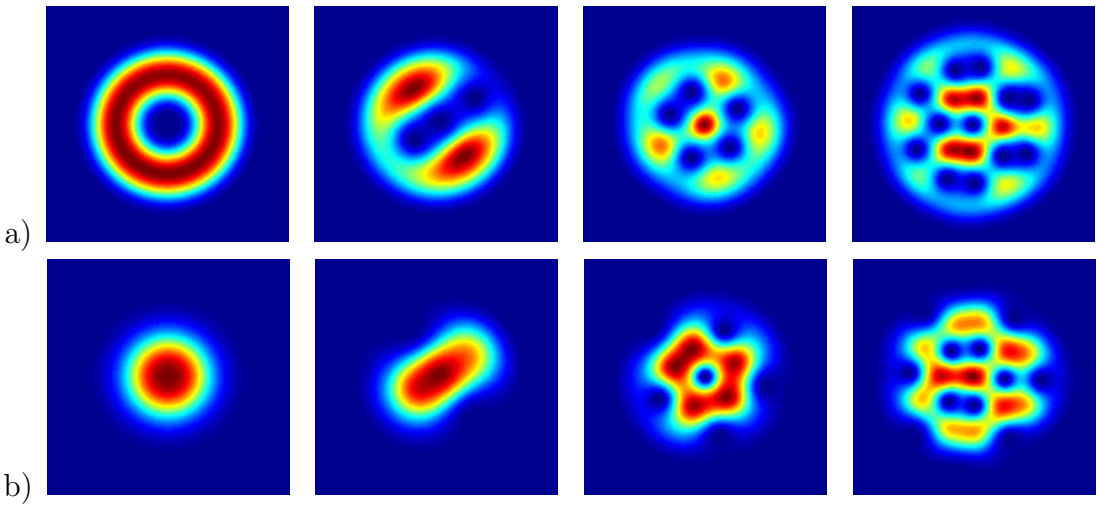

Figure 6.1: Contour plots of the ground state in two-component BEC with $\Omega = 0.3$, 0.4, 0.6 and 0.8 (from left to right). a). $|\phi_{g,1}|^2$; b). $|\phi_{g,2}|^2$.

in the other. When Ω increases, the number of vortices also increases to form two vortex lattices, and these two lattices interlock in such a way that a peak in the density of one component is located at the density hole of the other. According to the energy functional, the two components interact via the intercomponent interaction $\beta_{12}|\phi_1|^2|\phi_2|^2$, therefore this interlocked feature of two lattices can minimize the interaction energy, and further minimize the total energy.

6.2.2 Different inter-atomic interaction

To study the effect of intercomponent interactions, in this section, we compute the ground state solutions by fixing scattering length $a_{11} = a_{22} = 1$ and changing a_{12} from -1 to 3. The other parameters are chosen as $\beta_0 = 200$, $\Omega = 0.9$, $N_1^0 = N_2^0$ and $\gamma_{x,j} = \gamma_{y,j} = 1$ $(j = 1, 2)$.

Figure 6.2 depicts the contour plots of the ground states $|\phi_{g,j}|^2$ $(j = 1, 2)$ for different scattering length a_{12}. From it and our additional results, we can conclude that:

i). If $a_{12} < -1$, there is no ground state for this two-component condensate. In fact, in this case, the two components collapse to each other due to the strongly

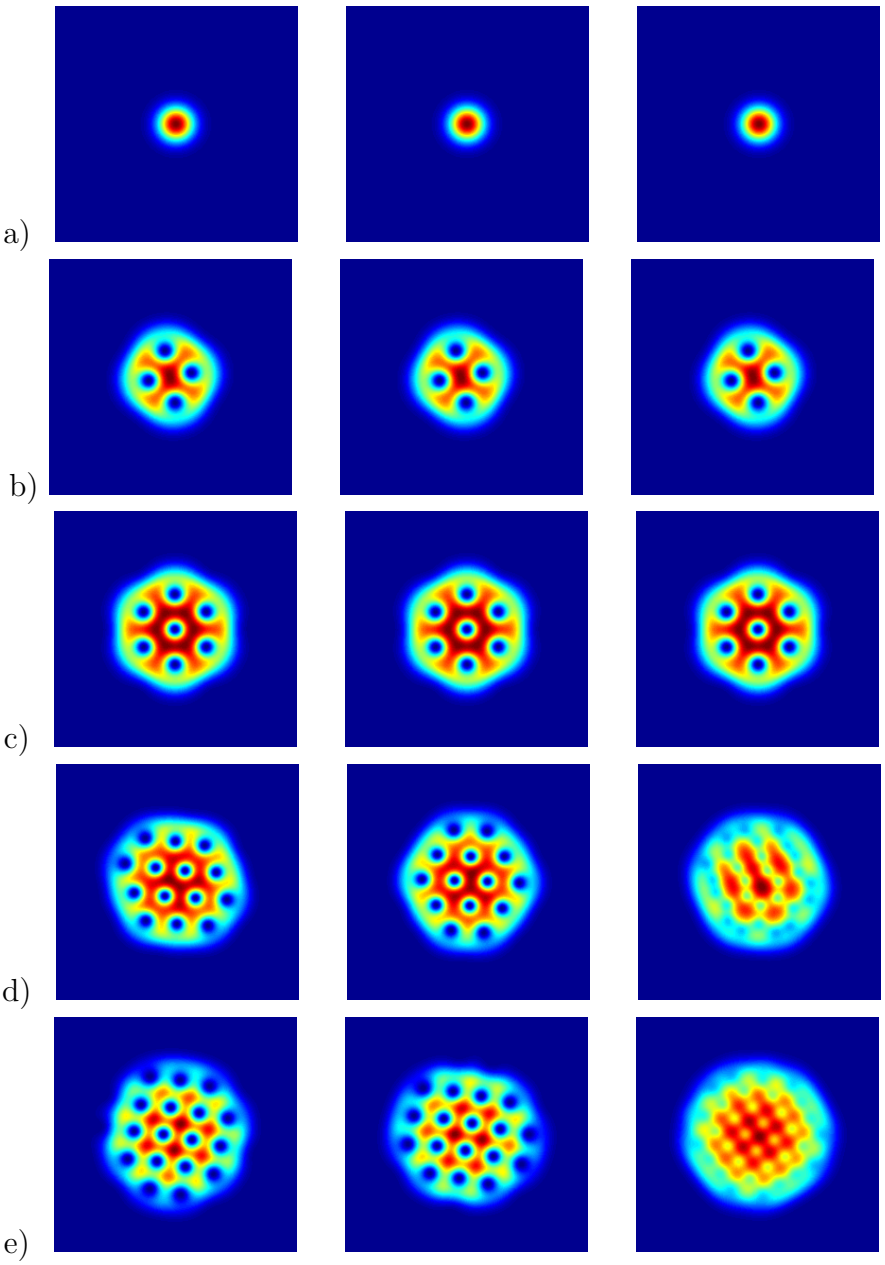

Figure 6.2: Contour plots of the ground state in two-component BEC with different scattering length a_{12}. a)-e): $a_{12} = -1, -0.8, -0.5, 0.1$ and 0.5. Left: $|\phi_{g,1}|^2$; Middle: $|\phi_{g,2}|^2$; Right: $|\phi_{g,1}|^2 + |\phi_{g,2}|^2$.

attractive interaction [58, 118].

ii). When $-1 \leq a_{12} < 0$, the ground states are two identical triangular vortex lattices (cf. Fig. 6.2a−c), i.e. $\phi_{g,1}(\mathbf{x}) \equiv \phi_{g,2}(\mathbf{x})$ for $\mathbf{x} \in \mathbb{R}^2$.

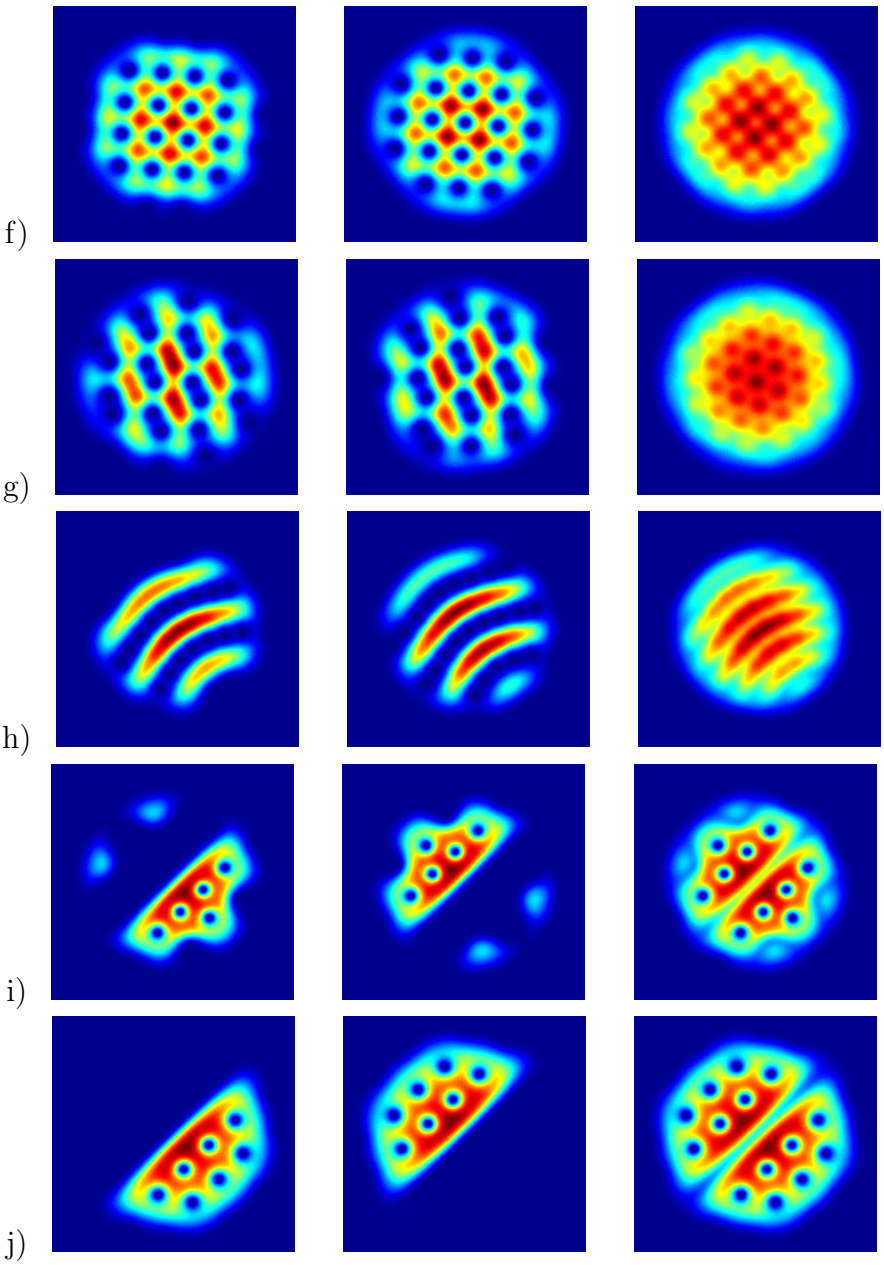

Figure 6.2 (cont'd): f)-j): $a_{12} = 0.8$, 1.0, 1.2, 1.6 and 3.0.

iii). Especially when $a_{12} = 0$, this two-component BEC becomes two independent single-component BECs, and the ground states are two triangular vortex lattices which are exactly the same after the rotation of an angle θ_0.

iv). With the increase of $0 < a_{12} < 1$, the position of vortex cores in one component gradually shifts from those of the other component, and the triangular lattices are

distorted. Eventually, the vortices in each component form a square lattice rather than a triangular one (cf. Fig. 6.2 d−f).

v). When $a_{12} = 1$, two "pair-vortex" lattices are formed, where the lattices in both components are made by pairs of vortices (cf. Fig. 6.2g).

vi). When $a_{12} > 1$ increases, vortices in the same component begin to overlap in lines to from a stripe pattern (cf. Fig. 6.2h). While if a_{12} is large enough, e.g. $a_{12} \geq 1.5$, the densities of two components are symmetrically separated (cf. Fig. 6.2i&j), which is caused by the strongly repulsive interaction between two components.

As we seen in Fig. 6.2a−c, when $-1 \leq a_{12} \leq 0$ the ground state solutions of the two components are exactly the same, so we may make the conjecture that in this case, the two-component BEC may be reduced to single-component BEC, and correspondingly the stationary problem (6.37)−(6.38) becomes

$$\mu\phi(\mathbf{x}) = -\frac{1}{2}\nabla^2\phi + V(\mathbf{x})\phi + \beta|\phi|^2\phi - \Omega L_z\phi, \quad \mathbf{x} \in \mathbb{R}^2, \quad \text{with} \quad \|\phi\|^2 = 1, \tag{6.40}$$

where

$$\mu = \mu_1 = \mu_2, \qquad \beta = \frac{1}{2}(\beta_{11} + \beta_{12}), \qquad V(\mathbf{x}) = V_1(\mathbf{x}) = V_2(\mathbf{x}).$$

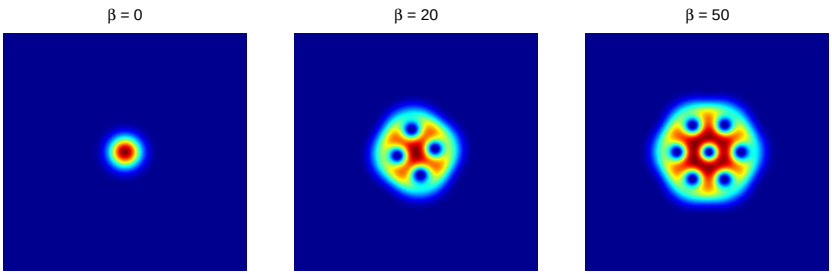

Figure 6.3: Contour plots of ground states in single-component BEC with $\Omega = 0.9$.

To verify our conjecture, Figure 6.3 depicts the contour plots of the ground state in single-component BEC with different β. Comparing Fig. 6.3 with Fig. 6.2a−c, we can see that the ground state solution of single-component BEC is the same as that of two-component BEC with corresponding parameters.

6.2.3 Different ratio of particle numbers N_1^0/N_2^0

By fixing the total particle number $N = N_1^0 + N_2^0$, in this part we study the ground state for different ratio N_1^0/N_2^0. The parameters are chosen as $a_{11} : a_{12} : a_{22} = 1.03 : 0.97 : 0.94$, $\beta_0 = 1000$, $\Omega = 0.9$ and $\gamma_{x,j} = \gamma_{y,j} = 1$ $(j = 1, 2)$.

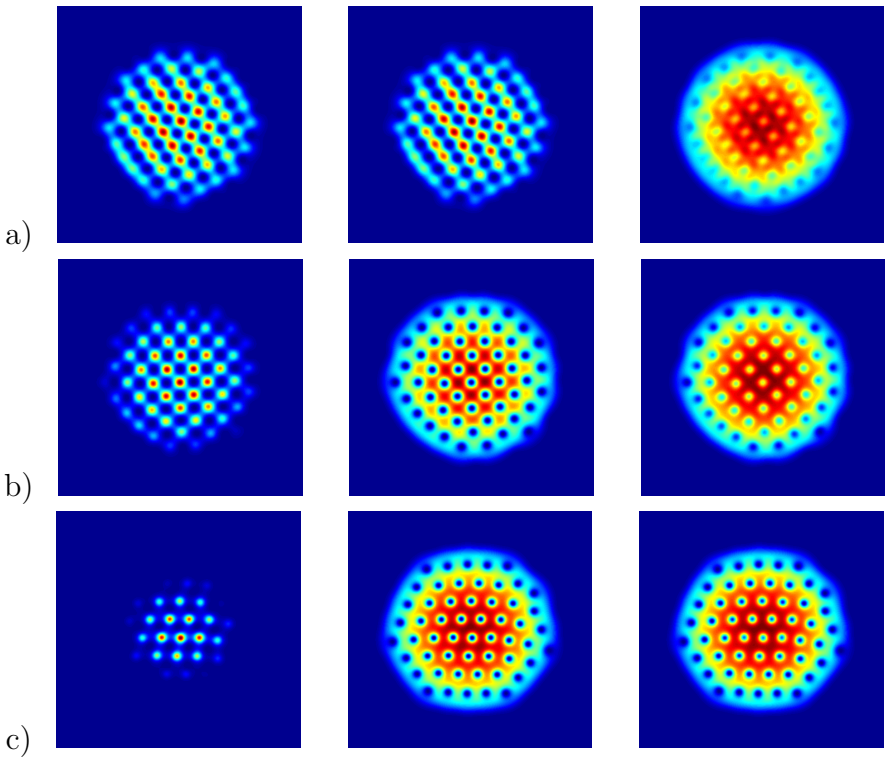

Figure 6.4: Contour plots of the ground state in two-component BEC with different ratio of particle number N_1^0/N_2^0. Left: $|\phi_{g,1}|^2$; Middle: $|\phi_{g,2}|^2$; Right: $|\phi_{g,1}|^2 + |\phi_{g,2}|^2$. a)$-$c): $N_1^0/N_2^0 = 1/2$, $1/5$ and $1/50$.

Figure 6.4 gives the contour plots of the ground states $|\phi_{g,j}|^2$ $(j = 1, 2)$. From it, we can see when $N_1^0 = O(N_2^0)$, e.g. $N_1^0 = N_2^0/2$, the ground states of two components are similar, which are two vortex stripes (cf. Fig. 6.4a). When the ratio N_1^0/N_2^0 decreases, the second component becomes dominant. It changes from a vortex stripe to a square lattice and eventually becomes a triangular lattice just like the ground state of single-component BEC (cf. Fig. 6.4c). The above observation confirms the analysis in Section 6.1.2.

6.2.4 Different trapping potentials

In this part, we study the effect of the trapping potential (6.13) by shifting its center from the origin $(0,0)$ to $(-c_j, c_j)$, i.e.

$$V_j(\mathbf{x}) = \frac{1}{2}\left((x+c_j)^2 + (y-c_j)^2\right), \qquad \mathbf{x} \in \mathbb{R}^2, \quad j = 1,2 \tag{6.41}$$

with c_j a constant. For simplicity, here we choose $c_1 = -c_2 = c \geq 0$. The other parameters are taken as $a_{11} : a_{12} : a_{22} = 1.03 : 1.0 : 0.97$, $\beta_0 = 200$, $\Omega = 0.9$ and $N_1^0 = N_2^0$. For non-rotating two-component BEC, according to [72, 38], if the centers of two potentials are displaced from each other by a distance which is small compared to the size of total condensate, the resulting separation of the centers of the condensate is much larger. While for rotating two-component BEC, there is still no similar result in the literature.

The contour plots of the ground state $|\phi_{g,j}|^2$ $(j = 1,2)$ for different parameter c are shown in Figure 6.5. From it, we can see if the distance $d_{12} = |c_1 - c_2|$ is small, e.g. $d_{12} = 0.02$, the two components are well overlapped, and the two resulting lattices interlock each other. Additionally, in this case the vortex pairs are preferred to form. When the distance d_{12} increases, the overlapping part gradually decreases. For example, when $d_{12} = 1$ the densities of the two components are well separated but there still exists a small "connecting" part due to the intercomponent interaction. Furthermore, comparing Fig. 6.5 with Fig. 6.2i&j, we can find that increasing the scattering length $a_{12} > \max\{a_{11}, a_{22}\}$ can have similar effects to those from increasing the distance between two potential centers.

6.3 Dynamics of two-component BEC

In this section, we first introduce some important quantities characterizing the dynamics of two-component BEC and derive dynamical laws for them. Then we propose an efficient and accurate numerical method for computing the dynamics of rotating two-component BEC with an external driven field, and apply this method

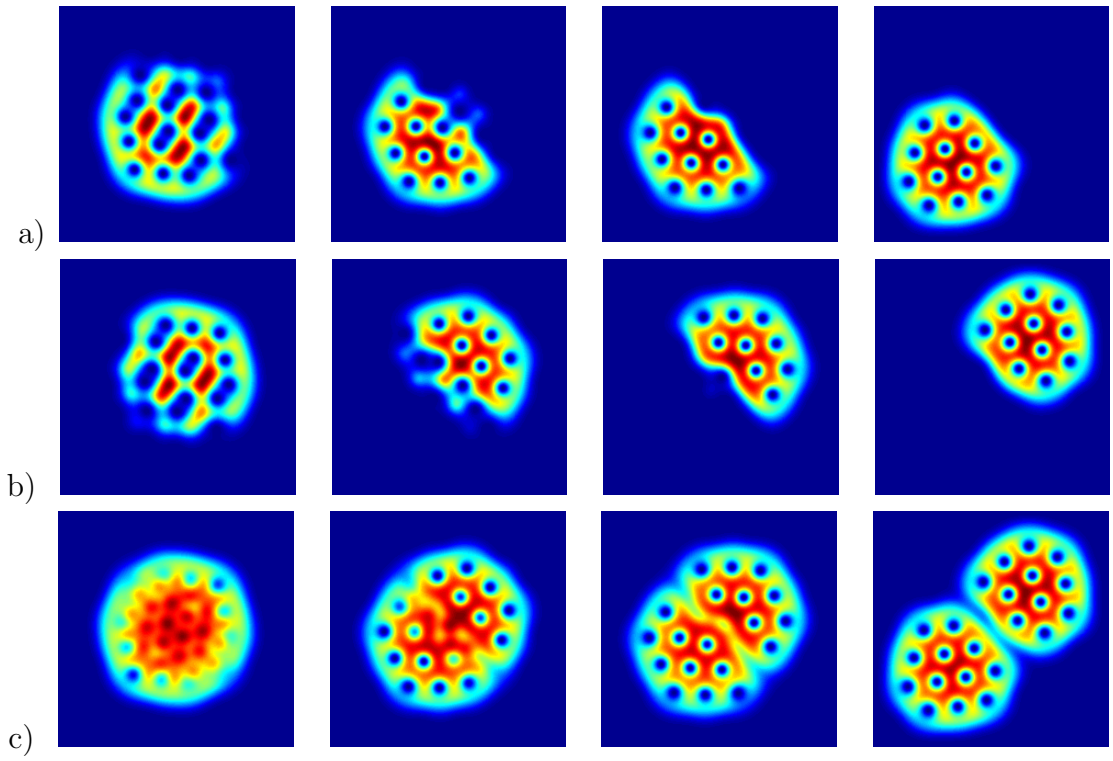

Figure 6.5: Contour plots of the ground state in two-component BEC with different trapping potentials (6.41). Left−right: $c = 0.01$, 0.1, 0.2 and 0.5. a). $|\phi_{g,1}|^2$; b). $|\phi_{g,2}|^2$; c). $|\phi_{g,1}|^2 + |\phi_{g,2}|^2$.

to verify the dynamical laws and also to study the dynamics of vortex lattices.

6.3.1 Dynamical laws

As we known, when $\lambda = 0$ in (6.10), the density of each component is conserved as specified in (6.18). When $\lambda \neq 0$, we have the following lemmas for the density of each component:

Lemma 6.1. Suppose $(\psi_1(\mathbf{x}, t), \psi_2(\mathbf{x}, t))$ is the solution of the CGPEs (6.10)−(6.11); then we have for $j = 1, 2$,

$$\frac{d^2 N_j(t)}{dt^2} = -2\lambda^2 \left[2N_j(t) - 1\right] + F_j(t), \qquad t \geq 0 \tag{6.42}$$

with initial conditions

$$N_j(0) = N_j^{(0)} = \int_{\mathbb{R}^d} |\psi_j^0(\mathbf{x})|^2 \, d\mathbf{x} = \frac{N_j^0}{N}, \tag{6.43}$$

$$\dot{N}_j(0) = N_j^{(1)} = 2\lambda \int_{\mathbb{R}^d} \mathrm{Im}\left[\psi_j^0(\mathbf{x}) \left(\psi_{k_j}^0(\mathbf{x})\right)^*\right] \, d\mathbf{x}; \tag{6.44}$$

where for $t \geq 0$,

$$F_j(t) = \lambda \int_{\mathbb{R}^d} \left(\psi_j^* \psi_{k_j} + \psi_j \psi_{k_j}^*\right) \Big[V_{k_j}(\mathbf{x}) - V_j(\mathbf{x}) \\ -(\beta_{jj} - \beta_{k_j j})|\psi_j|^2 + (\beta_{k_j k_j} - \beta_{j k_j})|\psi_{k_j}|^2\Big] d\mathbf{x}, \quad t \geq 0.$$

Proof. The proof is omitted here. □

By solving (6.42)−(6.44), we have

Lemma 6.2. (i) If the external trapping potentials are the same and the inter-/intra-component s-wave scattering lengths in (6.10) are the same, i.e.

$$V_1(\mathbf{x}) = V_2(\mathbf{x}) \quad \mathbf{x} \in \mathbb{R}^d, \qquad \text{and} \quad \beta_{11} = \beta_{12} = \beta_{22} \text{ (i.e. } a_{11} = a_{12} = a_{22}), \tag{6.45}$$

for any initial data $(\psi_1^0(\mathbf{x}), \psi_2^0(\mathbf{x}))$, we have, for $t \geq 0$,

$$N_j(t) = \|\psi_j(\cdot, t)\|^2 = \left(N_j^{(0)} - \frac{1}{2}\right) \cos(2\lambda t) + \frac{N_j^{(1)}}{2\lambda} \sin(2\lambda t) + \frac{1}{2}, \quad j = 1, 2. \tag{6.46}$$

Thus in this case, the density of each component is a periodic function with period $T = \pi/\lambda$ depending only on λ.

(ii) For all other cases, we have, for any $t \geq 0$,

$$N_j(t) = \left(N_j^{(0)} - \frac{1}{2}\right) \cos(2\lambda t) + \frac{N_j^{(1)}}{2\lambda} \sin(2\lambda t) + \frac{1}{2} + f_j(t), \quad j = 1, 2, \tag{6.47}$$

where $f_j(t)$ is the solution of the following second-order ODE:

$$\ddot{f}_j(t) + 4\lambda^2 f_j(t) = F_j(t), \qquad f_j(0) = \dot{f}_j(0) = 0. \tag{6.48}$$

In two-component BEC, we can also define the angular momentum expectation as

$$\langle L_z \rangle(t) = \langle L_z \rangle_1(t) + \langle L_z \rangle_2(t), \qquad t \geq 0, \tag{6.49}$$

where for $j = 1, 2$,

$$\langle L_z\rangle_j(t) = \int_{\mathbb{R}^d} \psi_j^*(\mathbf{x},t) L_z \psi_j(\mathbf{x},t)\, d\mathbf{x} = i\int_{\mathbb{R}^d} \psi_j^*(\mathbf{x},t)(y\partial_x - x\partial_y)\psi_j(\mathbf{x},t)\, d\mathbf{x}. \quad (6.50)$$

In fact, when $\lambda = 0$, due to the conservation of the density of each component, $N\langle L_z\rangle_j(t)/N_j^0$ is the angular momentum expectation of the jth component. For the dynamics of the angular momentum expectation in rotating two-component BEC, we have the following lemmas:

Lemma 6.3. Suppose $(\psi_1(\mathbf{x},t), \psi_2(\mathbf{x},t))$ is the solution of the CGPEs (6.10)−(6.11); then we have,

$$\begin{aligned}\frac{d\langle L_z\rangle_j(t)}{dt} &= \left(\gamma_{x,j}^2 - \gamma_{y,j}^2\right)\int_{\mathbb{R}^d} xy|\psi_j|^2\, d\mathbf{x} - \beta_{jk_j}\int_{\mathbb{R}^d} |\psi_j|^2(x\partial_y - y\partial_x)|\psi_{k_j}|^2\, d\mathbf{x} \\ &\quad -2\lambda\ \mathrm{Re}\left[\int_{\mathbb{R}^d} \psi_{k_j}^*(x\partial_y - y\partial_x)\psi_j\, d\mathbf{x}\right], \quad t \geq 0, \quad j = 1, 2. \end{aligned} \quad (6.51)$$

Furthermore, if the traps in (6.13) are radially symmetric in 2D, and resp. cylindrically symmetric in 3D, i.e. $\gamma_{x,1} = \gamma_{y,1}$ and $\gamma_{x,2} = \gamma_{y,2}$, then we have
i). For any given initial data $(\psi_1^0(\mathbf{x}), \psi_2^0(\mathbf{x}))$ in (6.11), the total angular momentum expectation is conserved, i.e.

$$\langle L_z\rangle(t) \equiv \langle L_z\rangle(0) = -\sum_{j=1}^{2}\int_{\mathbb{R}^d} \left(\psi_j^0(\mathbf{x})\right)^* L_z\psi_j^0(\mathbf{x})\, d\mathbf{x}, \qquad t \geq 0. \quad (6.52)$$

In addition, the energy for non-rotating part is also conserved, i.e.

$$\begin{aligned} E_n(\psi_1,\psi_2) &:= \int_{\mathbb{R}^d}\sum_{j=1}^{2}\left[\frac{1}{2}|\nabla\psi_j|^2 + V_j(\mathbf{x})|\psi_j|^2 + \sum_{l=1}^{2}\frac{\beta_{jl}}{2}|\psi_j|^2|\psi_l|^2 - 2\lambda\mathrm{Re}(\psi_1^*\psi_2)\right] d\mathbf{x} \\ &\equiv E_n\left(\psi_1^0,\psi_2^0\right), \qquad t \geq 0. \end{aligned} \quad (6.53)$$

ii). Suppose the initial data $\psi_j^0(\mathbf{x})$ $(j = 1, 2)$ in (6.11) is chosen as

$$\psi_j^0(\mathbf{x}) = f_j(r)e^{im_j\theta} \quad \text{with} \quad m_j \in \mathbb{Z} \quad \text{and} \quad f_j(0) = 0 \quad \text{when} \quad m_j \neq 0, \quad (6.54)$$

in 2D, and resp. in 3D,

$$\psi_j^0(\mathbf{x}) = f_j(r,z)e^{im_j\theta} \quad \text{with} \quad m_j \in \mathbb{Z} \quad \text{and} \quad f_j(0,z) = 0 \quad \text{when} \quad m_j \neq 0. \quad (6.55)$$

If $\lambda = 0$, then $\langle L_z\rangle_j(t)$ $(j = 1, 2)$ is also conserved, i.e.

$$\langle L_z\rangle_j(t) \equiv \langle L_z\rangle_j(0) = \int_{\mathbb{R}^d} \left(\psi_j^0(\mathbf{x})\right)^* L_z\psi_j^0(\mathbf{x})\, d\mathbf{x}, \quad t \geq 0, \;\; j = 1, 2. \tag{6.56}$$

The condensate width of a two-component BEC can be defined as

$$\sigma_\xi(t) = \sqrt{\delta_\xi(t)} = \sqrt{\delta_{\xi,1}(t) + \delta_{\xi,2}(t)}, \qquad \xi = x, y, \text{ or } z, \tag{6.57}$$

where

$$\delta_{\xi,j}(t) = \langle \xi^2\rangle_j(t) = \int_{\mathbb{R}^d} \xi^2 |\psi_j(\mathbf{x}, t)|^2\, d\mathbf{x}, \qquad t \geq 0, \qquad j = 1, 2. \tag{6.58}$$

Then in 2D with radially symmetric traps, we have the following lemma:

Lemma 6.4. In 2D with radially symmetrical traps, i.e. $d = 2$ and $\gamma_{x,1} = \gamma_{y,1} = \gamma_{x,2} = \gamma_{y,2} := \gamma_r$ in (6.10), if there is no external driven field, i.e. $\lambda = 0$ in (6.10), for any given initial data $(\psi_1^0(\mathbf{x}), \psi_2^0(\mathbf{x}))$ in (6.11), we have, for $t \geq 0$,

$$\delta_r(t) = \frac{E(\psi_1^0, \psi_2^0) + \Omega\langle L_z\rangle(0)}{\gamma_r^2}\left[1 - \cos(2\gamma_r t)\right] + \delta_r^{(0)}\cos(2\gamma_r t) + \frac{\delta_r^{(1)}}{2\gamma_r}\sin(2\gamma_r t), \tag{6.59}$$

where $\delta_r(t) = \delta_x(t) + \delta_y(t)$, $\delta_r^{(0)} := \delta_x(0) + \delta_y(0)$ and $\delta_r^{(1)} := \dot\delta_x(0) + \dot\delta_y(0)$. Furthermore, if the initial data satisfies (6.54), we have, for any $t \geq 0$,

$$\begin{aligned} \delta_x(t) &= \delta_y(t) = \frac{1}{2}\delta_r(t) \qquad (6.60)\\ &= \frac{E\left(\psi_1^0, \psi_2^0\right) + \Omega\langle L_z\rangle(0)}{2\gamma_r^2}[1 - \cos(2\gamma_r t)] + \delta_x^{(0)}\cos(2\gamma_r t) + \frac{\delta_x^{(1)}}{2\gamma_r}\sin(2\gamma_r t). \end{aligned}$$

Thus in this case, the condensate widths $\sigma_r(t)$, $\sigma_x(t)$ and $\sigma_y(t)$ are periodic functions with frequency doubling the trapping frequency.

Similar to Lemma 4.4, in rotating two-component BEC, when $\lambda = 0$ we have,

Lemma 6.5. If the initial data $(\psi_1^0(\mathbf{x}), \psi_2^0(\mathbf{x}))$ in (6.11) is chosen as

$$\psi_1^0(\mathbf{x}) = \phi_1^e(\mathbf{x} - \mathbf{x}_1^0), \quad \psi_2^0(\mathbf{x}) = \phi_2^e(\mathbf{x} - \mathbf{x}_2^0), \qquad \mathbf{x} \in \mathbb{R}^d, \tag{6.61}$$

where $\mathbf{x}_1^0$ and $\mathbf{x}_2^0$ are two given points in $\mathbb{R}^d$, when $\lambda = 0$, $\mathbf{x}_1^0 = \mathbf{x}_2^0 := \mathbf{x}^0$ and $V_1(\mathbf{x}) \equiv V_2(\mathbf{x})$, then the exact solution of the CGPEs (6.10)−(6.11) satisfies

$$\psi_j(\mathbf{x}, t) = \phi_j^e(\mathbf{x} - \mathbf{x}(t))e^{-i\mu_j^e t}e^{iw_j(\mathbf{x},t)}, \quad \mathbf{x} \in \mathbb{R}^d, \quad t \geq 0, \quad j = 1, 2, \tag{6.62}$$

where for any $t \geq 0$, $w_j(\mathbf{x}, t)$ is a linear function of $\mathbf{x}$, i.e. for $j = 1, 2$

$$w_j(\mathbf{x}, t) = \mathbf{c}_j(t) \cdot \mathbf{x} + g_j(t), \quad \mathbf{c}_j(t) = (c_{j,1}(t), \cdots, c_{j,d}(t))^T, \quad \mathbf{x} \in \mathbb{R}^d, \quad t \geq 0, \tag{6.63}$$

and $\mathbf{x}(t)$ satisfies the second-order ODE system (4.28)−(4.31).

Remark 6.1. When the two shifted centers at $t = 0$ are different or the trapping potentials are different, i.e. $\mathbf{x}_1^0 \neq \mathbf{x}_2^0$ or $V_1(\mathbf{x}) \neq V_2(\mathbf{x})$, our numerical results show that, in general, there isn't such an analytical construction of the solution as in (6.62) for this problem.

6.3.2 Numerical method

By extending the time-splitting type method for rotating single-component BEC, in this section, we present an efficient and accurate method for computing the dynamics of rotating two-component BEC with an external driven field. For simplicity, here we introduce the method for 2D case. Similarly, we truncate the problem (6.10)−(6.11) into a bounded domain and set homogeneous Dirichlet boundary conditions for it,

$$i\frac{\partial \psi_j(\mathbf{x}, t)}{\partial t} = \left[-\frac{1}{2}\nabla^2 + V_j(\mathbf{x}) - \Omega L_z + \sum_{l=1}^{2} \beta_{jl}|\psi_l|^2\right]\psi_j - \lambda\psi_{k_j}, \quad \mathbf{x} \in \Omega_{\mathbf{x}}, \tag{6.64}$$

$$\psi_j(\mathbf{x}, t) = 0, \quad \mathbf{x} \in \Gamma = \partial\Omega_{\mathbf{x}}, \quad t \geq 0, \tag{6.65}$$

$$\psi_j(\mathbf{x}, 0) = \psi_j^0(\mathbf{x}), \quad \mathbf{x} \in \overline{\Omega}_{\mathbf{x}}, \qquad \text{with} \quad \left\|\psi_1^0\right\|^2 + \left\|\psi_2^0\right\|^2 = 1, \tag{6.66}$$

where the computational domain $\Omega_{\mathbf{x}} = \{(x, y) \mid r = \sqrt{x^2 + y^2} \leq R\}$ with R sufficiently large.

Let $\Delta t > 0$ be the time step. From time $t = t_n = n\Delta t$ to $t = t_{n+1} = t_n + \Delta t$, the problem (6.64)−(6.66) can be solved in three splitting steps [11]. One first solves

$$i\partial_t \psi_j(\mathbf{x}, t) = V_j(\mathbf{x})\psi_j + \sum_{l=1}^{2} \beta_{jl}|\psi_l|^2\psi_j, \qquad j = 1, 2, \tag{6.67}$$

for the time step of length Δt, followed by solving

$$i\partial_t \psi_j(\mathbf{x},t) = -\lambda \psi_{k_j}, \qquad j=1,2, \tag{6.68}$$

for the same time step, and then by solving

$$i\partial_t \psi_j(\mathbf{x},t) = -\frac{1}{2}\nabla^2 \psi_j - \Omega L_z \psi_j, \qquad j=1,2, \tag{6.69}$$

for the same time step. For $t \in [t_n, t_{n+1}]$, the ODE (6.67) leaves $|\psi_j(\mathbf{x},t)|$ time invariant, i.e. $|\psi_j(\mathbf{x},t)| = |\psi_j(\mathbf{x},t_n)|$ $(j=1,2)$, and thus it can be integrated exactly to obtain, for $j=1,2$ and $t \in [t_n, t_{n+1}]$,

$$\psi_j(\mathbf{x},t) = \psi_j(\mathbf{x},t_n) \exp\left[-i\left(V_j(\mathbf{x}) + \sum_{l=1}^{2} \beta_{jl} |\psi_l(\mathbf{x},t_n)|^2\right)(t-t_n)\right]. \tag{6.70}$$

By denoting $\Psi = (\psi_1, \psi_2)^T$, we can rewrite the ODE system (6.68) as

$$i\partial_t \frac{\partial \Psi}{\partial t} = -\lambda \mathbf{A}\Psi, \qquad \text{with} \quad \mathbf{A} = \begin{pmatrix} 0 & 1 \\ 1 & 0 \end{pmatrix}. \tag{6.71}$$

Since $\mathbf{A}$ is a real and symmetric matrix, after a simple computation [11], we can obtain the solution of the ODE system (6.68) as

$$\psi_j(\mathbf{x},t) = \psi_j(\mathbf{x},t_n)\cos(\lambda(t-t_n)) + i\psi_{k_j}(\mathbf{x},t_n)\sin(\lambda(t-t_n)), \quad t \in [t_n, t_{n+1}]. \tag{6.72}$$

The equation (6.69) are now decoupled, and thus we can discretize it in r-direction by the finite difference method, in θ-direction by the Fourier pseudospectral method and in time by the Crank-Nicolson scheme. See the detailed scheme in Section 4.4.2. From time $t = t_n$ to $t = t_{n+1}$, we combine the splitting steps via the standard second-order splitting method to get the following scheme:

$$\begin{aligned}
\psi_j^{(1)} &= \psi_j(\mathbf{x},t_n) \exp\left[-\frac{i\Delta t}{2}\left(V_j(\mathbf{x}) + \sum_{l=1}^{2} \beta_{jl} \left|\psi_l(\mathbf{x},t_n)\right|^2\right)\right], \\
\psi_j^{(2)} &= \psi_j^{(1)} \cos\left(\lambda \Delta t/2\right) + i\psi_{k_j}^{(1)} \sin\left(\lambda \Delta t/2\right), \\
\psi_j^{(3)} &= \mathbf{F}\left(\psi_j^{(2)}\right), \\
\psi_j^{(4)} &= \psi_j^{(3)} \cos\left(\lambda \Delta t/2\right) + i\psi_{k_j}^{(3)} \sin\left(\lambda \Delta t/2\right), \\
\psi_j^{n+1} &= \psi_j^{(4)} \exp\left[-\frac{i\Delta t}{2}\left(V_j(\mathbf{x}) + \sum_{l=1}^{2} \beta_{jl} \left|\psi_l^{(4)}\right|^2\right)\right], \qquad j=1,2,
\end{aligned}$$

where $\mathbf{F}(\psi)$ is the discretization operator for the problem (4.101) with the initial data ψ as discussed in Section 4.4.2.

This scheme for rotating two-component BEC is of spectral accuracy in θ-direction and second-order accuracy in r-direction and in time. It is unconditionally stable and conserves the total density in the discretized level.

Remark 6.2. When $\lambda = 0$ in (6.64), in the above second-order Strang splitting method, the steps (ii) and (iv) can be removed, and then the method will consist of three steps. In this case, the density of each component is also conserved in the discretized level.

6.3.3 Numerical results

In this section, we apply our method to verify the dynamical laws in Lemmas 6.1−6.5 and study the dynamics of quantized vortex lattices in rotating two-component BEC. For simplicity of notations, we denote

$$\beta_{11} = \beta_0 \geq 0, \;\; \beta_{12} = a_{12}\beta_0, \;\; \beta_{22} = a_{22}\beta_0 \;\Leftrightarrow\; \beta_{11} : \beta_{12} : \beta_{22} = 1 : a_{12} : a_{22}. \quad (6.73)$$

Example 1. Dynamics of the densities of the two components. To verify the dynamics of the densities $N_j(t) = \|\psi_j(\cdot, t)\|^2$ $(j = 1, 2)$, we take $d = 2$, $\lambda = 1$, $\Omega = 0.6$, $\beta_0 = 500$ and $\gamma_{x,j} = \gamma_{y,j} = 1$ $(j = 1, 2)$. The initial data (6.11) is chosen as

$$\psi_1^0(\mathbf{x}) = \frac{x + iy}{\sqrt{\pi}} \exp\left(-\frac{x^2 + y^2}{2}\right), \qquad \psi_2^0(\mathbf{x}) \equiv 0, \qquad \mathbf{x} \in \mathbb{R}^2. \quad (6.74)$$

In the following, we consider two cases: i). $a_{11} = a_{22} = 1$ $(\Leftrightarrow \beta_{11} = \beta_{12} = \beta_{22})$; ii). $a_{12} = 0.6$ and $a_{22} = 0.8$ $(\Leftrightarrow \beta_{11} \neq \beta_{12} \neq \beta_{22})$. Figure 6.6 shows the time evolution of the densities for these two cases.

From it, we can see that: i). the total density $N(t)$ is conserved in the discrete level for both cases (cf. Fig. 6.6); ii). the densities of each component $N_j(t)$ $(j = 1, 2)$ is a periodic function of period $T = \pi/\lambda = \pi$ when $\beta_{11} = \beta_{12} = \beta_{22}$ (cf. Fig. 6.6a) and respectively a periodic function of period $T = \pi$ with a perturbation when $\beta_{11} \neq \beta_{12} \neq \beta_{22}$ (cf. Fig. 6.6b), which confirms the analytical results in Lemma 6.2.

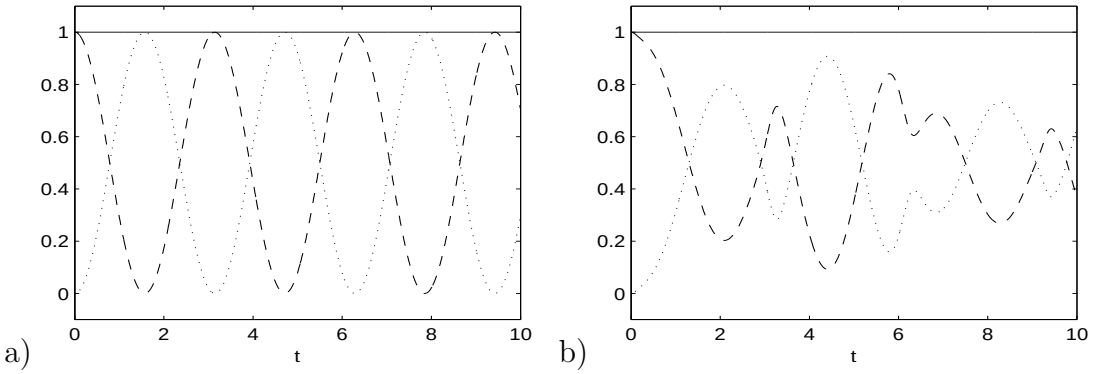

Figure 6.6: Time evolution of the densities $N_1(t) = \|\psi_1(\cdot,t)\|^2$ (dash line), $N_2(t) = \|\psi_2(\cdot,t)\|^2$ (dot line) and $N(t) = N_1(t) + N_2(t)$ (solid line). a). Case i); b). Case ii).

In the following two examples, we study the conservation of angular momentum expectations and the dynamics of condensate widths, respectively. In order to do so, we consider the 2D CGPEs (6.10), and take parameters $a_{12} = 0.97$, $a_{22} = 0.94$ and $\beta_0 = 400$ in (6.73) and $\Omega = 0.6$. The initial data (6.11) is taken as

$$\psi_1^0(\mathbf{x}) = \psi_2^0(\mathbf{x}) = \frac{x+iy}{\sqrt{2\pi}} \exp\left(-\frac{x^2+y^2}{2}\right), \qquad \mathbf{x} \in \mathbb{R}^2, \tag{6.75}$$

which satisfies the form (6.54).

Example 2. Conservation of angular momentum expectations. In this example, we choose the radially symmetric harmonic potentials by setting $\gamma_{x,1} = \gamma_{y,1} = 1$ and $\gamma_{x,2} = \gamma_{y,2} = 1.2$, and at time $t = 0$, we set $\lambda = 0$ or $\lambda = 1$ in (6.10).

Figure 6.7 plots time evolution of the angular momentum expectations. From it, we can see that for either $\lambda = 0$ or $\lambda = 1$, the angular momentum expectation $\langle L_z \rangle(t)$ is always conserved due to the symmetries of the external potential $V_1(\mathbf{x})$ and $V_2(\mathbf{x})$. Furthermore, if $\lambda = 0$, then $\langle L_z \rangle_1(t)$ and $\langle L_z \rangle_2(t)$ are also conserved (cf. Fig. 6.7a), which confirms the conclusions in Lemma 6.3.

Example 3. Dynamics of condensate widths. In this example, we set $\lambda = 0$ and study two cases about the trapping frequencies: i). $\gamma_{x,j} = \gamma_{y,j} = 1$ $(j = 1, 2)$; ii). $\gamma_{x,1} = \gamma_{y,2} = 1$ and $\gamma_{x,2} = \gamma_{y,1} = 1.2$.

Figure 6.8 plots time evolution of the condensate widths for the above two cases.

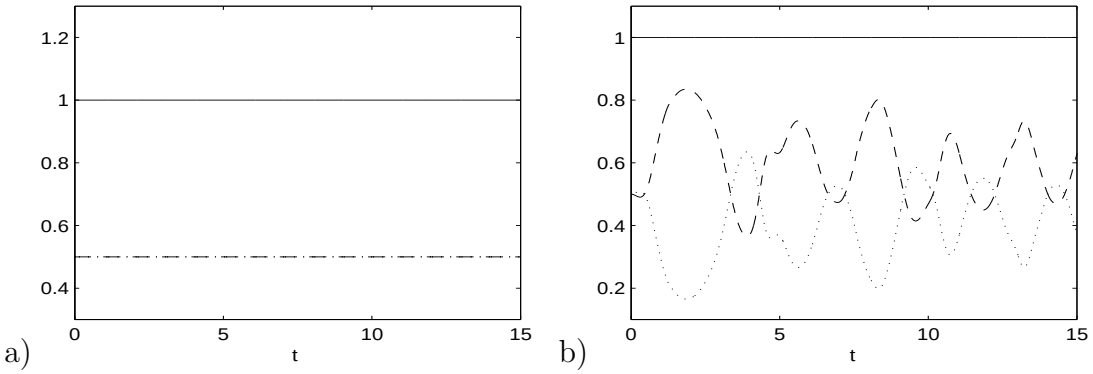

Figure 6.7: Time evolution of the angular momentum expectations $\langle L_z\rangle_1(t)$ (dash line), $\langle L_z\rangle_2(t)$ (dot line) and $\langle L_z\rangle(t)$ (solid line). a). $\lambda = 0$; b). $\lambda = 1$.

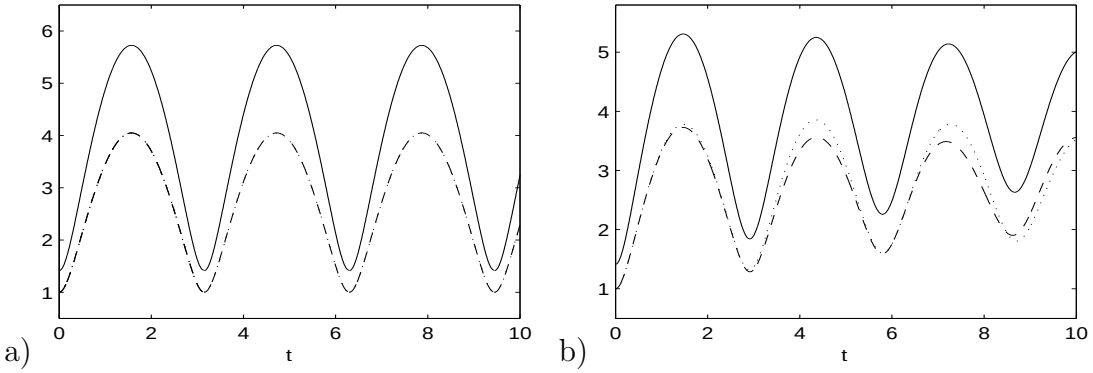

Figure 6.8: Time evolution of the condensate widths $\sigma_x(t)$ (dash line), $\sigma_y(t)$ (dot line) and $\sigma_r(t)$ (solid line). a). Case i); b). Case ii).

From it, we can find when $\gamma_{x,j} = \gamma_{y,j} = 1$ $(j = 1, 2)$, the condensate widths $\sigma_r(t)$, $\sigma_x(t)$ and $\sigma_y(t)$ evolve periodically with the same period $T = \pi/\gamma_x$, which confirms the results (6.59) and (6.60). Otherwise, for case ii), they are periodic functions with a perturbation.

Example 4. Dynamics of stationary states with their centers shifted. In this example, we study the dynamics of stationary states with their centers shifted. In order to do so, we take $\lambda = 0$, $\Omega = 1$ in (6.10), and $a_{12} = 0.97$, $a_{22} = 0.94$ and $\beta_0 = 200$ in (6.73), and then consider the following three cases:

i). with the same traps and the same shifted centers, i.e. $\mathbf{x}_1^0 = \mathbf{x}_2^0 = (1, 1)^T$

and $\gamma_{x,j} = \gamma_{y,j} = 1$ $(j = 1, 2)$;

ii). with the same shifted centers but different traps, i.e. $\mathbf{x}_1^0 = \mathbf{x}_2^0 = (1, 1)^T$ and $\gamma_{x,1} = \gamma_{y,1} = 1$, $\gamma_{x,2} = \gamma_{y,2} = 2$;

iii). with the same traps but different shifted centers, i.e. $\mathbf{x}_1^0 = (1, 1)^T$, $\mathbf{x}_2^0 = (-1, -1)^T$ and $\gamma_{x,j} = \gamma_{y,j} = 1$ $(j = 1, 2)$.

The initial data (6.11) is taken as

$$\psi_j^0(\mathbf{x}) = \phi_j(\mathbf{x} - \mathbf{x}_j^0), \qquad \mathbf{x} \in \mathbb{R}^2, \quad j = 1, 2 \tag{6.76}$$

where $\phi_j(\mathbf{x})$ is the central vortex state solution with winding number $m = 1$ [11], which is computed by using the same parameters in the above cases.

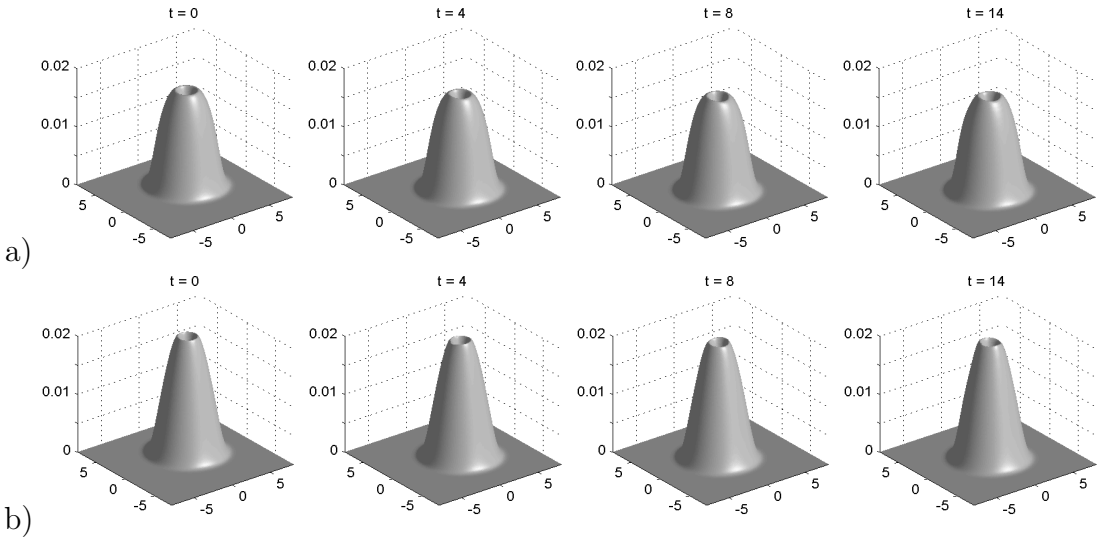

Figure 6.9: Surface plots of $|\psi_j|^2$ at different times in Case i). a). $|\psi_1|^2$; b). $|\psi_2|^2$.

Figures 6.9, 6.11 and 6.12 display the surface plots of $|\psi_j|^2$ at different times for the above three cases respectively. Figure 6.10 depicts the time evolution of the two component centers in Case i). From the surface plots, we can see when $\mathbf{x}_1^0 = \mathbf{x}_2^0$ and $V_1(\mathbf{x}) = V_2(\mathbf{x})$, the stationary states of each component move like solitons, and their shapes do not change during the dynamics (cf. Fig. 6.9). Furthermore, the time evolutions of the two component centers are exactly the same (cf. Fig. 6.10),

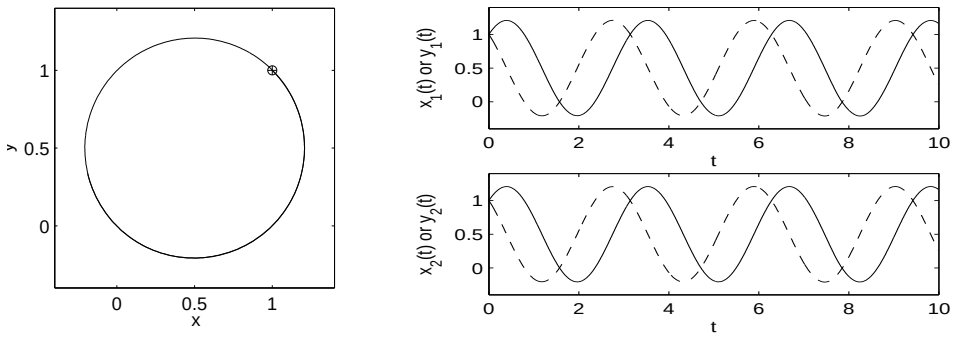

Figure 6.10: Time evolution of the two component centers in Case i) ('+/o': initial location of vortex centers).

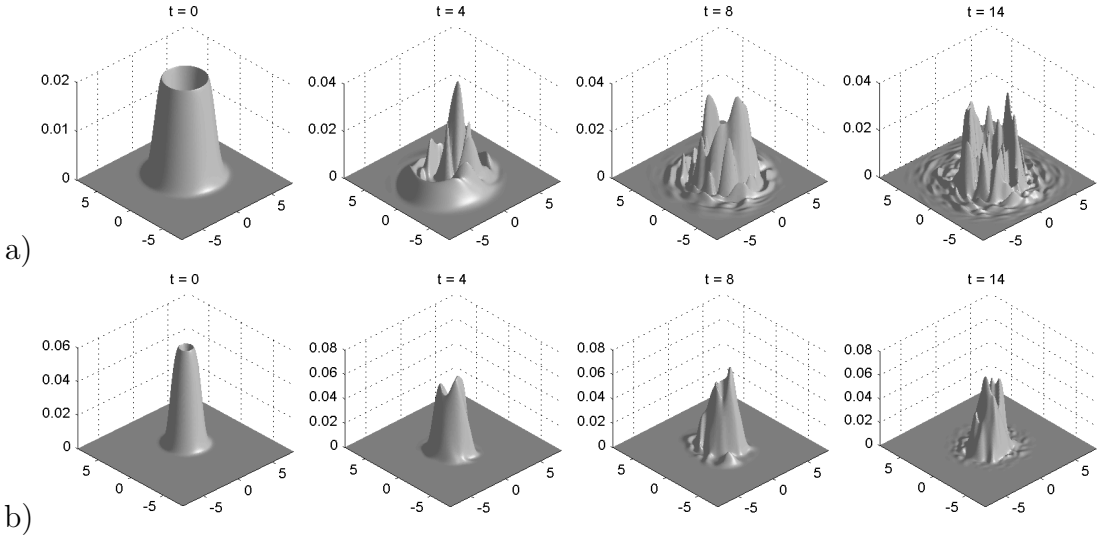

Figure 6.11: Surface plots of $|\psi_j|^2$ at different times in Case ii). a). $|\psi_1|^2$; b). $|\psi_2|^2$.

which satisfy the ODE system (4.28)−(4.30). On the other hand, if $\mathbf{x}_1^0 \neq \mathbf{x}_2^0$ or $V_1(\mathbf{x}) \neq V_2(\mathbf{x})$, the stationary states evolve chaotically (cf. Fig. 6.11, 6.12). This implies that there is no soliton-like construction of the solution in two-component BEC when $\mathbf{x}_1^0 \neq \mathbf{x}_2^0$ or $V_1(\mathbf{x}) \neq V_2(\mathbf{x})$.

Example 5. Dynamics of vortex lattices. In this example, the dynamics of quantized vortex lattices in rotating two-component BEC are studied. Initially, we choose the lattices as the ground states shown in Fig. 6.2f, that is, the parameters used here are $a_{12} = 0.8$, $a_{22} = 1$, $\beta_0 = 200$, $\Omega = 0.9$, $\lambda = 0$ and $\gamma_{x,j} = \gamma_{y,j} = 1$ $(j = 1, 2)$. Then at time $t = 0$, we either set $\lambda = 1$ or change the trapping frequencies

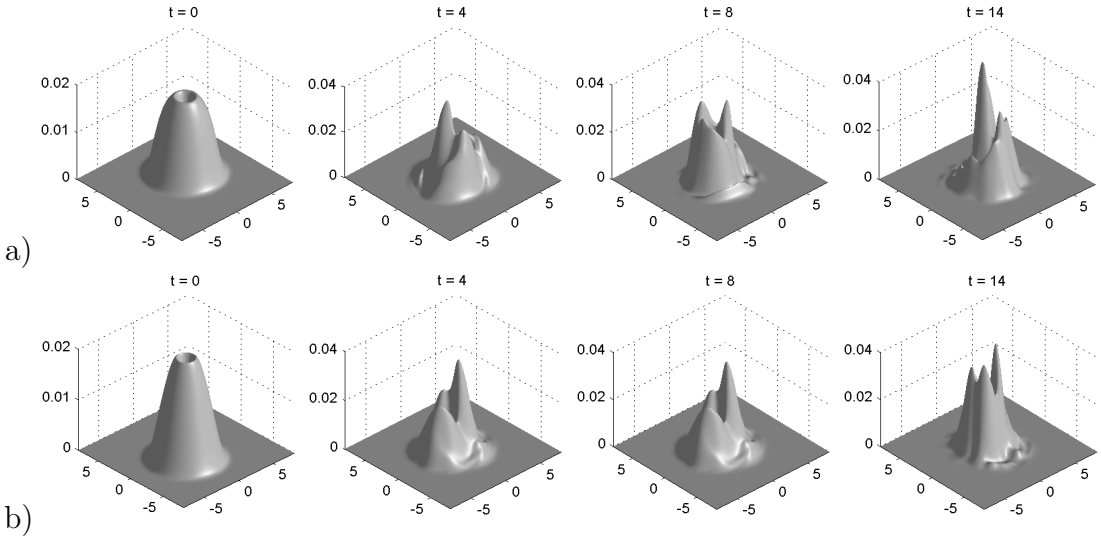

Figure 6.12: Surface plots of $|\psi_j|^2$ at different times in Case iii). a). $|\psi_1|^2$; b). $|\psi_2|^2$.

to $\gamma_{x,1} = \gamma_{y,1} = 0.9$ and $\gamma_{x,2} = \gamma_{y,2} = 1.1$.

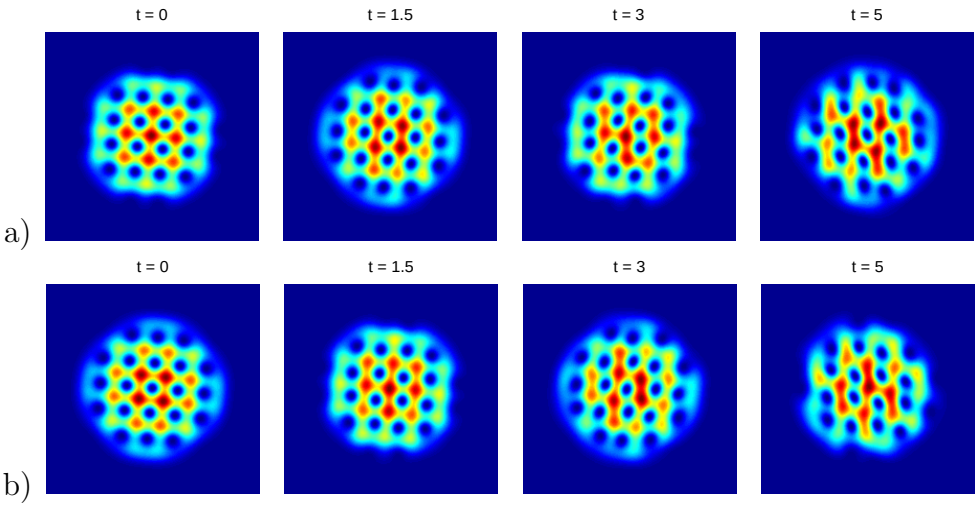

Figure 6.13: Dynamics of the vortex lattices by setting $\lambda = 1$ at $t = 0$. a). $|\psi_1|^2$; b). $|\psi_2|^2$.

Figures 6.13 and 6.14 depict the contour plots of the lattices at different times. From them, we can see when we set $\lambda = 1$, within a short time, the two lattices shift their shapes almost periodically (cf. Fig. 6.13). However, when t is large, their shapes are completely destroyed and can not be recovered. This is caused by the intercomponent interactions. On the other hand, if we change the trapping

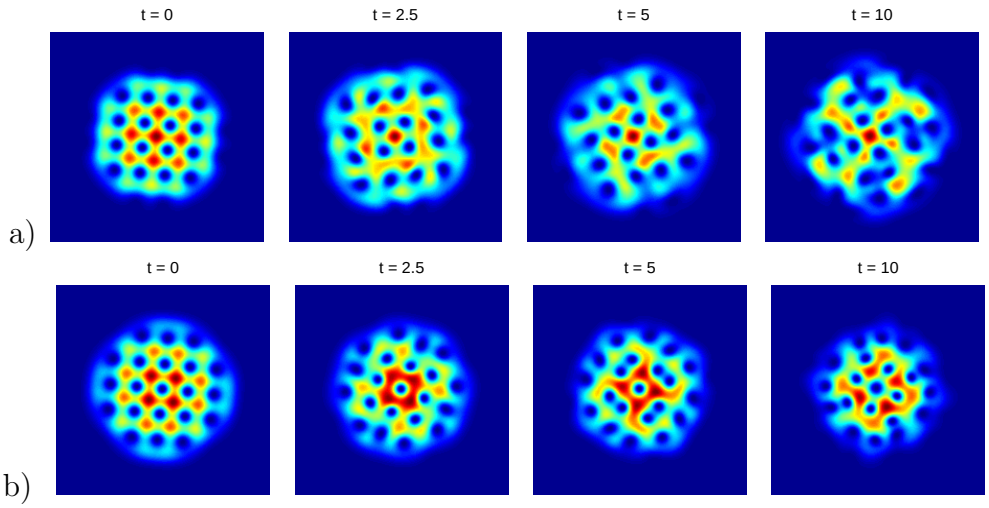

Figure 6.14: Dynamics of the vortex lattices by changing the trapping frequencies from $\gamma_{x,j} = \gamma_{y,j} = 1$ $(j = 1, 2)$ to $\gamma_{x,1} = \gamma_{y,1} = 0.9$ and $\gamma_{x,2} = \gamma_{y,2} = 1.1$. a). $|\psi_1|^2$; b). $|\psi_2|^2$.

frequencies at time $t = 0$, the structures of two lattices are changed, but the number of the vortices in each lattice is always preserved (cf. Fig. 6.14).

Chapter 7

Vortex dynamics in superconductivity and superfluidity

In this chapter, the vortex dynamics and interaction in superconductivity and superfluidity are investigated both analytically and numerically. Starting with the Ginzburg-Landau-Schrödinger equation (GLSE), we review the reduced dynamic laws governing the motion of vortex centers, and solve them analytically under some proper initial data. By extending the numerical method for rotating BEC, we introduce an efficient and accurate method for the GLSE and apply it to numerically study the vortex dynamics and interaction. The numerical results are compared with those from the reduced dynamic laws. Some conclusive experimental findings are obtained, and discussions on numerical and theoretical results are made to provide further understanding of vortex dynamics in the GLSE.

7.1 Ginzburg-Landau-Schrödinger equation

The Ginzburg-Landau-Schrödinger equation (GLSE) is one of the most studied nonlinear equations in the physics community. It describes a vast variety of phenomena from nonlinear waves to the second-order phase transitions, from superconductivity and superfluidity to liquid crystals and strings in the field theory. A specific form

of the GLSE we study here is given by:

$$(\alpha - i\beta)\partial_t \psi(\mathbf{x}, t) = \nabla^2 \psi + \frac{1}{\varepsilon^2}\left(V_0(\mathbf{x}) - |\psi|^2\right)\psi, \qquad \mathbf{x} \in \mathbb{R}^2, \quad t > 0, \tag{7.1}$$

$$\psi(\mathbf{x}, 0) = \psi_0(\mathbf{x}), \qquad \mathbf{x} \in \mathbb{R}^2 \tag{7.2}$$

with nonzero far field conditions

$$|\psi(\mathbf{x}, t)| \to 1 \text{ (e.g. } \psi \to e^{im\theta}), \quad t \geq 0, \quad \text{when } r = |\mathbf{x}| = \sqrt{x^2 + y^2} \to \infty, \tag{7.3}$$

where $\psi(\mathbf{x}, t)$ is a complex-valued wave function (or order parameter), $m \in \mathbb{Z}$ is a given integer, $V_0(\mathbf{x})$ is a real-valued external potential satisfying $\lim_{|\mathbf{x}|\to\infty} V_0(\mathbf{x}) \to 1$, $\varepsilon > 0$ is a constant, and α, β are two nonnegative constants satisfying $\alpha + \beta > 0$.

The GLSE (7.1) covers many nonlinear equations arising in various different applications. For example, when $\alpha = 1$ and $\beta = 0$, it collapses to the nonlinear heat equation (NLHE), also known as the Ginzburg-Landau equation (GLE) [105, 106]. The GLE with a complex order parameter is well known for modelling superconductivity [3, 49, 53, 50, 94], while that with a real order parameter, corresponding to the so called Allen-Cahn equation, is often used to study the phase transition [51]. When $\alpha = 0$ and $\beta = 1$, the GLSE reduces to the nonlinear Schrödinger equation (NLSE) [105, 108, 97, 6] for modelling, for example, superfluidity or BEC. While $\alpha > 0$ and $\beta > 0$, it is the complex Ginzburg-Landau equation (CGLE) or NLSE with a damping term [13, 14], which also arises in the study of the hydrodynamic instability [10].

The boundary condition (7.3) allows one to introduce the notation $\deg \psi$, i.e. degree of ψ, as an index (winding number) of ψ at ∞, considered as a vector field on $\mathbb{R}^2$, i.e.

$$\deg\, \psi = \frac{1}{2\pi} \int_{|\mathbf{x}|=R} d(\arg\, \psi), \tag{7.4}$$

for R sufficiently large. Based on (7.4), we can introduce the rescaled free energy or Lyapunov functional relative to (7.1), i.e.

$$E(\psi) = \int_{\mathbb{R}^2} \left[|\nabla \psi|^2 - \frac{(\deg\, \psi)^2}{|\mathbf{x}|^2} \chi(|\mathbf{x}|) + \frac{1}{\varepsilon^2}\left(V_0(\mathbf{x}) - |\psi|^2\right)^2 \right] d\mathbf{x}, \quad t \geq 0, \tag{7.5}$$

where $\chi(r)$ is a smooth positive function on $[0,\infty)$ vanishing at $r=0$ and converging to 1 as $r\to\infty$ [91]. Then the GLSE (7.1) can be written as

$$(\alpha - i\beta)\partial_t\psi(\mathbf{x},t) = -\frac{\delta E(\psi)}{\delta\psi^*}. \tag{7.6}$$

From (7.6), we can see when $\alpha > 0$, the GLSE is a dissipative system and the free energy decreases when time t increases, i.e. $\frac{dE(\psi)}{dt} \le 0$. On the other hand, when $\alpha = 0$, it is a dispersive system and also it is time reversible and time transverse invariant. Furthermore, it admits at least two important invariants: the **rescaled density**

$$\|\psi(\cdot,t)\|^2 := \int_{\mathbb{R}^2} \left[|\psi(\mathbf{x},t)|^2 - |\psi_0(\mathbf{x})|^2\right]\, d\mathbf{x} = 0, \qquad t \ge 0 \tag{7.7}$$

and the **rescaled free energy**

$$E(\psi(\cdot,t)) = E(\psi(\cdot,0)) = E(\psi_0), \qquad t \ge 0. \tag{7.8}$$

7.2 Stationary vortex states

To study stationary vortex states of the GLSE (7.1), we consider the following time-independent GLSE with $\varepsilon = 1$ and $V_0(\mathbf{x}) \equiv 1$ [105]:

$$\nabla^2\phi(\mathbf{x}) + \left(1 - |\phi(\mathbf{x})|^2\right)\phi(\mathbf{x}) = 0, \qquad \mathbf{x}\in\mathbb{R}^2, \tag{7.9}$$

$$|\phi(\mathbf{x})| \to 1, \qquad \text{when} \quad |\mathbf{x}|\to\infty\,, \tag{7.10}$$

where $\phi(\mathbf{x})$ is a complex-valued function and can be viewed as the steady state solution of the GLSE (7.1). Similar to (5.1), the vortex state solution $\phi_m(\mathbf{x})$ takes the form

$$\phi_m(\mathbf{x}) = f_m(r)\, e^{im\theta}, \qquad \mathbf{x} = (r\cos\theta, r\sin\theta)^T \in \mathbb{R}^2, \tag{7.11}$$

where $m\in\mathbb{Z}$ is called as winding number or index, and $f_m(r)$ is a real-valued function satisfying

$$\frac{1}{r}\frac{d}{dr}\left(r\frac{df_m(r)}{dr}\right) - \frac{m^2}{r^2}f_m(r) + \left(1 - f_m^2(r)\right)f_m(r) = 0, \qquad 0 < r < \infty, \tag{7.12}$$

$$f_m(0) = 0, \qquad f_m(r) = 1, \quad \text{when} \quad r\to\infty. \tag{7.13}$$

The asymptotic behavior of $f_m(r)$ as $r \to 0$ and $r \to \infty$ can be estimated by [105]

$$f_m(r) \sim \begin{cases} a\, r^{|m|} + O\left(r^{|m|+2}\right), & \text{as} \quad r \to 0, \\ 1 - \dfrac{m^2}{2r^2} + O\left(\dfrac{1}{r^4}\right), & \text{as} \quad r \to \infty, \end{cases} \tag{7.14}$$

where a is a constant.

To find the numerical solution of $f_m(r)$, we can truncate the problem (7.12)−(7.13) into a bounded interval $r \in [0, R]$ with R sufficiently large and set the artificial boundary condition $f_m(R) = 1$ at $r = R$. Then we discretize (7.12) by using the second-order finite difference method and solve the resulting nonlinear system by the Newton iteration. Note that a shooting method can also be employed to obtain such solutions [87]. Figure 7.1 shows the numerical results of $f_m(r)$ for different winding numbers m, and Figure 7.2 displays surface plots of the vortex states $|\phi_m|^2$ for $m = 1$ and $m = 3$.

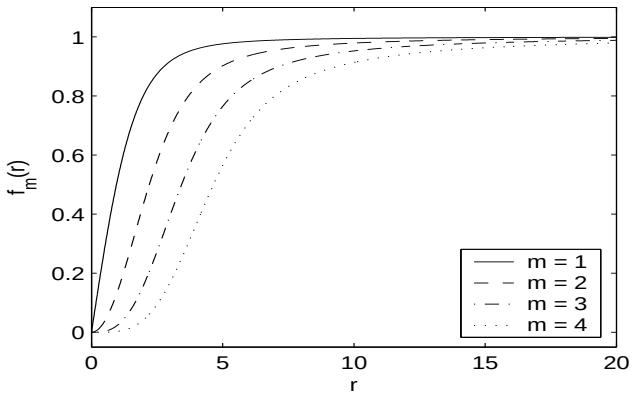

Figure 7.1: Numerical solutions of $f_m(r)$ for different winding numbers m.

Based on our numerical results in Sections 7.6−7.7, we hereby define the core size r_m^0 of a vortex state with winding number m by the condition $f_m(r_m^0) = 0.755$. Table 7.1 lists the core sizes of vortex states with different winding number m, in particular, $r_1^0 \approx 1.75$.

For (7.9)−(7.10) with a specified degree condition, solutions of the form (7.11) are the only vortex state solutions known in the literature, and the question whether there are other symmetry breaking solutions in the whole space remains open. A

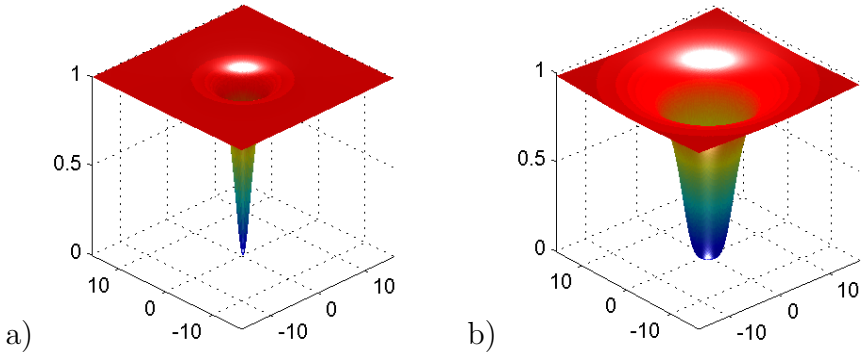

Figure 7.2: Surface plots of the vortex states $|\phi_m|^2$ in GLSE. a). $m = 1$; b). $m = 3$.

winding number	$m = \pm 1$	$m = \pm 2$	$m = \pm 3$	$m = \pm 4$
core size r_m^0	1.7500	3.3674	4.9128	6.4303

Table 7.1: Core sizes of the vortex states with different winding numbers m.

recent exploration of this issue was made in [111].

7.3 Reduced dynamic laws

To study the vortex dynamics of the GLSE, in the literature [105, 106, 97, 81], one always assumes that the vortex states with winding number $m = \pm 1$ are dynamically stable, which can be confirmed by our numerical results in Section 7.5. Thus it is of interest to study the interaction of a few vortices which have winding numbers $m = +1$ or $m = -1$. In order to do so, we take $\varepsilon = 1$ and $V_0(\mathbf{x}) \equiv 1$ in (7.1), and choose the initial data in (7.2) as

$$\psi_0(\mathbf{x}) = \prod_{j=1}^{N} \phi_{m_j}\left(\mathbf{x} - \mathbf{x}_j^0\right) = \prod_{j=1}^{N} \phi_{m_j}\left(x - x_j^0,\, y - y_j^0\right), \qquad \mathbf{x} \in \mathbb{R}^2, \tag{7.15}$$

where N is the total number of vortices, and ϕ_{m_j} is the vortex state in (7.11) with winding number m_j ($m_j = +1$ or -1). That is, we consider the interaction of N vortices by shifting their initial centers from the origin $(0, 0)$ to $\mathbf{x}_j^0 = \left(x_j^0,\, y_j^0\right)^T$ $(1 \le j \le N)$. Take $m = \sum_{j=1}^{N} m_j$ in (7.3) and refer to vortices with the same

winding numbers as like vortices while with different winding numbers as opposite vortices.

It is known that for N well-separated vortices of winding numbers $m_j = \pm 1$ and locations $\mathbf{x}_j$ $(1 \le j \le N)$, the leading asymptotic expansion of the energy is

$$E \sim \sum_{j=1}^{N} E_j - \pi \sum_{j \neq l} m_j \, m_l \ln |\mathbf{x}_l - \mathbf{x}_j| \,, \tag{7.16}$$

where E_j is the self-energy of the vortex at $\mathbf{x}_j$, and the second term corresponds to the well-known Kirchoff-Onsager Hamiltonian. From (7.16), we can obtain the vortex dynamic laws of the induced motion in the leading order, i.e. the adiabatic approximation [105]. For the GLE, i.e. $\alpha = 1$ and $\beta = 0$ in (7.1), the vortex dynamics satisfies,

$$\kappa \mathbf{v}_j(t) := \kappa \frac{d\mathbf{x}_j(t)}{dt} = 2m_j \sum_{l=1,\, l \neq j}^{N} m_l \frac{\mathbf{x}_j(t) - \mathbf{x}_l(t)}{|\mathbf{x}_j(t) - \mathbf{x}_l(t)|^2}, \qquad t \ge 0, \tag{7.17}$$

$$\mathbf{x}_j(0) = \mathbf{x}_j^0, \qquad 1 \le j \le N, \tag{7.18}$$

where κ is a constant determined from the initial setup (7.15). On the other hand, for the NLSE, i.e. $\alpha = 0$ and $\beta = 1$ in (7.1), it satisfies,

$$\mathbf{v}_j(t) := \frac{d\mathbf{x}_j(t)}{dt} = 2 \sum_{l=1,\, l \neq j}^{N} m_l \frac{\mathbf{G}\left(\mathbf{x}_j(t) - \mathbf{x}_l(t)\right)}{|\mathbf{x}_j(t) - \mathbf{x}_l(t)|^2}, \qquad t \ge 0, \tag{7.19}$$

$$\mathbf{x}_j(0) = \mathbf{x}_j^0, \qquad 1 \le j \le N, \tag{7.20}$$

where $\mathbf{G}$ is the symplectic matrix given in (2.54).

When $N = 2$, the nonlinear ODEs (7.17)−(7.18) and (7.19)−(7.20) can be solved analytically and their solutions are presented in the literature [109]. Here we solve them provided that for any $N \ge 2$, initially the vortex centers in (7.15) are located on a circle or its center. Without loss of generality, we assume that the center of this circle is $(0, 0)$ and its radius is $r_0 = a > 0$ with a a constant. For simplicity, we denote θ_0 as a given constant and $m_0 = +1$ or -1, and consider the following four cases for the initial condition in (7.15):

Pattern I. N ($N \geq 2$) like vortices uniformly locate on a circle, i.e. for $1 \leq j \leq N$,

$$\mathbf{x}_j^0 = a\left(\cos\left(\frac{2j\pi}{N} + \theta_0\right),\ \sin\left(\frac{2j\pi}{N} + \theta_0\right)\right)^T, \quad \text{with} \quad m_j = m_0. \tag{7.21}$$

Pattern II. N ($N \geq 3$) like vortices locate on a circle and its center, i.e.

$$\mathbf{x}_N^0 = (0,0)^T, \quad \text{with} \quad m_N = m_0, \tag{7.22}$$

and for $1 \leq j \leq N-1$,

$$\mathbf{x}_j^0 = a\left(\cos\left(\frac{2j\pi}{N-1} + \theta_0\right),\ \sin\left(\frac{2j\pi}{N-1} + \theta_0\right)\right)^T, \quad \text{with} \quad m_j = m_0. \tag{7.23}$$

Pattern III. Two opposite vortices, i.e. for $j = 1, 2$,

$$\mathbf{x}_j^0 = a\left(\cos\left(j\pi + \theta_0\right),\ \sin\left(j\pi + \theta_0\right)\right)^T, \quad \text{with} \quad m_1 = -m_2 = m_0. \tag{7.24}$$

Pattern IV. $N-1$ ($N \geq 3$) like vortices locate on a circle and one opposite vortex locates at its center, i.e.

$$\mathbf{x}_N^0 = (0,0)^T, \quad \text{with} \quad m_N = -m_0, \tag{7.25}$$

and for $1 \leq j \leq N-1$,

$$\mathbf{x}_j^0 = a\left(\cos\left(\frac{2j\pi}{N-1} + \theta_0\right),\ \sin\left(\frac{2j\pi}{N-1} + \theta_0\right)\right)^T, \quad \text{with} \quad m_j = m_0. \tag{7.26}$$

7.3.1 For Ginzburg-Landau equation

Summing (7.17) for $1 \leq j \leq N$, we can get

$$\begin{aligned}
\kappa \sum_{j=1}^{N} \frac{d\mathbf{x}_j(t)}{dt} &= \sum_{j=1}^{N} 2m_j \sum_{l=1, l\neq j}^{N} m_l \frac{\mathbf{x}_j(t) - \mathbf{x}_l(t)}{|\mathbf{x}_j(t) - \mathbf{x}_l(t)|^2} \\
&= 2\sum_{j=1}^{N-1} \sum_{j<l\leq N}^{N} m_j\, m_l \left[\frac{\mathbf{x}_j(t) - \mathbf{x}_l(t)}{|\mathbf{x}_j(t) - \mathbf{x}_l(t)|^2} + \frac{\mathbf{x}_l(t) - \mathbf{x}_j(t)}{|\mathbf{x}_l(t) - \mathbf{x}_j(t)|^2}\right] \\
&= 0, \qquad t \geq 0.
\end{aligned} \tag{7.27}$$

This immediately implies that the mass center of the N vortex centers is conserved for any initial setup in (7.15), i.e.

$$\overline{\mathbf{x}}(t) := \frac{1}{N}\sum_{j=1}^{N}\mathbf{x}_j(t) \equiv \overline{\mathbf{x}}(0) := \frac{1}{N}\sum_{j=1}^{N}\mathbf{x}_j(0) = \frac{1}{N}\sum_{j=1}^{N}\mathbf{x}_j^0, \qquad t \geq 0. \tag{7.28}$$

By considering (7.17), (7.18) and (7.28), we have the following lemmas for the above four patterns:

Lemma 7.1. If the initial data in (7.15) satisfy (7.21), i.e. Pattern I, then the solutions of (7.17)−(7.18) can be given by

$$\mathbf{x}_j(t) = \sqrt{a^2 + \frac{2\,(N-1)}{\kappa}\,t}\left(\cos\left(\frac{2j\pi}{N} + \theta_0\right),\ \sin\left(\frac{2j\pi}{N} + \theta_0\right)\right)^T, \quad t \geq 0, \tag{7.29}$$

for $1 \leq j \leq N$ with $N \geq 2$.

Proof. For simplicity, we first consider the case of $N = 2$. From the ODEs (7.17), we can get

$$\kappa\frac{d\mathbf{x}_1(t)}{dt} = 2\frac{\mathbf{x}_1(t) - \mathbf{x}_2(t)}{|\mathbf{x}_1(t) - \mathbf{x}_2(t)|^2}, \qquad \kappa\frac{d\mathbf{x}_2(t)}{dt} = 2\frac{\mathbf{x}_2(t) - \mathbf{x}_1(t)}{|\mathbf{x}_2(t) - \mathbf{x}_1(t)|^2},$$

which implies that

$$\kappa\frac{d\left[\mathbf{x}_1(t) - \mathbf{x}_2(t)\right]}{dt} = 4\frac{\mathbf{x}_1(t) - \mathbf{x}_2(t)}{|\mathbf{x}_1(t) - \mathbf{x}_2(t)|^2}, \qquad t \geq 0. \tag{7.30}$$

On the other hand, from (7.28), we have

$$\mathbf{x}_1(t) = -\mathbf{x}_2(t), \qquad t \geq 0. \tag{7.31}$$

Inserting (7.31) into (7.30) gives

$$\kappa\frac{d\mathbf{x}_1(t)}{dt} = \frac{\mathbf{x}_1(t)}{|\mathbf{x}_1(t)|^2}, \qquad t \geq 0, \qquad \text{with} \quad \mathbf{x}_1(0) = \mathbf{x}_1^0. \tag{7.32}$$

Solving (7.32) and noticing (7.31), we get when $N = 2$, the solutions of (7.17)−(7.18) are

$$\mathbf{x}_j(t) = \sqrt{a^2 + \frac{2}{\kappa}\,t}\left(\cos\left(j\pi + \theta_0\right),\ \sin\left(j\pi + \theta_0\right)\right)^T, \quad t \geq 0, \ \ j = 1, 2. \tag{7.33}$$

For the cases of $N > 2$, we can generalize the solution (7.33) by assuming

$$\mathbf{x}_j(t) = c(t)\left(\cos\left(\frac{2j\pi}{N}+\theta_0\right),\ \sin\left(\frac{2j\pi}{N}+\theta_0\right)\right)^T, \quad t \geq 0, \quad 1 \leq j \leq N, \quad (7.34)$$

where $c(t)$ is a function of time t and $c(0) = a$. Substituting (7.34) into (7.17), we can obtain

$$c(t) = \sqrt{a^2 + \frac{2(N-1)}{\kappa}\, t}, \qquad t \geq 0. \quad (7.35)$$

Thus the solution (7.29) is a combination of (7.33)−(7.35). □

The results in Lemma 7.1 imply that for any time $t \geq 0$, these N vortices are always located on a circle whose radius depends on time t, i.e. $r(t) = \sqrt{a^2 + 2(N-1)t/\kappa}$.

Lemma 7.2. If the initial data in (7.15) satisfy (7.22)−(7.23), i.e. Pattern II, then the solutions of (7.17)−(7.18) are:

$$\mathbf{x}_N(t) \equiv (0,0)^T, \quad t \geq 0, \quad (7.36)$$

and for $1 \leq j \leq N-1$ with $N \geq 3$,

$$\mathbf{x}_j(t) = \sqrt{a^2 + \frac{2N}{\kappa}\, t}\left(\cos\left(\frac{2j\pi}{N-1}+\theta_0\right),\ \sin\left(\frac{2j\pi}{N-1}+\theta_0\right)\right)^T, \quad t \geq 0. \quad (7.37)$$

Proof. The proof follows the analogous results in Lemma 7.1. □

That is, the vortex initially at the center of the circle does not move for any time $t \geq 0$, and the other $N-1$ ones initially on a circle would always locate on a circle which has a time-dependent radius $r(t) = \sqrt{a^2 + 2Nt/\kappa}$ for $t \geq 0$.

Lemma 7.3. If the initial data in (7.15) satisfy (7.24), i.e. Pattern III, then the solutions of (7.17)−(7.18) can be given by

$$\mathbf{x}_j(t) = \sqrt{a^2 - \frac{2}{\kappa}\, t}\ \left(\cos\left(j\pi+\theta_0\right),\ \sin\left(j\pi+\theta_0\right)\right)^T, \quad 0 \leq t \leq t_c, \quad j = 1, 2, \quad (7.38)$$

where $t_c = \kappa a^2/2$. Solutions (7.38) implies that, when $0 \leq t < t_c$, the two vortices move along a line passing through their initial centers, and their velocities are

$$\mathbf{v}_1(t) = -\mathbf{v}_2(t) = -\frac{2}{\sqrt{\kappa\left(\kappa a^2 - 2\right) t}}\left(\cos\theta_0,\ \sin\theta_0\right)^T, \qquad 0 \leq t < t_c. \quad (7.39)$$

When $t = t_c$, they collide at the origin $(0,0)$.

Proof. The proof follows the analogous results in Lemma 7.1 for $N = 2$. □

Lemma 7.4. If the initial data in (7.15) satisfy (7.25)−(7.26), i.e. Pattern IV, then the solutions of (7.17)−(7.18) are:

$$\mathbf{x}_N(t) \equiv (0,0)^T, \tag{7.40}$$

for $1 \le j \le N-1$ with $N \ge 3$,

$$\mathbf{x}_j(t) = \sqrt{a^2 + \frac{2(N-4)}{\kappa}\, t}\left(\cos\left(\frac{2j\pi}{N-1} + \theta_0\right),\ \sin\left(\frac{2j\pi}{N-1} + \theta_0\right)\right)^T. \tag{7.41}$$

Proof. The proof follows the analogous results in Lemma 7.1. □

From the results in Lemma 7.4, we can draw the following conclusions:

i). During the interaction, the vortex initially at the center does not move.

ii). When $N = 3$, before $t = t_c = \kappa a^2/2$, the other two vortices move towards each other along the line passing through their initial centers, and their velocities are given in (7.39). When $t = t_c$, they collide at the origin $(0, 0)$.

iii). When $N = 4$, all these four vortices would stay at their initial locations for any time $t \ge 0$.

iv). When $N \ge 5$, the $N-1$ vortices initially located on a circle would move outside along the lines which connect their initial centers and the origin. For any time $t \ge 0$, they are always on a circle having radius $r(t) = \sqrt{a^2 + 2(N-4)t/\kappa}$.

7.3.2 For nonlinear Schrödinger equation

Multiplying (7.19) by m_j and summing it for $1 \le j \le N$, we have

$$\begin{aligned}
\sum_{j=1}^{N} m_j \frac{d\mathbf{x}_j(t)}{dt} &= \sum_{j=1}^{N} 2m_j \sum_{l=1,\, l\neq j}^{N} m_l \frac{\mathbf{G}\left(\mathbf{x}_j(t) - \mathbf{x}_l(t)\right)}{|\mathbf{x}_j(t) - \mathbf{x}_l(t)|^2} \\
&= 2\sum_{j=1}^{N-1} \sum_{j<l\le N}^{N} m_j\, m_l \left[\frac{\mathbf{G}\left(\mathbf{x}_j(t) - \mathbf{x}_l(t)\right)}{|\mathbf{x}_j(t) - \mathbf{x}_l(t)|^2} + \frac{\mathbf{G}\left(\mathbf{x}_l(t) - \mathbf{x}_j(t)\right)}{|\mathbf{x}_l(t) - \mathbf{x}_j(t)|^2}\right] \\
&= 0, \qquad t \ge 0\,.
\end{aligned} \tag{7.42}$$

This implies that the signed mass center of the N vortex centers is conserved for any initial setup in (7.15), i.e.

$$\widetilde{\mathbf{x}}(t) := \frac{1}{N}\sum_{j=1}^{N} m_j\,\mathbf{x}_j(t) \equiv \widetilde{\mathbf{x}}(0) := \frac{1}{N}\sum_{j=1}^{N} m_j\,\mathbf{x}_j(0) = \frac{1}{N}\sum_{j=1}^{N} m_j\,\mathbf{x}_j^0, \quad t \geq 0. \quad (7.43)$$

By considering (7.19), (7.20) and (7.43), we have the following lemmas:

Lemma 7.5. If the initial data in (7.15) satisfy (7.21), i.e. Pattern I, then the solutions of (7.19)−(7.20) can be given by

$$\begin{aligned}\mathbf{x}_j(t) \;&=\; a\Bigg(\cos\left(\frac{2j\pi}{N} + \theta_0 + \frac{m_0(N-1)}{a^2}\,t\right),\\ &\qquad \sin\left(\frac{2j\pi}{N} + \theta_0 + \frac{m_0(N-1)}{a^2}\,t\right)\Bigg)^T, \qquad t \geq 0, \end{aligned} \quad (7.44)$$

for $1 \leq j \leq N$ with $N \geq 2$.

Proof. Again for simplicity, we first consider the case of $N = 2$. From (7.19), we have

$$\frac{d\mathbf{x}_1(t)}{dt} = 2m_0\frac{\mathbf{G}\left(\mathbf{x}_1(t) - \mathbf{x}_2(t)\right)}{|\mathbf{x}_1(t) - \mathbf{x}_2(t)|^2}, \qquad \frac{d\mathbf{x}_2(t)}{dt} = 2m_0\frac{\mathbf{G}\left(\mathbf{x}_2(t) - \mathbf{x}_1(t)\right)}{|\mathbf{x}_2(t) - \mathbf{x}_1(t)|^2},$$

which implies that

$$\frac{d\left[\mathbf{x}_1(t) - \mathbf{x}_2(t)\right]}{dt} = 4m_0\frac{\mathbf{G}\left(\mathbf{x}_1(t) - \mathbf{x}_2(t)\right)}{|\mathbf{x}_1(t) - \mathbf{x}_2(t)|^2}, \qquad t \geq 0. \quad (7.45)$$

While from (7.43), we can get

$$\mathbf{x}_1(t) = -\mathbf{x}_2(t), \qquad t \geq 0. \quad (7.46)$$

Plugging (7.46) into (7.45), we obtain the first-order ODE for $\mathbf{x}_1(t)$ as

$$\frac{d\mathbf{x}_1(t)}{dt} = m_0\frac{\mathbf{G}\,\mathbf{x}_1(t)}{|\mathbf{x}_1(t)|^2}, \qquad t \geq 0, \qquad \text{with} \quad \mathbf{x}_1(0) = \mathbf{x}_1^0. \quad (7.47)$$

Solving (7.47) and noticing (7.46), we get the general solutions of $\mathbf{x}_j(t)$ as

$$\mathbf{x}_j(t) = a\left(\cos\left(j\pi + \theta_0 + \vartheta(t)\right),\, \sin\left(j\pi + \theta_0 + \vartheta(t)\right)\right)^T, \quad t \geq 0, \quad j = 1, 2, \quad (7.48)$$

where $\vartheta(t)$ is a function of time t and $\vartheta(0) = 0$. Inserting (7.48) into the ODEs (7.19) and solving them, we obtain $\vartheta(t) = m_0 t/a^2$ and thus give the solutions when $N = 2$ as

$$\mathbf{x}_j(t) = a\left(\cos\left(j\pi + \theta_0 + \frac{m_0}{a^2}t\right),\ \sin\left(j\pi + \theta_0 + \frac{m_0}{a^2}t\right)\right)^T, \quad t \geq 0. \tag{7.49}$$

Generally, for $N \geq 2$, we can assume that the solutions $\mathbf{x}_j(t)$ take the form

$$\mathbf{x}_j(t) = a\left(\cos\left(\frac{2j\pi}{N} + \theta_0 + \vartheta(t)\right),\ \sin\left(\frac{2j\pi}{N} + \theta_0 + \vartheta(t)\right)\right)^T, \quad t \geq 0, \tag{7.50}$$

for $1 \leq j \leq N$. Inserting (7.50) into (7.19)−(7.20), we can obtain $\vartheta(t)$ as

$$\vartheta(t) = \frac{m_0(N-1)}{a^2}\,t, \qquad t \geq 0, \tag{7.51}$$

and combining (7.49)−(7.51) we can immediately get the solutions (7.44). □

The results in Lemma 7.5 imply that in this case, the $N \geq 2$ vortices would always rotate along the circle (counter clockwise if $m_0 = +1$, and clockwise if $m_0 = -1$) with a frequency $\omega(a) = (N-1)/a^2$.

Lemma 7.6. If the initial data in (7.15) satisfy (7.22)−(7.23), i.e. Pattern II, then the solutions of (7.19)−(7.20) are:

$$\mathbf{x}_N(t) \equiv (0,0)^T, \qquad t \geq 0, \tag{7.52}$$

and for $1 \leq j \leq N-1$ with $N \geq 3$,

$$\mathbf{x}_j(t) = a\left(\cos\left(\frac{2j\pi}{N-1} + \theta_0 + \frac{m_0 N}{a^2}\,t\right),\ \sin\left(\frac{2j\pi}{N-1} + \theta_0 + \frac{m_0 N}{a^2}\,t\right)\right)^T. \tag{7.53}$$

Proof. The proof follows the analogous results in Lemma 7.5. □

In this case, the vortex initially at $(0,0)$ does not move, and the other $N-1$ ones would rotate along the circle (counter clockwise if $m_0 = +1$, and clockwise if $m_0 = -1$) with a frequency $\omega(a) = N/a^2$.

Lemma 7.7. If the initial data in (7.15) satisfy (7.24), i.e. Pattern III, then the solutions of (7.19)−(7.20) can be given by

$$\mathbf{x}_j(t) = \mathbf{x}_j^0 + \frac{m_0}{a}\,t\,(-\sin\theta_0,\ \cos\theta_0)^T, \qquad t \geq 0, \quad j = 1, 2. \tag{7.54}$$

This implies that these two opposite vortices move along two parallel lines which are perpendicular to the line passing through the two vortex centers at $t = 0$, and their velocities are

$$\mathbf{v}_1(t) = \mathbf{v}_2(t) = \frac{m_0}{a}\left(-\sin\theta_0,\ \cos\theta_0\right)^T, \qquad t \geq 0. \tag{7.55}$$

Proof. From the conservation of the signed mass center (7.43), we have

$$\widetilde{\mathbf{x}}(t) = \mathbf{x}_1(t) - \mathbf{x}_2(t) \equiv \mathbf{x}_1(0) - \mathbf{x}_2(0) = 2a\left(\cos\theta_0,\ \sin\theta_0\right)^T, \qquad t \geq 0. \tag{7.56}$$

On the other hand, form the ODEs (7.19), we obtain

$$\frac{d\mathbf{x}_1(t)}{dt} = -2m_0\frac{\mathbf{G}\left(\mathbf{x}_1(t) - \mathbf{x}_2(t)\right)}{|\mathbf{x}_1(t) - \mathbf{x}_2(t)|^2}, \qquad \frac{d\mathbf{x}_2(t)}{dt} = 2m_0\frac{\mathbf{G}\left(\mathbf{x}_2(t) - \mathbf{x}_1(t)\right)}{|\mathbf{x}_2(t) - \mathbf{x}_1(t)|^2},$$

which gives

$$\frac{d\left[\mathbf{x}_1(t) + \mathbf{x}_2(t)\right]}{dt} = -4m_0\frac{\mathbf{G}\left(\mathbf{x}_1(t) - \mathbf{x}_2(t)\right)}{|\mathbf{x}_1(t) - \mathbf{x}_2(t)|^2}, \qquad t \geq 0. \tag{7.57}$$

Combining (7.56) and (7.57), we get the following ODE for $\mathbf{x}_1(t)$:

$$\frac{d\mathbf{x}_1(t)}{dt} = -\frac{m_0}{a}\mathbf{G}\left(\cos\theta_0,\ \sin\theta_0\right)^T, \quad t \geq 0, \quad \text{with} \quad \mathbf{x}_1(0) = \mathbf{x}_1^0. \tag{7.58}$$

Solving (7.58) and noticing (7.56), we can obtain (7.54) immediately. Then noticing

$$\mathbf{v}_j(t) = \frac{d\mathbf{x}_j(t)}{dt}, \qquad t \geq 0, \tag{7.59}$$

we can compute their velocities as (7.55). □

Lemma 7.8. If the initial data in (7.15) satisfy (7.25)−(7.26), i.e. Pattern IV, then the solutions of (7.19)−(7.20) are:

$$\mathbf{x}_N(t) \equiv (0,0)^T, \qquad t \geq 0, \tag{7.60}$$

and

$$\mathbf{x}_j(t) = a\Bigg(\cos\left(\frac{2j\pi}{N-1} + \theta_0 + \frac{m_0(N-4)}{a^2}\,t\right), \\ \sin\left(\frac{2j\pi}{N-1} + \theta_0 + \frac{m_0(N-4)}{a^2}\,t\right)\Bigg)^T, \quad 1 \leq j \leq N-1. \tag{7.61}$$

Proof. The proof follows the analogous results in Lemmas 7.5. □

Following the discussion in Lemma 7.4, we can draw the following conclusions:

i). The vortex initially at the center does not move.

ii). When $N = 3$, the two vortices initially located on a circle would rotate along this circle (clockwise if $m_0 = +1$, and counter clockwise if $m_0 = -1$) with a frequency $\omega(a) = 1/a^2$.

iii). When $N = 4$, all these four vortices would stay at their initial locations for any time $t \geq 0$.

iv). When $N \geq 5$, the vortices initially located on a circle would always rotate along this circle with a frequency $\omega(a) = (N-4)/a^2$. However, their rotation directions are different from those when $N = 3$, that is, when $N \geq 5$, the vortices rotate counter clockwise if $m_0 = +1$, and respectively clockwise if $m_0 = -1$.

7.4 Numerical method

In this section, we propose an efficient numerical method for the GLSE by extending the time-splitting type method for rotating BEC. Similarly, in practical implementation, we truncate the problem (7.1)−(7.3) to one defined in a bounded computational domain with inhomogeneous Dirichlet boundary conditions:

$$(\alpha - i\beta)\partial_t \psi(\mathbf{x}, t) = \nabla^2 \psi + \frac{1}{\varepsilon^2}\left[V(\mathbf{x}, t) - |\psi|^2\right]\psi, \qquad \mathbf{x} \in \Omega_R, \quad t \geq 0, \tag{7.62}$$

$$\psi(\mathbf{x}, 0) = \psi_0(\mathbf{x}), \qquad \mathbf{x} \in \overline{\Omega}_R, \tag{7.63}$$

$$\psi(\mathbf{x}, t) = e^{im\theta}, \qquad \mathbf{x} \in \Gamma = \partial\Omega_R, \quad t \geq 0, \tag{7.64}$$

where the computational domain $\Omega_R = \left\{(x, y) \mid r = \sqrt{x^2 + y^2} \leq R\right\}$ with R sufficiently large to assure that the effect of domain truncation remains insignificant, and the external potential $V(\mathbf{x}, t) = V_0(\mathbf{x}) + W(\mathbf{x}, t)$ with $W(\mathbf{x}, t)$ an external driven field satisfying $\lim_{|\mathbf{x}|\to\infty} W(\mathbf{x}, t) = 0$.

Let $\Delta t > 0$ be the time step. From $t_n = n\Delta t$ to $t_{n+1} = t_n + \Delta t$, the GLSE (7.62) is

solved in two splitting steps. One first solves

$$(\alpha - i\beta)\partial_t \psi(\mathbf{x}, t) = \nabla^2 \psi, \tag{7.65}$$

for the time step of length Δt, then followed by solving

$$(\alpha - i\beta)\partial_t \psi(\mathbf{x}, t) = \frac{1}{\varepsilon^2}\left[V(\mathbf{x}, t) - |\psi|^2\right]\psi, \tag{7.66}$$

for the same time step. Following the same lines as (4.102)−(4.107), we can solve (7.66) and get, for $t \in [t_n, t_{n+1}]$,

$$\psi(\mathbf{x}, t) = \psi(\mathbf{x}, t_n)\sqrt{U_n(\mathbf{x}, t)}\exp\left[\frac{i\beta}{\varepsilon^2(\alpha^2+\beta^2)}\left(V_n(\mathbf{x}, t) - \int_{t_n}^{t}\rho(\mathbf{x}, \tau)d\tau\right)\right], \tag{7.67}$$

where $V_n(\mathbf{x}, t) = \int_{t_n}^{t} V(\mathbf{x}, \tau)\, d\tau$ and $\rho(\mathbf{x}, t) = |\psi(\mathbf{x}, t)|^2 = U_n(\mathbf{x}, t)|\psi(\mathbf{x}, t_n)|^2$ with

$$U_n(\mathbf{x}, t) = \frac{\exp\left[\eta V_n(\mathbf{x}, t)\right]}{1 + \eta|\psi(\mathbf{x}, t_n)|^2 \int_{t_n}^{t}\exp\left[\eta V_n(\mathbf{x}, \tau)\right] d\tau}, \qquad \eta = \frac{2\alpha}{\varepsilon^2(\alpha^2+\beta^2)}. \tag{7.68}$$

If $V(\mathbf{x}, t) = V_0(\mathbf{x})$, i.e. $W(\mathbf{x}, t) \equiv 0$, we can integrate (7.67) exactly and obtain

$$\psi(\mathbf{x}, t) = \psi(\mathbf{x}, t_n)\begin{cases} \exp\left[\frac{i}{\varepsilon^2\beta}\left(V_0(\mathbf{x}) - |\psi(\mathbf{x}, t_n)|^2\right)(t - t_n)\right], & \alpha = 0, \\ \sqrt{\widehat{U}_n(\mathbf{x}, t)}\ \exp\left[\frac{i\beta}{2\alpha}\ln\ \widehat{U}_n(\mathbf{x}, t)\right], & \alpha \neq 0, \end{cases} \tag{7.69}$$

where

$$\widehat{U}_n(\mathbf{x}, t) = \begin{cases} \dfrac{1}{1 + \eta|\psi(\mathbf{x}, t_n)|^2(t - t_n)}, & V_0(\mathbf{x}) = 0, \\ \dfrac{V_0(\mathbf{x})}{|\psi(\mathbf{x}, t_n)|^2 + \left(V_0(\mathbf{x}) - |\psi(\mathbf{x}, t_n)|^2\right)\exp(-\eta(t - t_n)V_0(\mathbf{x}))}, & V_0(\mathbf{x}) \neq 0. \end{cases}$$

Remark 7.1. If the function $V_n(\mathbf{x}, t)$ as well as other integrals in (7.67) can not be evaluated analytically, we can approximate them by the numerical quadrature in Remark 4.1.

To solve (7.65), we adopt the polar coordinate so as to match the highly oscillatory boundary condition (7.3) in the transverse direction, and try to formulate it in a variable separable form. Then we discretize it in θ-direction by Fourier pseudospectral method, in time by the Crank-Nicolson (C-N) scheme and in r-direction by

finite element method (FEM) instead of the finite difference method used in Section 4.4.2 so that we can use non-uniform grids in r-direction. With the same expansion as (4.109), i.e.

$$\psi(r,\theta,t) = \sum_{l=-L/2}^{L/2-1} \widehat{\psi}_l(r,t)\, e^{il\theta}, \tag{7.70}$$

where L is an even positive integer and $\widehat{\psi}_l(r,t)$ is the Fourier coefficient for the lth mode, we get, for $-\frac{L}{2} \le l \le \frac{L}{2}-1$,

$$(\alpha - i\beta)\,\partial_t \widehat{\psi}_l(r,t) = \frac{1}{r}\frac{\partial}{\partial r}\left(r\frac{\partial \widehat{\psi}_l(r,t)}{\partial r}\right) - \frac{l^2}{r^2}\widehat{\psi}_l(r,t), \quad 0 < r < R, \tag{7.71}$$

$$\widehat{\psi}_l(0,t) = 0 \quad (\text{for } l \neq 0), \qquad \widehat{\psi}_l(R,t) = \delta_{lm} \quad (\text{for all } l); \tag{7.72}$$

where δ_{lm} is the Kronecker delta satisfying

$$\delta_{lm} = \begin{cases} 1, & l = m, \\ 0, & l \neq m. \end{cases}$$

Let P^k denote all polynomials with degree at most k, $J > 0$ be a chosen integer, $0 = r_0 < r_1 < r_2 < \cdots < r_J = R$ be a partition for the interval $[0, R]$ with a mesh size $h = \max_{0\le j<J}\{r_{j+1} - r_j\}$. Define a finite element space

$$U^h = \left\{u^h \in C[0,R] \mid u^h|_{[r_j,\, r_{j+1}]} \in P^k,\ 0 \le j < J,\ u^h(R) = \delta_{lm}\right\}, \quad \text{for} \quad l = 0,$$

and for $l \neq 0$,

$$U^h = \left\{u^h \in C[0,R] \mid u^h|_{[r_j,\, r_{j+1}]} \in P^k,\ 0 \le j < J,\ u^h(0) = 0,\ u^h(R) = \delta_{lm}\right\}.$$

Then we can obtain the FEM approximation for (7.71)−(7.72) as: Find $\widehat{\psi}_l^h(\cdot,t) \in U^h$ such that for all $\varphi^h \in U^h$ and $t_n \le t \le t_{n+1}$,

$$(\alpha - i\beta)\frac{d}{dt}A\left(\widehat{\psi}_l^h(\cdot,t), \varphi^h\right) = B\left(\widehat{\psi}_l^h(\cdot,t), \varphi^h\right) + l^2 C\left(\widehat{\psi}_l^h(\cdot,t), \varphi^h\right), \tag{7.73}$$

where for $u^h, v^h \in U^h$,

$$A(u^h, v^h) = \int_0^R r u^h(r) v^h(r)\, dr, \qquad B(u^h, v^h) = -\int_0^R r\frac{du^h(r)}{dr}\frac{dv^h(r)}{dr}\, dr,$$

$$C(u^h, v^h) = -\int_0^R \frac{1}{r}\, u^h(r)\, v^h(r)\, dr\ .$$

The ODE system (7.73) can be discretized by the standard Crank-Nicolson scheme and the resulting linear system can be solved by applying fast algorithms.

In practice, we always use the second-order Strang splitting [126] to combine (7.65) and (7.66). For the discretization considered here, the total memory requirement is $O(JL)$ and the total computational cost per time step is $O(JL \ln L)$.

In the following sections, the vortex dynamics, such as stability of quantized vortices, interaction of a few vortices, dynamics of vortex lattices and vortex motion under an inhomogeneous external potential, are numerically investigated.

7.5 Stability of stationary vortex states

In order to study the stability of vortex states in the GLSE, we take $\varepsilon = 1$ and $V_0(\mathbf{x}) \equiv 1$ in (7.62) and choose the initial data (7.63) as

$$\psi_0(\mathbf{x}) = \phi_m(\mathbf{x}) = f_m(r)e^{im\theta}, \qquad \mathbf{x} \in \Omega_R,$$

where $f_m(r)$ is the numerical solution of (7.12)−(7.13) as depicted in Figure 7.1.

As it is commonly accepted that the stability of vortices depends on the type of perturbations, we thus consider two types of perturbations in the following cases:

> Type 1. Small perturbation on the initial data; an example is given by artificially setting $\psi_0(\pm 0.2, 0) = 0$ and choosing $W(\mathbf{x}, t) \equiv 0$ in (7.62);
>
> Type 2. Perturbation on the external potential; an example is given by introducing a far-blue detuned Gaussian laser beam stirrer defined in (4.80).

The numerical results for the GLE under a perturbation on the initial data, i.e. Type 1, are illustrated in Figure 7.3. In comparison, Figure 7.4 shows similar results for the NLSE under a perturbation on the external potential, i.e. Type 2. In addition, Figure 7.5 presents time evolution of the vortex centers, and Figure 7.6 depicts the wave radiation in the same stability study of a vortex state ($m = 2$) of NLSE. In

our implementation, the parameters in (4.80) are chosen as

$$(x_s(t), y_s(t)) \equiv (3, 0), \qquad \omega_s = 1, \qquad W_s(t) = \begin{cases} -5\sin^2(2t), & t \in [0, \pi/2], \\ 0, & t \geq \pi/2. \end{cases}$$

That is, the perturber is only introduced when $t \in [0, \pi/2]$, and when $t > \pi/2$, it is removed.

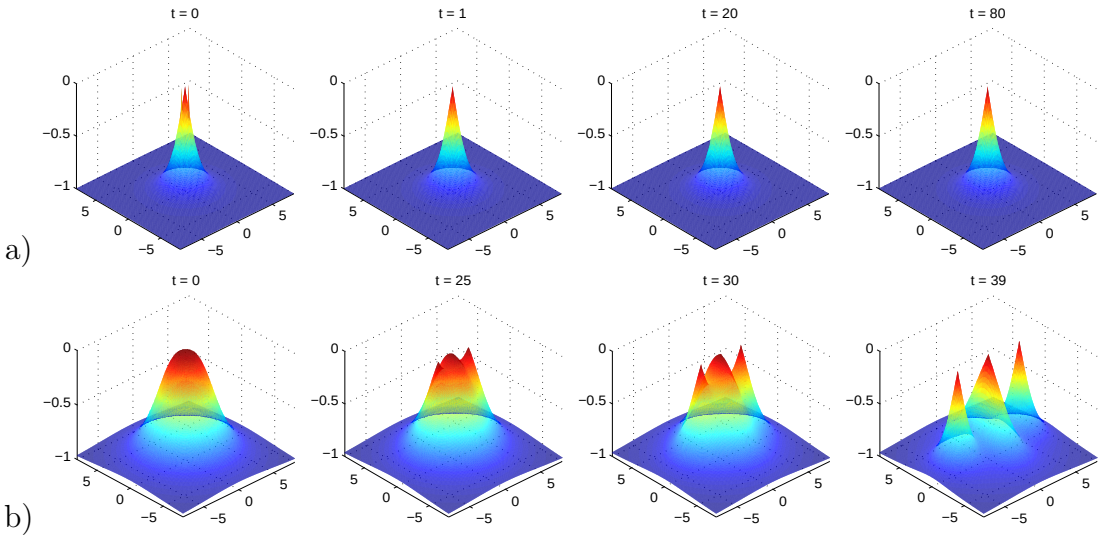

Figure 7.3: Surface plots of $-|\psi|$ at different times for the stability study of vortex states in GLE under Type 1 perturbation. a). $m = 1$; b). $m = 3$.

From Figs. 7.3−7.6 and similar numerical experiments (omitted here for brevity), we may draw the following conclusions for the stability of vortex states in the GLSE: First, the vortex states with winding numbers $m = \pm 1$ are dynamically stable in all three cases, i.e. in GLE, NLSE and CGLE (cf. Fig. 7.3a and Fig. 7.4a). This substantiates the stability assumption used in the studies of such vortex dynamics in the literature for GLE and NLSE [97].

Second, for the vortex states with winding numbers $|m| > 1$, there are two different scenarios. On one hand, for GLE and CGLE, they are dynamically unstable under either Type 1 or Type 2 perturbations (cf. Fig. 7.3b). When t is large, a vortex state initially with winding number m splits into $|m|$ well-separated vortices with winding numbers $+1$ when $m > 0$, and respectively -1 when $m < 0$. The details of the

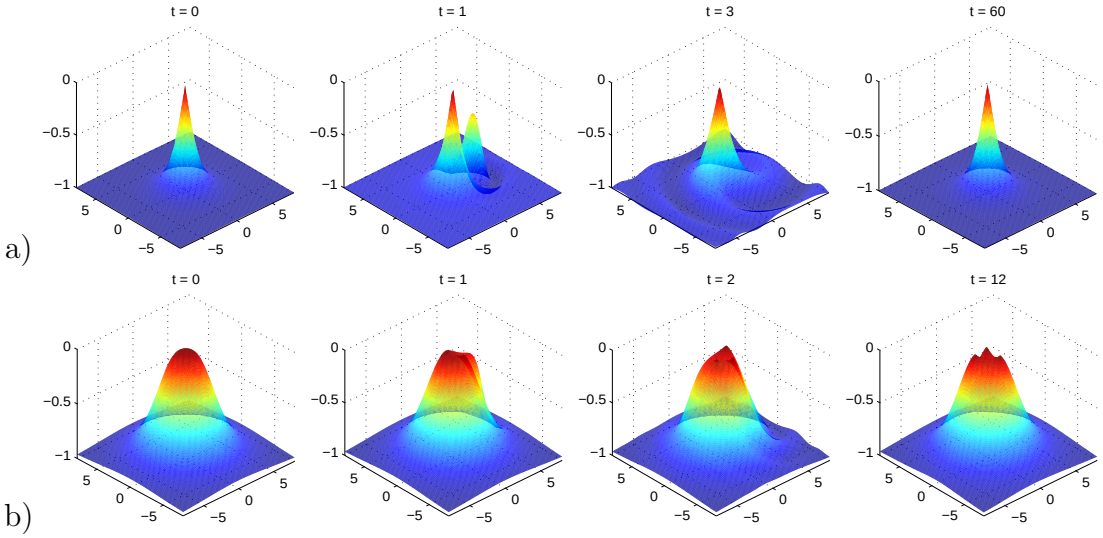

Figure 7.4: Surface plots of $-|\psi|$ at different times for the stability study the vortex states in NLSE under Type 2 perturbation. a). $m = 1$; b). $m = 3$.

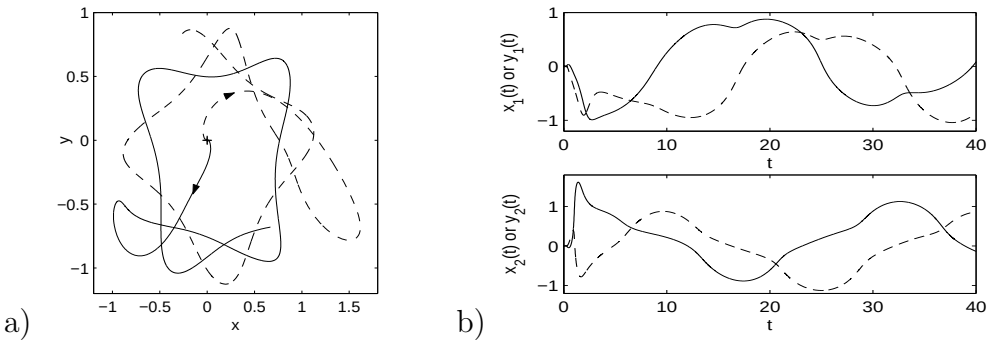

Figure 7.5: Time evolution of the vortex centers in the stability study of the vortex state with $m = 2$ in NLSE under a Type 2 perturbation. a). Trajectory; b). time-evolution of $x(t)$ (solid line) and $y(t)$ (dash line).

splitting and the motion of the $|m|$ separated vortices depend on the perturbation. These results agree very well with those for GLE in the literature [105, 53]. On the other hand, for NLSE, vortex states with winding numbers $|m| > 1$ are dynamically stable under Type 1 perturbation but unstable under Type 2 (cf. Fig. 7.4b). Under a Type 2 perturbation, a vortex state with winding number m splits into $|m|$ vortices, though the cores of these $|m|$ vortices are well overlapped (cf. Fig. 7.4b). We also conducted some studies on the effect of radiation for this set of experiments

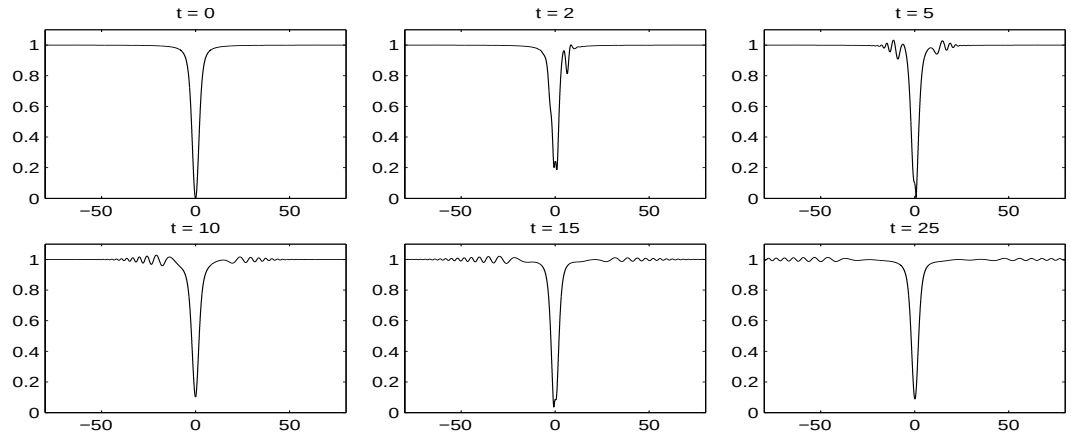

Figure 7.6: Plots of $|\psi(x, 0, t)|$ at different times in the same study as Fig. 7.5.

(cf. Fig. 7.6). It was predicted that, for example in [91], a perturbed vortex with $m = 2$ in NLSE would rotate and emit radiation which carries away energy. The vortex configuration would then make adjustment by finding a configuration of lower energy, that is to say, by splitting up into two $m = 1$ vortices. It is unclear which type of perturbation is implied in [91], but the above prediction is nevertheless consistent with our simulation using a perturbation on the external potential (cf. Figs. 7.5−7.6).

7.6 Interaction of vortices in GLE

To verify the reduced dynamic laws in Lemmas 7.1−7.4, the vortex interactions in GLE are numerically studied with respect to the four initial patterns (7.21)−(7.26). The results are reported only for the case of $m_0 = +1$, and for $m_0 = -1$, they are similar and thus omitted here for brevity.

Patterns I and II. For Pattern I, Figure 7.7 shows time evolution of the vortex centers for different N, and especially for $N = 2$, Figure 7.8 displays the surface plots of $-|\psi|$ at different times. Figure 7.9 shows time evolution of the vortex centers in Pattern II. From them and our additional results, we can draw the following conclusions:

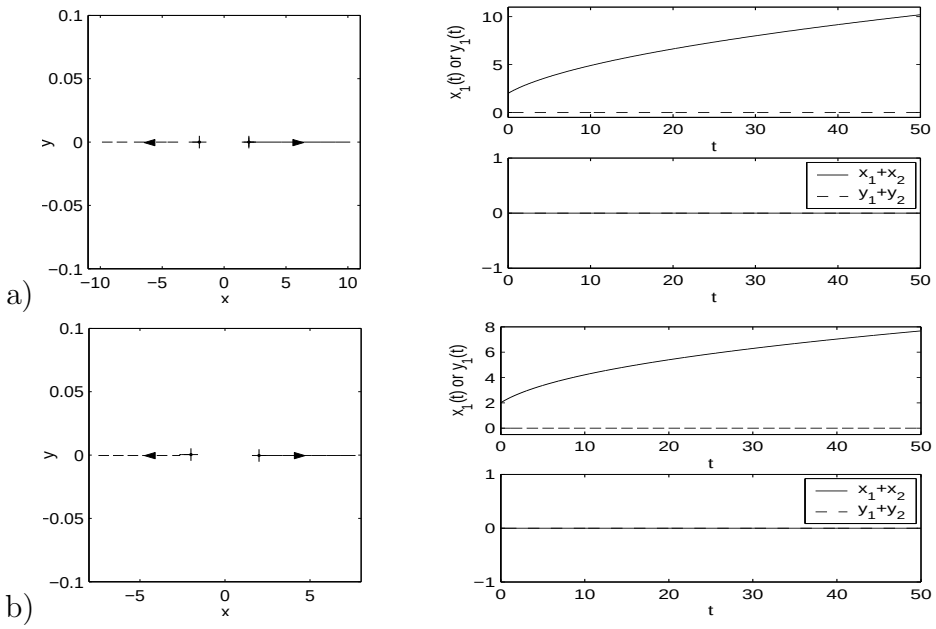

Figure 7.7: Time evolution of the vortex centers in GLE for Pattern I with $a = 2$. From the reduced dynamic laws with $\kappa = 1$ (a&c) and direct simulations of GLE (b&d). Case I: $N = 2$.

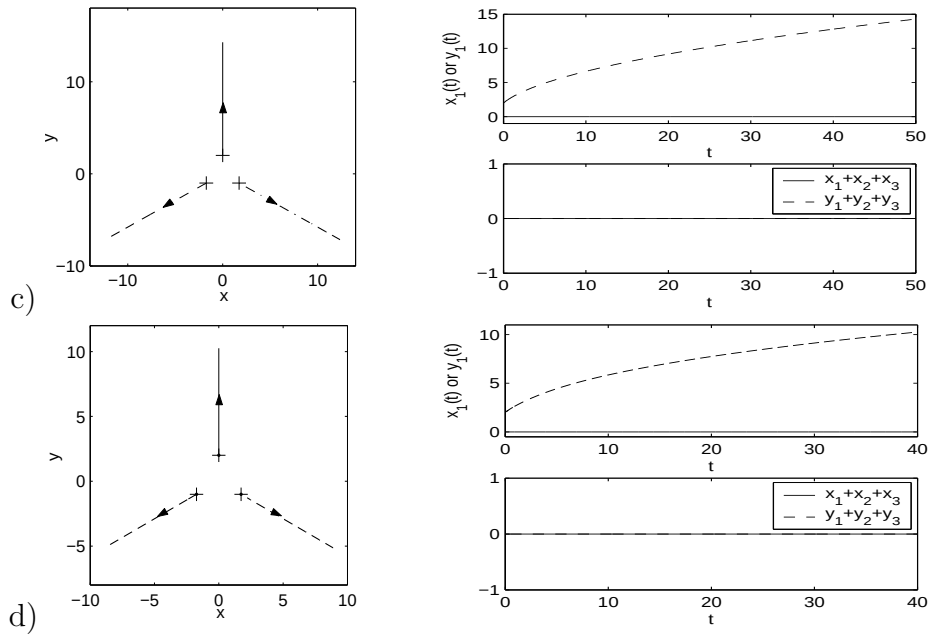

Figure 7.7 (cont'd): Case II: $N = 3$.

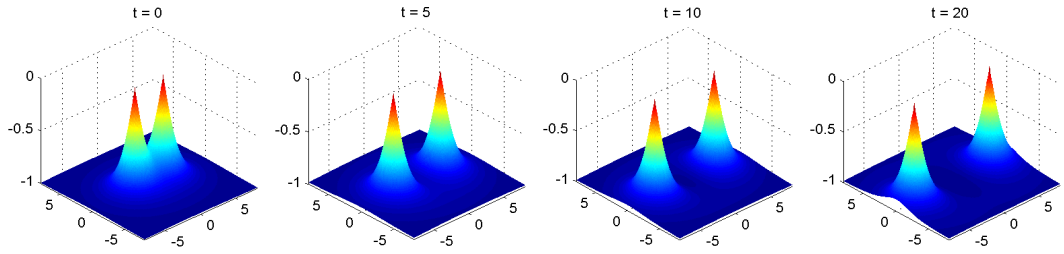

Figure 7.8: Surface plots of $-|\psi|$ at different times in GLE for Pattern I with $N = 2$.

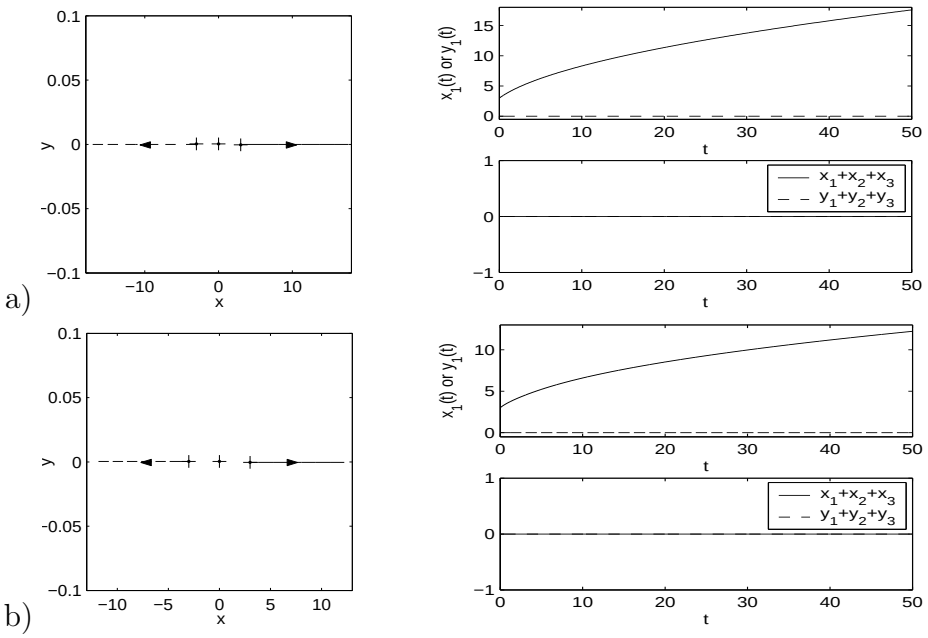

Figure 7.9: Time evolution of the vortex centers in GLE for Pattern II with $a = 3$. From the reduced dynamic laws with $\kappa = 1$ (a&c) and direct simulations of GLE (b&d). Case I: $N = 3$.

i). The mass center of the vortex centers is conserved for any time $t \geq 0$, which confirms the dynamic law in (7.28).

ii). Vortices with the same winding numbers undergo repulsive interactions and they never collide. Their speeds depend on their distances to the origin, i.e. the larger is the distance, the slower is the motion. In Pattern II, the vortex initially at the origin $(0, 0)$ does not move during the dynamics.

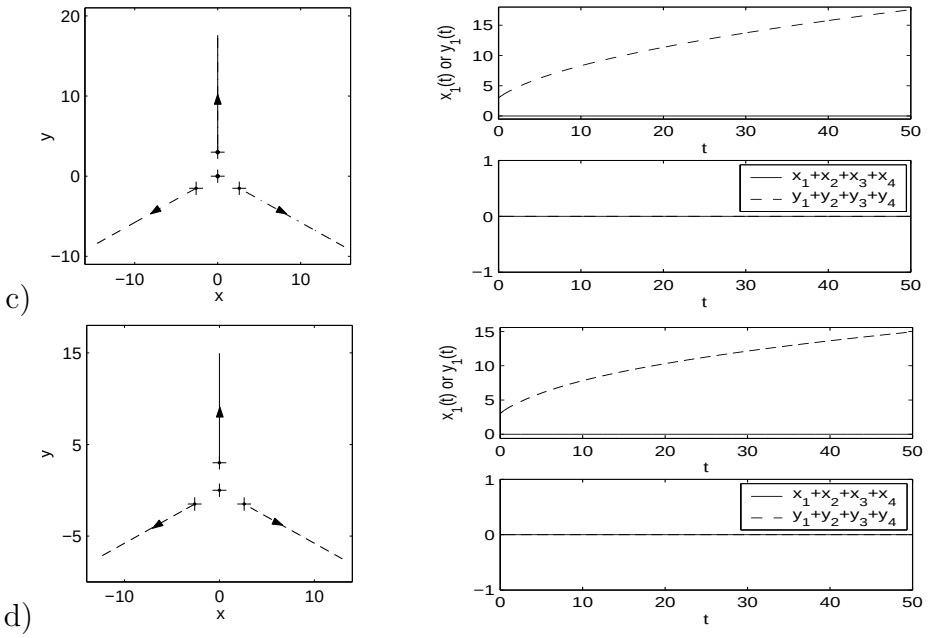

Figure 7.9 (cont'd): Case II: $N = 4$.

iii). Vortices initially located on a circle would move outside along the lines passing through their initial centers and the origin, and the symmetry of their initial locations is preserved for any $t \geq 0$, i.e. they are always on a circle which has a time-dependent radius $r(t)$ (cf. Fig. 7.7b&d, 7.9b&d).

v). The solutions of the reduced dynamic laws agree with our numerical results if a proper κ is chosen, which depends on the initial setup in (7.15). For example, we numerically find that in Pattern I with $N = 2$, if $a = 3$, then $\kappa \approx 1.6411$, while if $a = 6$, $\kappa \approx 1.7080$.

Pattern III. In this pattern, we study the interaction of two vortices with opposite winding numbers. Figure 7.10 shows time evolution of the two vortex centers, and Figure 7.11 displays the surface plots of $-|\psi|$ at different times.

From them, we can draw the following conclusions:

i). The mass center of the two vortex centers is conserved before they collide, which confirms the dynamic law in (7.28).

ii). Two opposite vortices undergo an attractive interaction, and they move along

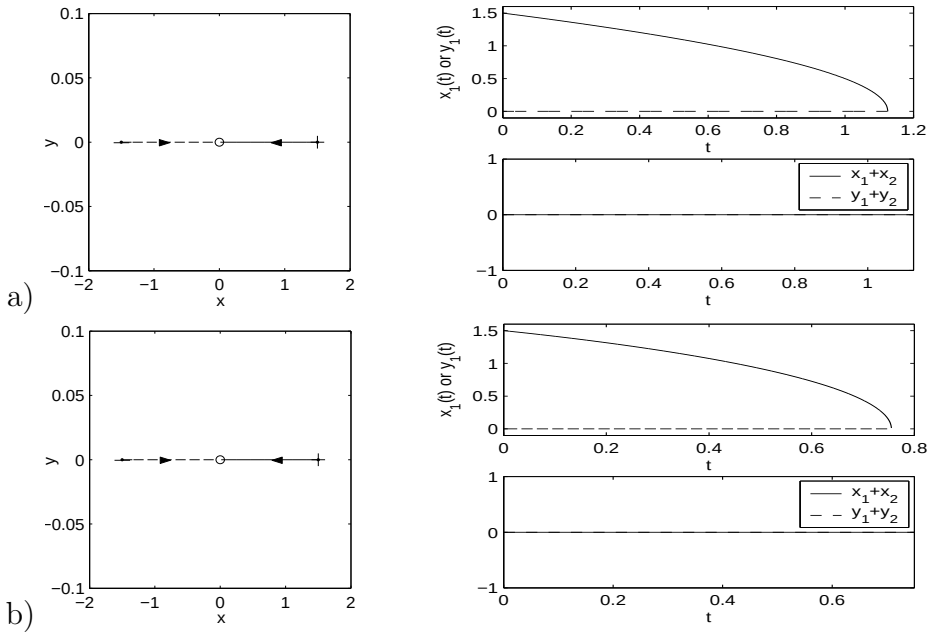

Figure 7.10: Time evolution of the two vortex centers in GLE for Pattern III with $a = 1.5$, where 'o' is the collision point. From the reduced dynamic laws with $\kappa = 1$ (a) and direct simulations of GLE (b).

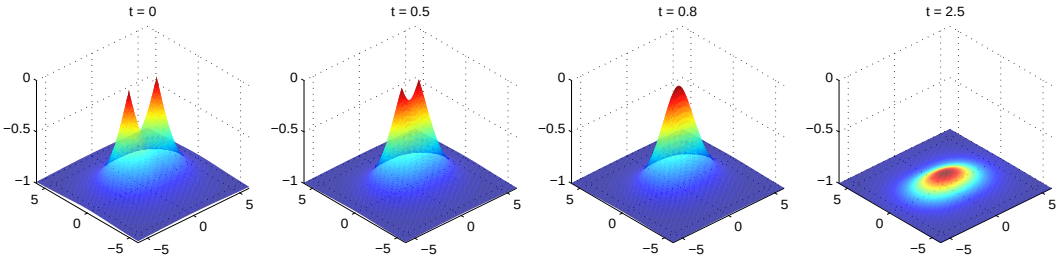

Figure 7.11: Surface plots of $-|\psi|$ at different times in GLE for Pattern III.

the lines passing through their initial centers (cf. Fig. 7.10, 7.11). Their speeds depend on their distance, i.e. the larger is the distance, the smaller is the speed.

iii). At a critical time $t_c > 0$, the two vortices would collide at the origin $(0, 0)$, and the collision time t_c can be numerically approximated by

$$t_c \approx \frac{1}{14.8710}\, d_0^{2.0715}, \qquad \text{with} \quad d_0 = 2a. \tag{7.74}$$

Immediately, (7.74) implies that $t_c = O\left(a^2\right)$, which confirms the analytical results in Lemma 7.3.

iv). The solutions of the reduced dynamic laws agree with our numerical results if we choose proper κ, which depends on the initial distance of the two vortex centers.

Pattern IV. According to Lemma 7.4, for different N, the motion of vortex centers in this pattern are distinctly different. Here we consider the interactions for some special N, e.g. $N = 3$, 4 and 5. The time evolution of the vortex centers are shown in Figure 7.12.

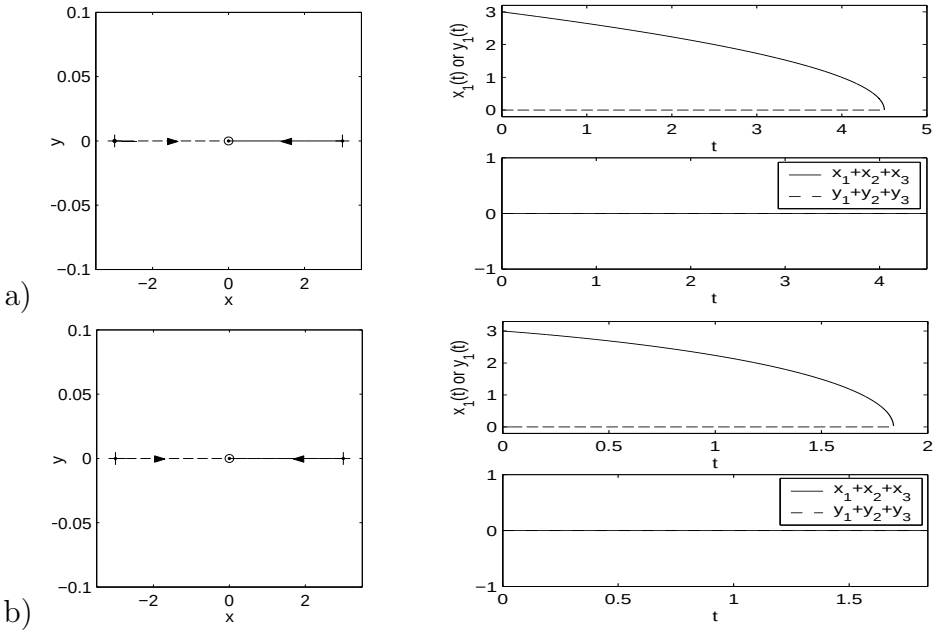

Figure 7.12: Time evolution of the vortex centers in GLE for Pattern IV with $a = 3$, where 'o' is the collision point. From the reduced dynamic laws with $\kappa = 1$ (a, c&e) and direct simulations of GLE (b, d&f). Case I: $N = 3$.

From Fig. 7.12, we can get the following conclusions:

i). During the interaction, the mass center of the vortex centers is conserved very well, which again confirms the dynamic law in (7.28), and the vortex initially at the origin does not move.

ii). When $N = 3$, the three opposite vortices undergo attractive interactions. Before a critical time $t_c > 0$, the two vortices initially on a circle would move towards the center along the line passing through their initial centers (cf. Fig. 7.12b). When

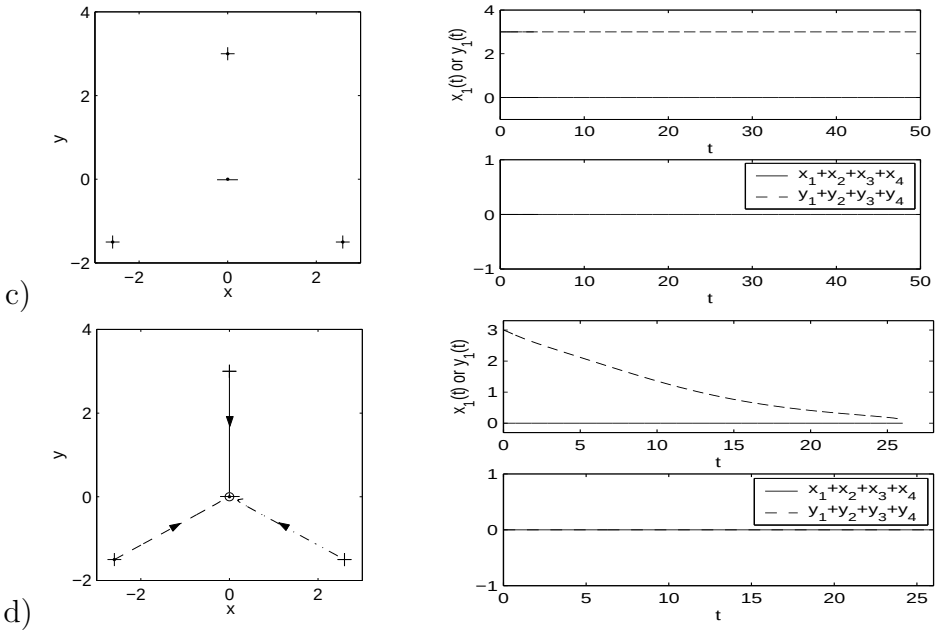

Figure 7.12 (cont'd): Case II: $N = 4$.

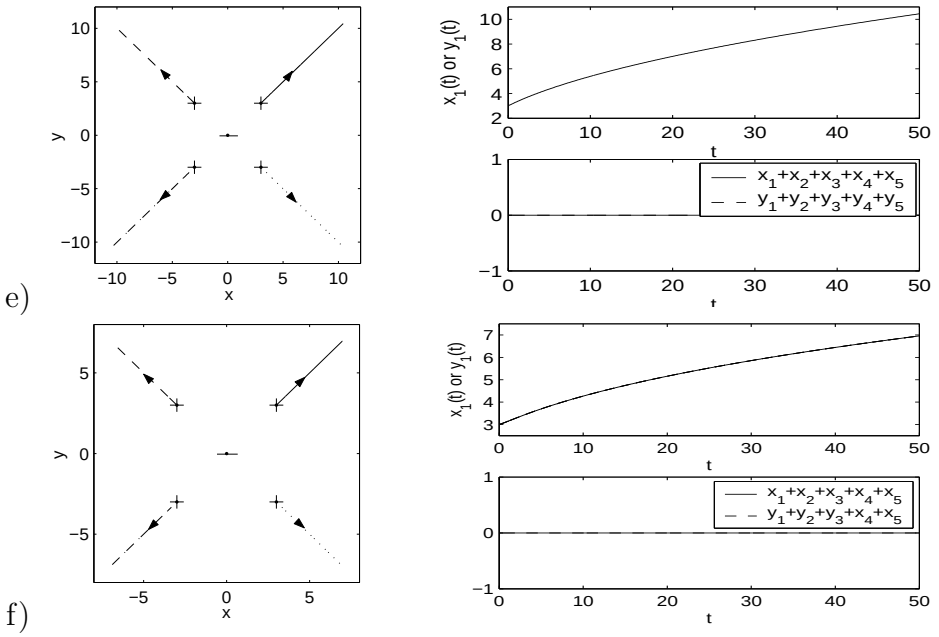

Figure 7.12 (cont'd): Case III: $N = 5$.

$t = t_c$, three vortices collide at the point $(0, 0)$, and after it, only one vortex with winding number m_0 is left, which would stay at the point $(0, 0)$ for any time $t > t_c$. The numerical results in this case are consistent with the dynamic laws in Lemma 7.4.

iii). When $N = 4$, the three vortices located on a circle would move towards the center before a critical time t_c. At time $t = t_c$, they collide at the center (cf. Fig. 7.12d), and after it, there are two like vortices left, which have winding numbers m_0 and undergo a repulsive interaction. In this case, the numerical results are different from those of the reduced dynamic law, where the four vortices would stay at their initial locations for any time $t \geq 0$ (cf. Fig. 7.12c). This difference is caused by neglecting the next order terms in the asymptotic approximations when we get the ODEs (7.17), so we can make some corrections on the reduced dynamic laws from our numerical results.

iv). When $N \geq 5$, the N vortices undergo repulsive interactions and they never collide, which confirms the dynamic laws in Lemma 7.4 (cf. Fig. 7.12f).

7.7 Interaction of vortices in NLSE

In this section, we numerically study the vortex interactions in NLSE and compare them with the reduced dynamic laws in Lemmas 7.5−7.8. For the NLSE, the magnitude of a plays an important role in vortex interactions, so for each example we consider two cases, i.e. small $|a|$ and large $|a|$. For brevity, the results are reported only for $m_0 = +1$.

Pattern I. For $N = 2$, Figure 7.13 shows the surface plots of $-|\psi|$ at different times, and Figure 7.14 depicts the plots of $|\psi(x, 0, t)|$ to study the sound wave propagation during the interaction. Figure 7.15 gives time evolution of the vortex centers for different N.

From Figs. 7.13−7.15, we can draw the following conclusions:

i). Vortices with same winding numbers never collide during the interaction, and the signed mass center of the vortex centers is conserved very well.

ii). Vortices initially located on a circle would move first to another circle with a radius $a_1 > a$ within time $0 \leq t \leq t_0$, where t_0 is dependent on a. After $t \geq t_0$,

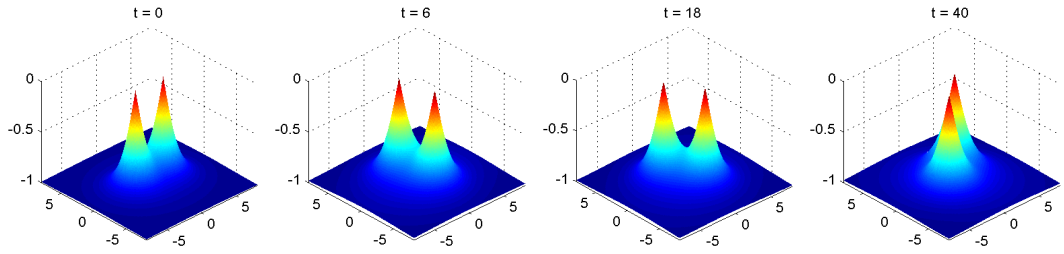

Figure 7.13: Surface plots of $-|\psi|$ at different times in NLSE for Pattern I with $N = 2$ and $a = 2$.

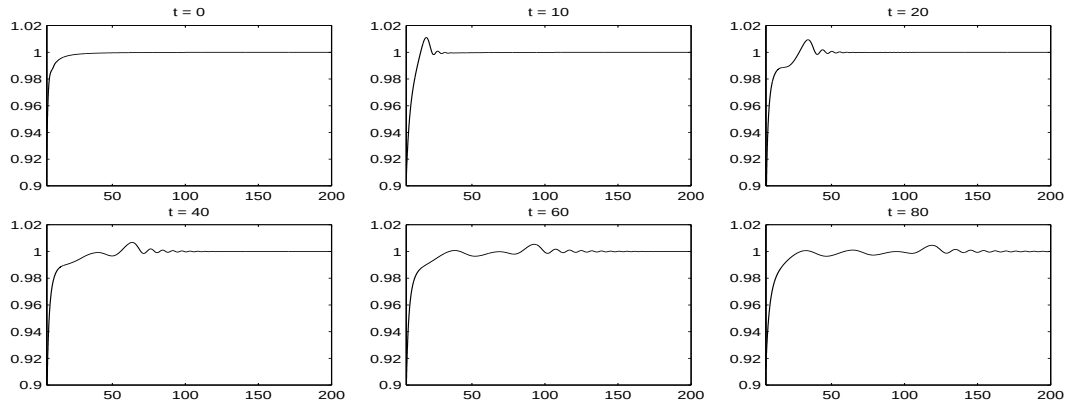

Figure 7.14: Plots of $|\psi(x, 0, t)|$ $(x \geq 4)$ in NLSE for Pattern I with $N = 2$ and $a = 2$.

they would rotate (counter clockwise when $m_0 = +1$, and respectively clockwise when $m_0 = -1$) on a circle whose radius depends on time t, i.e. $r = r(t) \geq a_1$ and $\frac{dr(t)}{dt} \geq 0$.

iii). All our numerical results show that the reduced dynamic laws are only valid for large a, which is caused by neglecting the next order terms when we derive the ODEs (7.19). While for the case of small a, our numerical results suggest a correction for the dynamic laws.

iv). The reduced dynamic laws fail to take into account the effect of the excessive energy and the radiation effect (cf. Fig. 7.14) which play important roles in vortex dynamics.

For the case of $N = 2$, we do more detailed numerical studies to compare with the

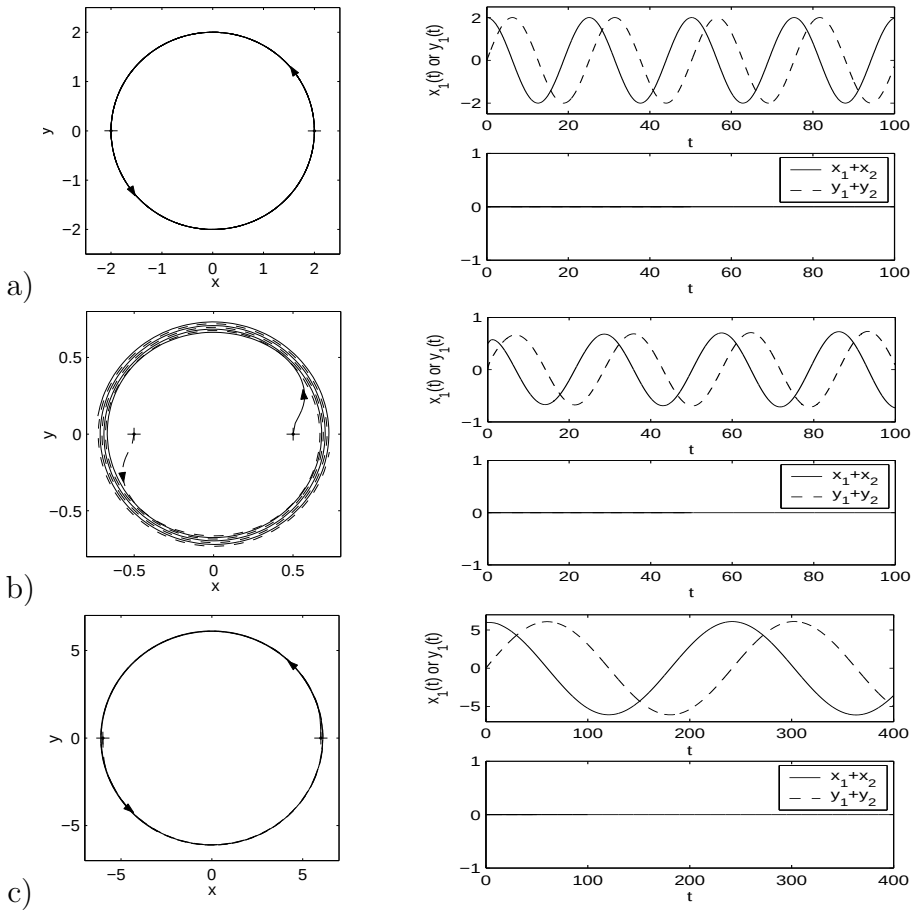

Figure 7.15: Time evolution of the vortex centers in NLSE for Pattern I. From the reduced dynamic laws (a&d) and direct simulations of NLSE with $a = O\left(r_1^0\right)$: (b&e) and $a \gg r_1^0$: (c&f). Case I. $N = 2$: a). $a = 2$; b). $a = 0.5$; c). $a = 6$.

dynamic laws in [109]. Figure 7.16 presents the dynamical laws obtained from our numerical simulations.

According to (7.44), two like vortices would rotate with an angular frequency $\omega(a) = 1/a^2$. This is confirmed by our numerical simulations (cf. Fig. 7.16a) when $d_0 = 2a$ is large, however, it is invalid when d_0 is small because the reduced dynamic laws (7.19) are not correct when the vortex pairs have overlap support. On the other hand, from our numerical results, we find that after some time t_0, the two vortices would rotate on a circle which has a time-dependent diameter $d(t) = 2r(t)$, and if these two vortices are initially well-separated, i.e. $d_0 = 2a \gg 1$, the diameter $d(t)$

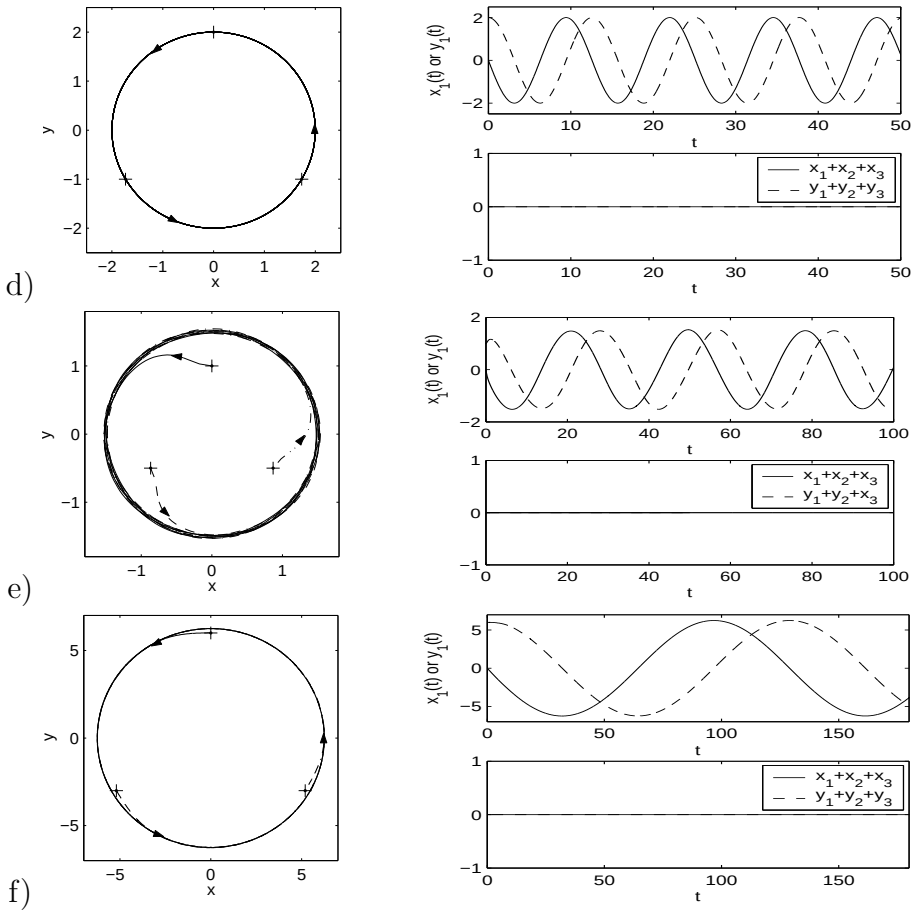

Figure 7.15 (cont'd): Case II. $N = 3$: d). $a = 2$; e). $a = 1$; f). $a = 6$.

increases at $O\left(t^{1/6}\right)$ [108], so we fit it by

$$d(t) = |\mathbf{x}_1(t) - \mathbf{x}_2(t)| = \left[d_0(t_0)^6 + \alpha(d_0)(t - t_0)\right]^{1/6}, \qquad t \geq t_0, \tag{7.75}$$

with $\alpha(d_0)$ a constant depending on d_0. The numerical results show that (7.75) is a very good predication (cf. Fig. 7.16b). Of course, much more detailed information on the vortex dynamics in this case can be found through our numerical simulations. For example, our simulations suggest that when the initial distance d_0 increases, the time t_0 increases, the diameter $d_1 = |\mathbf{x}_1(t_0) - \mathbf{x}_2(t_0)|$ increases (cf. Fig. 7.16c), and $\alpha(d_0)$ in (7.75) also increases (cf. Fig. 7.16b). From Fig. 7.16, we have the numerical dynamic laws for the diameter d_1 when $t \geq t_0$:

$$d_1 \approx \begin{cases} d_0 + d_0^{0.9053}/2.9189, & d_0 < 2r_1^0, \\ d_0 + 1.4453/d_0^{0.7996}, & d_0 > 2r_1^0, \end{cases} \tag{7.76}$$

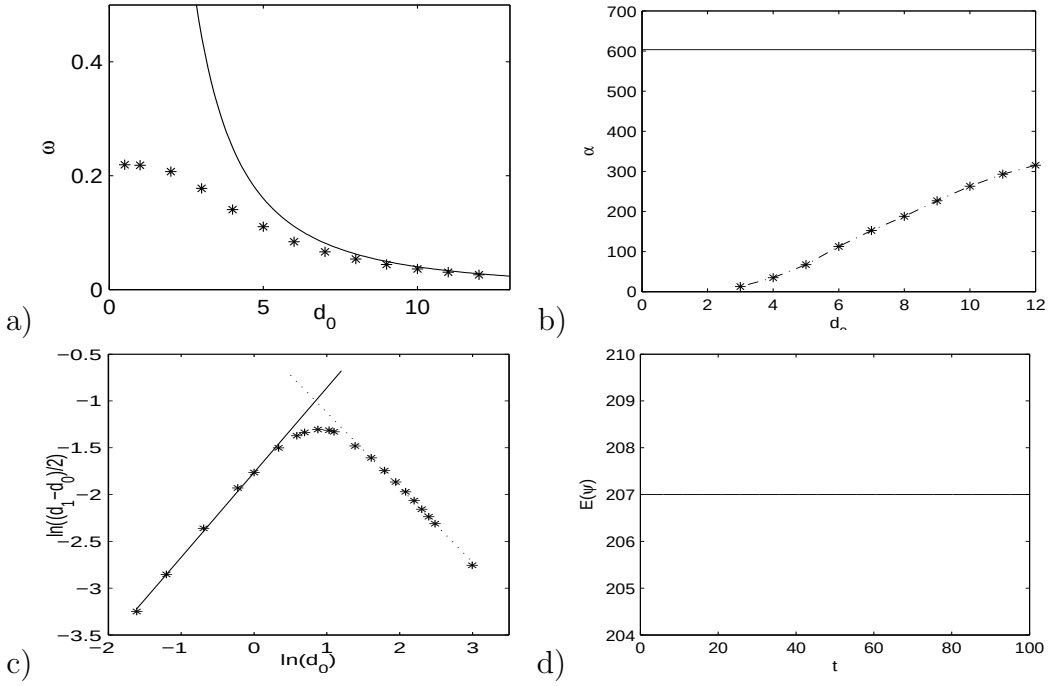

Figure 7.16: Dynamic laws for two like vortices in NLSE. a). Frequency ω (solid line from (7.44); '*': numerical results); b). $\alpha(d_0)$ in (7.75) (solid line: $\alpha = 2^6 \cdot 3\pi$ [108]; '*': numerical results); c). diameter $d_1 = |\mathbf{x}_1(t_0) - \mathbf{x}_2(t_0)|$; d). time-evolution of the free energy.

with r_1^0 being the core size of the vortex with winding number $m = \pm 1$. In addition, from Fig. 7.16d, we can see that the rescaled free energy $E(\psi)$ is conserved very well during the dynamics.

Pattern II. In this case, we study the interaction between three or four like vortices. The time evolution of the vortex centers are shown in Figure 7.17.

From Fig. 7.17 and our additional results, we can get the same conclusions as i)−iv) drawn for the interaction in Pattern I. Additionally, in this case, the vortex initially at the center does not move for any time $t \geq 0$.

Pattern III. In this case, we consider two opposite vortices for different $d_0 = 2a$. Figures 7.18 and 7.21 display the surface plots of $-|\psi|$ at different times for $d_0 = 3$ and $d_0 = 10$ respectively, and Figures 7.19, 7.20 and 7.22 plot $|\psi(x, y(t), t|$ or

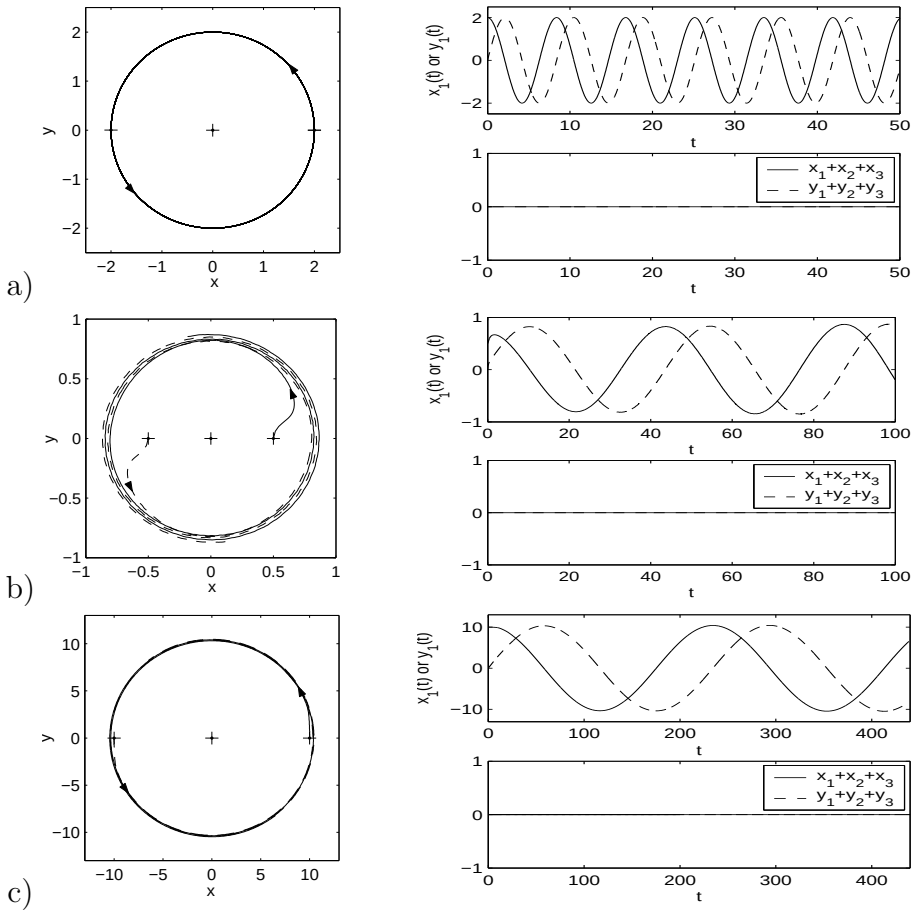

Figure 7.17: Time evolution of the vortex centers in NLSE for Pattern II. From the reduced dynamic laws (a&d) and direct simulations of NLSE with $a = O\left(r_1^0\right)$: (b&e) and $a \gg r_1^0$: (c&f). Case I. $N = 3$: a). $a = 2$; b). $a = 0.5$; c). $a = 10$.

$|\psi(0, y, t)|$ to show the sound wave propagation during the dynamics. Figure 7.23 shows time evolution of the two vortex centers for different d_0.

From Figs. 7.18−7.23, we can draw the following conclusions:

i). The signed mass center of the two vortex centers is conserved only when the initial distance between two vortices, i.e. d_0, is large enough, while when d_0 is small, it is not conserved any more.

ii). There exists a critical distance d_{cr}, such that for $d_0 < d_{cr}$, the two vortices approach each other while drifting sideways and then collide and annihilate at time $t = t_c$ (cf. Figs. 7.18, 7.23b), while for $d_0 > d_{cr}$, they move almost in parallel

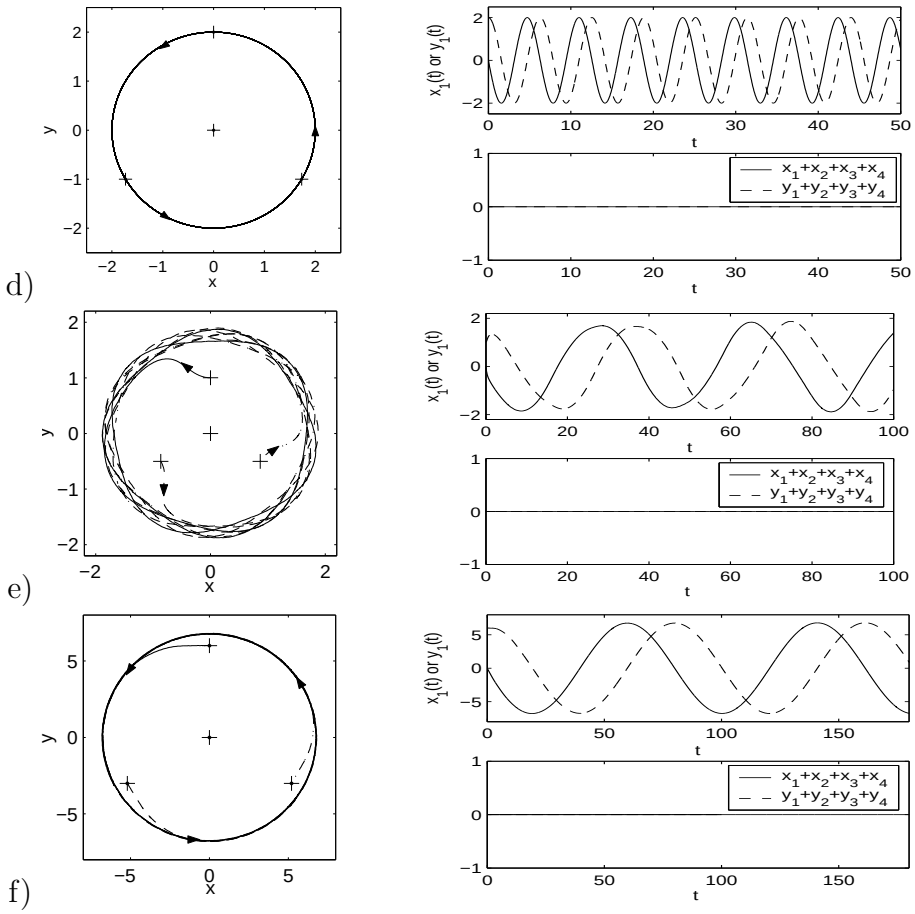

Figure 7.17 (cont'd): Case II: $N = 4$: d). $a = 2$; e). $a = 1$; f). $a = 6$.

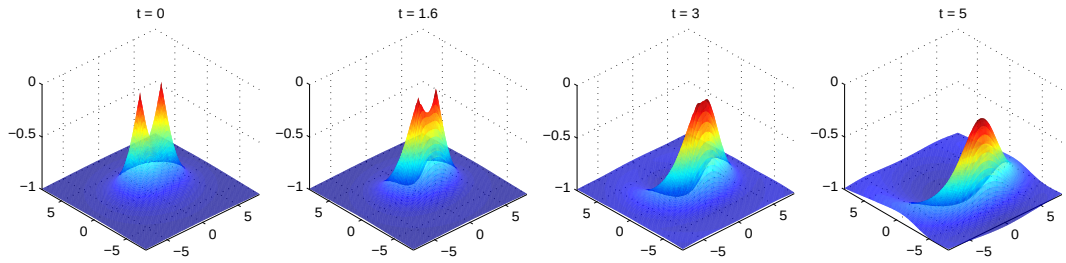

Figure 7.18: Surface plots of $-|\psi|$ at different times in NLSE for Pattern III with $d_0 = 3$.

courses (cf. Figs. 7.21, 7.23c&d). Our numerical simulations suggest that $d_{cr} \approx 2r_1^0 = 2 \times 1.75 = 3.5$, i.e. two times of the core size r_1^0, which is almost three times of the theoretical prediction $d_{cr} \approx \sqrt{2}$ derived in [108].

iii). When $d_0 < d_{cr} = 2r_1^0$, before collision, our numerical simulation reveals that

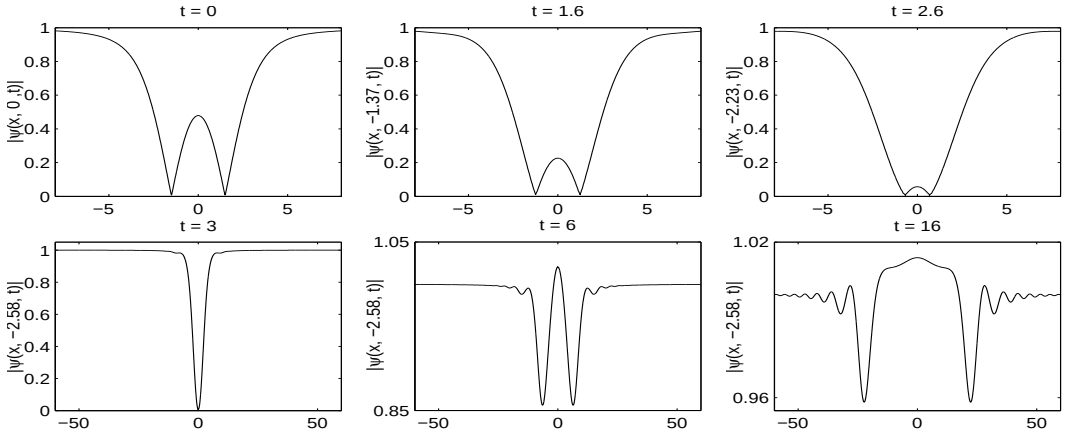

Figure 7.19: Plots of $|\psi(x, y(t), t)|$ at different times in NLSE for Pattern III with $d_0 = 3$. Here $y = y(t)$ is the line passing through two vortex centers before $t_c \approx 3.0$.

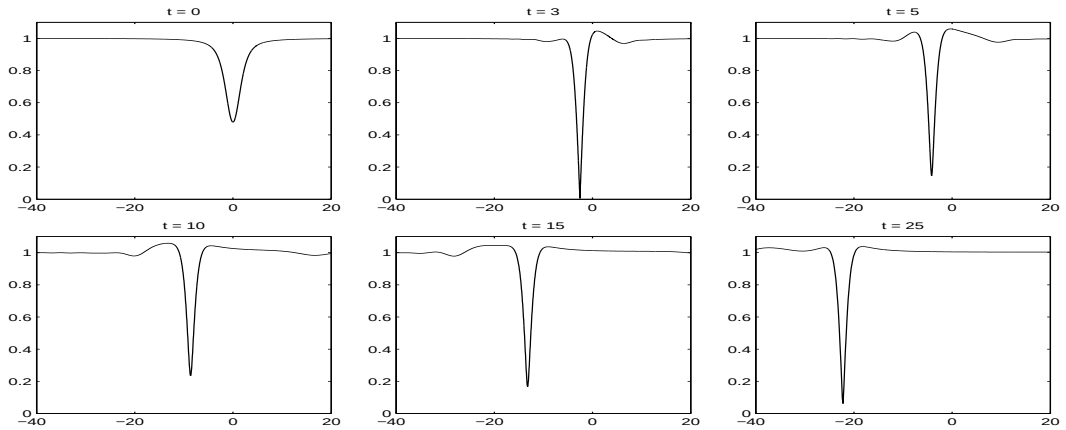

Figure 7.20: Plots of $|\psi(0, y, t)|$ at different times in NLSE for Pattern III with $d_0 = 3$.

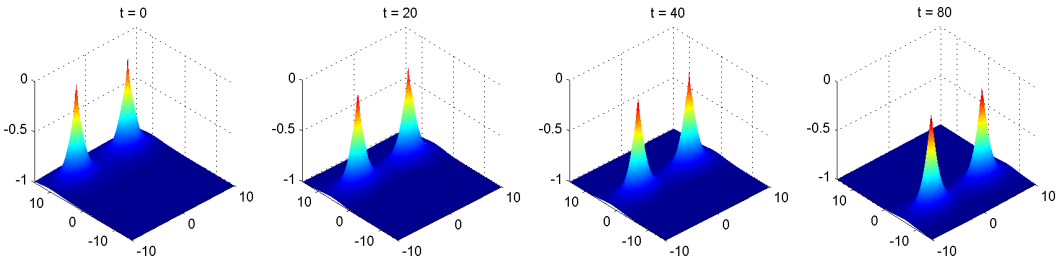

Figure 7.21: Surface plots of $-|\psi|$ at different times in NLSE for Pattern III with $d_0 = 10$.

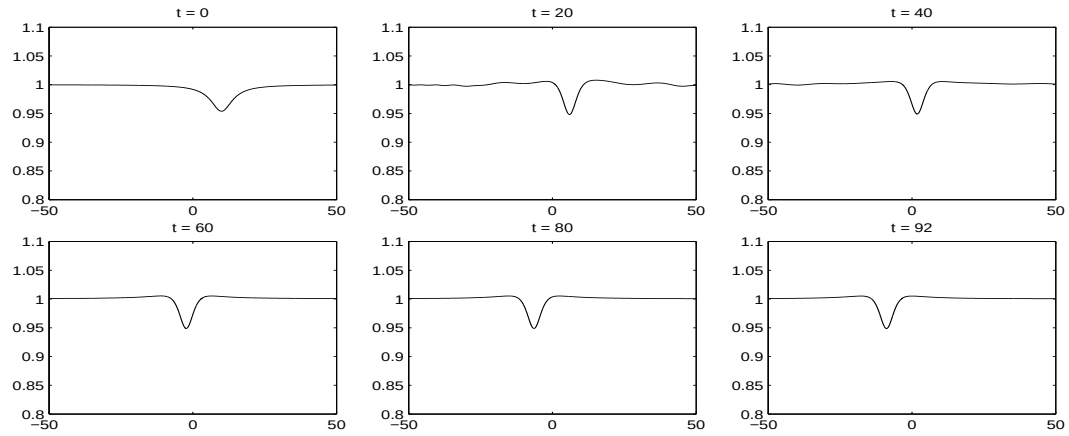

Figure 7.22: Plots of $|\psi(0, y, t)|$ at different times in NLSE for Pattern III with $d_0 = 10$.

two sound waves moving towards each other are generated along the line joining the two vortex centers (cf. Fig. 7.19), which cause the collision, while no radiation is observed; after the collision, some outgoing radiation is observed along with a solitary-like sound wave also being observed in the y-axis (cf. Fig. 7.20). In addition, a discontinuity or shock wave in the hydrodynamical velocity is observed just after the collision. Furthermore, for the initial setup in Pattern III, the two vortices collide at the point $(0, -d_2)$ with $d_2 > 0$ when $t = t_c$. When the initial distance d_0 increases, both t_c and d_2 increase, and our numerical results suggest the following relation between them:

$$t_c \approx \frac{1}{7.0790}\, d_0^{2.0954}, \qquad d_1 \approx \frac{1}{1.9300}\, d_0^{1.0365}, \quad \text{with} \quad d_1 = \sqrt{d_0^2 + d_2^2}. \tag{7.77}$$

iv). When $d_0 \gg d_{cr} = 2r_1^0$, the two vortices drift almost on two parallel lines perpendicular to the line joining them, with a constant speed. Our numerical results confirm the speed (7.55) (cf. Fig. 7.24). Additionally, a solitary wave is observed during the dynamics (cf. Fig. 7.22).

v). Again, in Pattern III, the solutions of the reduced dynamic laws agree with our numerical results qualitatively when $a \gg r_1^0$, and they are completely invalid when a is small (cf. Fig. 7.23).

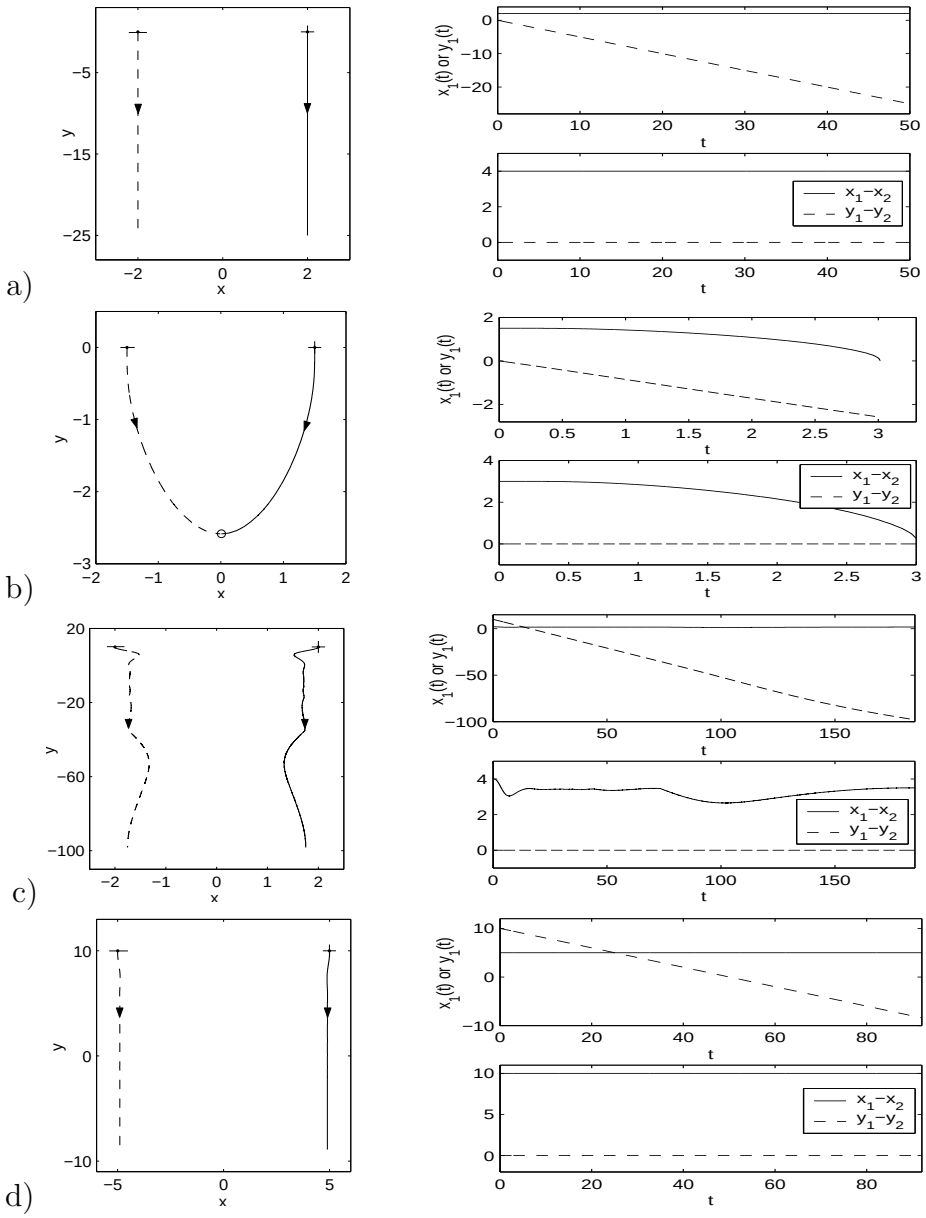

Figure 7.23: Time evolution of the two vortex centers in NLSE for Pattern III, where 'o' is the collision point. From the reduced dynamic laws (a) and direct simulations of NLSE with $a < r_1^0$: (b), $a = O(r_1^0)$: (c), and $a \gg r_1^0$: (d).

Pattern IV. Figure 7.25 shows time evolutions of the vortex centers for $N = 3$, 4 and 5. Form it, we can draw the following conclusions:

i). During the interaction, the signed mass center of the vortex centers is conserved, and the vortex initially at the center does not move.

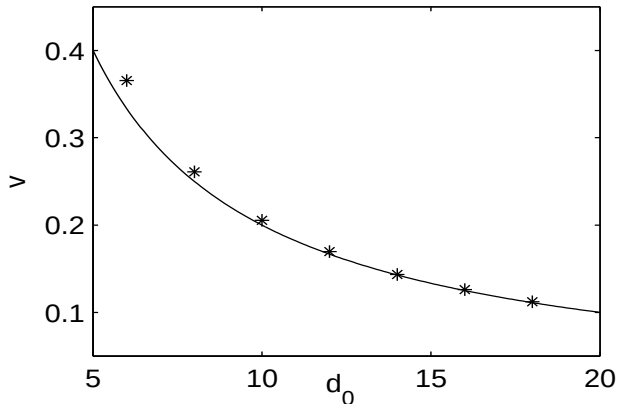

Figure 7.24: Comparisons of numerical speed ('*') and dynamical laws from (7.55) (solid line) in NLSE for Pattern III with $d_0 > d_{cr}$.

ii). For the case of $N = 3$, when $a < 2r_1^0$, three opposite vortices undergo attractive interactions, and the two vortices initially on a circle would move symmetrically towards the center before a critical time t_c. When $t = t_c$, they collide at the origin (cf. Fig. 7.25b), and after it, only one vortex with winding number m_0 is left and it would stay at the point $(0, 0)$ for any time $t > t_c$. On the other hand, when $a > 2r_1^0$, the two vortices would rotate (clockwise for $m_0 = +1$, and respectively counter clockwise for $m_0 = -1$) on a circle whose radius depends on time t, i.e. $r = r(t)$, and $\frac{dr(t)}{dt} \geq 0$ (cf. Fig. 7.25c).

iii). When $N = 4$, the three vortices initially on a circle would move first to another circle with radius $a_1 < a$, then they would rotate (clockwise for $m_0 = +1$, and respectively counter clockwise for $m_0 = -1$) on a circle which has a time-dependent radius $r = r(t)$ and $\frac{dr(t)}{dt} \geq 0$ (cf. Fig. 7.25e&f) .

iv). When $N \geq 5$, the four vortices would rotate on a circle with a time-dependent radius $r(t)$ and $\frac{dr(t)}{dt} \geq 0$. If $m_0 = +1$, they rotate counter clockwise, and otherwise they rotate clockwise.

v). For any $N \geq 3$, if a is large, our numerical results confirm the reduced dynamic laws, while when a is small, some corrections need to make on the reduced dynamic laws.

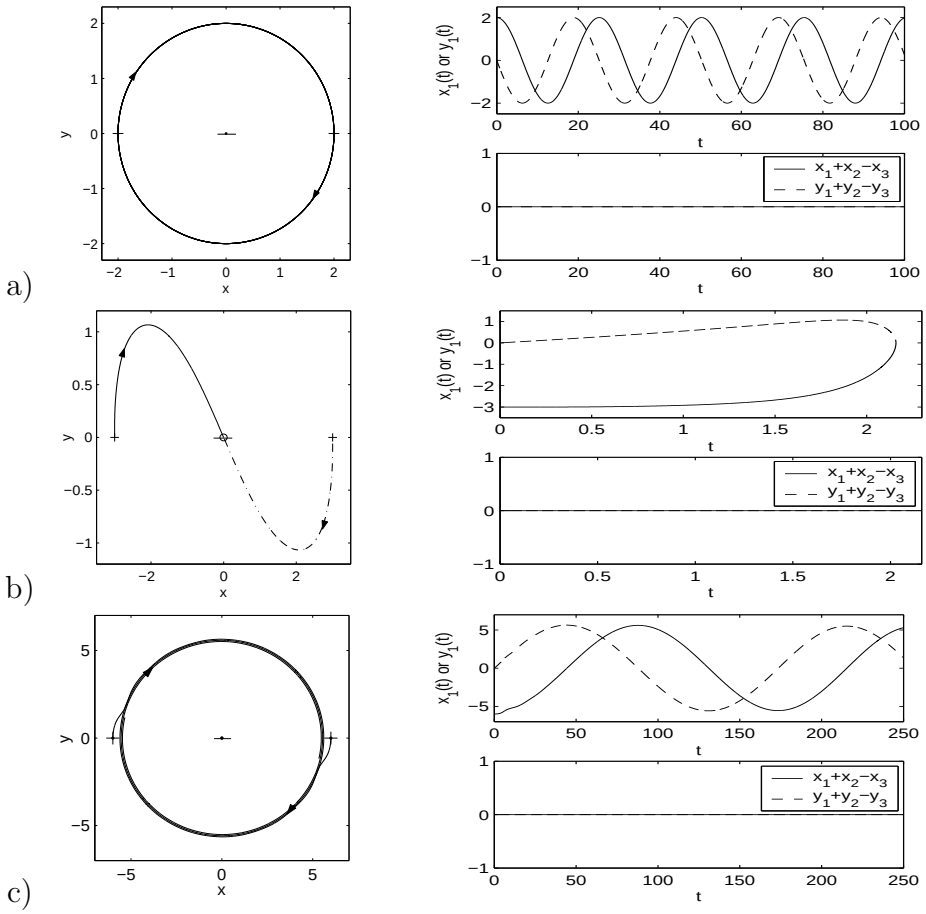

Figure 7.25: Time evolution of the vortex centers in NLSE for Pattern IV, where 'o' is the collision point. From the reduced dynamic laws (a, d&g) and direct simulations of NLSE with $a = O\left(r_1^0\right)$: (b, e&h) and $a \gg r_1^0$: (c, f&i). Case I. $N = 3$: a). $a = 2$; b). $a = 3$; c). $a = 6$.

7.8 Dynamics of vortex lattices

In this section, we study the dynamics of vortex lattices in GLE and NLSE. In order to do so, we take $\varepsilon = 1$ and $V_0(\mathbf{x}) \equiv 1$ in (7.1) and choose the initial data (7.2) as

$$\psi_0(\mathbf{x}) = \prod_{j=1}^{N} \phi_1\left(\mathbf{x} - \mathbf{x}_j^0\right) = \prod_{j=1}^{N} \phi_1\left(x - x_j^0,\, y - y_j^0\right), \qquad \mathbf{x} \in \mathbb{R}^2, \tag{7.78}$$

where N is the total number of vortices in the lattice, and ϕ_1 is the vortex state solution in (7.11) with winding number $+1$. Then we take $m = N$ in (7.3) and study

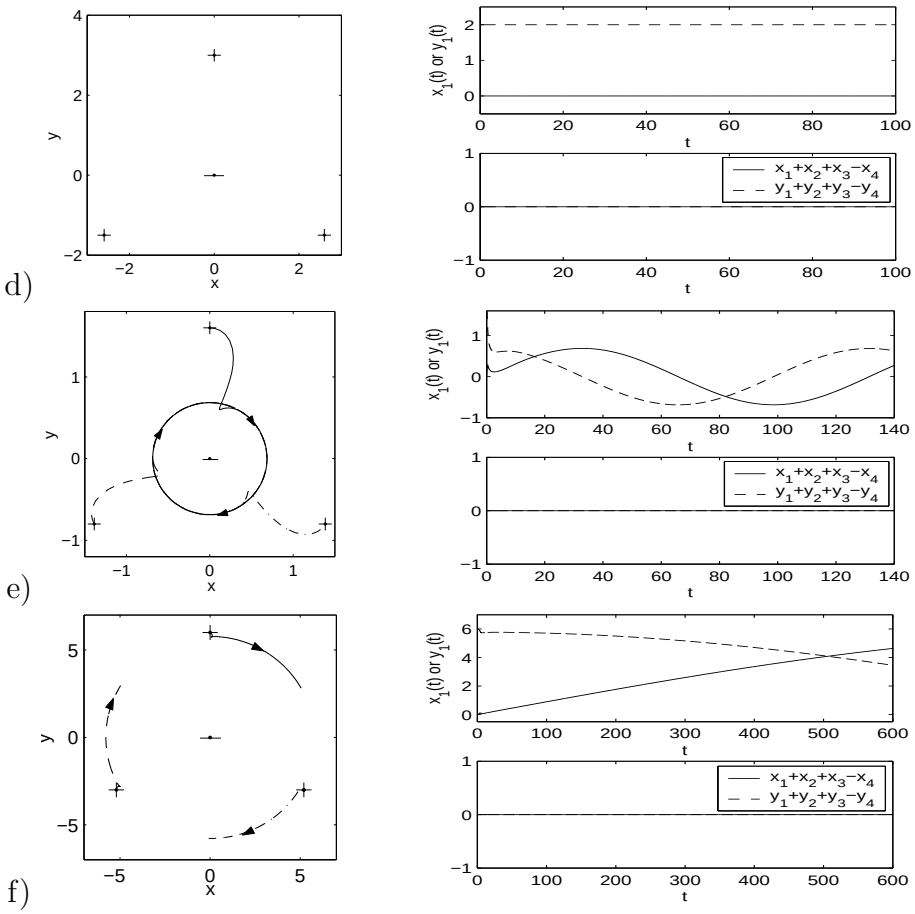

Figure 7.25 (cont'd): Case II. $N = 4$: d). $a = 2$; e) $a = 1.6$; f). $a = 6$.

two cases:

Case I. $N = 9$ and the initial vortex centers are located on a uniform 3×3 mesh points of the rectangle $[-4, 4] \times [-4, 4]$. That is, one vortex is located at the origin and the other ones are uniformly located on two homocentric circles with radii $r_1 = 4$ and $r_2 = 4\sqrt{2}$, respectively.

Case II. $N = 25$ and the initial vortex centers are located on a uniform 5×5 mesh points of the rectangle $[-4, 4] \times [-4, 4]$.

For Case I, Figures 7.26 and 7.27 show the surface plots of $-|\psi|$ and time evolutions of the vortex centers in GLE and NLSE respectively, and Figure 7.28 plots $|\psi(x, 0, t)|$ $(x \geq 0)$ at different times in NLSE. For Case II, Figure 7.29 shows the contour plots

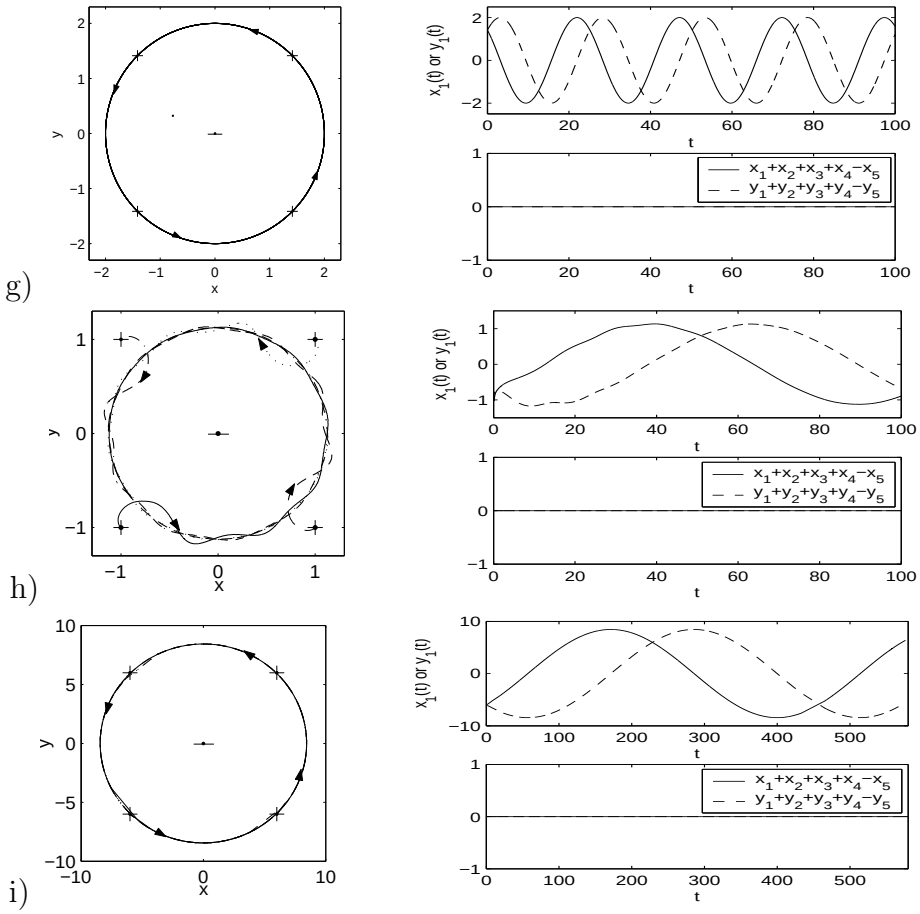

Figure 7.25 (cont'd): Case III. $N = 5$: g). $a = 2$; h). $a = \sqrt{2}$; i). $a = 6\sqrt{2}$.

of $-|\psi|$ in NLSE.

Based on Figs. 7.26−7.29, we can draw the following conclusions: First, for GLE and NLSE, the vortex initially at the origin does not move due to the symmetry (cf. Figs. 7.26a&b, 7.27a&b, 7.29).

Second, for GLE in Case I, each vortex moves outward along the line passing through its initial center and the origin (cf. Fig. 7.26b), and after some time, the lattice splits into 9 well-separated vortices with winding numbers +1 (cf. Fig. 7.26a). For any time $t \geq 0$, the symmetry of their initial locations is preserved, i.e. they are always located on two homocentric circles, and when time t increases, the radii of the two circles, i.e. $r_1(t)$ and $r_2(t)$, increase, but their distance, i.e. $|r_1(t) - r_2(t)|$, decreases (cf. Fig. 7.26c).

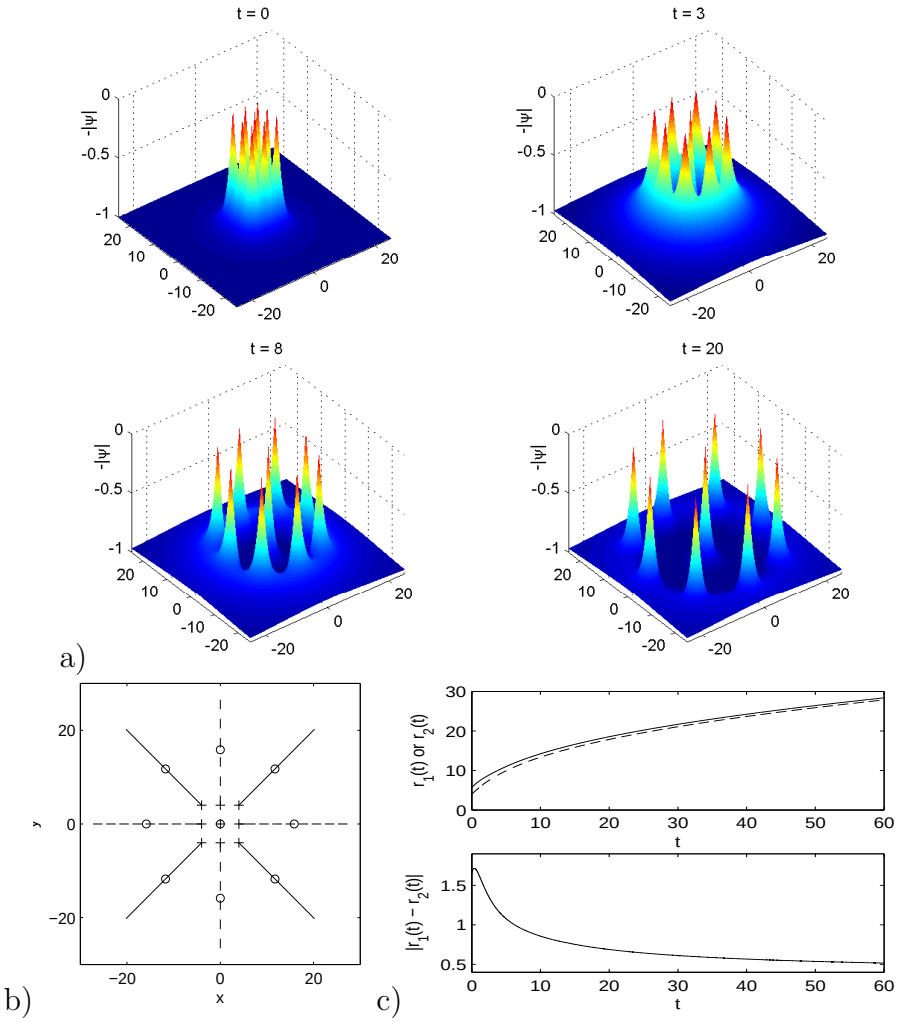

Figure 7.26: Dynamics of a vortex lattice in GLE for Case I. a). Surface plots of $-|\psi|$ at different times; b). trajectory of the vortex centers ('+': $t = 0$ and 'o': $t = 15$); c) time evolution of the radius $r_1(t)$ and $r_2(t)$.

Third, for NLSE, the vortices rotate counterclockwise and the initial symmetry of their locations is preserved. In Case I, the distance between two circles, i.e. $|r_1(t) - r_2(t)|$, changes periodically (cf. Fig. 7.27c). The vortex cores are well-overlapped for a very long time. During the time evolution, sound waves are generated and they radiate outward (cf. Fig. 7.28). In Case II, similar results can be observed, but the dynamics are more complicated (cf. Fig. 7.29).

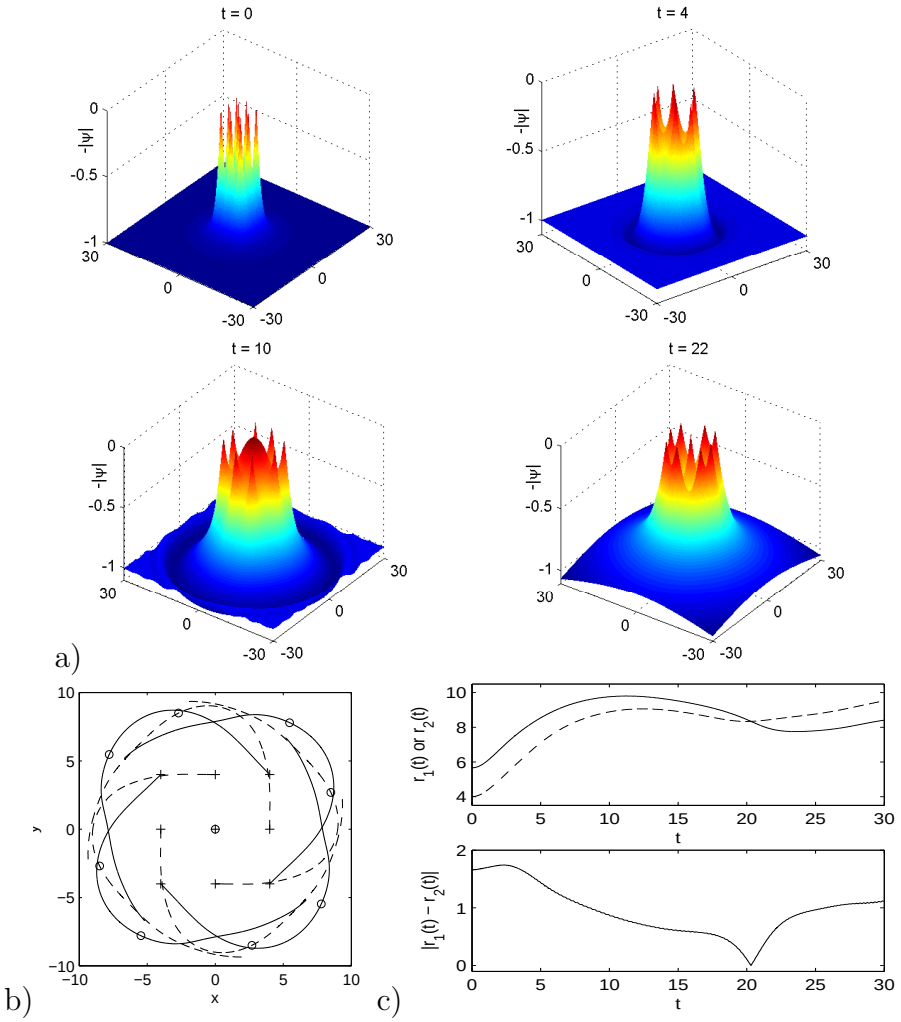

Figure 7.27: Dynamics of a vortex lattice in NLSE for Case I. a). Surface plots of $-|\psi|$ at different times; b). trajectory of the vortex centers ('+': $t = 0$ and 'o': $t = 15$); c) time evolution of the radius $r_1(t)$ and $r_2(t)$.

7.9 Vortex motion in inhomogeneous potential

In this section, we study the vortex motion under an inhomogeneous external potential. In order to do so, we take the external driven field $W(\mathbf{x}, t) \equiv 0$ and

$$V_0(\mathbf{x}) = \frac{\frac{1}{2} + \gamma_x x^2 + \gamma_y y^2}{1 + \gamma_x x^2 + \gamma_y y^2} = 1 - \frac{1}{2\left(1 + \gamma_x x^2 + \gamma_y y^2\right)}, \qquad \mathbf{x} \in \mathbb{R}^2, \tag{7.79}$$

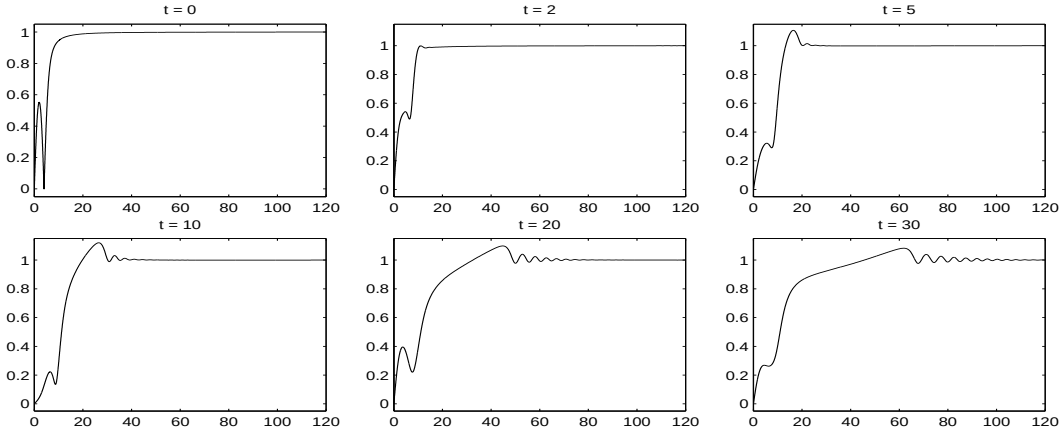

Figure 7.28: Plots of $|\psi(x,0,t)|$ $(x \geq 0)$ at different times in NLSE for Case I.

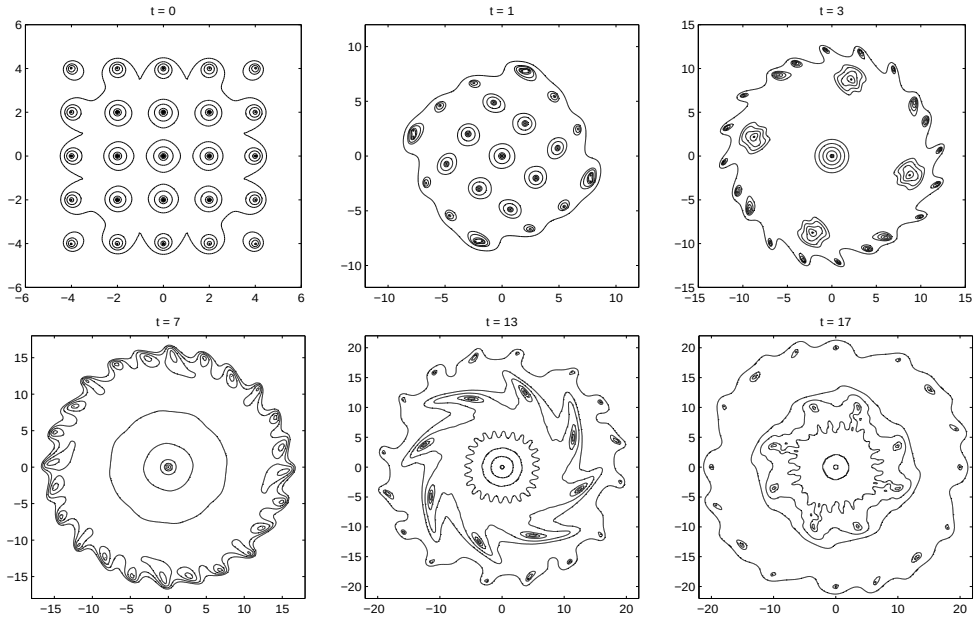

Figure 7.29: Contour plots of $-|\psi|$ at different times in NLSE for Case II.

where γ_x and γ_y are two positive constants. It is easy to see that $V_0(\mathbf{x})$ attains its minimum value $1/2$ at the origin $(0,0)$. The initial data (7.2) is chosen as

$$\psi(\mathbf{x},0) = \psi_0(\mathbf{x}) = \phi_1\left(\mathbf{x} - \mathbf{x}^0\right), \qquad \mathbf{x} \in \mathbb{R}^2, \tag{7.80}$$

where $\phi_1(\mathbf{x})$ is the vortex state (7.11) with winding number $m = +1$.

We study the dynamics of a vortex under two types of inhomogeneous external potentials:

Case I. Isotropic external potential, e.g. $\gamma_x = \gamma_y = 1$ in (7.79);

Case II. Anisotropic external potential, e.g. $\gamma_x = 1$ and $\gamma_y = 5$ in (7.79).

For the GLE, i.e. $\alpha = 1$ and $\beta = 0$ in (7.1), the velocity of the induced motion due to the inhomogeneous impurities was obtained in [81], i.e.

$$\mathbf{v}(t) := \frac{d\mathbf{x}(t)}{dt} = -\nabla \ln V_0(\mathbf{x}(t)), \quad t \geq 0, \qquad \text{with} \quad \mathbf{x}(0) = \mathbf{x}^0. \tag{7.81}$$

This implies that in this case, the vortex would move to the minimizer of the external potential $V_0(\mathbf{x})$. Furthermore, if the external potential is isotropic, the trajectory is a segment connecting $\mathbf{x}^0$ and the minimizing point of $V_0(\mathbf{x})$. While for the NLSE and CGLE, the dynamic laws with impurities remain to be established.

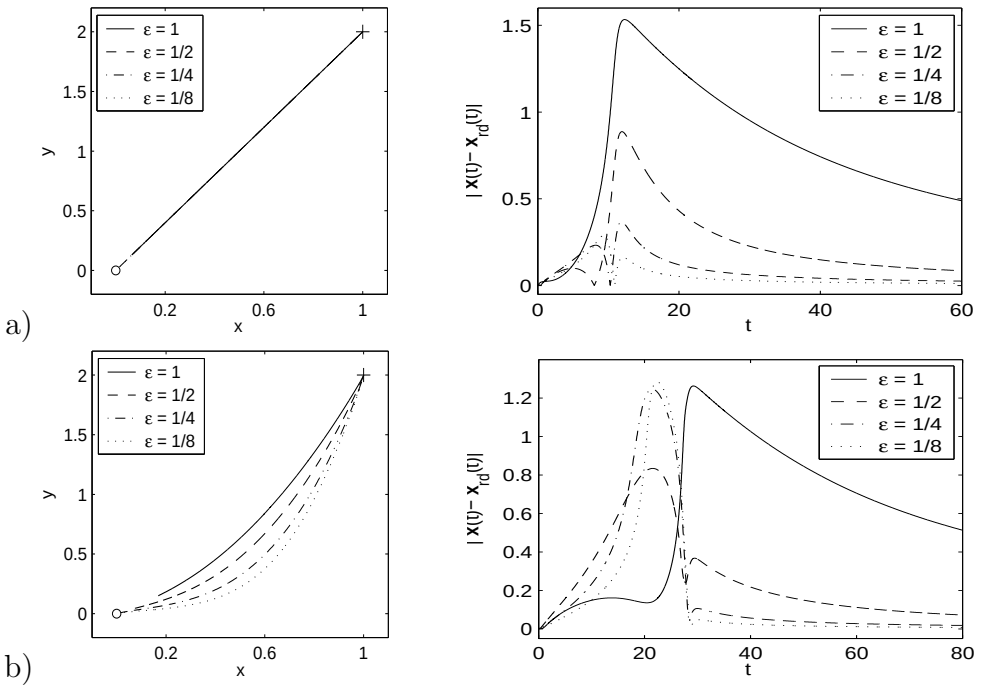

Figure 7.30: The trajectory of vortex center trajectory and errors between the numerical results and those from (7.81) for GLE. a). Case I; b). Case II.

In the following, we study the vortex motion by directly simulating the GLSE (7.1)−(7.3). For GLE, Figure 7.30 shows the trajectory of the vortex center for different ε with $\mathbf{x}^0 = (1, 2)^T$ and plots the errors between the numerical results and

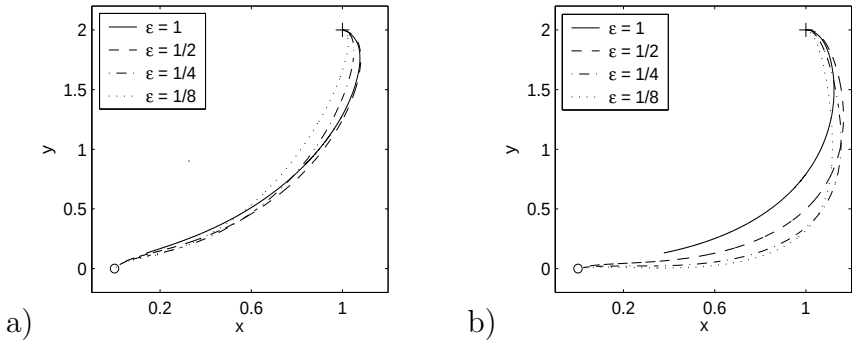

Figure 7.31: The trajectory of vortex center under an inhomogeneous external potential for CGLE. a). Case I; b). Case II.

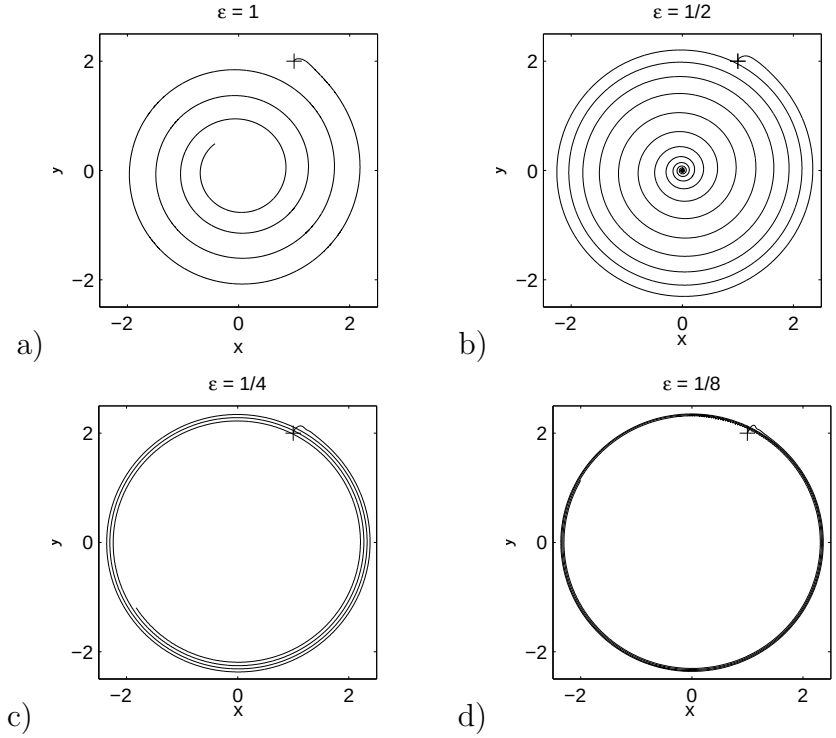

Figure 7.32: The trajectory of vortex center under an inhomogeneous external potential for the NLSE in Case I.

those from (7.81). Similarly, Figures 7.31 and 7.32 display the trajectory of the vortex center in CGLE and NLSE respectively.

From Figs. 7.30−7.32, we can draw the following conclusions: First, for GLE and

CGLE, the vortex center moves monotonically to the point where the external potential $V_0(\mathbf{x})$ attains its minimum value (cf. Fig. 7.30, 7.31). The speed of the motion depends on the values of the parameter ε. The trajectory of the vortex center depends on the external potential $V_0(\mathbf{x})$, which agrees with the analytical results for GLE in [80, 81, 96]. After the vortex reaches the minimum point of the external potential, it would stay there for any time $t \geq 0$, which illustrates the pinning effect. Second, for NLSE, the vortex center moves rotationally clockwise to the minimum point of the external potential (cf. Fig. 7.32). When ε is small, the smaller is the ε, the longer time the vortex center stays on a circle. Additional experiments were carried out for Case II, and similar motion patterns are observed, so the results are omitted here.

Based on our numerical results in Figs. 7.31−7.32, we make the following conjectures about the vortex motion in NLSE and CGLE. For the NLSE under an inhomogeneous potential, the velocity of the induced motion would satisfy

$$\mathbf{v}(t) := \frac{d\mathbf{x}(t)}{dt} = -m\mathbf{G}\nabla \ln V_0(\mathbf{x}(t)), \quad t \geq 0, \qquad \text{with} \quad \mathbf{x}(0) = \mathbf{x}^0, \tag{7.82}$$

where m is the winding number of the vortex, and $\mathbf{G}$ is the symplectic matrix given in (2.54). While for the CGLE, it can be given by

$$\mathbf{v}(t) := \frac{d\mathbf{x}(t)}{dt} = -\mathbf{Q}\nabla \ln V_0(\mathbf{x}(t)), \quad t \geq 0, \qquad \text{with} \quad \mathbf{x}(0) = \mathbf{x}^0, \tag{7.83}$$

where the matrix $\mathbf{Q} = \mathbf{G} + \mathbf{I}$ with $\mathbf{G}$ and $\mathbf{I}$ being the symplectic matrix in (2.54) and identity matrix respectively. Rigorous mathematical justification for (7.82) and (7.83) are still not available.

Chapter 8

Conclusion

The main purpose of this thesis was to conduct an extensive analytical and numerical investigation of Bose-Einstein condensation (BEC) in dilute alkali gases. In this chapter, we summarize the main results described in previous chapters and discuss the directions for future research works.

8.1 Conclusion and remark

This work considers the condensate in the mean field limit which is a low temperature limit well described by the Gross-Pitaevskii equation (GPE). The time-dependent GPE is time reversible and time transverse invariant. It also conserves the normalization of the wave function and the energy.

Ground state is the most studied stationary state since it has the lowest energy and it is the most stable state. In both weakly interacting regime, i.e. $|\beta_d| \ll 1$, and strongly repulsive interacting regime, i.e. $\beta_d \gg 1$, we derived the asymptotic approximations for the ground state and its energy and chemical potential. These approximations are up to $o(1)$ in terms of the parameter β_d. Along the numerical front, the backward forward Euler Fourier pseudospectal (BFFP) method was developed to compute the ground state of non-rotating and rotating BEC. Compared

to the finite difference methods in [4, 5, 23], the BFFP method is more efficient and accurate, especially for the case of fast rotating BEC with strongly repulsive interaction, where a large number of vortices appear to form a dense lattice and thus its numerical description needs high spatial resolution. The ground states in different potentials were numerically studied for two dimensional (2D) and three dimensional (3D) cases.

The dynamics of BEC were investigated both analytically and numerically, based on the time-dependent GPE. Along the analytical side, we proved that the angular momentum expectation is conserved when the external trapping potential is radially symmetric in 2D case, and respectively cylindrically symmetric in 3D case. A second-order ordinary differential equation (ODE) was derived to describe the time evolution of the condensate width as a period function with/without a perturbation, and the frequency of the periodic function doubles the trapping frequency in that direction. Also a second-order ODE system was presented, which characterizes the dynamics of a stationary state with its center shifted. By analytically solving this ODE system, we classified different motion patterns for the mass center of a stationary state. On the numerical side, we developed several numerical methods to compute the dynamics of non-rotating and rotating BEC. For non-rotating BEC, a second-order or fourth-order time-splitting sine pseudospectral (TSSP) method is proposed, and the merit of this method is that it is explicit and unconditionally stable. It is also time reversible and time transverse invariant, and preserves the position density, which are consistent with the properties of time-dependent GPE. Due to the appearance of the rotation term in the GPE, these high-order TSSP methods cannot be directly used for simulating the dynamics of rotating BEC. Thus we proposed another two time reversible methods: time-splitting type method and leap-frog Fourier pseudospectral (LFFP) method. The time-splitting type method adopts the polar coordinate or cylindrical coordinate so as to make the angular momentum rotation term become a term with constant coefficient. It is unconditionally

stable, usually of second or fourth-order accuracy in radial direction and spectral accuracy in other directions of space, and also conserves the total density. The LFFP method adopts the Cartesian coordinate and it is explicit, of spectral accuracy in all directions of space and easy to program. It is stable under a stability condition. Due to its fully spectral resolution in space, the LFFP method can resolve better dynamics of vortex lattice in rotating BEC, especially in the fast rotating regimes with strongly repulsive interaction where a large number of vortices appears in the condensate and thus spatial resolution is one of the key issues.

By directly simulating the time-dependent GPE, we demonstrated that the central vortex states with winding number $|m| = 1$ are dynamically stable, while those with winding number $|m| > 1$ are dynamically unstable and they can split into $|m|$ well overlapped vortices with winding number $+1$ if $m > 0$, and respectively -1 if $m < 0$. Under two different initial patterns, the interactions between two $|m| = 1$ vortices were studied. We found that for both patterns, the interactions in non-interacting BEC, i.e. $\beta_d = 0$, and interacting BEC, i.e. $\beta_d \neq 0$, are distinctly different. The dynamics of vortex lattices in an anisotropic potential were also discussed.

We also extended our investigation on single-component BEC to rotating two-component condensates. In certain limiting regime of particle numbers, we reduced the two component condensate to single component. The ground states of two-component rotating BEC were numerically studied for different experiment setups. An efficient numerical method was developed to study the dynamics of this two-component system, and some numerical results were also reported.

The vortex dynamics and interactions in superconductivity and superfluidity were investigated asymptotically and numerically, by considering the Ginzburg-Landau-Schrödinger equation (GLSE) which covers Ginzburg-Landau equation (GLE), nonlinear Schrödinger equation (NLSE) and complex Ginzburg-Landau equation (CGLE). We reviewed the reduced dynamic laws characterizing the motion of vortex centers during the interactions, and solved them analytically under some proper initial

data. On the other hand, the vortex interactions were numerically studied by directly solving the GLSE. Comparing to our numerical results, we found that the reduced dynamic laws are valid only when the initial distance between vortices is large enough, which is caused by neglecting the next-order terms when they were derived. Furthermore, for the NLSE, the reduced dynamic laws fail to consider the sound wave propagation in the dynamics, which can be observed in our simulations. In addition, our numerical simulations for small initial distance presented interesting interaction results and provided further understanding of vortex interactions. In an inhomogeneous external potential, we numerically found that the vortex moves to the point where the external potential attains its minimum after a long time. For GLE, there has been a first-order ODE presented in [81] to govern the motion of the vortex center, which is consistent with our numerical results. For NLSE and CGLE, we made some conjectures about the vortex motion based on our numerical results.

8.2 Directions for future work

The numerical methods developed in this thesis have broad application in computing the ground state and dynamics of BEC, and we have adapted them to two-component condensates. They can similarly be applied to other multi-component system which has been an extremely hot topic recently. Although there are many studies on this system, issues like role of different scattering lengths, collective modes of the system and the relation to the phenomenon of superfluidity are still open problems waiting to be investigated.

With recent observations of vortices in experiments [99, 100, 9], vortex dynamics in BEC are attracting intense current research interest. Our efficient and accurate numerical methods can be used to further investigate the rich dynamics of them. They can also be applied to study the dynamics and interaction of vortex line states in 3D case.

The vortex dynamics in superconductivity and superfluidity in the whole space have

been investigated in this thesis. Those in the bounded domain is also an interesting topic, and recently there have been some theoretical studies about it [95]. In the future, one could use the methods introduced in this thesis to study it, and then compare the theoretical results with numerical ones.

A further extension would treat finite temperature effects in BEC by including the collision terms in the kinetic equation for the mean field and fluctuations [114, 137]. In fact, the ZGN theory, named after Zaremba, Griffin and Nikuni [137], was proposed to model BEC at finite temperatures. But its numerical simulation is extremely challenging and results are very limited.

Bibliography

[1] S. K. Adhikari, Numerical solution of the two-dimensional Gross-Pitaevskii equation for trapped interacting atoms, *Phys. Lett. A*, **265** (2000), pp. 91-96.

[2] S. K. Adhikari and P. Muruganandam, Bose-Einstein condensation dynamics from the numerical solution of the Gross-Pitaevskii equation, *J. Phys. B: At. Mol. Opt. Phys.*, **35** (2002), pp. 2831-2843.

[3] S. L. Adler and T. Piran, Relaxation methods for gauge field equilibrium equations, *Rev. Mod. Phys.*, **56** (1984), pp. 1-40.

[4] A. Aftalion and I. Danaila, Three-dimensional vortex configurations in a rotating Bose-Einstein condensate, *Phys. Rev. A*, **68** (2003), pp. 023603.

[5] A. Aftalion and I. Danaila, Giant vortices in combined harmonic and quartic traps, *Phys. Rev. A*, **69** (2004), pp. 033608.

[6] A. Aftalion and Q. Du, Vortices in a rotating Bose-Einstein condensate: critical angular velocities and energy diagrams in the Thomas-Fermi regime, *Phys. Rev. A*, **64** (2001), pp. 063603.

[7] A. Aftalion and T. Riviere, Vortex energy and vortex bending for a rotating Bose-Einstein condensate, *Phys. Rev. A*, **64** (2001), pp. 043611.

[8] M. H. Anderson, J. R. Ensher, M. R. Matthews, C. E. Wieman and E. A. Cornell, Observation of Bose-Einstein condensation in a dilute atomic vapor, *Science*, **269** (1995), pp. 198-201.

[9] B. P. Anderson, P. C. Haljan, C. E. Wieman and E. A. Cornell, Vortex precession in Bose-Einstein condensates: observations with filled and empty cores, *Phys. Rev. Lett.*, **85** (2000), pp. 2857-2860.

[10] I. S. Aranson and L. Kramer, The world of the complex Ginzburg-Landau equation, *Rev. Mod. Phys.*, **74** (2002), pp. 99-133.

[11] W. Bao, Ground states and dynamics of multicomponent Bose-Einstein condensates, *Multiscale Model. Simul.*, **2** (2004), pp. 210-236.

[12] W. Bao, I. -L. Chern and F. Y. Lim, Efficient and spectrally accurate numerical methods for computing ground and first excited states in Bose-Einstein condensates, J. Comput. Phys., to appear.

[13] W. Bao and Q. Du, Computing the ground state solution of Bose-Einstein condensates by a normalized gradient flow, *SIAM J. Sci. Comput.*, **25** (2004), pp. 1674-1697.

[14] W. Bao, Q. Du and Y. Zhang, Dynamics of rotating Bose-Einstein condensates and their efficient and accurate numerical computation, *SIAM J. Appl. Math.*, **66** (2006), pp. 758-786.

[15] W. Bao and D. Jaksch, An explicit unconditionally stable numerical method for solving damped nonlinear Schrödinger equations with a focusing nonlinearity, *SIAM J. Numer. Anal.*, **41** (2003), pp. 1406-1426.

[16] W. Bao, D. Jaksch and P. A. Markowich, Numerical solution of the Gross-Pitaevskii equation for Bose-Einstein condensation, *J. Comput. Phys.*, **187** (2003), pp. 318-342.

[17] W. Bao, D. Jaksch and P. A. Markowich, Three-dimensional simulation of jet formation in collapsing condensates, *J. Phys. B: At. Mol. Opt. Phys.*, **37** (2004), pp. 329-343.

[18] W. Bao, S. Jin and P. A. Markowich, On time-splitting spectral approximations for the Schrödinger equation in the semiclassical regime, *J. Comput. Phys.*, **175** (2002), pp. 487-524.

[19] W. Bao, S. Jin and P. A. Markowich, Numerical study of time-splitting spectral discretizations of nonlinear Schrödinger equations in the semiclassical regimes, *SIAM J. Sci. Comput.*, **25** (2003), pp. 27-64.

[20] W. Bao, F. Y. Lim and Y. Zhang, Energy and chemical potential asymptotics for the ground state of Bose-Einstein condensates in the semiclassical regime, *Trans. Theory Stat. Phys.*, to appear.

[21] W. Bao and J. Shen, A fourth-order time-splitting Laguerre-Hermite pseudo-spectral method for Bose-Einstein condensates, *SIAM J. Sci. Comput.*, **26** (2005), pp. 2010-2028.

[22] W. Bao and W. Tang, Ground state solution of Bose-Einstein condensate by directly minimizing the energy functional, *J. Comput. Phys.*, **187** (2003), pp. 230-254.

[23] W. Bao, H. Wang and P.A. Markowich, Ground, symmetric and central vortex states in rotating Bose-Einstein condensates, *Comm. Math. Sci.*, **3** (2005), pp. 57-88.

[24] W. Bao and Y. Zhang, Dynamics of the ground state and central vortex states in Bose-Einstein condensation, *Math. Mod. Meth. Appl. Sci.*, **15** (2005), pp. 1863-1896.

[25] I. Bialynicki-Birula and Z. Bialynicka-Birula, Center-of-mass motion in the many-body theory of Bose-Einstein condensates, *Phys. Rev. A*, **65** (2002), pp. 063606.

[26] S. N. Bose, Plancks Gesetz und Lichtquantenhypothese, *Zeitschift Für Physik A*, **26** (1924), pp. 178-181.

[27] C. C. Bradley, C. A. Sackett, J. J. Tollett and R. G. Hulet, Evidence of Bose-Einstein condensation in an atomic gas with attractive interactions, *Phys. Rev. Lett.*, **75** (1995), pp. 1687-1690.

[28] V. Bretin, S. Stock, Y. Seurin and J. Dalibard, Fast rotation of a Bose-Einstein condensate, *Phys. Rev. Lett.*, **92** (2004), pp. 050403.

[29] B. M. Caradoc-Davies, R. J. Ballagh and P. B. Blakie, Three-dimensional vortex dynamics in Bose-Einstein condensates, *Phys. Rev. A*, **62** (2000), pp. 011602.

[30] B. M. Caradoc-Davies, R. J. Ballagh and K. Burnett, Coherent dynamics of vortex formation in trapped Bose-Einstein condensates, *Phys. Rev. Lett.*, **83** (1999), pp. 895-898.

[31] Y. Castin and R. Dum, Bose-Einstein condensates with vortices in rotating traps, *Eur. Phys. J. D*, **7** (1999), pp. 399-412.

[32] M. M. Cerimele, M. L. Chiofalo, F. Pistella, S. Succi and M. P. Tosi, Numerical solution of the Gross-Pitaevskii equation using an explicit finite difference scheme: an application to trapped Bose-Einstein condensates, *Phys. Rev. E*, **62** (2000), pp. 1382-1389.

[33] S. -M. Chang, C. -S. Lin, T. -C. Lin and W. -W. Lin, Segregated nodal domains of two-dimensional multispecies Bose-Einstein condensates, *Physica D*, **196** (2004), pp. 341-361.

[34] S. -M. Chang, W. -W. Lin and S. -F. Shieh, Gauss-Seidel-type methods for energy states of a multi-component Bose-Einstein condensate, *J. Comput. Phys.*, **202** (2005), pp. 367-390.

[35] S. J. Chapman and G. Richardson, Motion of vortices in type II superconductors, *SIAM J. Appl. Math.*, **55** (1995), pp. 1275-1296.

[36] Z. Chen and S. Dai, Adaptive Galerkin methods with error control for a dynamical Ginzburg-Landau model in superconductivity, SIAM *J. Numer. Anal.*, **38** (2001), pp. 1961-1985.

[37] M. L. Chiofalo, S. Succi and M. P. Tosi, Ground state of trapped interacting Bose-Einstein condensates by an explicit imaginary-time algorithm, *Phys. Rev. E*, **62** (2000), pp. 7438-7444.

[38] S. T. Chui, V. N. Ryzhov and E. E. Tareyeva, Amplification of trap centers position difference in mixtures of Bose-Einstein condensates, *J. Phys.: Condens. Matter.*, **14** (2002), pp. L77-L82.

[39] J. E. Colliander and R. L. Jerrard, Vortex dynamics for the Ginzburg-Landau-Schrödinger equation, *Math. Res. Notes*, **7** (1998), pp. 333-358.

[40] S. L. Cornish, N. R. Claussen, J. L. Roberts, E. A. Cornell and C. E. Wieman, Stable ^{85}Rb Bose-Einstein condensations with widely tunable interactions, *Phys. Rev. Lett.*, **85** (2000), pp. 1795-1798.

[41] F. Dalfovo and S. Stringari, Bosons in anisotropic traps: ground state and vortices, *Phys. Rev. A*, **53** (1996), pp. 2477-2485.

[42] K. B. Davis, M. -O. Mewes, M. R. Andrews, N. J. van Druten, D. S. Durfee, D. M. Kurn and W. Ketterle, Bose-Einstein condensation in a gas of sodium atoms, *Phys. Rev. Lett.*, **75** (1995), pp. 3969-3973.

[43] J. Deang, Q. Du and M. Gunzburger, Stochastic dynamics of Ginzburg-Landau vortices in superconductors, *Phys. Rev. B*, **64** (2001), pp. 052506.

[44] J. Deang, Q. Du, M. Gunzburger and J. Peterson, Vortices in superconductors: modelling and computer simulations, *Phil. Tran. Roy. Soc. London. A*, **355** (1997), pp. 1957-1968.

[45] R. J. Dodd, Approximate solutions of the nonlinear Schrödinger equation for ground and excited states of Bose-Einstein condensates, *J. Res. Natl. Inst. Stand. Technol.*, **101** (1996), pp. 545-552.

[46] F. P. Dos Santos, J. Leonard, J. Wang, C. J. Barrelet, F. Perales, E. Rasel, C. S. Unnikrishnan, M. Leduc and C. Cohen-Tannoudji, Bose-Einstein condensation of metastable Helium, *Phys. Rev. Lett.*, **86** (2001), pp. 3459-3462.

[47] Q. Du, Finite element methods for the time dependent Ginzburg-Landau model of superconductivity, *Comp. Math. Appl.*, **27** (1994), pp. 119-133.

[48] Q. Du, Diverse vortex dynamics in superfluids, *Contemp. Math.*, **329** (2003), pp. 105-117.

[49] Q. Du, M. Gunzburger and J. S. Peterson, Analysis and approximation of the Ginzburg-Landau model of superconductivity, *SIAM Rev.*, **34** (1992), pp. 54-81.

[50] Q. Du, M. Gunzburger and J. Peterson, Computational simulation of type-II superconductivity including pinning phenomena, *Phys. Rev. B*, **51** (1995), pp. 16194-16203.

[51] Q. Du and W. Zhu, Stability analysis and application of the exponential time differencing schemes, *J. Comput. Math.*, **22** (2004), pp. 200-209.

[52] V. Dunjko, V. Lorent and M. Olshanii, Bosons in cigar-shaped traps: Thomas-Fermi regime, Tonks-Girardeau regime, and in between, *Phys. Rev. Lett.*, **86** (2001), pp. 5413-5416.

[53] W. E, Dynamics of vortices in Ginzburg-Landau theories with applications to superconductivity, *Physica D*, **77** (1994), pp. 383-404.

[54] M. Edwards and K. Burnett, Numerical solution of the nonlinear Schrödinger equation for small samples of trapped neutral atoms, *Phys. Rev. A*, **51** (1995), pp. 1382-1386.

[55] M. Edwards, R. J. Dodd, C. W. Clark, P. A. Ruprecht and K. Burnett, Properties of a Bose-Einstein condensate in an anisotropic harmonic potential, *Phys. Rev. A*, **53** (1996), pp. R1950-R1953.

[56] A. Einstein, Quantentheorie des einatomigen idealen gases, *Sitzber. Kgl. Preuss. Akad. Wiss.*, **261** (1924).

[57] P. Engels, I. Coddington, P. Haijan and E. Cornell, Nonequilibrium effects of anistropic compression applied to vortex lattices in Bose-Einstein condensates, *Phys. Rev. Lett.*, **89** (2002), pp. 100403.

[58] B. D. Esry, C. H. Greene, J. P. Burke, Jr. and J. L. Bohn, Hartree-Fock theory for double condensates, *Phys. Rev. Lett.*, **78** (1999), pp. 3594-3597.

[59] D. L. Feder, C. W. Clark and B. I. Schneider, Nucleation of vortex arrays in rotating anisotropic Bose-Einstein condensates, *Phys. Rev. A*, **61** (1999), pp. 011601.

[60] D. L. Feder, C. W. Clark and B. I. Schneider, Vortex stability of interacting Bose-Einstein condensates confined in anisotropic harmonic traps, *Phys. Rev. Lett.*, **82** (1999), pp. 4956-4959.

[61] D. L. Feder, A. A. Svidzinsky, A. L. Fetter and C. W. Clark, Anomalous modes drive vortex dynamics in confined Bose-Einstein condensates, *Phys. Rev. Lett.*, **86** (2001), pp. 564-567.

[62] A. L. Fetter, Vortex stability in a trapped Bose Condensate, *Journal of Low Temperature Physics*, **113** (1998), pp. 189-194.

[63] A. L. Fetter and J. D. Walecka, Quantum theory of many-particle systems, *McGraw-Hill, San Francisco*, 1971.

[64] B. Fornberg and T. A. Driscoll, A fast spectral algorithm for nonlinear wave equations with linear dispersion, *J. Comput. Phys.*, **155** (1999), pp. 456-467.

[65] D. G. Fried, T. C. Killian, L. Willmann, D. Landhuis, S. C. Moss, D. Kleppner and T. J. Greytak, Bose-Einstein condensation of atomic hydrogen, *Phys. Rev. Lett.*, **81** (1998), pp. 3811-3814.

[66] J. J. García-Ripoll and V. M. Pérez-García, Stability of vortices in inhomogeneous Bose-Einstein condensates subject to rotation: a three-dimensional analysis, *Phys. Rev. A*, **60** (1999), pp. 4864-4874.

[67] J. J. García-Ripoll and V. M. Pérez-García, Vortex nucleation and hysteresis phenomena in rotating Bose-Einstein condensates, *Phys. Rev. A*, **63** (2001), pp. 041603.

[68] J. J. García-Ripoll and V. M. Pérez-García, Vortex bending and tightly packed vortex lattices in Bose-Einstein condensates, *Phys. Rev. A*, **64** (2001), pp. 053611.

[69] J. J. García-Ripoll and V. M. Pérez-García and V. Vekslerchik, Construction of exact solutions by spatial translations in inhomogeneous nonlinear Schrödinger equations, *Phys. Rev. E*, **64** (2001), pp. 056602.

[70] T. K. Ghosh, Vortex formation in a slowly rotating Bose-Einstein condensate confined in a harmonic-plus-Gaussian laser trap, *Eur. Phys. J. D*, **31** (2004), pp. 101-105.

[71] R. Glowinski and P. Le Tallec, Augmented Lagrangian and operator splitting methods in nonlinear mechanics, *SIAM, Philadelphia*, 1989.

[72] D. S. Hall, M. R. Matthews, J. R. Ensher, C. E. Wieman and E. A. Cornell, Dynamics of component separation in a binary mixture of Bose-Einstein condensates, *Phys. Rev. Lett.*, **81** (1998), pp. 1539-1542.

[73] D. S. Hall, M. R. Matthews, C. E. Wieman and E. A. Cornell, Measurements of relative phase in two-component Bose-Einstein condensates, *Phys. Rev. Lett.*, **81** (1998), pp. 1543-1546.

[74] A. D. Jackson, G. M. Kavoulakis and C. J. Pethick, Solitary waves in clouds of Bose-Einstein condensed atoms, *Phys. Rev. A*, **58** (1998), pp. 2417-2422.

[75] B. Jackson, J. F. McCann and C. S. Adams, Vortex formation in dilute inhomogeneous Bose-Einstein condensates, *Phys. Rev. Lett.*, **80** (1998), pp. 3903-3906.

[76] B. Jackson, J. F. McCann and C. S. Adams, Vortex line and ring dynamics in trapped Bose-Einstein condensates, *Phys. Rev. A*, **61** (2000), pp. 013604.

[77] B. Jackson, J. F. McCann and C. S. Adams, Dissipation and vortex creation in Bose-Einstein condensed gases, *Phys. Rev. A*, **61** (2000), pp. 051603.

[78] D. Jaksch, C. Bruder, J. I. Cirac, C. W. Gardiner and P. Zoller, Cold bosonic atoms in optical lattices, *Phys. Rev. Lett.*, **81** (1998), pp. 3108-3111.

[79] R. L. Jerrard and H. M. Soner, Dynamics of Ginzburg-Landau vortices, *Arch. Rational Mech. Anal.*, **142** (1998), pp. 99-125.

[80] H. Y. Jian, The dynamical law of Ginzburg-Landau vortices with a pinning effect, *Appl. Math. Lett.*, **13** (2000), pp. 91-94.

[81] H. Y. Jian and B. H. Song, Vortex dynamics of Ginzburg-Landau equations in inhomogeneous superconductors, *J. Diff. Eqs.*, **170** (2001), pp. 123-141.

[82] H. Y. Jian and Y. D. Wang, Ginzburg-Landau vortices in inhomogeneous superconductor, *J. Partial Diff. Eqs.*, **15** (2002), pp. 45-60.

[83] O. Karakashian and C. Makridakis, A space-time finite element method for the nonlinear Schrödinger equation: the discontinuous Galerkin method, *Math. Comput.*, **67** (1998), pp. 479-499.

[84] K. Kasamatsu, M. Tsubota and M. Ueda, Nonlinear dynamics of vortex lattice formation in a rotating Bose-Einstein condensate, *Phys. Rev. A*, **67** (2003), pp. 033610.

[85] K. Kasamatsu, M. Tsubota and M. Ueda, Vortex phase diagram in rotating two-component Bose-Einstein condensates, *Phys. Rev. Lett.*, **91** (2003), pp. 150406.

[86] K. Kasamatsu, M. Tsubota and M. Ueda, Vortices in multicomponent Bose-Einstein condensates, *Int. J. Mod. Phys. B*, **19** (2005), pp. 1835-1904.

[87] M. K. Kwong, On the one-dimensional Ginzburg-Landau BVPs, *Diff. Int. Equations*, **8** (1995), pp. 1395-1405.

[88] M. -C. Lai, W. -W. Lin and W. Wang, A fast spectral/difference method without pole conditions for Poisson-type equations in cylindrical and spherical geometries, *IMA J. Numer. Anal.*, **22** (2002), pp. 537-548.

[89] M. -C. Lai and W. -C. Wang, Fast direct solvers for Poisson equation on 2D polar and spherical geometries, *Numer. Methods Partial Differential Eqs.*, **18** (2001), pp. 56-68.

[90] L. D. Landau and E. M. Lifshitz, Quantum mechanics: non-relativistic theory, *Pergamon Press*, New York, 1977.

[91] O. Lange and B. J. Schroers, Unstable manifolds and Schrödinger dynamics of Ginzburg-Landau vortices, *Nonlinearity*, **15** (2002), pp. 1471-1488.

[92] P. Leboeuf and N. Pavloff, Bose-Einstein beams: coherent prepagation through a guide, *Phys. Rev. A*, **64** (2001), pp. 033602.

[93] E. H. Lieb, R. Seiringer and J. Yngvason, Bosons in a trap: a rigorous derivation of the Gross-Pitaevskii energy functional, *Phys. Rev. A*, **61** (2000), pp. 043602.

[94] F. -H. Lin, Some dynamical properties of Ginzburg-Landau vortices, *Comm. Pure. Appl. Math.*, **XLIX** (1996), pp. 323-359.

[95] F. -H. Lin, Complex Ginzburg-Landau equations and dynamics of vortices, filaments and codimension-2 submanifolds, *Comm. Pure Appl. Math.*, **51** (1998), pp. 385-441.

[96] F. -H. Lin and Q. Du, Ginzburg-Landau vortices: dynamics, pinning, and hysteresis, *SIAM J. Math. Anal.*, **28** (1997), pp. 1265-1293.

[97] F. -H. Lin and J. X. Xin, On the dynamical law of the Ginzburg-Landau vortices on the plane, *Comm. Pure Appl. Math.*, **52** (1999), pp. 1189-1212.

[98] E. Lundh, C. J. Pethick and H. Smith, Vortices in Bose-Einstein-condensed atomic clouds, *Phys. Rev. A*, **58** (1998), pp. 4816-4823.

[99] K. W. Madison, F. Chevy, W. Wohlleben and J. Dalibard, Vortex formation in a stirred Bose-Einstein condensate, *Phys. Rev. Lett.*, **84** (2000), pp. 806-809.

[100] M. R. Matthews, B. P. Anderson, P. C. Haljan, D. S. Hall, C. E. Wieman and E. A. Cornell, Vortices in a Bose-Einstein condensate, *Phys. Rev. Lett.*, **83** (1999), pp. 2498-2501.

[101] M. R. Matthews, D. S. Hall, D. S. Jin, J. R. Ensher, C. E. Wieman and E. A. Cornell, Dynamical response of a Bose-Einstein condensate to a discontinuous charge in internal state, *Phys. Rev. Lett.*, **81**(1998), pp. 243-247.

[102] G. Modugno, G. Ferrari, G. Roati, R. J. Brecha, A. Simoni and M. Inguscio, Bose-Einstein condensation of potassium atomis by sympathetic cooling, *Science*, **294** (2001), pp. 1320-1322.

[103] M. Modugno, L. Pricoupenko and Y. Castin, Bose-Einstein condensates with a bent vortex in rotating traps, *Eur. Phys. J. D*, **22** (2003), pp. 235-257.

[104] P. Muruganandam and S. K. Adhikari, Bose-Einstein dynamics in three dimensions by the pseudospectral and finite-difference methods, *J. Phys. B: At. Mol. Opt. Phys.*, **36** (2003), pp. 2501-2513.

[105] J. C. Neu, Vortices in complex scalar fields, *Physica D*, **43** (1990), pp. 385-406.

[106] J. C. Neu, Vortex dynamics of the nonlinear wave equation, *Physica D*, **43** (1990), pp. 407-420.

[107] Y. N. Ovchinnikov and I. M. Sigal, The Ginzburg-landau equation I. Static vortices, *Part. Diff. Eqn and their Appl. CRM proceedings*, **12** (1997), pp. 199-220.

[108] Y. N. Ovchinnikov and I. M. Sigal, The Ginzburg-Landau equation III. vortex dynamics, *Nonlinearity*, **11** (1998), pp. 1277-1294.

[109] Y. N. Ovchinnikov and I. M. Sigal, Long-time behaviour of Ginzburg-Landau vortices, *Nonlinearity*, **11** (1998), pp. 1295-1309.

[110] Y. N. Ovchinnikov and I. M. Sigal, Asymptotic behavior of solutions of Ginzburg-Landau and related equations, *Rev. Math. Phys.*, **12** (2000), pp. 287-299.

[111] Y. N. Ovchinnikov and I. M. Sigal, Symmetric breaking solutions of the Ginzburg-Landau equation, *Journal of Experimental and Theoretical Physics*, **99** (2004), pp. 1090-1107.

[112] L. Peres and J. Rubinstein, Vortex dynamics in U(1) Ginzburg-Landau models, *Physica D*, **64** (1993), pp. 299-309.

[113] V. M. Pérez-García and J. J. García-Ripoll, Two-mode theory of vortex stability in multicomponent Bose-Einstein condensates, *Phys. Rev. A*, **62** (2000), pp. 033601.

[114] C. J. Pethick and H. Smith, Bose-Einstein condensation in dilute gases, *Cambridge University Press*, 2002.

[115] L. M. Pismen and J. D. Rodriguez, Mobility of singularities in the dissipative Ginzburg-Landau equation, *Phys. Rev. A*, **42** (1990), pp. 2471-2474.

[116] L. P. Pitaevskii and S. Stringari, Bose-Einstein condensation, *Clarendon Press*, 2003.

[117] N. -P. Proukakis, Microscopic mean field theories of trapped Bose-Einstein condensates, Dphil thesis, New colledge, University of Oxford, 1997.

[118] F. Riboli and M. Modugno, Topology of the ground state of two interacting Bose-Einstein condensates, *Phys. Rev. A*, **65** (2002), pp. 063614.

[119] A. Robert, O. Sirjean, A. Browaeys, J. Poupard, S. Nowak, D. Boiron, C. I. Westbrook and A. Aspect, A Bose-Einstein condensate of metastable atoms, *Science*, **292** (2001), pp. 461-464.

[120] D. S. Rokhsar, Vortex stability and persistent currents in trapped Bose gases, *Phys. Rev. Lett.*, **79** (1997), pp. 2164-2167.

[121] P. Rosenbusch, V. Bretin and J. Dalibard, Dynamics of a single vortex line in a Bose-Einstein condensate, *Phys. Rev. Lett.*, **89** (2002), pp. 200403.

[122] P. A. Ruprecht, M. J. Holland, K. Burnett and M. Edwards, Time-dependent solution of the nonlinear Schrödinger equation for Bose-condensed trapped neutral atoms, *Phys. Rev. A*, **51** (1995), pp. 4704-4711.

[123] V. Schweikhard, I. Coddington, P. Engels, V. P. Mogendorff and E. A. Cornell, Rapidly rotating Bose-Einstein condensates in and near the lowest Landau level, *Phys. Rev. Lett.*, **92** (2004), pp. 040404.

[124] R. Seiringer, Gross-Pitaevskii theory of the rotating Bose gas, *Comm. Math. Phys.*, **229** (2002), pp. 491-509.

[125] P. Sokol, Bose-Einstein condensation, *Cambridge University Press*, 1995.

[126] G. Strang, On the construction and comparison of difference schemes, *SIAM J. Numer. Anal.*, **5** (1968), pp. 506-517.

[127] A. A. Svidzinsky and A. L. Fetter, Dynamics of a vortex in a trapped Bose-Einstein condensate, *Phys. Rev. A*, **62** (2000), pp. 063617.

[128] M. Tinkham, Introduction to superconductivity, 2nd edition, (Dover Publications, NY, 2004).

[129] M. Tsubota, K. Kasamatsu and T. Araki, Dynamics of quantized vortices in superfluid helium and rotating Bose-Einstein condensates, cond-mat/0309364.

[130] M. Tsubota, K. Kasamatsu and M. Ueda, Vortex lattice formation in a rotating Bose-Einstein condensate, *Phys. Rev. A*, **65** (2002), pp. 023603.

[131] H. Wang, Numerical studies on the split step finite differnce method for nonlinear Schrödinger equations, *Appl. Math. Comput.*, **170** (2005), pp. 17-35.

[132] T. Weber, J. Herbig, M. Mark, H. -C. Nägerl and R. Grimm, Bose-Einstein condensation of Cesium, *Science*, **299** (2003), pp. 232.

[133] J. Weiner, V. S. Bagnato, S. Zilio and P. S. Julienne, Experiments and theory in cold and ultracold collisions, *Rev. Mod. Phys.*, **71** (1999), pp. 1-85.

[134] M. I. Weinstein and J. Xin, Dynamics stability of vortex solutions of Ginzburg-Landau and nonlinear Schrödinger equations, *Comm. Math. Phys.*, **180** (1996), pp. 389-428.

[135] J. P. Wolfe, J. L. Lin and D. W. Snoke, Bose-Einstein condensation, *Cambridge University Press*, 1995.

[136] H. Yoshida, Construction of higher order symplectic integrators, *Phys. Lett. A*, **150** (1990), pp. 262-268.

[137] E. Zaremba, T. Nikuni and A. Griffin, Dynamics of trapped Bose gases at finite temperatures, *Journal of Low Temperature Physics*, **116** (1999), pp. 277-345.

[138] Y. Zhang and W. Bao, Dynamics of the center of mass in rotating Bose-Einstein condensates, *Appl. Numer. Math.*, to appear.

[139] Y. Zhang, W. Bao and Q. Du, Numerical simulation of vortex dynamics in Ginzburg-Landau-Schrödinger equation, preprint.

[140] Y. Zhang, W. Bao and Q. Du, The dynamics and interaction of quantized vortices in Ginzburg-Landau-Schrödinger equation, preprint.

[141] Y. Zhang and W. Bao, Dynamics of rotating two-component Bose-Einstein condensates and its efficient computation, preprint.

[142] M. W. Zwierlein, J. R. Abo-Shaeer, A. Schirotzek, C. H. Schunck and W. Ketterle, Vortices and superfluidity in a strongly interacting fermi gas, *Nature*, **435** (2005), pp. 1047.

[143] M. W. Zwierlein, C. A. Stan, C. H. Schunck, S. M. F. Raupach, S. Gupta, Z. Hadzibabic and W. Ketterle, Observation of Bose-Einstein condensation of molecules, *Phys. Rev. Lett.*, **91** (2003), pp. 250401.

List of Publications

1). W. Bao and Y. Zhang, Dynamics of the ground state and central vortex states in Bose-Einstein condensation, *Math. Mod. Meth. Appl. Sci.*, **15** (2005), pp. 1863-1896.

2). W. Bao, Q. Du and Y. Zhang, Dynamics of rotating Bose-Einstein condensates and their efficient and accurate numerical computation, *SIAM J. Appl. Math.*, **66** (2006), pp. 758-786.

3). W. Bao, F. Lim and Y. Zhang, Energy and chemical potential asymptotics for the ground state of Bose-Einstein condensates in the semiclassical regime, *Trans. Theory Stat. Phys.*, to appear.

4). Y. Zhang and W. Bao, Dynamics of the center of mass in rotating Bose-Einstein condensates, *Appl. Numer. Math.*, to appear.

5). Y. Zhang, W. Bao and Q. Du, Numerical simulation of vortex dynamics in Ginzburg-Landau-Schrödinger equation, preprint.

6). Y. Zhang and W. Bao, Dynamics of rotating two-component Bose-Einstein condensates and its efficient computation, preprint.

7). Y. Zhang, W. Bao and Q. Du, The dynamics and interaction of quantized vortices in Ginzburg-Landau-Schrödinger equation, preprint.

8). Vortex lattice in rotating Bose-Einstein condensates with strong repulsive interaction, in preparation.

MATHEMATICAL ANALYSIS AND NUMERICAL SIMULATION OF BOSE-EINSTEIN CONDENSATION

ZHANG YANZHI

NATIONAL UNIVERSITY OF SINGAPORE

2006

MATHEMATICAL ANALYSIS AND NUMERICAL SIMULATION OF BOSE-EINSTEIN CONDENSATION

ZHANG YANZHI

2006